Optical Multiple Input and Multiple Output (MIMO) in Multimode Fibre

Ran Li

Linacre College

Department of Engineering Science

University of Oxford

A thesis submitted for the degree of

Doctor of Philosophy

Michaelmas Term 2013

I would like to dedicate this thesis to my parents and my wife.

Abstract

Recently, there has been a dramatic increase in the amount of data transmission within short range local area networks (LAN). Multimode fibre (MMF) is widely used in local area networks because of its coupling and alignment along with the low cost of related components. Graded index MMF has become common due to the reduction in pulse spreading; however, as demands for high bandwidth increase towards a future gigabit rate network, the typical MMF using conventional transmission methods will not be suitable. Meanwhile, this increasing demand for high speed data transmission will soon reach the Shannon capacity limit of single mode fibres. After multiple input and multiple output (MIMO) technology was successfully used in wireless communication, the researcher realised that the same idea could also be applied to an optical fibre network. Optical MIMO techniques are gaining interest in order to create parallel channels over orthogonal modes in a MMF or a few mode fibre (FMF). This approach could lead to a significant increase in the bandwidth distance product and be employed in the next 40Gb/s or even 100Gb/s optical fibre transmission systems. Generally speaking, optical MIMO appears to be the best solution to the bandwidth limitation problem in either short distance MMF or long distance FMF systems.

This thesis focuses on designing a simple, cost-effective, and energy efficient optical MIMO system based on MMFs. This proposed system can be realised by combining radial offset launching and annular multi-segment detectors. First, in the initial work, we performed a theoretical and numerical study of the key impairments of MMFs, and the mode propagation in an MMF was analysed mathematically. The variation in electrical field intensity for linearly polarised (LP) modes in the core region of an MMF and the analytical solutions for power coupling coefficients in either radial

offset launching or centre launching were presented. In addition, the modal time delays, impulse response, and transfer function were all introduced. Subsequently, the near field intensity pattern (NFP) was simulated at the output facet of the MMF, which indicated that the overall NFP suffered from blurring when it contained mode mixing, and that the intensity pattern was particularly sensitive to the random phase. According to the spatial distribution of the NFP, the annular detector can be exploited more efficiently. All of the results were calculated and plotted using the MATLAB program.

Secondly, the optical MIMO model in the multimode fibre was briefly summarised, including the MIMO channel matrix H expression, a mathematical expression of optical MIMO capacity, MIMO channel estimation and an equalization method. Two metrics can be used to characterise the MIMO channel performance: condition number and crosstalk at each receiver. The numerical results demonstrated that the new type of annular multi-segment detector exhibits superior performance compared to the conventional multiple single mode fibre (SMF) detectors, making them attractive for future optical MIMO systems.

Finally, the core work of this thesis can be divided into two parts: the modelling of a 10Gb/s intensity modulation direct detection (IM-DD) optical MIMO MMF system; and the modelling of an advanced 10Gb/s coherent differential phase shift keying (DPSK) MIMO FMF system. In both simulation systems, the important transmission parameters of intra-group mode mixing, modal dispersion, chromatic dispersion, and mode attenuation were considered and discussed in detail. In the IM-DD optical MIMO system, the optimization of the transceiver can be based upon the laser spot

size and the power flux distribution emitted by the transmitter. Results from the simulation showed that the intra-group mode mixing had a limited impact on system performance, and due to its inability to compensate for linear impairments, the IM-DD optical MIMO was not favourable for long distance transmission systems. Nevertheless, the new type of optical fibre FMF seems to be the most promising candidate for use in long haul transmission systems. Therefore, the well-known DPSK modulation format in conjugation with the coherent detection deployed in FMF was studied. Both heterodyne and intradyne detection schemes were analysed followed by mathematical derivation and numerical simulation; the results illustrated that similar system performances can be achieved in both schemes. Meanwhile, the coherent DPSK simulation results also demonstrated that the linear impairments were almost compensated by the frequency domain MIMO equalization process, which resulted in system performance being independent to transmission distance for up to 10km. This advantage proved that the coherent optical DPSK MIMO system can be employed in long haul networks. As with an IM-DD optical MIMO system, optimization of a coherent MIMO system was also possible. However, in contrast to the optimization of an IM-DD MIMO system, a trade-off had to be made between sufficient spatial diversity at the transceiver and differential modal delay caused by modal dispersion; consequently, the numerical results showed that the proposed coherent optical DPSK MIMO gained reasonable good results without using any active device, such as a spatial light modulator and a mode converter. In conclusion, this proposed optical MIMO system provided easy implementation and integration and is feasible for use in future optical communication systems.

Acknowledgements

First and foremost I would like to express my gratitude to my supervisor Dr. Frank Payne for his patience, help and expert guidance during my DPhil study, and also for his precious advice to write up this thesis. I would also to thank my supervisor for his endless support when I faced problems in either my research work or personal life.

At the same time, I am grateful to Dr. Xianqing Jin, the post doctor in our research group, for his valuable advice and helpful discussion. Thanks to all of the colleagues in our office who have been helpful and supportive throughout my stay.

Secondly, I would like to thank the director of graduate study Professor. David Murray and college senior tutor Dr. Hazel Assender for their understanding and support during my hard time.

I am particularly grateful to my parents for providing me with the opportunity to progress educationally and their unconditional belief in me through all my studies. Their support gave me enough confidence to make me believe in myself, so I would also like to thank my parents for their constant support, encouragement and love.

Finally, I have to say a special and important thank you to my wife Xiaolu for her unconditional love, encouragement, understanding, and care. I have really appreciated what she has contributed during this time.

Table of Contents

List of Figures

List of Tables

List of Acronyms

MIMO	multiple-input-multiple-output
LP	linearly polarized
IM-DD	intensity modulation and direct detection
LED	light emitting diode
MGDM	mode group diversity multiplexing
MMF	multimode fibre
SCM	Sub-carrier multiplexing
SISO	single Input and single output
SNR	signal to noise ratio
WDM	wavelength division multiplexing
LED	light emitting diode
DMD	differential mode delay
COMIMO	coherent optical multiple input and multiple output
GI	graded Index
EDC	electronic dispersion compensation
ISI	inter-symbol Interference
DPSK	differential phase shift keying
NA	numerical aperture
OFL	overfilled Launch
VCSEL	vertical cavity surface emitting laser
EMB	effective modal bandwidth
MPD	mode power distribution
FMF	few mode fibre
EM	electromagnetic
RMS	root mean square
NFP	near field pattern
ZF	zero forcing
MMSE	minimum mean square errors
BER	bit error rate
PRBS	pseudorandom binary sequence
AWGN	additive white Gaussian noise
NA	numerical aperture

SLM	spatial light modulator
MDM	mode division multiplexing
CSI	channel state information
NAPF	normalized annular power flux
EF	encircled flux
CW	continuous wave
MZIM	Mach-Zehnder intensity modulator
MFD	modal field diameter
OOK	on-off keying
DPSK	differential phase shift keying
VOA	optical attenuator
LO	local oscillator
IF	intermediate frequency
ASE	amplified spontaneous emission noise
EDFA	Erbium doped fibre amplifier
OSNR	optical signal to noise ratio
i.i.d	independent and identically distributed random variables
PMD	polarization mode dispersion
CD	chromatic dispersion
PSK	phase shift keying modulation
FFE	feed forward equalizer
DFE	decision feedback equalizer
IIR	infinite impulse response
FIR	finite impulse response
FWHM	full width at half maximum

Chapter 1: Introduction

In this chapter, an overview of a multimode fibre communication network is introduced. The related works and current state of multimode fibre bandwidth improvement techniques are briefly summarised. Finally, the objective of this research work and the structure of the thesis are both outlined at the end of this chapter.

1.1 Multimode fibre communication network

Since optical fibres were first used in telecommunication links, they have provided high speed and reliable communications. Communication systems can be characterised by their geographical range, which varies from long haul networks to short distance connections in which the distance does not exceed a few kilometres. Multimode fibre (MMF) can be used in many areas such as industry, transport, medicine and defence. Typically, MMF is predominantly used in high speed and short-range networks, for instance, local access networks (LAN), building networks, and super computer networks [1]. In access networks, fibre to the home appears to be a promising solution to meet the future requirements of broadband communications. MMFs have become the dominant transmission medium in LANs or backbone networks because of the ease of coupling, connecting, aligning, and the low cost of related components. Due to their large core diameter and numerical aperture (NA), MMFs can be easily coupled with more light than single mode fibres with narrow core diameter. This significant advantage allows the use of low cost optical light sources such as light emitting diodes (LEDs) and vertical cavity surface emitting lasers (VCSELs), which operate in the 850nm wavelength window. At the same time, when compared with the expensive transceiver design in a single mode fibre network,

the inexpensive MMF network makes MMF a good choice in short distance networks [2].

At the beginning of the optical fibre transmission age in 1970, MMFs used LEDs to provide optical links with low bit rates (below 200Mb/s) [3]. The graded index MMF became a predominant type of MMF due to its reduction in intermodal dispersion, which resulted in reduced pulse spreading. Building backbone links were mainly built using 62.5/125μm graded index MMF, mostly for less than 300 meters [4-6]. The 10Mb/s Ethernet used LEDs with wavelength of 850nm, while the 100Mb/s one used 1300nm LEDs due to the lower attenuation and dispersion at a wavelength of 1300nm [7-9]. To further increase the data rate, LEDs cannot play a major role in high speed links, which are primarily created by providing a large time delay difference between each mode in the MMF. An alternative solution uses spectrally narrow, highly collimated VCSEL beams as an efficient light source instead of LEDs, especially for data rates exceeding 100Mb/s [10]; however, this strategy requires new MMF launching conditions. In 2003, a 500m 1Gb/s network solution using 62.5μm MMF and short wavelength (830-860nm) laser transceivers with VCSELs was developed [11]. Furthermore, a 10Gb/s solution using 50μm MMF fibre achieved a standard building-backbone link of up to 300 metres [12].

Apart from the development of various optical sources, the high bandwidth and laser launch optimized 50μm-core MMFs (OM3, OM4) have proven to be the most cost-effective medium in high speed and short range transmission networks. The OM3 and more recently OM4 fibres can support 10Gb/s at 850nm (10G-BASE-S) over 300 and 400m respectively, at a low bit error rate ($<10^{-12}$) without forward error correction [1,

13-15]. In order to boost the bandwidth even more, the commercial 1300nm VCSEL became available and was deployed in the current LANs [10, 16]. Although the 1300nm VCSELs are readily available, their high cost causes the 850nm VCSEL to still be the preferred optical source in short distance networks. By the end of last decade, the low cost, low power consumption, circular output beam, and fast direct modulation of VCSELs could reliably support 10Gb/s and potentially 40Gb/s at a wavelength of 850nm [1, 17].

The current internet traffic growth rate is approximately 100% each year [3, 12], making it necessary to increase our transmission capacity and bandwidth in the existing fibre infrastructure. In 2010, a new high speed IEEE 40/100Gbps standard (802.3ba) was approved to allow OM3 and OM4 fibres to be used to transmit for 100 and 150m, respectively [18]. The combination of 850nm VCSEL with 5μm oxide apertures and integrated mode filter in MMFs has already been demonstrated to enable error free (bit error rate $<10^{-12}$) transmission at 25Gbit/s over 500m of OM3 fibre [19]. An improved high speed oxide confined 850nm VCSEL [20] can achieve error free data transmission at 47Gb/s at room temperature and at 40Gb/s under extreme conditions (85 degrees Celsius) [21].

More recently, researchers have begun to study the interaction between chromatic dispersion and modal dispersion in MMFs since the optical spectra of VCSELs exhibit spatial dependence when the transversal multimode VCSELs are coupled to MMFs. Conceptually, the lowest order modes of the optical source that exhibit the longest wavelength mainly couple to the lowest order modes in MMF; therefore, chromatic dispersion will delay the lowest order modes compared with the higher

order modes. Consequently, chromatic dispersion compensated MMFs can be designed by carefully changing the refractive index profiles of MMFs to allow differential mode delays with an opposite sign [22]. The use of chromatic dispersion compensated MMFs could achieve 40/100GbE links of up to 400m and bridge 150m at 25Gbps without equalization or forward error correction [23]. This would lead to a significant improvement in transmission distance.

Currently, the expected bit rate of an MMF link has jumped to 40 or 100Gb/s from most service providers; the conventional transmission method of MMF will not be suitable for future gigabit links. The new challenge facing us now is to utilize the deployed MMFs in 40/100Gbps networks for short distances (<10km). Although significant improvement in transmission speed was made in the last ten years, the exploitation of the MMF itself has still not been fully considered. When MIMO technology was successfully used in wireless communications, researchers realised that the same principle could also be applied to optical MMF networks. The simultaneous transmission of vast signals through different guided modes in either MMFs [24-27] or few mode fibres (FMFs) [28-30] is currently attracting enormous attention as it seems to be the most promising and cost-effective solution to the imminent capacity crunch of optical fibre communication systems [31, 32]. This optical MIMO approach could lead to a significant improvement in bandwidth and be employed in the next 40Gb/s and 100Gb/s networks.

1.2 Improving multimode fibre bandwidth

In optical communication systems, the term bandwidth-distance product is often used to compare the performances of different fibre links and measure the transmission capacities of optical fibre links in $MHz \cdot Km$. Due to the increased demand for high-speed LAN networks, there is much interest in studying the effective use of existing MMFs. A brief review of these research methods is necessary. In this chapter, research on high bit rate MMF transmission networks is reviewed, including selective mode excitation, refractive index profile enhancement, electronic dispersion compensation, subcarrier multiplexing, wavelength division multiplexing (WDM), and the recently developed and important optical MIMO technology. Lastly, the objectives and organization of the thesis are introduced.

1.2.1 Selective mode excitation

The conventional excitation method is designed to uniformly excite all the guided modes within an MMF using a low intensity LED or laser; this is called overfilled launching. Overfilled launching can only achieve 500MHz·Km at a wavelength of 1.3μm (low material dispersion window) [33-35]. Several studies have shown that the transmission bandwidth can be increased significantly by using restricted offset launch techniques [36, 37]. The basic idea of selective excitation is to excite only a subset of all of the propagation modes with a similar modal propagation constant in MMF. This greatly reduces the ISI, resulting in an enhancement in bandwidth. The offset launching technique has been experimentally and theoretically studied by Raddatz [34, 35]. By radially offsetting the laser spot from the core centre, the number of excited modes was largely reduced compared to the number of excited

modes in conventional overfilled launch (OFL). As a result, it was successfully demonstrated that the bandwidth can be increased by four times compared to the conventional launching method [34]. An experimental study also demonstrated that a bandwidth-distance product of 7.5Gb/s.km can be achieved using a standard MMF by employing an offset launch, indicating the feasibility of transmitting multiple gigabits over 1 to 2km in MMF links [35]. Even though offset launching provides a higher bandwidth in MMF links, it is difficult to generate repeatable offset launching in practice without knowing the exact offset value because of small alignment tolerances of less than 10μm [36]. However, this problem can be overcome by using a fibre with an angled (20 degree) end surface, which can produce bandwidth improvement with a large alignment tolerance [34]. However, the precise alignment and geometry of the transmitter and receiver are still limiting factors.

Several other proposed methods can be used for MMF excitation, including: employing a computer-generated optical mask [38]; creating a line launch using a passive beam shaper on the MMF front facet, enabling the launching of a single mode group [39]; using spatial light modulation (binary phase modulator) at the MMF input [40]; and combining spatial light modulation with binary phase spatial light filters [41, 42]. The drawback of the above methods is the need for an extra optic lens and a spatial light modulator (SLM), which increases the cost and complexity.

1.2.2 Electronic dispersion compensation (EDC)

The most robust and cost-effective method to mitigate the ISI caused by modal dispersion is electronic equalization. Electronic dispersion compensation (EDC) can be used in either the analog or digital domain and implemented at the receiving end

by an equalization process. In general, the electronic equalization of 10Gb/s MMF links employs either a feed forward equalizer (FFE) or a decision feedback equalizer (DFE) as the adaptive filter. An FFE is actually a finite impulse response (FIR) filter, while a DFE is an infinite impulse response (IIR) filter [43-47]. Many reports have shown that FIR filters are more stable than IIR filters; however, DFE filters have a higher capability to compensate for the distorted signal in 10Gb/s MMF networks [47-49].

FIR filters manipulate the inverse impulse response of the fibre dispersive channel in order to compensate the distorted signal. This can be completed by matching the time-delayed weights to the amplitude of the MMF impulse response by using the least mean squares algorithm, minimising the mean square error, or by using other advanced algorithms to compensate the errors [44, 45, 48, 50]. In 2002, a researcher used a decision feedback equalizer to demonstrate a 10Gb/s transmission through a 1.5km 62.5μm MMF [50]. Furthermore, the demonstration of a third order infinite impulse response (IRR) filter that could equalize a 40Gb/s data stream over 50m in MMF links with a compensation of over 90% of the modal dispersion has been reported [51]. Recently, with the advances in integrated circuit technology, a 7-tap FIR equalizer based on a tuneable active delay line can successfully operate from 10 to 25Gb/s was realised in a 28-nm low power CMOS [52]. Although the EDC is capable of adapting the variation in the response of different fibre and launching conditions, faster and more accurate circuits for processing the received signals are needed. In addition, for the equalization strategies implemented in 25Gb/s networks, the thermal noise of the receiver, the large area of the photodiode, and the limited available power budget (VCSEL based MMF links) all remain significant challenges

[53, 54], even if the impairments in MMF links can be mitigated.

1.2.3 Improvement in refractive index profile

Due to the difficulties in fabricating GI-MMF fibres with ideal refractive index profiles, some profile defects must be taken into account, such as a dip or tip at the centre of the fibre core region and sudden or exponential core-cladding defects [55, 56]. Fibres with non-ideal refractive index profiles suffer from increases in intermodal dispersion, which can significantly affect the MMF transmission characteristics. The refractive index profile optimization depends on the fibre geometry, wavelength, and material properties. A new manufacturing process known as plasma assisted chemical vapour deposition (PCVD) has successfully produced optical fibres with almost ideal refractive index profiles [57, 58]. In spite of the many efforts that have been made to optimize the refractive index profile of MMF, in reality, most installed MMFs have non-ideal refractive index profiles. The cost of replacing restricts their usage in improving the existing MMF bandwidth.

1.2.4 Wavelength division multiplexing (WDM)

WDM is an important method of simultaneously transmitting data from different sources over the same fibre using different wavelengths for each independent signal channel [55]; the aggregate bandwidth then increases dramatically with the number of wavelengths exploited, but the wavelength must be properly spaced in order to avoid inter-channel interference. WDM includes dense WDM (DWDM) and coarse WDM (CWDM); CWDM, which is sometimes called wideband WDM, is a low cost and has more tolerance with respect to variations in wavelength [59]. Both DWDM [59-61] and CWDM [62, 63] implementations show reliable and robust performances in MMF

links, but CWDM is more appropriate for use in MMFs because of its more relaxed requirements for system design and system components. The advantage of WDM is that each of the optical channels can transmit any signal format by using different wavelengths, and that there is no need for a common signal structure [64].

It has also been demonstrated that the all-fibre WDM in an MMF network can be achieved by using a fibre Bragg grating fabricated in a mutlishell MMF. The purpose of the MMF fibre Bragg grating for spectral filtering is to eliminate the coupling losses between the fibre and bulk optics [65]. Subsequently, further effort was made to combine WDM transmission and low linewidth distributed feedback laser (DFB) with centre launching. This combination scheme can successfully achieve 10x20Gb/s 200GHz-spced ITU grid's C-band through a 5km link of a 62.5μm graded index silica multimode fibre without error, and an aggregate bit rate per length product of 1Tb/s·km has been reported [66]. The ultra-wideband (850, 1310, and 1550nm) 3x10Gb/s WDM transmission in a 1km long GI-MMF using photonic crystal fibre as a centre launching and mode filtering device was later successfully demonstrated [67]. In addition, the combination of WDM and mode group division multiplexing became another method of increasing the bandwidth, and an 80Gb/s transmission over a 20m GI-MMF has been experimentally demonstrated [68].

Although WDM is a promising solution, the stable and precise wavelength of the optical laser source, selectivity of the optical filter and cost issues are the constraining factors in the current commercial WDM system. More importantly, the installed MMFs are expected to transmit more data over a longer distance, which limits the exploitation of WDM. This is due to the sensitivity to polarization mode dispersion

and nonlinearity induced by fibre imperfection when the data rate reaches 40Gb/s or even higher. Furthermore, WDM may not be compatible with the equalizer at 40Gb/s or higher.

1.2.5 Subcarrier multiplexing (SCM)

Until now, the above mentioned methods only utilized the baseband of the MMF frequency response and have not exploited the MMF frequency response in the high frequency range. Many researchers have shown that the MMF frequency response does not decrease rapidly in the high frequency region, and the frequency response in the high frequency range becomes relatively flat. One interesting approach to exploit the high frequency region is subcarrier multiplexing (SCM) [69-71]. SCM is a simple and low cost method that can substantially increase the bandwidth of MMF links. It works by dividing the high bit rate signal into many low bit rate signals; these low bit rate signals are then multiplexed and transmitted in the radio frequency domain using a single wavelength [69, 71-73]. The subcarrier frequency may be chosen at the deep nulls and regions where the amplitude of frequency response is 10dB below the average value [74-77]. The frequency spacing between the neighbouring subcarrier is much narrower than in a conventional WDM system. In addition, using optical single-sideband modulation in the SCM system can reduce the impact of fibre chromatic dispersion and improve the bandwidth efficiency.

An experiment with a 10Gb/s SCM MMF system in which 4x2.5Gb/s data streams were combined into one single wavelength demonstrated that occupied an optical bandwidth of approximately 20GHz [72]. The combination of WDM and SCM provides a more flexible platform for high speed optical networks with high optical

bandwidth efficiency and a higher dispersion tolerance [6, 76, 78]. It has been shown the possibility of a 40x5.1Gb/s WDM/SCM system over both 500m of worst case 62.5μm MMF and 3km of 50μm MMF [6]. In the same manner as frequency division multiplexing, orthogonal frequency division multiplexing (OFDM) can be regarded as another candidate for improving MMF bandwidth. OFDM splits the high bit rate data signal into many low bit rate signals and modulates onto the orthogonal subcarriers for transmission. The experiment presented a 107Gb/s coherent optical OFDM signal in both non-amplified and amplified MMF links, and a record performance of 10Tb/s.km was achieved by using centre launching and OFDM equalization [79, 80]. The 2x2 MIMO transmission using SCM with modal diversity and direct detection has shown a superior performance compared to conventional intensity modulation direct detection schemes [81]. Although SCM has revealed some advantages over the WDM scheme, the bandwidth gain of SCM may still be less than that of WDM.

1.2.6 Optical MIMO in multimode fibre (MMF)

Several common techniques used for increasing bandwidth have been summarised so far, and each of these techniques has shown substantial enhancement in the bandwidth distance product but these techniques do not reveal the theoretical potential to increase MMF bandwidth by exploiting its inherent capacity [82]. The wireless MIMO (multiple input and multiple output) systems, which refers to the use of multiple antennas at the transmitters and receivers to improve the performance of radio communication systems provides a significant increase in data throughout and link range without additional bandwidth or transmit power, while it can also improve the spectrum efficiency. In wireless MIMO, the scattering or multipath nature is the key factor to increase the capacity linearly with the number of antennas [83]. The

facts that the MMF links can be considered to be dispersion limited rather than noise limited, and each guided mode can be regarded as an individual scattering path similar to wireless MIMO implies a sufficient spatial degree of freedom; therefore, most of the principles in the wireless MIMO system can also be adapted to optical MIMO in MMF networks [42]. The following subsections give a short overview of the optical MIMO MMF system and present current research on optical MIMO, including optical MIMO implementations and various detection methods. Lastly, some problems that may be involved in exploiting optical MIMO systems are discussed.

1.2.6.1 Dispersive multiplexing

The first report about optical MIMO was introduced by H.R.Stuart and called dispersive multiplexing, which improves the capacity of MMF by exploiting modal dispersion rather than avoiding it. Figure 1.1 depicts the proposed system reported in reference [82].

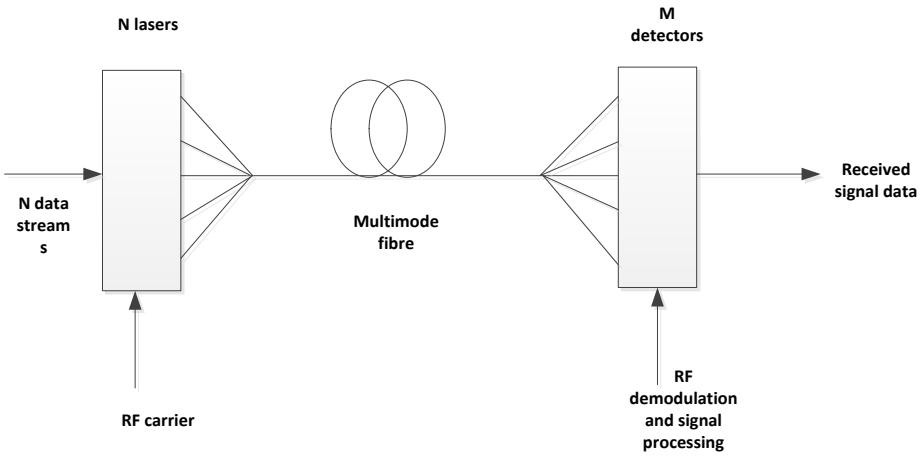

Figure 1.1 The dispersive multiplexing system diagram

In dispersive multiplexing the independent phase modulated electrical subcarrier signals are used to modulate laser intensity, and a splitter is then used to combine them together into the MMF. At the receiver side, the optical beam is split between

two photodetectors and each detector receives power from all transmitters. A complex valued matrix H can be used to relate the electrical input signal and the output signal. This system works based on the modal coupling diversity at both the input and output of the MMF. If the modal dispersion is sufficient, each element of the transmission matrix H can be modelled as an uncorrelated Gaussian random variable that is analogous to the Rayleigh fading model in wireless MIMO. The transmission matrix must be estimated and inverted in order to recover the transmitted signal, and once the system has insufficient coupling diversity or insufficient dispersion, the inversion of the matrix will then generate a large multiplicative factor to noise, which reduces transmission performance [82]. In other words, the more guided modes or modal coupling diversity there is, the closer the channel matrix becomes to a random complex Gaussian matrix with uncorrelated elements, thus providing maximum capacity [84]. To keep sufficient modal diversity, a minimum fibre length is required. Typically, a fibre length of 1km to 2km with a subcarrier frequency of 500MHz to 1GHz is required [84, 85]; however, this typical length is much longer than the installed MMF in LAN. Meanwhile, the biggest difficulty in utilizing this scheme may result from coupling multiple light sources into the core region of MMF and multiple detections at the receiver end.

1.2.6.2 Modal multiplexing

In an MMF, there are many guided modes that can be used as an independent channel for transporting signals. Each mode is excited separately and detected with the aid of the modal fields, and such a scheme is called modal multiplexing [86]. In order to allow this modal dispersion scheme to be deployed in the MMF links, the mode power coupling between each mode must be minimised, or, in other words, the mode

coupling should be avoided. Therefore, this inevitable mode coupling limits its usage and reduces the feasibility in MMFs. Furthermore, the accuracy of exciting and detecting each mode is not trivial, but a 2x2 optical MIMO system using computer generated holograms and an optical correlator for channel multiplexing and de-multiplexing in an optical MIMO system has been demonstrated [87, 88]. Apart from the merit of accurate mode selection, another advantage of the holographic method is that it operates in an optical domain, which can improve the robustness of the system without any electronic implementation.

1.2.6.3 Mode group diversity multiplexing (MGDM)

Mode group diversity multiplexing is actually an intensity modulation and a direct detection optical MIMO technique. MGDM can be implemented with radial offset Gaussian beams at the input facet of GI-MMF via SMF launching or MMF couplers and spatially selective detecting of the optical power at the output [25, 89, 90]. According to the spatial distribution of the near field intensity pattern, the output signals can be detected using multiple single mode fibres positioned at the output facet of the MMF or multi-segment detectors (MSD). The basis of MGDM is to excite different groups of modes and use them as an individual channel. The numbers of transmitters (N) and receivers (M) should identical in order to minimise the power penalty caused by a higher power-splitting factor and SNR [90].

In the MGDM system the transceiver design is independent of fibre length and provides high coupling efficiency for all input beams. Moreover, MGDM is also transparent to the signal format as the channel matrix is linear with respect to optical intensity, which means that the signal processing in MGDM is also independent of

signal format. At the moment, the 2x2 and 3x3 optical MIMO systems based on MGDM have both been reported [89, 91, 92], and a 2x2 MIMO system with a data rate of 10.7Gb/s over a 300m GI-MMF has been demonstrated [93]. The MGDM can be used in either a step index MMF with angular offset launching or a graded index MMF with radial offset launching, and both methods have good performance histories [94]. A better MGDM performance can be achieved in conjugation with space time block code rather than employing MGDM alone [95].

1.2.6.4 Coherent optical MIMO

Coherent optical fibre communication is a good choice for future communication systems, and the receiving sensitivity is improved by 20 dB compared with incoherent optical fibre communication[96]. In addition to the above merit, coherent optical fibre communication provides higher frequency selectivity, which means that more channels and more users can be accommodated [64]. In addition, the key advantage of coherent detection is that it provides full information about the received signal (i.e. not only the amplitude, but also the phase information), improving the detection process.

In dispersive multiplexing, the RF subcarrier modulation and detection requires a long length MMF and a larger subcarrier frequency to retain modal coupling diversity, so this significantly restrains its usage. Additionally, due to its incoherent nature in conventional IM-DD optical MIMO systems the phase modulated transmissions are not supported. Fortunately, these problems can be solved by using a coherent optical MIMO with a larger optical carrier frequency (an order of hundreds of THz) compared to RF subcarriers. The large value of carrier frequency in coherent optical

MIMO systems ensures that the phase term of the transmission matrix (H) entirely spans over $(0, 2\pi)$, even for short fibre lengths. This particular phase characteristic gives rise to a random complex Gaussian variable of each element in the channel matrix H, which is one of the conditions for maximum capacity in MIMO systems [97]. In a coherent optical MIMO system, the offline digital signal processing needs to be applied, this will significantly improve the system performance in the electrical domain. A schematic of the typical coherent MIMO system is shown in Figure 1.2.

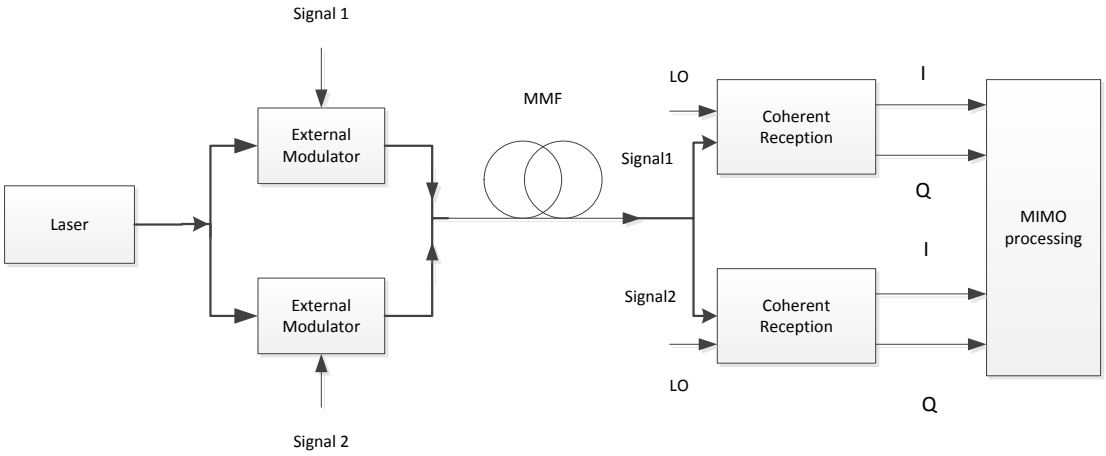

Figure 1.2: The coherent optical MIMO system

Figure 1.2 displays the basic operation of a coherent optical MIMO system. The laser source is split into two parts, and the two signals are modulated by external modulators. The signals from the two external modulators are combined together into the MMF. At the receiver part, these received signals are separated by a splitter, and each of the signals is combined with the two quadrature carriers from the local oscillator to produce a total of four outputs. Afterwards, the four output signals are detected by two balanced receivers that create both in-phase and quadrature baseband components. Finally, the received signals are separated via offline signal processing. Coherent optical MIMO systems have a variety of research directions, such as C and L band WDM coherent optical MIMO transmission over 10km GI-MMF under

selective mode excitation conditions [98], coherent MMF MIMO transmission with spatial constellation modulation [99], and quantifying the coherent MIMO equalizer complexity in terms of matrix size with respect to radius of fibre bends [100]. Recent research has established a complete analytical model for coherent optical MIMO systems over MMF with ring launching and receiving [101]. Nevertheless, the most promising research area in coherent optical MIMO systems is mode division multiplexing. Although coherent optical MIMO systems have many advantages, their complicated components such as external modulators, narrow linewidth local oscillators, complicated equalizers, and even balanced receivers impose more complexity on implementation. Meanwhile, it comes at the expense of complexity due to the optical coherent demodulation.

1.2.6.5 Few mode fibre (FMF)

Few mode fibre combines the advantages of SMF and MMF. The core diameter of FMF is approximately 12μm, resulting in a low splicing loss and more immunity to nonlinear effects. FMFs can avoid the larger modal dispersion and mode coupling of conventional MMFs and also provide a stable channel for MIMO systems. The chromatic dispersion, polarization dispersion, modal dispersion, and differential modal attenuation are the impairments during data transmission. Currently, the FMF communication technique can be grouped into two types: the FMF in the single-mode operation model that utilizes only the fundamental mode of FMF by means of a larger effective area, which helps to reduce the nonlinear effect; and the multi-mode operation model, in which mode division multiplexing can be employed to improve the system capacity. As the FMF is designed for long haul communications, the target of fabricating FMF is to own low group delay and mode loss.

1.2.6.6 Mode division multiplexing (MDM)

Using orthogonal modes in MMF to carry information is the key idea in mode division multiplexing (MDM) systems. A large number of linearly independent guided modes ensures the maximum capacity in the optical MIMO system from an information theoretical viewpoint. MDM is based on the excitation of individual modes with orthogonal near field intensity patterns. In recent years, researchers have focused on MDM in FMFs, which transmits only a few spatial modes. Compared to MMFs, they are sufficiently resistant to mode coupling with less nonlinearity, but they still have a large core diameter compared to SMF [102]. These advantages make MDM more attractive in long haul systems. Using FMFs that are optimized for reducing the mode coupling rather than increasing it may hinder the excitation techniques. Moreover, the challenge in MDM is the selective mode excitation. Since computer generated holograms have long been used in MMFs [38], some methods have been proposed to convert the fundamental mode from SMF into the higher order modes of FMF, which include a free space optics based glass phase plate [103, 104], spatial light modulator [105, 106], and long period grating [107]. All of the above implementations can be utilized to realise the mode multiplexing and de-multiplexing of MDM systems.

A scheme that combines polarization multiplexing, spatial mode multiplexing, and coherent MIMO processing all together has been recently reported [28, 104, 107, 108]. The results demonstrated a robust and substantial improvement in bandwidth; for instance, a total of 240Gb/s MDM over 96km of FMF using coherent 6x6 MIMO processing was demonstrated experimentally [108]. Furthermore, transmission at 2x100Gb/s over a two-mode fibre of 40km with the aid of MDM coherent MIMO

processing was also achieved [28]. Although these recent contributions have shown that it is feasible to increase the transmission capacity in FMFs, the mode conversion at both the transmitter and receiver ends and the complicated off-line coherent MIMO signal processing brings more complexity into the system implementation. Nevertheless, the complexity may be eased by employing a single spatial light modulator for multi-excitation at the FMF input [106], but the extra optic components and active devices are still the main barriers to the realisation of a practical MDM system.

1.3 Objective of the research

High speed digital connections have grown very quickly in our local area networks (i.e. high demand on cloud computing or video streaming) since the internet has been developed, so there is a need to increase or upgrade our transmission capacity in the existing fibre infrastructure, especially in short distance multimode fibre networks. In order to avoid a capacity crunch in our data transmission networks, the optical MIMO becomes a most promising candidate for improving the bandwidth as it exploits the spatial dimension provided by MMF to increase the transmission distance and bandwidth. Not only that, but it also provides a good trade-off between the power budget and the bandwidth distance product, making it more suitable for the future 40Gb/s, 100Gb/s, and even higher data rate networks. Current optical MIMO techniques are mainly applied in multi-core MMFs, standard MMFs, FMFs, and ring fibre by using the orbital angular momentum modes. According to the multiplexing scheme, the optical MIMO technique includes mode group diversity multiplexing and mode division multiplexing. Both schemes need complicated designs in multiplexing at the transmitter and de-multiplexing at the receiver. These designs will inevitably

increase the cost and difficulty of implementation in practice; for example, the MGDM has to use several SMF detectors and some fibre couplers; the MDM needs to use spatial mode multiplexers, de-multiplexers, and mode converters. Because of the existing complications in both multiplexing schemes, the need for a simple and cost-effective optical MIMO design in which both systems can be used seems to be very important.

The aim of this research is to design and investigate a simple and cost-effective optical MIMO system in multimode fibres for future high speed networks and demonstrate the feasibility of this method. The proposed optical MIMO system can be realised with selective excitation and spatial selective detection rather than the use of complicated free space optic components (i.e. lens, beam splitter/coupler, and SLM). The new proposed annular multi-segment detectors show a significant improvement in optical MIMO performance. Previous studies on MGDM only focused on experimental works; less attention has been paid to the optimization of the proposed systems. Apart from offering a new approach to MGDM, this work introduces an optimization method. The main contribution is the optimization of the offset launching and design of the annular detector in optical MIMO MMF systems by using the condition number of the channel matrix.

Furthermore, this specific optical MIMO design is exploited not only in short distance MMF links, but also in long haul FMF links. In our work, an optical DPSK coherent MIMO is selected to overcome the limitations of the bandwidth distance product in conventional IM-DD optical MIMO MMF systems. The main advantages of employing a coherent optical DPSK signal are a higher tolerance of phase noise,

which is notable in coherent MIMO systems, higher receiver sensitivity, and the full ability to compensate all linear impairments. This proposed optical DPSK MIMO system can not only be applied to the heterodyne coherent system, but also to the intradyne coherent system with phase diversity receiver. Both systems show good performances.

To the best of my knowledge, this is the first simulation of an optical DPSK coherent MIMO system in conjunction with FMF using the selective launching scheme and annular multi-segment detectors. Owning to the absence of mode converters, this proposed scheme can largely reduce the design complexity of a coherent optical MIMO system in FMF and make this system more practicable.

In addition, the simulation results are used to analyse and estimate the improvement in system performance in comparison to conventional MIMO detectors (i.e. multiple SMF detectors) in both incoherent and coherent optical MIMO systems. Moreover, the results demonstrate the feasibility and potential of using this easy and cost-effective scheme in future optical MIMO systems.

1.4 Structure of thesis

This thesis contains seven main chapters that provide a theoretical basis and simulation models for research on an optical MIMO system in multimode fibres. From here onwards, each chapter is briefly outlined.

Chapter 2: Chapter 1 looked briefly at the evolution of optical fibre transmission technologies and the introduction of a new concept, optical MIMO. Each technique has its own advantages and limitations in practical systems; however, the application of MIMO in any type of transmission system is regarded as the addition of a new dimension of information mapping, thereby increasing the capacity. This chapter is dedicated to the basis of MMF in optical fibre transmission systems, and we review the modal field expression within MMF transmission systems. The mode group delay, mode power coupling coefficient, and the overall MMF frequency response or transfer function have been derived and simulated.

Chapter 3: This chapter presents the near field intensity pattern at the output facet of MMF. The required mathematical formulations are derived to understand the theoretical results. Different impairments during the MMF transmissions are discussed, for example, the modal dispersion, differential mode attenuation, and intra-group mode mixing. The factors that affect the near field pattern are also analysed. In addition, the schematic results show the near field intensity pattern when there is intra-group mode mixing and no intra-group mode mixing. Analysing the near field intensity pattern can lead an efficient way to design the multiple receivers in an optical MIMO system.

Chapter 4: In this chapter, a model for an optical MIMO system in MMF is developed mathematically. The chapter comprises a comprehensive theoretical MIMO model and a numerical discussion of this system. Meanwhile, the optical MIMO channel matrix H and the MIMO capacity are both derived. A simple off-line MIMO signal processing (zero forcing method) is introduced in this chapter. Following this, a detailed analysis of the geometry of the optical MIMO transceiver is provided in Section 4.5, encompassing the optimization of transmitters and receivers and the proposed annular multi-segment detectors. This is followed by simulations of the channel matrix condition number and crosstalk in the MIMO system. Lastly, we prove that the annular detectors can achieve a better performance than conventional multiple SMF detectors and can also minimise the receiver crosstalk effect.

Chapter 5: This chapter contains one of the core works of our research. It shows the design and development of a radial offset launch IM-DD optical MIMO system by utilizing both conventional SMF detectors and annular detectors. The detailed transmitter design specification is studied by optimizing the launched narrow Gaussian beam spot size and the radial offset launch value. Our method of designing an efficient annular detector is introduced to improve the MIMO system performance, and the advantages of this method are presented. The simulated BER, MIMO capacity, and average received optical power analysis are all presented to characterise the system performance. Finally, the intra-group mode mixing effects in both the 2x2 and the 3x3 MIMO systems are investigated with various fibre lengths and signal data rates.

Chapter 6: The optical MIMO model created in Chapter 5 can be extended in the few mode fibre (two mode FMF) coherent detection MIMO system. Two coherent optical DPSK MIMO systems are modelled: the optical heterodyne DPSK MIMO system and the optical intradyne DPSK MIMO system. Firstly, the mathematical descriptions of these two optical MIMO systems are presented. Next, the schematic diagrams of these two coherent optical MIMO systems are discussed along with a brief outline of their components. Meanwhile, some commentary regarding the limitations and challenges faced by the coherent MIMO systems is included. A numerical analysis with versatile simulation results follows the comprehensive theoretical introduction. The results include the estimated BER and OSNR analysis, transmission distance limitation, and all other factors that can affect the performance in IM-DD optical MIMO systems (i.e. modal dispersion, attenuation, intra-group mode mixing and chromatic dispersion). Lastly, optical MIMO systems with different configurations are compared.

Chapter 7: This chapter presents the conclusion of the thesis along with potential directions for future research.

Chapter 2: Basics of Multimode Fibre Systems

To fully understand MMF communication systems, one must first study the basics of MMFs and review the theory behind MMF transmissions, particularly the frequency response or transfer function of the MMF. Modal time delay and power coupling coefficient are calculated for each mode. The channel impulse response is presented.

2.1 Multimode fibre (MMF)

In the past thirty years, optical fibre has played an important role in both telecommunications and data communication, not only because of its high bandwidth and low attenuation, but also due to its high reliability. Optical fibre is actually a cylindrical dielectric waveguide that contains a larger cladding radius and a smaller core radius. The core has a higher refractive index than the cladding region refractive index so the light in the optical fibre suffers total internal reflection. According to the different refractive index profiles and the total support modes, the optical fibre can be divided into two groups: single mode fibre and multimode fibre with either step index profile or graded index profile. As their names suggest, single mode fibre has only one mode, whereas multimode fibre has more than one mode. The mode is a solution to the electromagnetic wave equation, and each mode has two orthogonal polarizations. The standard multimode fibre has a core radius of either 25μm or 31.25μm, which is larger than the single mode fibre (typically 4.5μm or less). There are two common types of multimode fibre, namely step index multimode fibre (MMF) and graded index MMF. Step index MMF has a uniform refractive index in the core and undergoes step changes at the cladding region boundary [96]. When the refractive index decreases gradually as a function of radial distance from the fibre centre and

finally drops to the same value as the cladding, it is called graded index fibre. Figure 2.1 schematically represents the graded index MMF geometry.

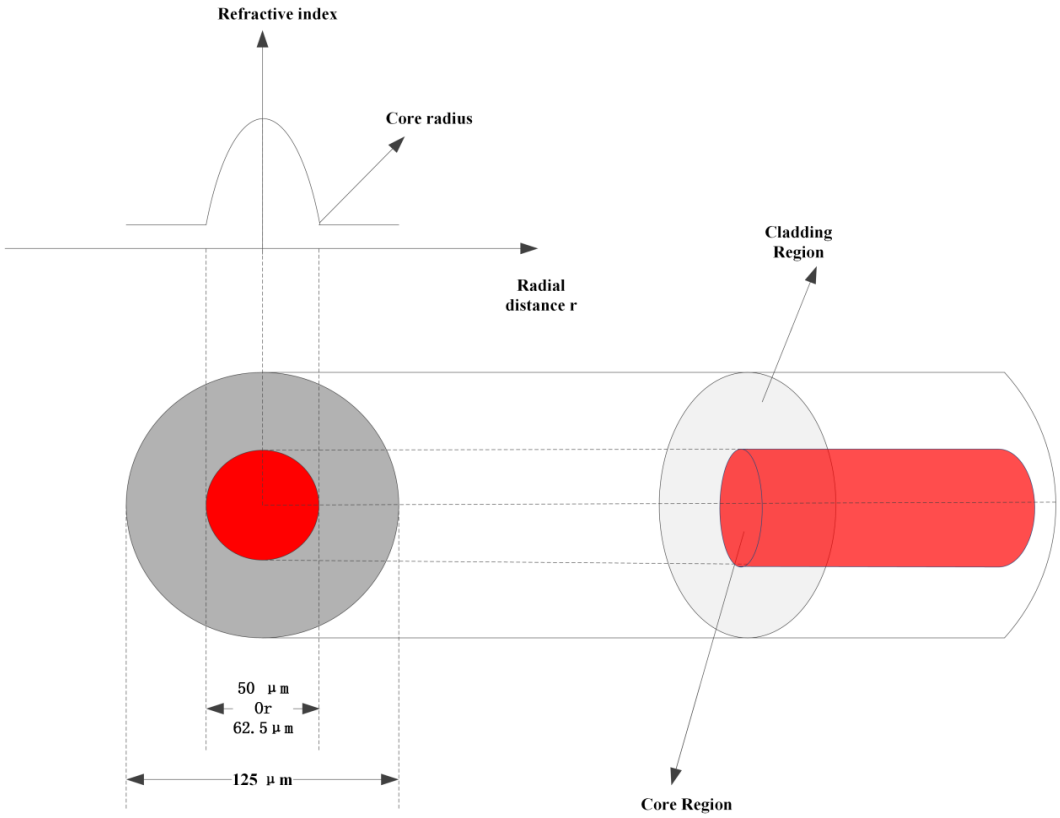

Figure 2.1 Graded index MMF geometry

A power law expression can be used to describe the refractive index of MMF, which is given as:

$$n(r)=\begin{cases} n_1\sqrt{[1-2\Delta(\frac{r}{a})^{\alpha}]}, & 0\le r\le a \\ n_1\sqrt{(1-2\Delta)}, & r\ge a \end{cases} \qquad \Delta=\frac{n_1^2-n_2^2}{2n_1^2} \qquad (2.1)$$

where Δ is the profile height parameter, r is the radial distance apart from the fibre centre, n_1 and n_2 are the maximum core refractive index and cladding refractive index, respectively, a is the core radius of MMF, and α is the index profile, which determines the shape of the refractive index profile. Because of the large diameter of the core in MMF along with the numerical aperture, many light waves will propagate along the core region, leading to significant intermodal dispersion. Consequently,

larger pulse spreading induced by the intermodal dispersion limits to the bandwidth in MMF means that multimode fibre only carries a third or less of the information capacity of a single mode fibre [64]. The most practical MMF used is graded index MMF, which has an approximately perfect parabolic index profile ($\alpha = 2$). In graded index multimode fibre (GI-MMF) each mode travels at a different speed. The higher order mode travels faster over a long distance and the lower order mode travels slower over a short distance, this allows all of the light rays to arrive at approximately the same time, thus reducing modal dispersion. Figure 2.2 shows the refractive index profiles of single mode fibre (SMF) and multimode fibre (MMF).

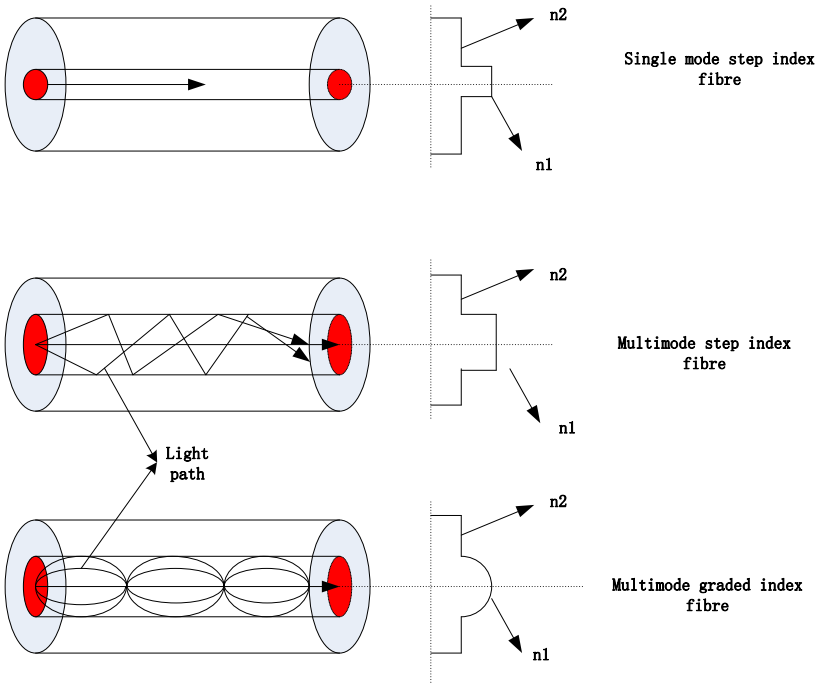

Figure 2.2 Optical fibre index profiles and fibre cross-sections

For weakly guiding fibres $n_1 \approx n_2$ therefore, the profile height parameter is simplified to $\Delta \approx \frac{n_1 - n_2}{n_1}$ and the refractive index in the core region changes to [109]:

$$n_{core}(R) = \sqrt{n_1^2 (1 - 2\Delta R^2)} \quad \text{and} \quad R = \frac{r}{a} \tag{2.2}$$

The MMF can be made of silica, polymer, or a combination of the two materials

together. In this thesis, an ideal parabolic index profile silica based graded index MMF is used. The total number of modes "*M*" in a graded index ($\alpha = 2$) MMF is determined as: [110]

$$M = \frac{V^2}{4} \qquad \text{and} \qquad V = \frac{2\pi a}{\lambda}(n_1^2 - n_2^2)^{\frac{1}{2}} = \frac{2\pi a}{\lambda} NA \tag{2.3}$$

where *V* is normalized frequency, $NA = \sqrt{n_{core}^2 - n_{clad}^2}$ is the numerical aperture which determines how much light can be launched into the core region, and *a* is the core radius. Table 2.1 gives the typical values of the NA for different MMFs [3].

MMF type	**Numerical aperture**
62.5/125 μm	0.275
50/125 μm	0.200

Table 2.1 The typical numerical aperture values of the MMFs

Nowadays, many efforts are focused on improving the bandwidth of multimode fibres such as the recently developed OM4 fibre, which is a laser-optimized, high bandwidth 50 μm multimode fibre. It enables the cost-effective VCSELs to operate at 850nm for 1Gb/s and 10Gb/s applications and even in future 40Gb/s and 100Gb/s systems. Meanwhile, its effective bandwidth can reach 4700 MHz.km, which is almost more than double that of the standard IEEE 10Gb/s requirement [111]. Table 2.2 outlines several commonly used MMFs and their associated bandwidths in the communication market.

Fibre Name	**EMB (MHz.km) at 850nm**	**OFL (MHz.km) at 850nm**	**OFL (MHz.km) at 1300nm**
OM1 (62.5 μm)	N/A	200	500
OM2 (50 μm)	N/A	500	500
OM3 (laser optimized 50 μm)	2000	1500	500
OM4 (laser optimized 50 μm)	4700	3500	500

Table 2.2 The ISO/IEC 11801OM designations and bandwidths [111]; EMB represents the effective modal bandwidth, OFL represents the overfilled launching, and OM stands for optical multimode fibre.

2.2 Properties of modes in multimode fibre

Optical fibre is a dielectric waveguide that operates in the optical frequency region, and the propagation lights along the waveguide can be described in terms of a set of guided electromagnetic waves called modes of the waveguide [96]. Under the weakly guiding approximation, the combining of appropriate EH, HE, TE, and TM modes can generate linear polarized modes denoted as $LP_{l,n}$ modes, where "l" is the azimuthal mode number and refers to the angular variation, and "n" is the radial mode number and refers to the radial variation. Mode analysis is very important when considering the many applications of MMF links. In general, these modes can be separated into two groups: discrete guided modes, which are trapped in the core region; and infinite continued radiation modes, which are refracted out of the core region [64] so that they cause optical power attenuation. Only a certain number of guided modes are able to propagate along the fibre core region if they satisfy the homogeneous wave equation and boundary condition. Each guided mode can be treated as a pattern of electric and magnetic field distributions [64, 96, 110]. As long as the propagation constant β is within the following condition:

$$n_2 k < \beta < n_1 k , \tag{2.4}$$

The predominant mode is guided mode or bound mode; conversely, if $n_2 k > \beta$, the leaky mode occurs. $\beta = n_2 k$ is a cut off condition, where n_1, n_2 are the refractive index in the core and cladding region, respectively, and $k = \frac{2\pi}{\lambda}$ is the free space propagation constant.

The total number of guided modes for an infinite parabolic index profile MMF is given in Equation 2.3. The vector field of each mode is the solution of Maxwell's

vector wave equation [112]. The derivation of Maxwell's equation is only available for a few known refractive index profiles, and even small changes in the refractive index will cause more difficulty in deriving an analytical solution [112]. Weakly guiding is a fundamental approximation which states that the refractive index difference between the core and cladding regions is very small, or equivalently, $n_1 \cong n_2$. This approximation can simplify the original vector wave equation to a scalar wave equation, thus reducing the derivation. Apart from the weakly guiding assumption, some other assumptions are employed in the ideal graded index multimode fibre (GI-MMF), including the assumptions of fibre circular symmetry, longitudinal invariance, and Cartesian EM filed representation.

2.2.1 Modal field expression of multimode fibre

Here, we assume that the field expansion is formed only in the forward propagation direction, and symmetric backward propagation is neglected. The total EM field is represented by the sum of the guided mode and radiated mode fields:

$$E(x,y,z) = E_{bound}(x,y,z) + E_{radiated}(x,y,z) \qquad (2.5)$$

Due to translational invariance, the modal field for each individual mode can be expressed in the separable form:

$$E_{l,n}(x,y,z) = E_{l,n}(x,y)\exp(j\beta_{l,n}z) \qquad (2.6)$$

Sometimes cylindrical polar coordinates may be used to express the modal field instead of Cartesian coordinates: $E_{l,n}(r,\phi,z) = E_{l,n}(r,\phi)\exp(j\beta_{l,n}z)$ (2.7)

Each LP mode contains transverse and longitudinal components, which are denoted by subscripts *t* and *z*: $E_{l,n}(r,\phi) = E_{t,ln}(r,\phi) + E_{z,ln}(r,\phi)\hat{z}$ (2.8)

Both electric and magnetic fields have the modal indices l and n, which are

represented as the sum of transversal and longitudinal components. $\hat{z}$ represents the unit vector in the direction of the fibre axis. The transverse modal field can be given as:

$$E_{t,ln}(r,\phi) = e_{x,l,n}(r,\phi)\hat{x} + e_{y,l,n}(r,\phi)\hat{y} \qquad \text{or}$$

$$E_{t,ln}(x,y) = e_{x,l,n}(x,y)\hat{x} + e_{y,l,n}(x,y)\hat{y} \qquad (2.9)$$

where $e_{x,l,n}$ and $e_{y,l,n}$ are the solutions of Maxwell's scalar wave equation, $\hat{x}$ and $\hat{y}$ are unit vectors parallel to the x and y-axes, respectively, both of which are perpendicular to the fibre axis shown in Figure 2.3.

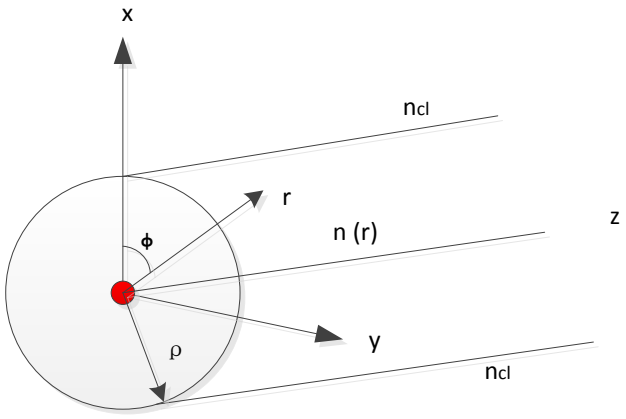

Figure 2.3 Fibre core symmetric cross section

When the modal amplitude $a_{l,n}$ and $\beta_{l,n}$ scalar propagation constant are assigned to each LP mode, the total bound modes electric field is:

$$E_{bound}(r,\phi,z) = \sum_{l,n} a_{l,n} E_{l,n}(r,\phi)\exp(j\beta_{l,n}z) \qquad (2.10)$$

Suppose the fibre has a uniform medium of core refractive index, and the modal fields are the fields of transverse electromagnetic or TEM wave propagating in the z-direction parallel to the fibre axis. The longitudinal components are set to zero, and the transverse electric and magnetic field of weakly guiding waveguides have the

following relationship: $$h_t(x,y)=\left(\frac{\varepsilon_0}{\mu_0}\right)^{\frac{1}{2}} n_1 \hat{z}\times e_t(x,y) \qquad (2.11)$$

where ε_0 and μ_0 are the permittivity and permeability values in free space, respectively, and n_1 is the refractive index in the fibre core region.

2.2.2 Analytical solution of the modal field in graded index fibre

The derivation of the modal field $E_{l,n}(r,\phi)$ and propagation constant can be found by solving the scalar Maxwell's wave equation, [112]

$$[\nabla_t^{\,2}+k^2n^2(r)-\tilde{\beta}^2]\psi=0, \quad \nabla_t^{\,2}\psi=\frac{1}{r}\frac{\partial^2}{\partial r}\left(r\frac{\partial\psi}{\partial r}\right)+\frac{1}{r^2}\frac{\partial^2\psi}{\partial\phi^2} \qquad (2.12)$$

where ψ indicates either the radial dependence electrical value $e_{x,l,n}$ in the x-axis or $e_{y,l,n}$ in the y-axis for a given mode with exact azimuthal and radial mode numbers, and r is the radial distance from the fibre core centre. Using the method of separation of variables the solution has two separable forms [112]:

$$\psi=F_{l\,n}(r)\cos l\phi \qquad and \qquad \psi=F_{l\,n}(r)\sin l\phi \;\; where\; l=0,1,2..... \qquad (2.13)$$

Here, $F_{l\,n}(r)$ satisfies the ordinary differential equation as shown below: [112]

$$\left\{\frac{d^2}{dr^2}+\frac{1}{r}\frac{d}{dr}+k^2n^2(r)-\frac{l^2}{r^2}-\beta^2\right\}F_{l\,n}(r)=0 \qquad (2.14)$$

For an infinite parabolic profile of $n^2(R)=n^2_{co}(1-2\Delta \mathrm{R}^2)$ with $R=\frac{r}{\rho}$, r is the radius of the MMF core, and ρ is the radial position from the MMF core centre.

For weakly guiding fibres: $$\Delta\cong\frac{n_{co}-n_{cl}}{n_{co}} \qquad (2.15)$$

Letting $$\beta=\frac{V}{\rho(2\Delta)^{\frac{1}{2}}}\left\{1-\frac{4\Delta}{V}(2n+l+1)\right\} \qquad (2.16)$$

$$U = \{2V(2n + l + 1)\}^{\frac{1}{2}} \quad (2.17)$$

(*n*=radial mode number, *l*=azimuthal mode number)

Normalized frequency is given by: $V = k\rho n_{co}(2\Delta)^{\frac{1}{2}}$ (2.18)

Substitution of eq. (2.15-2.18) into Eq.2.14, the scalar wave equation becomes:

$$\left\{\frac{d^2}{dR^2} + \frac{1}{R}\frac{d}{dR} - \frac{l^2}{R^2} + U^2 - V^2R^2\right\}F_{l\,n}(R) = 0 \quad (2.19)$$

where both *U* and *V* are function of ρ.

Finally, the differential equation can be solved numerically to obtain the radial dependence of the electric field, $F_{l\,n}(R)$, which is given by:

$$F_{l\,n}(R) = R^l L_n^l(VR^2)\exp(-\frac{1}{2}VR^2) \quad (2.20)$$

where *R* is the normalized radius, *V* is the normalized frequency, ρ is the core radius and $L_n^l(x)$ is the Laguerre polynomial in terms of radial and azimuthal mode number, given by:

$$L_n^l(x) = \Gamma(n + l + 1)\sum_{r=0}^{n}\frac{(-1)^r x^r}{r!(n-r)!\Gamma(r + l + 1)} \quad (2.21)$$

Therefore, the modal field includes angle dependence and becomes: [20]

$$\psi_{l,n}(R,\phi) = R^l L_n^l(VR^2)\exp(-\frac{1}{2}VR^2)\begin{Bmatrix}\cos(l\phi)\\ \sin(l\phi)\end{Bmatrix} \quad (2.22)$$

The modal field is normalized for further analysis, and assuming that the modal field has the angle term $\cos(l\phi)$. Therefore, the normalized electric field can be written as:

$$\psi_n = N\psi_n, \quad thus \;\; \psi_n = NR^l L_n^l(VR^2)\exp(-\frac{1}{2}VR^2)\cos(l\phi) \quad (2.23)$$

Factor *N* is the normalized factor; in order to determine the normalized factor, the integral of the electric field intensity over the core area must be unit:

$$\int_{\phi}\int_{R}\psi_n^2 R dR d\phi = 1 \quad (2.24)$$

Substituting Equation (2.23) into Equation (2.24) gives:

$$\int_{R}\int_{\phi} N^2 R^{2l+1}[L_n^l(VR^2)]^2 \exp(-VR^2)\cos^2(l\phi)dRd\phi = 1 \qquad (2.25)$$

The angular part of Equation (2.25) can be solved separately, thus,

$$\int_{\phi=0}^{2\pi} \cos^2(l\phi) = \begin{Bmatrix} 2\pi, & for\ l=0 \\ \pi, & for\ l\neq 0 \end{Bmatrix} \qquad (2.26)$$

Rewriting: $$\int_{\phi=0}^{2\pi} \cos^2(l\phi) = (1+\delta_{ol})\pi, \qquad \delta_{ol} = \begin{Bmatrix} 1, & when\ l=0 \\ 0, & when\ l=1 \end{Bmatrix} \qquad (2.27)$$

where δ_{ol} is a Kronecker delta function.

Substituting Equation (2.27) back into Equation (2.25) yields:

$$N^2\pi(1+\delta_{ol})\int_{R=0}^{\infty} R^{2l+1}[L_n^l(VR^2)]^2 \exp(-VR^2)dR = 1 \qquad (2.28)$$

If $x = VR^2$, $dx = 2VRdR$, and Equation (2.28) becomes:

$$\frac{N^2\pi(1+\delta_{ol})}{2V^{l+1}}\int_{0}^{\infty} x^l[L_n^l(x)]^2 \exp(-x)dx = 1 \qquad (2.29)$$

By using the orthogonal relation of Laguerre polynomials [113],

$$\int_{0}^{\infty} x^l \exp(-x)L_m^l(x)L_n^l(x)dx = \frac{\Gamma(1+l+n)\delta_{mn}}{n!}, \text{ and } \delta_{mn} = \begin{Bmatrix} 1, & for\ m=n \\ 0, & for\ m\neq n \end{Bmatrix} \qquad (2.30)$$

Substituting Equation (2.30) into Equation (2.29) gives:

$$\frac{N^2\pi(1+\delta_{ol})}{2V^{l+1}}\cdot\frac{\Gamma(1+l+n)}{n!} = 1, \qquad N = \sqrt{\frac{2V^{l+1}n!}{\pi(\delta_{ol}+1)\Gamma(1+n+l)}} \qquad (2.31)$$

The final normalized electric field in GI-MMF is given by:

$$\psi_{l,n}(R,\phi) = \sqrt{\frac{2V^{l+1}n!}{\pi(\delta_{ol}+1)\Gamma(1+n+l)}}\cdot R^l L_n^l(VR^2)\exp(-\frac{1}{2}VR^2)\cos(l\phi) \qquad (2.32)$$

$$\text{or} \quad \psi_{l,n}(R,\phi) = \sqrt{\frac{2V^{l+1}n!}{\pi(\delta_{ol}+1)\Gamma(1+n+l)}}\cdot R^l L_n^l(VR^2)\exp(-\frac{1}{2}VR^2)\sin(l\phi) \qquad (2.33)$$

("Γ" indicates the gamma function)

The Matlab simulation of the $LP_{l,n}$ modal field intensity of weakly guiding GI-MMF (62.5/125 μm) with an infinite parabolic refractive index ($\alpha = 2$), $n_1 = 1.45$, $n_2 = 1.44$, and V=39.27 is illustrated in Figure 2.4. The simulation assumes that the transverse electric field only contains the $F_{ln}(r)\cos l\phi$ part.

Electrical Field Intensity for *l*=0, *n*=1

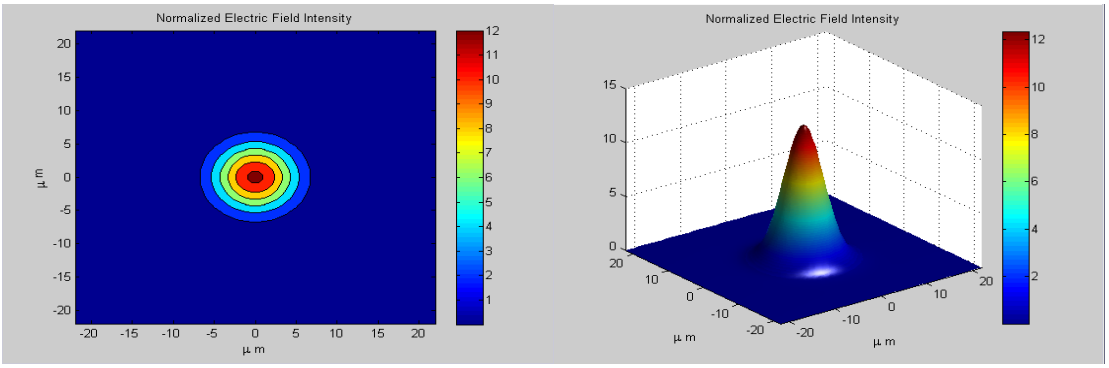

(a)

Electrical Field Intensity for *l*=1, *n*=1

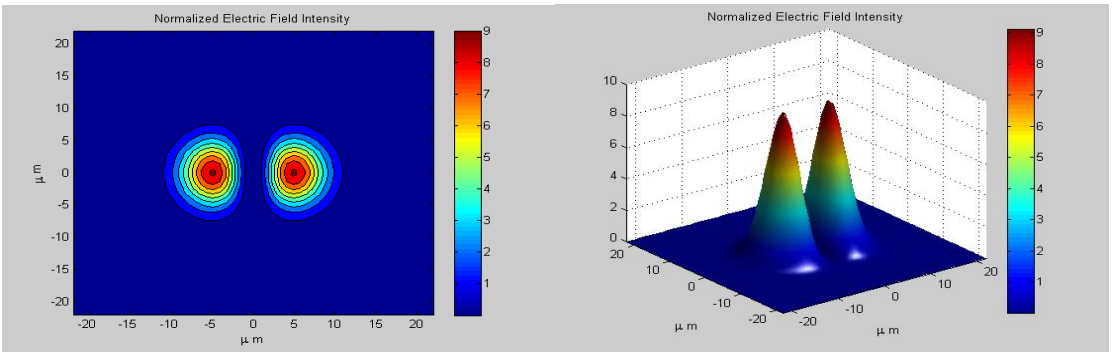

(b)

Electrical Field Intensity for *l*=1, *n*=2

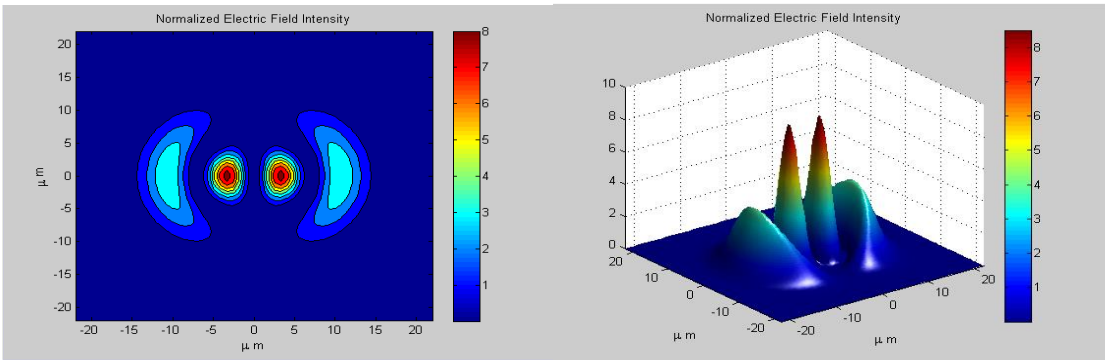

(c)

Electrical Field Intensity for *l*=2, *n*=1

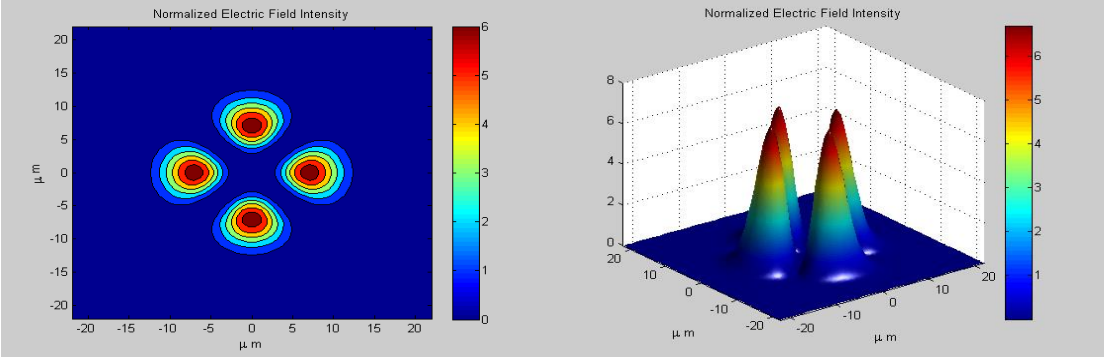

(d)

Electrical Field Intensity for *l*=3, *n*=3

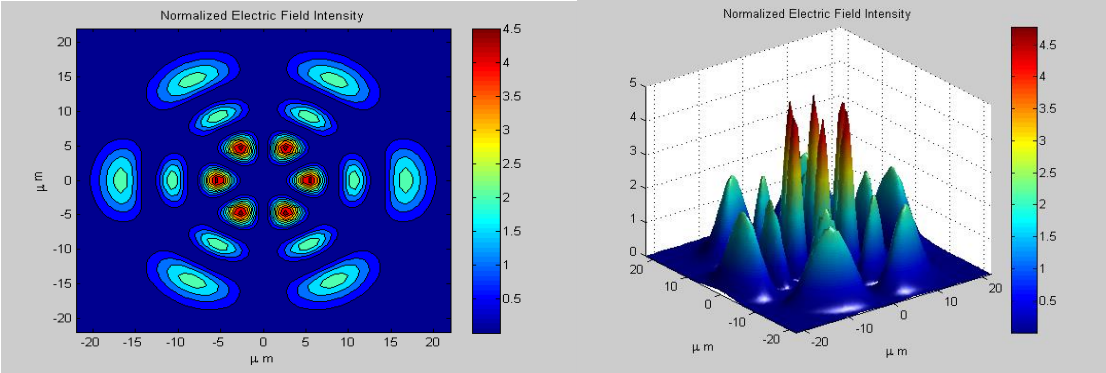

(e)

Electrical Field Intensity for *l*=4, *n*=2

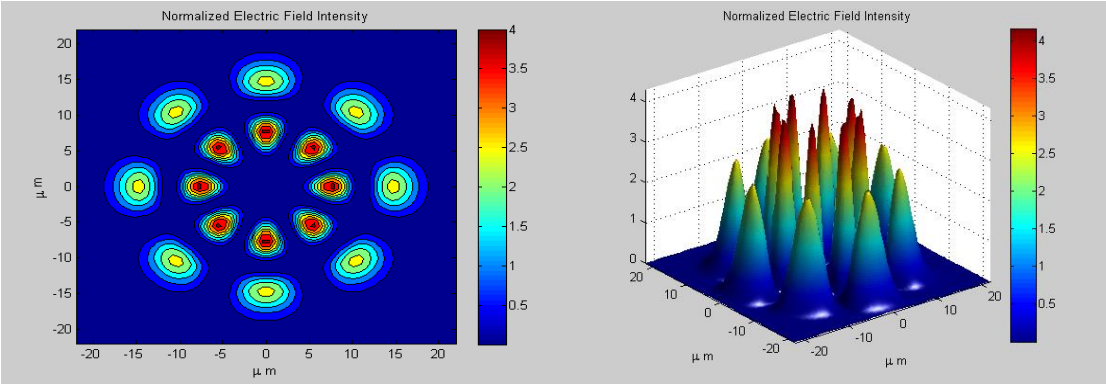

(f)

Electrical Field Intensity for *l*=5, *n*=1

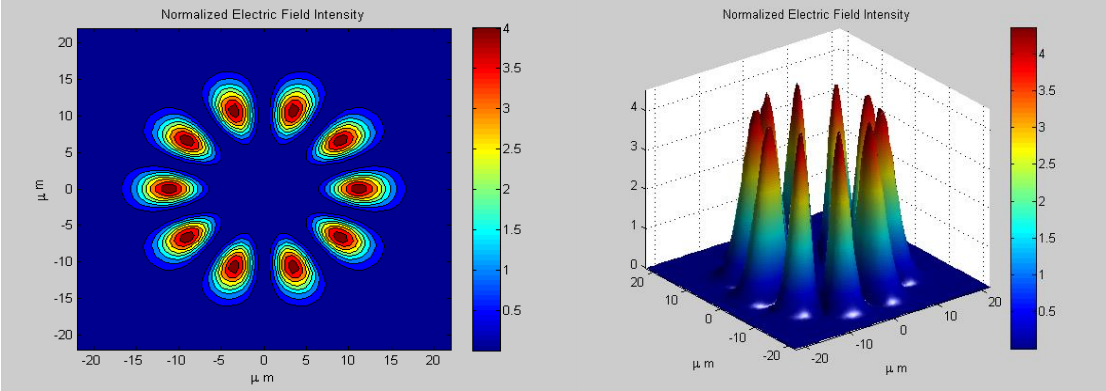

(g)

Electrical Field Intensity for *l*=5, *n*=3

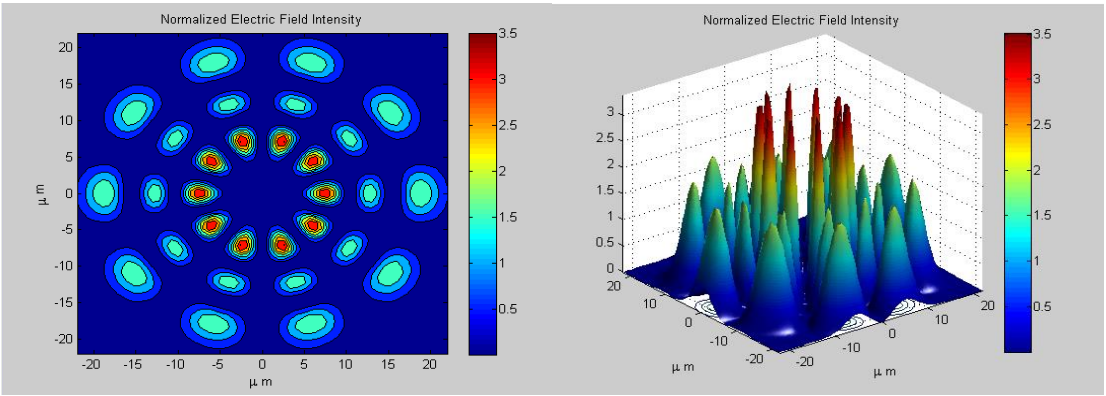

(h)

Figure 2.4 Normalized transverse electric field intensity distribution for typical $LP_{l,n}$ modes of a graded-index MMF under the weakly guiding approximation

Although the modal field expression can be derived, it does not give any polarization information or the vector field direction. The vector field direction can only be determined from the fibre symmetry and fibre polarization properties. Because the two degenerate solutions ($\psi_{ln} = F_{ln}(r)\cos l\phi,\ \psi_{ln} = F_{ln}(r)\sin l\phi$) for the LP mode at the single scalar propagation constant $\tilde{\beta}$ so that any pair of orthogonal x and y axes can be chosen as the optical axes in the fibre cross section [18]. There are a total of four possible polarization directions for the transverse field $e_{l,n}$ depending on the

combination of the two degenerate solutions of the scalar wave equation. The complete transverse mode intensity pattern for LP_{11} and its two solutions of the scalar wave equation are plotted in Figure 2.5, where LP_{11a} and LP_{11b} represent $\psi_{11a} = F_{ln}(r)\cos l\phi$ and $\psi_{11b} = F_{ln}(r)\sin l\phi$, respectively. The total LP_{11} electric field is composed of the two solutions of the scalar wave equation.

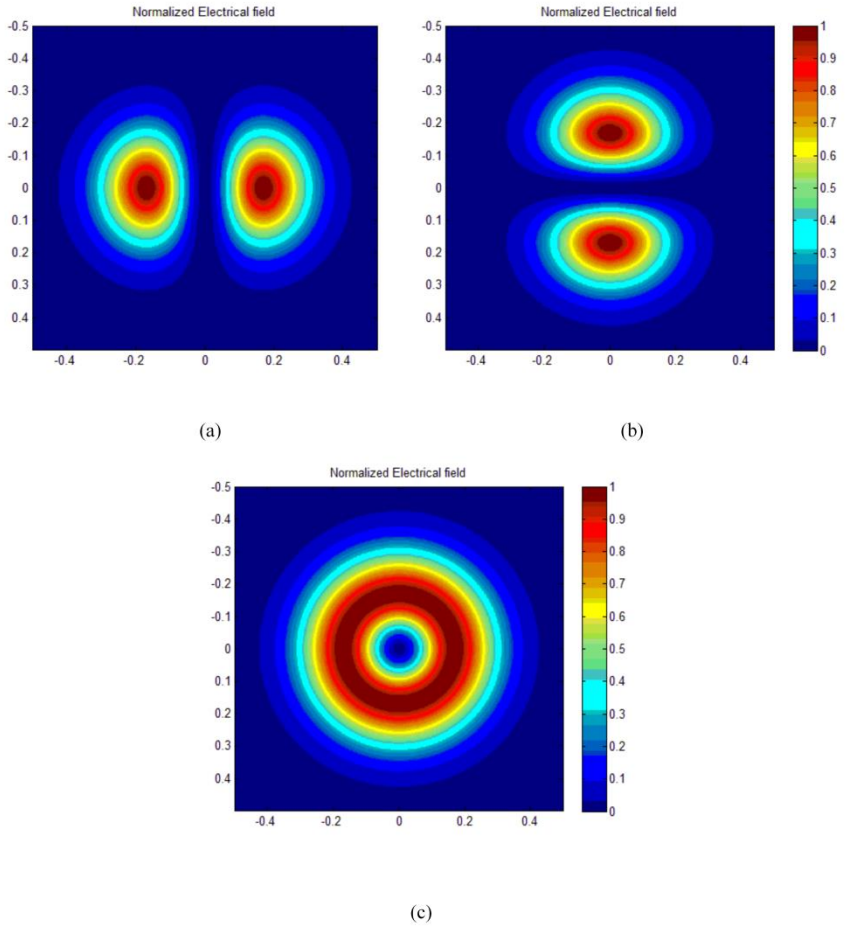

Figure 2.5 Mode intensity pattern for $n_1 = 1.45,\ n_2 = 1.44$, and $\lambda = 850nm$ for: (a) LP_{11a} (b) LP_{11b} and (c) overall of LP_{11}

The linearly polarized LP mode can be degenerated back to the traditional modes TE, TM, EH, HE [96, 112], as shown in Table 2.3. The TE mode has no electric field in the propagation direction, and there is only a magnetic field along the direction of propagation. Similarly, the TM mode has no magnetic field in the propagation direction, and there is only an electrical field along the propagation direction. The

hybrid mode contains non-zero electric and magnetic field components in the direction of propagation, and when the magnetic field is more dominant than the electric field, it is called the HE mode. In contrast, the EH mode is formed once the electric field component is more dominant than the magnetic field component.

- LP_{0m} is from the HE_{1m} mode.
- LP_{1m} comes from the $TE_{0m,}$ TM_{0m}, HE_{2m} modes.
- LP_{lm} $(l \geq 2)$ is degenerated to both $HE_{l+1,m}$ *and* $EH_{l-1,m}$ modes.

Degenerate mode number, i	**Mode**	e_{lm}
Fundamental HE_{11} and HE_{1m} (l = 0) modes		
1	Even HE_{lm}	$\hat{x} F_{lm}$
3	Odd HE_{lm}	$\hat{y} F_{lm}$
Higher-order modes (l ≥ 0)		
1	Even $HE_{l+1,\,m}$	$\{\hat{x} \cos l\phi - \hat{y} \sin l\phi\} F_{lm}$
2	TM_{0m} $(l=1)$	$\{\hat{x} \cos l\phi + \hat{y} \sin l\phi\} F_{lm}$
2	Even $EH_{l-1,\,m}$ $(l>1)$	$\{\hat{x} \cos l\phi + \hat{y} \sin l\phi\} F_{lm}$
3	Odd $HE_{l+1,\,m}$	$\{\hat{x} \sin l\phi + \hat{y} \cos l\phi\} F_{lm}$
4	TE_{0m} $(l=1)$	$\{\hat{x} \sin l\phi - \hat{y} \cos l\phi\} F_{lm}$
4	Odd $EH_{l-1,\,m}$ $(l>1)$	$\{\hat{x} \sin l\phi - \hat{y} \cos l\phi\} F_{lm}$

Table 2.3: Modal fields of weakly guiding circular fibre. This table is reproduced from page 304 of reference [18]; here, the radial mode number m is equal to n+1 in Equations 2.32 and 2.33.

The subscript i in Table 2.3 denotes the degenerate mode numbers. There are two degenerate modes (i=1, 2) for fundamental modes with l=0; for higher order modes ($l \geq 0$), there are four different degenerate modes with subscript i=1, 2, 3, 4. In this thesis, Equations (2.32) and (2.33) are mainly used for generating modal electrical

fields. Because the Laguerre polynomial is an orthogonal function on the interval [0, ∞], [113], the different LP modal electric fields are also orthogonal, which gives:

$$\int_{R=0}^{\infty}\int_{\phi=0}^{2\pi}\psi_1\psi_2 RdRd\phi \qquad (2.34)$$

$$\int_{R=0}^{\infty}\int_{\phi=0}^{2\pi}[N_1R^{l_1}L_{n_1}^{l_1}(VR^2)\exp(-\frac{1}{2}VR^2)\cos(l_1\phi)][N_2R^{l_2}L_{n_2}^{l_2}(VR^2)\exp(-\frac{1}{2}VR^2)\cos(l_2\phi)]RdRd\phi$$

Rearranging yields:

$$\left[\int_{\phi=0}^{2\pi}\cos(l_1\phi).\cos(l_2\phi)d\phi\right]\left[\int_{R=0}^{\infty}[N_1R^{l_1}L_{n_1}^{l_1}(VR^2)\exp(-\frac{1}{2}VR^2)N_2R^{l_2}L_{n_2}^{l_2}(VR^2)\exp(-\frac{1}{2}VR^2)]RdR\right]$$

As $\int_{\phi=0}^{2\pi}\cos(l_1\phi)\cos(l_2\phi)d\phi = 0,$ *for* $l_1 \neq l_2$ *due to orthogonality condition* (2.35)

$$\int_{R=0}^{\infty}\int_{\phi=0}^{2\pi}\psi_1\psi_2 RdRd\phi = 0, \quad for\ l_1 \neq l_2 \qquad (2.36)$$

Modes satisfying Equation 2.36 are called orthonormal modes.

2.2.3 Propagation constant of bound modes in graded index fibre

Assume that the fibre is an ideal waveguide that is non-absorbing, has a dielectric structure, is uniform along its length, and possesses cylindrical symmetry. For a weakly guiding MMF, the modal propagation constant is approximately [64, 114]:

$$\beta(m,\lambda) = 2\pi\frac{n_1(\lambda)}{\lambda}\left\{1-2\Delta(\lambda)[\frac{m}{M(\lambda)}]^{2\alpha/(\alpha+2)}\right\}^{1/2} \qquad (2.37)$$

where *m* is the principal mode group number, and $M(\lambda)$ is the total number of mode groups in the MMF, is given by:

$$M(\lambda) = 2\pi\rho\frac{n_1(\lambda)}{\lambda}[\frac{\alpha\Delta(\lambda)}{\alpha+2}]^{1/2} \qquad (2.38)$$

where λ is the wavelength of the excitation light, ρ is the core radius, and α is the refractive index profile number. The principal group number m is defined as $m = 2n + l + 1$, in which the parameters n and l refer to the radial and azimuthal mode numbers, respectively, and Δ is the profile height parameter given in Equation 2.1. The guided modes within the same principal mode group will have the same propagation constant.

Alternatively, the propagation constant may also be written in terms of the azimuthal and radial mode numbers:

$$\beta(l,n) = 2\pi \frac{n_1(\lambda)}{\lambda}\left\{1 - 2\Delta(\lambda)[\frac{2n+l+1}{M(\lambda)}]^{2\alpha/(\alpha+2)}\right\}^{1/2} \qquad (2.39)$$

For an infinite parabolic refractive index profile ($\alpha = 2$) the propagation constant is given by:

$$\tilde{\beta}(l,n) = \tilde{\beta}_0\left\{1 - 2\Delta(\lambda)[\frac{2n+l+1}{M(\lambda)}]^{2\alpha/(\alpha+2)}\right\}^{1/2} \qquad (2.40)$$

$$\tilde{\beta}_0 = 2\pi \frac{n_1(\lambda)}{\lambda} = \frac{V}{\rho\sqrt{(2\Delta)}} \qquad (2.41)$$

where $\tilde{\beta}_0$ is the scalar propagation constant for the fundamental mode. Substituting Equations 2.41 and 2.38 into Equation 2.40, the propagation constant can be defined as:

$$\tilde{\beta} = \frac{V}{\rho\sqrt{(2\Delta)}}\left[1 - \frac{4\Delta}{V}(2n+l+1)\right]^{\frac{1}{2}}, \quad l = 0,1,2....; n = 0,1,2..... \qquad (2.42)$$

As the waveguide structure introduces a polarization effect, the exact propagation constant for the i^{th} degenerate mode of LP_{ln} mode is given by:

$$\beta_{l,n} = \tilde{\beta}_{l,n} + \delta\beta_i \qquad (2.43)$$

where $\delta\beta_i$ is the propagation constant correction factor.

The correction factor for an infinite parabolic index profile is defined as:

$$\delta\beta_1 = \delta\beta_3 = -\frac{l+1}{2\rho V}(2\Delta)^{\frac{3}{2}}, \quad \delta\beta_2 = \delta\beta_4 = \frac{l-1}{2\rho V}(2\Delta)^{\frac{3}{2}} \qquad (2.44)$$

2.2.4 Modal power

The portion of source power exciting each mode depends on the nature of the source. For a non-absorbing fibre with no power coupling loss, the energy flux density of an electromagnetic field is given by the Poynting vector [112]:

$$S = \frac{1}{2}\mathrm{Re}(E \times H^*) \qquad (W \cdot m^{-2}) \qquad (2.45)$$

Referring to the field expression in Equation 2.10 of the $LP_{l,n}$ mode, the Poynting vector in the direction of fibre axis gives:

$$S_{z,(l,n)}(R,\phi) = \frac{1}{2}\mathrm{Re}[E_{t,(l,n)}(R,\phi) \times H^*_{t,(l,n)}(R,\phi)]\tilde{z} \qquad (2.46)$$

where * denotes the complex conjugate.

The power flow of each mode parallel to the fibre axis can be calculated by integrating the Poynting vector over the infinite cross section area *A*:

$$P_{l,n} = \int_A S_{z,(l,n)}(R,\phi)dA \qquad (2.47)$$

Replacing dA with $\rho^2 RdRd\phi$ yields:

$$P_{l,n} = \int_R \int_\phi \rho^2 \cdot R \cdot [S_{z,(l,n)}(R,\phi)]dRd\phi \qquad (2.48)$$

2.3 Multimode fibre impulse response and transfer function

Multimode fibre impulse response and transfer function are very important for characterising the performance of optical fibre communication links. Both the nonlinear properties and chromatic dispersion in a single mode fibre would in principle be present even for each individual mode in MMFs [3]. However, in MMF, the modal dispersion is dominant over other limitation factors, and the MMF transfer function is mostly affected by the mode power coupling coefficient and modal time delay. These factors will have greater effects on the degradation of the system performance. The larger core diameter of MMF and the transmission of low-energy pulses from low power light sources (e.g. VCSELs) will lead to the neglect of nonlinear effects in short distance MMF communication systems.

2.3.1 Mode power coupling coefficient

In the IEEE 802.3ae 10Gb/s standard Ethernet a low cost vertical cavity surface emitting laser (VCSEL) has been selected as the transmitter. The output of VCSEL is assumed to be a Gaussian beam with a specific spot size launch to the fibre core region. The incident electric field has a unit value within the spot; otherwise, the field becomes zero, and the normalized incident beam is given below (the derivation of the normalized incident electric field expression is showed in Appendix –a):

$$E_{in} = \frac{1}{\sqrt{\pi}\Omega}\exp\left(-\frac{R^2}{2\Omega^2}\right)\hat{x},\ \Omega = \frac{\rho_s}{\rho}\ \text{is the spot core ratio,}\ \rho_s\ \text{is the spot size,} \qquad (2.49)$$

$$\text{and} \qquad E_{in} = \begin{cases} 1, & 0 \le R \le \rho_s \\ 0, & \rho_s \le R \le \infty \end{cases} \qquad (2.50)$$

In general, the power from the incident beam cannot be totally transmitted to MMF due to the refraction occurring at the interface between the fibre and the surrounding medium. The amount of power received is determined by the Fresnel power transmission coefficient T, which is defined as [112]:

$$T = \frac{4n_i n_{co}}{(n_i + n_{co})^2} \tag{2.51}$$

where n_i is the refractive index of surrounding medium. For the sake of simplicity, the transverse fields are assumed to be equal to the incident fields ($E_{in} = E_{t,}\ H_{in} = H_t$). The geometric launching on the MMF cross section is illustrated in Figure 2.6.

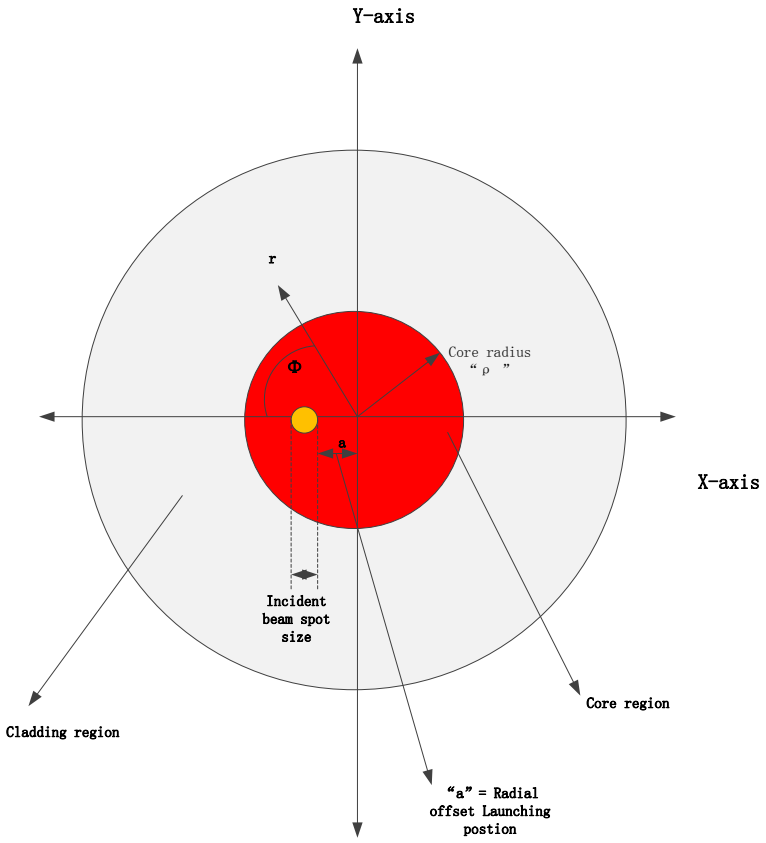

Figure 2.6 The geometric launching cross section on MMF; the yellow spot is the launching spot, " ρ " is the core radius, and "a" is the distance between the spot centre and fibre centre.

Conventionally, the power coupled into the $LP_{l,n}$ is given by the power coupling coefficient:

$$\eta_{l,n} = \frac{\left| \iint\limits_{Acore} E_{in}(x,y) \cdot \psi_{l,n}{}^{*}(x,y) dxdy \right|^2}{\iint\limits_{Acore} \left| E_{in}(x,y) \right|^2 dxdy \cdot \iint\limits_{Acore} \left| \psi_{l,n}(x,y) \right|^2 dxdy} \tag{2.52}$$

Letting $dxdy = RdRd\phi$ gives:

$$\eta_{l,n} = \frac{\left| \iint\limits_{Acore} E_{in}(R) \cdot \psi_{l,n}{}^{*}(R,\phi) RdRd\phi \right|^2}{\iint\limits_{Acore} \left| E_{in}(R) \right|^2 RdRd\phi \cdot \iint\limits_{Acore} \left| \psi_{l,n}(R,\phi) \right|^2 RdRd\phi} \tag{2.53}$$

where $\psi_{l,n}$ is the LP mode transverse electric field, E_{in} is the Gaussian incident electric field, A_{core} is the fibre core cross-section area, and R is the normalized radius $R = \frac{r}{\rho}$, where r is the distance from the fibre centre axis, and ρ is the radius of the core.

The normalized power coupling coefficient launched by a Gaussian beam in both centre launching and radial offset launching conditions are given in reference [115]:

$$\eta_{l,n} = \frac{8A^{2l}}{\Omega^{4l+2}} \left[\frac{V^{l+1}\Gamma(n+1)}{(\delta_{0l}+1)\Gamma(l+n+1)} \right] \left(\frac{1}{\Omega^2} - V \right)^{2n} \left(\frac{1}{\Omega^2} + V \right)^{-2(l+n+1)} \times \exp\left[\frac{A^2}{\Omega^2} \left(\frac{1}{1+V\Omega^2} - 1 \right) \right] \left[L_n^l \left(\frac{V(\frac{A}{\Omega^2})^2}{\frac{1}{\Omega^4} - V^2} \right) \right]^2 \tag{2.54}$$

where $A = \frac{a}{\rho}$ is the normalized radial offset value, Γ is the gamma function, $\Omega = \frac{\rho_s}{\rho}$ denotes the normalized spot size or radius of the incident light beam, δ_{ol} is the Kronecker delta function (Eq. 2.27), and $L_n^l(x)$ represents the Laguerre polynomial in terms of the radial and azimuthal mode number (n, l) shown in Equation 2.21.

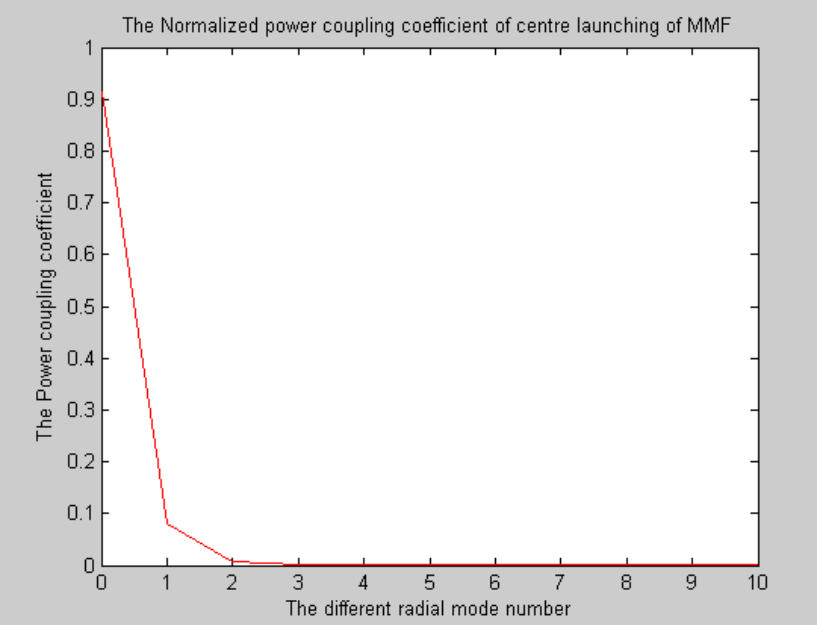

Figure 2.7 The centre launching normalized power coupling coefficient in GI-MMF; spot size =3.677 μm, λ=850nm, V=39.27, $l=0$, and $n_1=1.45$, $n_2=1.44$.

The power coupling by centre launching with a different radial mode number is depicted in Figure 2.7. It is clearly observed that the lowest order mode $LP_{0,1}$ gains a large amount of power from the light source, and there is no power in the higher order modes. Equation 2.55 reflects the power conservation,

$$\sum_{n=0,l=0}^{\infty} \eta_{l,n} = 1 \tag{2.55}$$

The q_{th} mode group power coupling coefficient is the sum of each mode belonging to the corresponding mode group, this gives:

$$\eta_q = \sum_{l,n}^{q} \eta_{l,n} \tag{2.56}$$

where q is the principal mode group number with a value of $q=2n+l+1$.

2.3.2 Modal time delay

Recalling Equations 2.1, 2.17 and 2.42, the propagation constant for the infinite parabolic index profile $\alpha = 2$ graded index MMF is given by the following equation:

$$\beta_q = \frac{\omega n_{co}}{c}\left[1 - \frac{2NAn_{co}^2 cq}{\omega\rho}\right]^{\frac{1}{2}} \tag{2.57}$$

As the group velocity is the reciprocal of the first-order derivative of the propagation constant with respect to angular frequency, the group velocity is expressed as:

$$v_g = \frac{d\omega}{d\beta_q} \qquad NA = \sqrt{n_{co}^2 - n_{cl}^2} \tag{2.58}$$

Differentiating Equation 2.57, we have (Appendix-a):

$$\frac{d\beta_q}{d\omega} = \frac{n_{co}}{c\sqrt{\omega\rho}}\left[\frac{\omega\rho - NAn_{co}^2 cq}{\sqrt{\omega\rho - 2NAn_{co}^2 cq}}\right] \tag{2.59}$$

Substituting Equation 2.59 back into 2.58, the modal time delay after a distance L is given by:

$$\tau_g = \frac{L}{v_g} = \frac{Ln_{co}}{c\sqrt{\omega a}}\left[\frac{\omega a - NAn_{co}^2 cq}{\sqrt{\omega a - 2NAn_{co}^2 cq}}\right] \tag{2.60}$$

Alternatively, it may be written in terms of the radial mode number and azimuthal mode number (l, n):

$$\tau_{l,n} = \frac{Ln_{co}}{c\sqrt{\omega a}}\left[\frac{\omega a - NAn_{co}^2 c\left(2n + l + 1\right)}{\sqrt{\omega a - 2NAn_{co}^2 c\left(2n + l + 1\right)}}\right] \tag{2.61}$$

Due to imperfections in the fibre manufacturing process, the perfect index profile $\alpha = 2$ is difficult to achieve, and the index profile parameter varies between 1.8 to 2.2 [116]. The general expression for modal time delay in any index profile (α) GI-MMF may be derived as [117]: (the detailed derivation is presented in Appendix-b and Appendix-c)

$$\tau_q = \frac{L}{v_g}$$

$$= \frac{Ln_{co}}{c}\left[1-\left(\frac{NA}{n_{co}}\right)^2\left(\frac{\sqrt{2}qc}{\rho\omega NA}\right)^{\frac{2\alpha}{\alpha+2}}\left(\frac{2}{\alpha}\right)\left(\frac{\alpha}{\alpha+2}\right)^{\frac{2}{\alpha+2}}\right]\times\ldots\ldots$$
$$\left[1-\left(\frac{NA}{n_{co}}\right)^2\left(\frac{\alpha+2}{\alpha}\right)^{\frac{\alpha}{\alpha+2}}\left(\frac{\sqrt{2}qc}{\rho\omega NA}\right)\frac{2\alpha}{\alpha+2}\right]^{-\frac{1}{2}}$$

or,

$$\tau_{l,n} = \frac{Ln_{co}}{c}\left[1-\left(\frac{NA}{n_{co}}\right)^2\left(\frac{\sqrt{2}qc}{\rho\omega NA}\right)^{\frac{2\alpha}{\alpha+2}}\left(\frac{2}{\alpha}\right)\left(\frac{\alpha}{\alpha+2}\right)^{\frac{2}{\alpha+2}}\right]\times\ldots\ldots$$
$$\left[1-\left(\frac{NA}{n_{co}}\right)^2\left(\frac{\alpha+2}{\alpha}\right)^{\frac{\alpha}{\alpha+2}}\left(\frac{\sqrt{2}(2n+l+1)c}{\rho\omega NA}\right)\frac{2\alpha}{\alpha+2}\right]^{-\frac{1}{2}} \quad (2.62)$$

2.3.3 Multimode fibre transfer function

Assuming linear propagation conditions, incoherent nature and no mode interaction, the modal impulse response is described by superposing all supported modal contributions. In addition, both the effects of the modulated light source spectral width and input pulse spectral content are neglected [118-120]. The impulse response expression can then be written as:

$$h(t) = \sum_{l,n}^{\infty} \eta_{l,n}\delta(t-\tau_{l,n}) \quad (2.63)$$

where $\eta_{l,n}$ and $\tau_{l,n}$ are the power coupling coefficient and time delay that are defined in Equations 2.54 and 2.61, respectively. The symbol δ denotes the delta function.

The impulse response is analysed by plotting the power coupling coefficient versus

the modal time delay for different LP modes through a 1km long MMF. The results obtained are presented in Figure 2.8 with a range of radial offset values. The 850nm VCSEL is utilized as the optical light source.

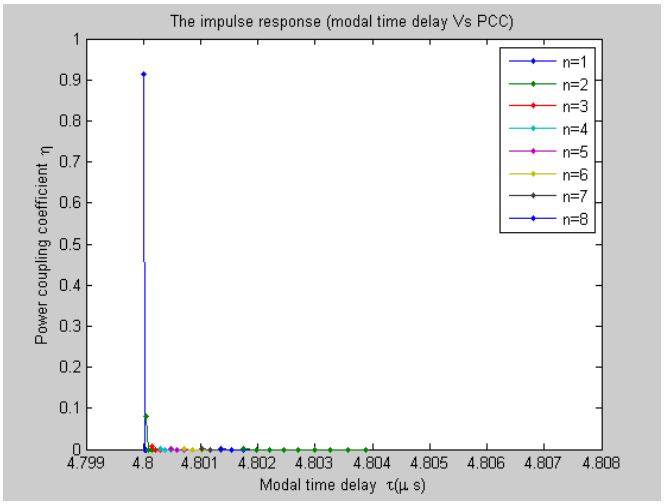

(a)

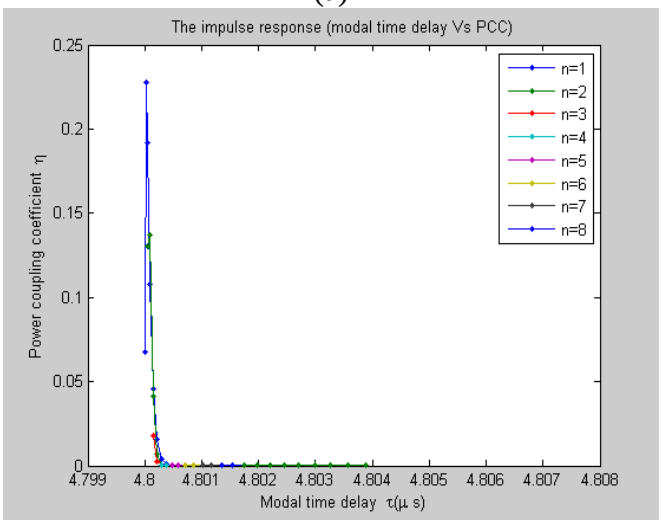

(b)

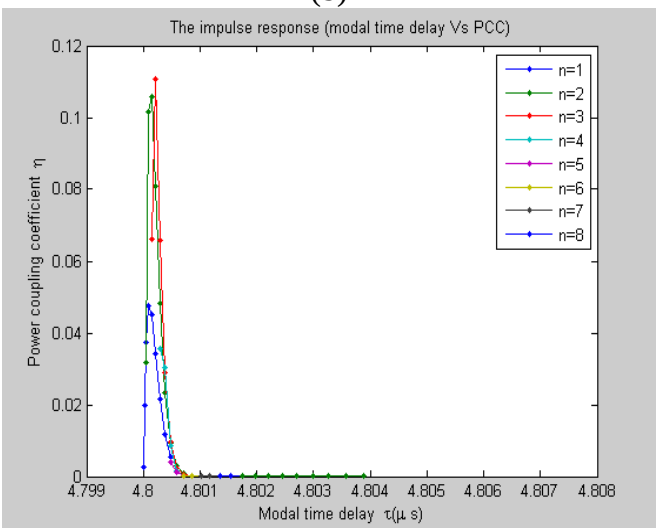

(c)

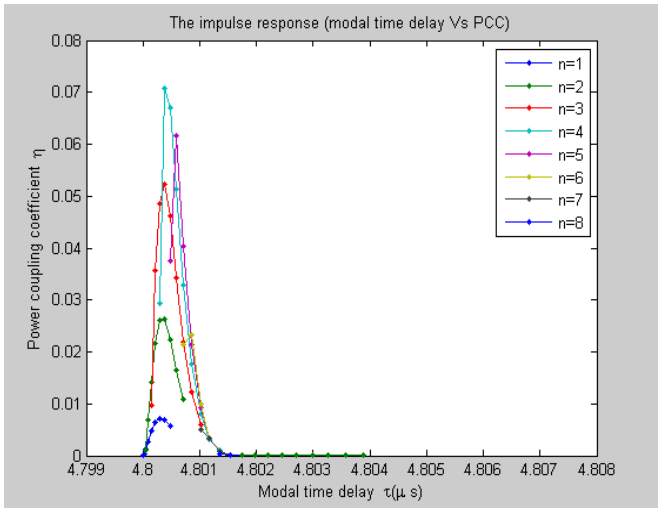

(d)

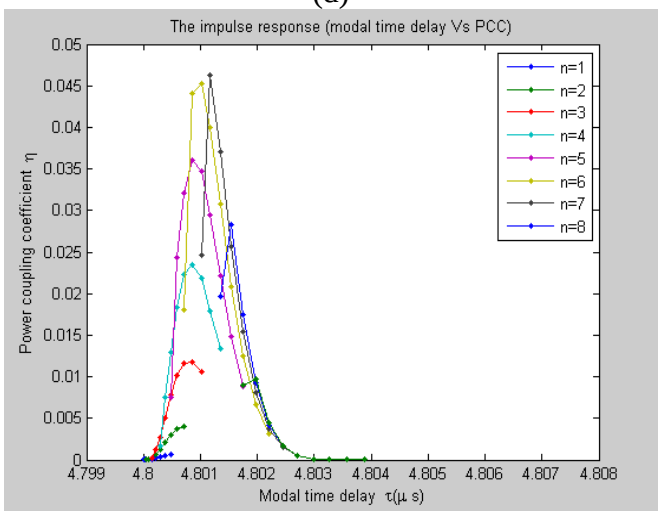

(e)

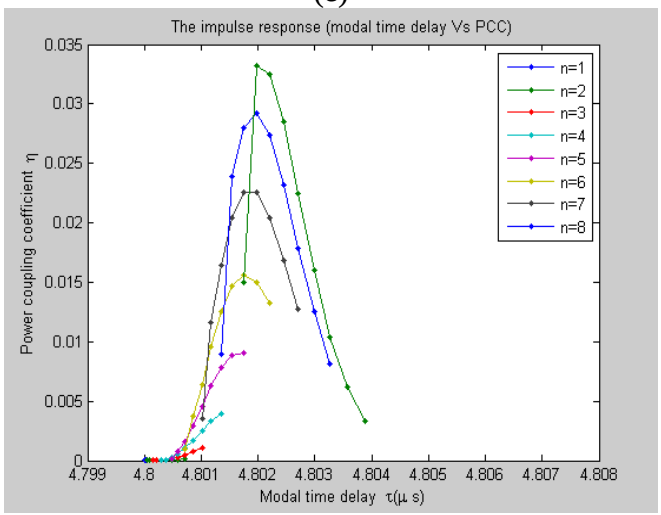

(f)

Figure 2.8 Impulse response for various radial mode numbers (n) and azimuthal mode numbers (l) of a parabolic index profile ($\alpha = 2$) GI-MMF with $n_1 = 1.45$, $n_2 = 1.44$, $\lambda = 850nm$ under different offsets: (a) 0 μm offset; (b) 10 μm offset; (c) 15 μm offset; (d) 20 μm offset; (e) 25 μm offset; and (f) 30 μm offset.

In Figure 2.8, each curve corresponds to a single radial mode number *n*, and each point on the curves represents an azimuthal mode number l. The time delay for the maximum coupling coefficient gradually increases with increasing radial offset due to the fact that the maximum coupling coefficient moves to the higher order modes if the radial offset becomes larger. The modal dispersion is proportional to the delay spread, indicating a time difference between the lower order and higher order modes. More excited modes correspond to more serious modal dispersion. The principle behind this phenomenon is that the power coupling coefficient starts to shift to the higher order modes.

Under the linear propagating regime and neglecting the chromatic dispersion contribution for the moment, the $H(\omega)$ transfer function of GI-MMF describes a relationship between the input impulse and the output frequency response of the optical fibre. This parameter is very useful to estimate the 3dB bandwidth. If the input signal is defined as a unit impulse, the MMF impulse response in Equation 2.63 can be easily transformed to frequency response via Fourier Transform, as shown in Equation 2.64 [3]:

$$H(\omega) = \sum_{l,n=0}^{\infty} \eta_{l,n} \exp(-i\omega\tau_{l,n}) \qquad (2.64)$$

$$= \sum_{l,n=0}^{\infty} \eta_{l,n} \exp(-i2\pi f\tau_{l,n}) \qquad f = optical\ \ carrier\ \ frequency$$

A parabolic index profile $\alpha = 2$ GI-MMF frequency response has been simulated using the parameters listed in Table 2.4, and the results are shown in Figure 2.9.

n_1	n_2	V	ρ /core radius	ρ_s /spot size	λ /wavelength	L /fibre length
1.45	1.44	39.27	31.25 μm	3.677 μm	850nm	1km, 3km

Table 2.4 The MMF transfer function or frequency response simulation parameters; n_1 , n_2 are the refractive index at the centre of the core and cladding region, respectively, and V is the normalized frequency.

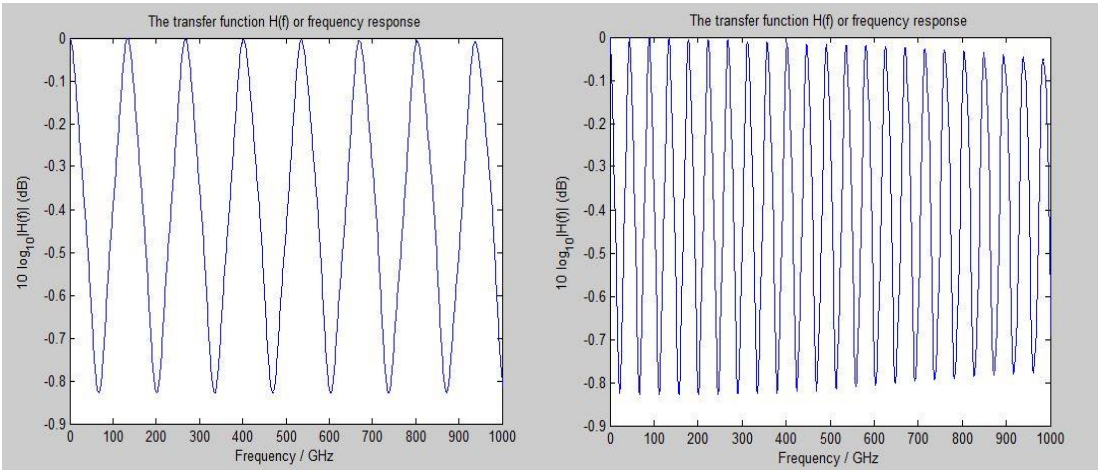

Figure 2.9 Transfer function of GI-MMF for various offset launches and fibre lengths: (a) offset=0 μm, L=1000m (b) offset=0 μm, L=3000m (c) offset=15 μm, L=1000m (d) offset=15 μm, L=3000m.

Figure 2.9 reveals some extremely important behaviour the frequency response of GI-MMF does not monotonically decrease as the frequency increases. As the

transmission distance increases the modal dispersion gets progressively larger and results in a frequency response with greater oscillation. Similarly, the extent of the offset launch also influences frequency response.

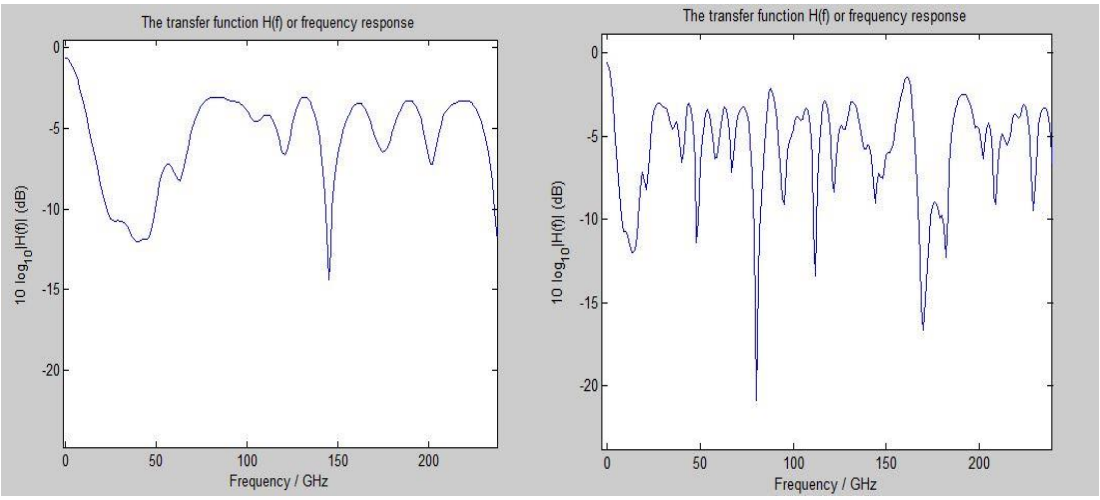

(a) (b)

Figure 2.10 Low frequency range transfer function of GI-MMF for various fibre lengths with offset=15 μm: (a) L=1000m and (b) L=3000m.

In the range between 50GHz and 120GHz in Figure 2.10, the frequency response decreases sharply and its shape becomes similar to Gaussian shape. Beyond the 3dB bandwidth point the frequency response starts to oscillate at higher frequency, but it gradually becomes relatively flat. This high frequency region can be efficiently employed in a subcarrier multiplexing, leading to a high data rate transmission system. Another feature is that the amplitude of frequency response $|H(\omega)|$ shows a Rayleigh distribution within the high frequency region; this property is similar to the wireless MIMO channel [97, 121]. The explicit implication of this is that GI-MMF may provide huge potential for high data rate transmissions, such as optical MIMO. Meanwhile, it also indicates that in the low frequency range, the frequency response is dominated by the lower order modes, which have larger time delays, while in the high frequency region, its frequency response is dominated by the higher order modes

associated with smaller time delays.

In addition to the modal time delay, the intrinsic chromatic dispersion due to the dispersion relationship between the modal propagation constant and optical light source spectrum may also affect the frequency response of the MMFs [3, 114, 120], especially in long transmission systems. In the absence of nonlinearity and mode mixing, the total impulse response of a multimode fibre should be described as a superposition of each guided mode that suffers both intermodal dispersion and chromatic dispersion; thus, the total frequency response will be defined as a product of the chromatic frequency response and the conventional MMFs frequency response [64, 96, 110]:

$$H(f) = \sum_{l,n=0}^{\infty} \eta_{l,n} \exp(-i2\pi f \tau_{l,n}) H_{CD}(f) \tag{2.65}$$

where $H_{CD}(f)$ is the chromatic frequency response.

2.4 Conclusion

The fundamental properties of multimode fibres have been reviewed, and the mathematical expression for a weakly guiding MMF modal electric field has been presented and simulated. The intensity pattern of different $LP_{l,n}$ modes has been simulated using the Matlab program. The full details of the channel impulse response and transfer function of weakly guiding GI-MMF have also been discussed, including the modal time delay and power coupling coefficient. It can be concluded that the frequency responses of MMFs can be affected by the offset launch conditions, transmission distance and the number of guided modes. The frequency response comprises the power coupling coefficient and modal time delay, both of which can be affected by guided modes that are excited by offset launching.

Chapter 3: Near Field Pattern of Multimode Fibre

In the previous chapter, the complete channel impulse response and transmission features of the GI-MMF were introduced. For a deeper understanding of such transmission features in MMF, the characteristics of modes propagating along the MMF must be clarified. This chapter will analyse the near field intensity pattern at the output of a lossless GI-MMF that is excited by the radial offset via SMF, a step-index single mode fibre with a laser spot size of $3.677\mu m$. The light source operates at a wavelength of 1310nm and is pigtailed to SMF. In the absence of modal noise, the simulated results are found to be in good agreement with the reported results of Ref. [122]. A further simulation of the near field pattern with minor changes in fibre length, core diameter and refractive index demonstrates the robustness of the simulation results. According to the spatial properties of the intensity pattern the specific optical power at the output facet can be calculated by simply integrating the near field intensity with respect to the corresponding detector area.

3.1 Multimode fibre transmission impairments

The impact of transmission impairments are mainly attributed to dispersion, mode mixing, and differential mode attenuation. Dispersion results in pulse broadening as they propagate along the fibre, with each pulse broadening and overlapping with its neighbours. This leads to an indistinguishable detection, causing inter-symbol interference (ISI) [64]. Consequently, this ISI distorts the signal waveform and affects the bit error rate. The mode mixing or so-called mode coupling tends to average out the propagation delays associated with the mode, thereby reducing the intermodal

dispersion [55, 123-125]. Mode attenuation may be considered as a power loss factor, and in MMFs, each guided mode experiences different attenuations. Due to the large core radius of MMFs, the power density across the core area is not very large so that nonlinear effects are not considered.

3.1.1 Chromatic dispersion

As the group velocity is frequency dependent, thus different spectrum components of the transmitted pulse travel at different speeds. This phenomenon is called group velocity dispersion or chromatic dispersion. This effect may be caused by either the dispersive properties in the fibre material (material dispersion) or the guiding effect in the fibre structure (waveguide dispersion) [64]. In MMFs, waveguide dispersion is generally negligible compared with material dispersion. Mathematically, the propagation constant along the fibre can be expanded in a Taylor series about the centre optical frequency ω_0:

$$\beta(\omega) \cong \beta_0 + \beta_1(\omega - \omega_0) + \frac{\beta_2}{2}(\omega - \omega_0)^2 \tag{3.1}$$

$$\beta_n = \left(\frac{d^n \beta}{d\omega^n} \right)_{\omega=\omega_0}, \quad n = 1, 2 \tag{3.2}$$

where ω_0 is the optical carrier frequency, β_0 is the propagation constant at the carrier frequency, $\beta_1 = \frac{1}{v_g}$ is related to the group velocity, β_2 is the group velocity dispersion parameter, and β_n is the n^{th} order derivative of the propagation constant.

Chromatic dispersion affects the frequency response of each excited mode in MMFs and alters the transmitted pulse shape. A parameter D is used to measure the degree of

chromatic dispersion, which is defined as:

$$D = \frac{d}{d\lambda}\left(\frac{1}{v_g}\right) = -\frac{2\pi c\beta_2}{\lambda^2} \qquad \text{(ps/km/nm)} \quad (3.3)$$

where β_2 is in units of ps^2 / km and determines the degree of pulse broadening along the MMFs. The chromatic dispersion in optimized 50 μm MMFs is typically around 100ps/nm/km at a wavelength of 850nm [126].

The chromatic dispersion in an MMF can be characterised by its transfer function:

$$H_{CD}(f) = \exp\left(-i\beta_2 2\pi^2 f^2 L\right) \qquad (3.4)$$

Substituting Equation 3.3 into 3.4 yields

$$H_{CD}(f) = \exp\left(i\frac{\pi D\lambda^2 f^2 L}{c}\right) \qquad (3.5)$$

In most cases the chromatic dispersion is small compared with the intermodal dispersion in a practical short distance MMF system, but it must be accounted for in long distance, high speed systems. It has been shown that modal and chromatic dispersion can interact and compensate for each other [126, 127], giving rise to chromatic dispersion compensated MMFs that will largely reduce the limitations of chromatic dispersion in future 40/100GbE systems.

3.1.2 Modal dispersion

Modal dispersion is a major dispersion that needs to be considered in MMFs, and is a results of each guided mode having a different propagation constant value at a single frequency [55]. The large mode time delay spread between the fastest mode and slowest mode leads to ISI, increasing the difficulty in detecting the correct signal while also limiting the transmission distance. This impairment becomes more serious

as we increase the bit rate and transmission distance. Fortunately, it can be eliminated by using graded index multimode fibre (GI-MMF), which is why GI-MMF is widely employed in current MMF networks. Meanwhile, due to manufacturing imperfections, variations in the refractive index profiles may also affect intermodal dispersion. The time delay for the LP modes through a fibre length L is given in Equations 2.61 and 2.62. Although the inherent modal dispersion distorts the transmitted signal, it may be exploited rather than avoided for improving the bandwidth in MMF; and this idea is the principle behind dispersive multiplexing in MMFs [82].

3.1.3 Polarization mode dispersion

In an ideal circularly symmetric fibre there are two orthogonally polarized modes that have the same transmission speed along the fibre. In fact, due to random imperfections during the fibre manufacturing process, fibre core asymmetries or mechanical stress induced material birefringence in MMFs cause the two polarizations to travel at different speeds, resulting in pulse broadening. Since the imperfections and asymmetries exist randomly, the polarization mode dispersion effect has a random nature. A mean polarization dependent time differential $\Delta\tau$ can be used to measure the polarization mode dispersion, which is proportional to the square root of the transmission distance L [64]. It is denoted as:

$$\Delta\tau = D_{PDM}\sqrt{L} \tag{3.6}$$

where D_{PDM} is the average polarization mode dispersion parameter in units of $ps/\sqrt{km}$. Even though its random nature may make the analysis more complicated, polarization mode dispersion can be compensated either optically or electrically by various equalizers. Under the weakly guiding approximation, polarization effects are

limited because of the waveguide structure. Indeed, their impact is considerably less compared to the impact of modal dispersion [3, 128, 129]. For a 10Gb/s system, the required polarization mode delay is less than 10ps, and currently produced fibres can achieve a PMD $< 0.5ps/\sqrt{km}$ or $0.3ps/\sqrt{km}$ [130]. Here, we assumed that the impulse response of the unperturbed ideal multimode fibre with cylindrical symmetry is independent of the orientation of the linear input polarization. For simplicity, we also assumed a launching with a linear polarization with a direction that coincides with the excited fibre modal filed direction and that the two polarization states had the same speed; thus, the polarization mode dispersion in an ideal MMF is negligible in this thesis [3].

3.1.4 Mode mixing

In practical systems, the pulse distortion will increase less rapidly after a certain fibre distance as the mode mixing will average out the time delays associated with the modes, thus reducing the intermodal dispersion [55, 123, 125]. The mode mixing is caused by structural imperfections such as fibre core diameter fluctuations, refractive index variations, and microbends [131]. However, the recent new fibre fabrication technique compensates the core and refractive index imperfections so that the external causes become the main dominant source in silica glass fibre mode mixing, for example the microbends of fibre itself [114, 124, 131, 132]. Under the mode mixing phenomenon the guided mode power will couple into the neighbouring modes as long as those modes have an identical propagation constant. Furthermore, the guided mode power will be transferred to the unguided modes that produce extra losses [123]. In principle, the mode mixing can be divided into two categories: intra-group mode mixing and inter-group mode mixing. Intra-group mode mixing, as its name suggests

occurs within the same mode group and it appears more easily and quickly than inter-group mode mixing. In modern silica-based GI-MMFs, the spatial modes within the same group are fully coupled after a distance on the order of 300m [36, 133]. In contrast, the spatial modes in different groups are only partially coupled after a distance of 100km [108, 134, 135]. For the analysis, only intra-group mode mixing with a transmission distance of less than 10km has been considered [94, 132].

3.1.5 Differential mode attenuation

Mode dependent attenuation arises from intrinsic material losses and waveguide properties along with material imperfection and waveguide irregularities [136]. The intrinsic material losses originate from conventional loss mechanisms such as Rayleigh scattering produced by fluctuation in refractive index [114, 137], UV absorption [136], and reflection losses at the boundary between the core and cladding in fibres [114]. Differential mode attenuation is defined as the attenuation variation among the guided modes. The different modes in silica fibres will experience attenuation in a slightly different manner, which is given by:

$$\gamma_{l,n}(\lambda) = \gamma_0(\lambda) + \gamma_0(\lambda) I_9 \left[7.35 \left(\frac{m-1}{Q} \right)^{\frac{2\alpha}{\alpha+2}} \right] \tag{3.7}$$

where Q is the total mode group number, $\gamma_0(\lambda)$ is the attenuation of the lowest order mode, m is the principal mode group number, I_9 is the 9^{th}-order modified Bessel function of the first kind, and α is the index profile number [114, 138-141]. From Equation 3.7, it is known that attenuation is the same for all modes within the same mode group *m*. The total wavelength dependent attenuation coefficient Γ can be written into the total power term, which is the sum of the individual received powers

from all excited modes [120]:

$$\sum_{m=1}^{Q} e^{-\gamma_m(\lambda)\cdot L} = 10^{-\Gamma(\lambda)\cdot L} \tag{3.8}$$

When intra-group mode mixing is taken into account the expression of mode-dependent attenuation for each individual mode is given by $\exp(-\gamma_{u,v}L)$, where L is the transmission distance.

3.2 Near field pattern without intra-group mode mixing

Assuming the electric field of the optical pulse is linearly polarized in the x-direction and under the incoherent property of modes, the modal electric field propagates through a GI-MMF with a distance z is given by:

$$E_x(r,\phi,z) = \sum_{l,n} C_{l,n}\cdot\psi_{l,n}\cdot e^{-j\beta_{l,n}z} \tag{3.9}$$

When z=0, $E_x = E_{in}$, where E_{in} is the incident electric field:

$$E_{in} = \sum_{l,n} C_{l,n}\cdot\psi_{l,n} \tag{3.10}$$

Multiplying $\psi_{l,n}$ to both sides of Equation 3.10 and integrating the product over the entire area of the fibre core gives:

$$\iint E_{in}(r,\phi)\cdot\psi_{l,n}(r,\phi)rdrd\phi = C_{l,n}\iint \psi^2{}_{l,n}(r,\phi)rdrd\phi \tag{3.11}$$

Letting $R = \frac{r}{\rho}$, where R is the normalized radius and ρ is the core radius, Equation 3.11 may be rewritten as:

$$\rho^2\iint E_{in}(R,\phi)\cdot\psi_{l,n}(R,\phi)RdRd\phi = \rho^2 C_{l,n}\iint \psi^2{}_{l,n}(R,\phi)RdRd\phi \tag{3.12}$$

Using the property of a normalized modal electrical field: $\iint \psi^2{}_{l,n}(R,\phi)RdRd\phi = 1$,

Thus, $$C_{l,n} = \iint E_{in}(R,\phi) \cdot \psi_{l,n}(R,\phi) R dR d\phi \quad (3.13)$$

where C is the modal amplitude, which can be written in terms of the coupling coefficient $\eta_{l,n}$.

$$C_{l,n} = \sqrt{\eta_{l,n}} \quad (3.14)$$

The total electric field that arrives at the output facet is the sum of all possible guided modes in the GI-MMF and it is given by:

$$E_x = \sum_{l,n} C_{l,n} \cdot \psi_{l,n} \cdot e^{-j\beta_{l,n} z} \hat{x} = \sum_{l,n} \sqrt{\eta_{l,n}} \cdot \psi_{l,n} \cdot e^{-j\beta_{l,n} z} \hat{x} \quad (3.15)$$

The magnetic field under the weakly guiding approximation may be expressed as:

$$H_y = \sqrt{\frac{\varepsilon_0}{\mu_0}} \cdot n_{co} \cdot \sum_{l,n} C_{l,n} \cdot \psi_{l,n} \cdot e^{-j\beta_{l,n} z} \hat{y} = \sqrt{\frac{\varepsilon_0}{\mu_0}} \cdot n_{co} \cdot \sum_{l,n} \sqrt{\eta_{l,n}} \cdot \psi_{l,n} \cdot e^{-j\beta_{l,n} z} \hat{y} \quad (3.16)$$

Finally, the intensity at the output facet of GI-MMF is written as:

$$S = \frac{1}{2} \mathrm{Re}\left(E_x \cdot H_y^* \right) \hat{z}, \quad (3.17)$$

$$= \frac{1}{2} \mathrm{Re}\left(\sum_{l,n} \sqrt{\eta_{l,n}} \cdot \psi_{l,n} \cdot e^{-j\beta_{l,n} z} \hat{x} \cdot \left(\sqrt{\frac{\varepsilon_0}{\mu_0}} \cdot n_{co} \cdot \sum_{l,n} \sqrt{\eta_{l,n}} \cdot \psi_{l,n} \cdot e^{-j\beta_{l,n} z} \right)^* \hat{y} \right)$$

where the parameter z denotes the propagation length, and $\hat{x}, \hat{y}, \hat{z}$ are the unit vectors parallel to the x-axis, y-axis, and fibre axis, respectively. Figure 3.1 corresponds to the results of the near field pattern with various fibre lengths and using different launch conditions. The simulated $62.5/125 \mu$m GI-MMF supports a total of 12 mode groups and is excited with a light source operating at a wavelength of 1310nm. Assuming that the continuous wave laser is used to excite different modes, and the input Gaussian beam with a specific spot size ($3.677 \mu m$) is launched into the fibre's core. The energy of each excited mode can be obtained from a power coupling coefficient and, each mode will gain a specific propagation constant. Therefore, the electrical field of

guided modes arriving at the MMF output can be calculated. Under the weakly guiding approximation, the magnetic field can be obtained from Equation 3.16. Consequently, the intensity of each mode is given by Equation 3.17, whereas the total near field intensity pattern is merely the sum of all intensities generated by these guided modes once they are incoherent.

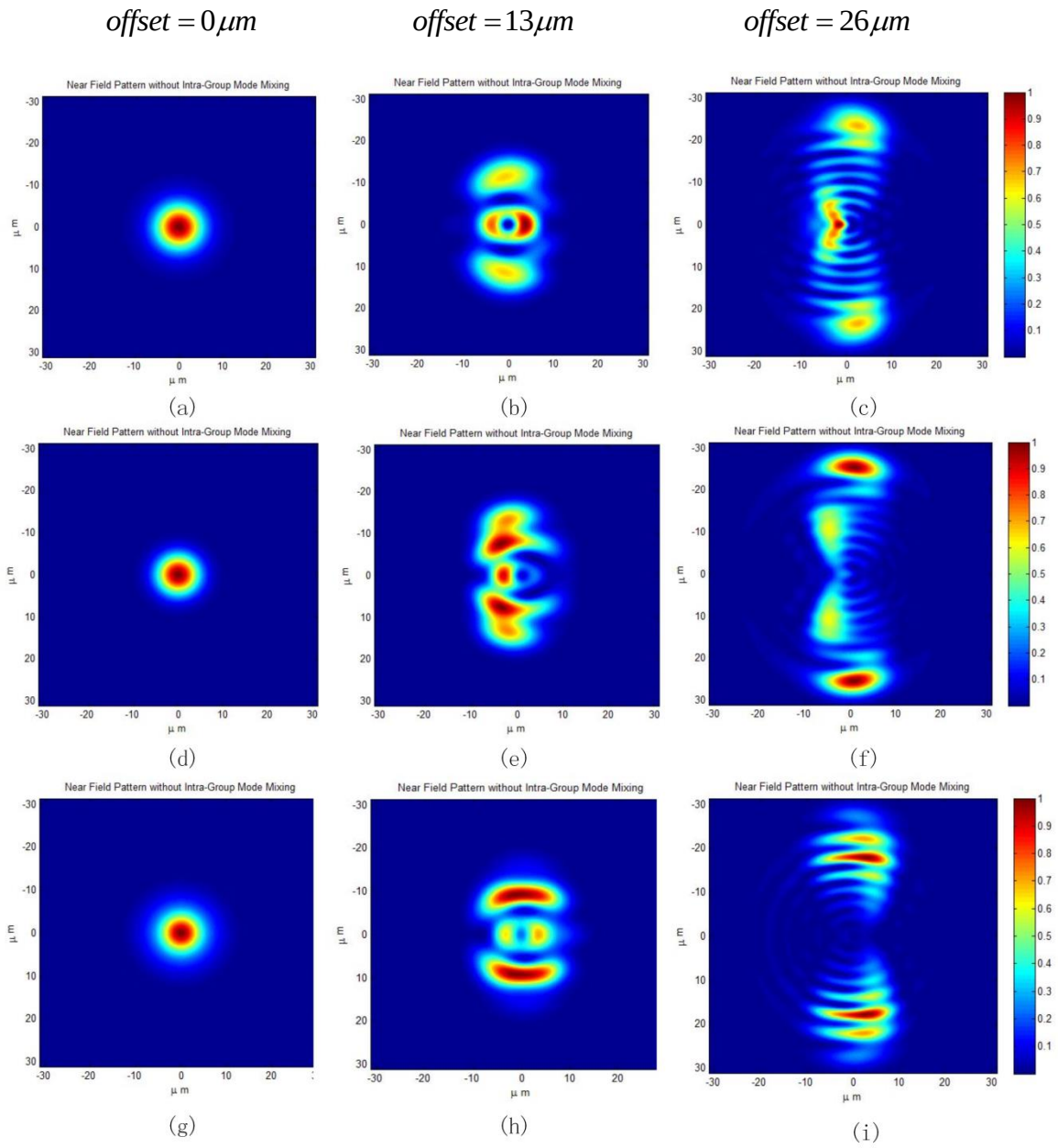

Figure 3.1 Simulation of NFP at the output of GI-MMF under selective excitation with radial offsets of $0\mu m, 13\mu m, 26\mu m$, index profile $\alpha = 2$, and $\lambda = 1310nm$: (a-c) NFP of a 50m long GI-MMF, (d-f) NFP of a 500m long GI-MMF, (g-i) NFP of a 1km long GI-MMF.

Figure 3.1 shows that the propagation distance does not affect the overall near field intensity pattern (overall disk shape), even for a 1km long GI-MMF. The NFP remains confined within a disk shaped area whose radius is determined by the SMF radial offset; however, with a sufficiently long fibre length, the speckle contrast will finally decrease [142, 143]. It should be noted that the result shown in Figure 3.2 is slightly different to that reported in Ref. [122], because only the polarized ($F_{l,n}\cos l\phi$) transverse electric field for $LP_{l,n}$ modes were used instead of two ϕ -dependence solutions. In Figure 3.2, the simulated NFP with refractive index profile defects demonstrates that the speckle pattern has a distinct dependency on the refractive index profile, but it still has no significant impact on the overall outer shape of the NFP. For a zero radial offset, the speckle pattern spans when increasing the index profile value; this tendency may be caused by the specific shape of the refractive index profile, which has a significant effect on the distribution of the guided optical power. Although the index profile has no critical effect on the overall shape of the GI-MMF NFP up to a length of 1km, it may strongly affect the GI-MMF bandwidth [114].

$offset = 0\mu m$ $offset = 13\mu m$ $offset = 26\mu m$

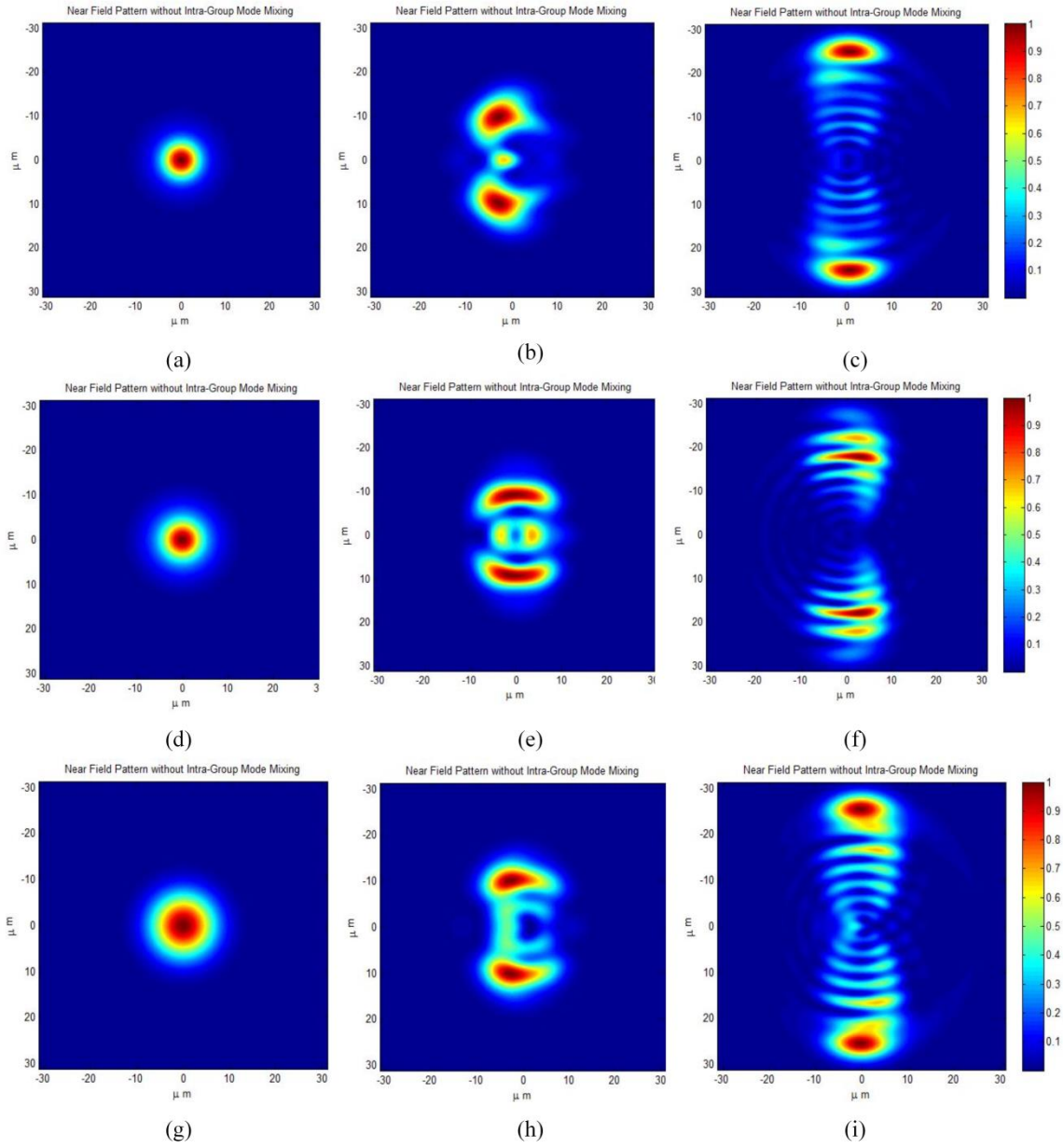

Figure 3.2 Simulation NFP for a GI-MMF with L=1km and different refractive index defects (e.g. $\alpha = 1.9$ or $\alpha = 2.1$) and a perfect parabolic index profile $\alpha = 2$ assuming no intra-group mode mixing with $\lambda = 1310nm$: (a-c) NFP of GI-MMF with $\alpha = 1.9$, (d-f) NFP of GI-MMF with $\alpha = 2$, (g-i) NFP of GI-MMF with $\alpha = 2.1$.

3.3 Near field pattern with intra-group mode mixing

Under intra-group mode mixing the total power launched in a specific m^{th} principal mode group will redistribute evenly among all modes within the group. The modulus of the amplitude $\overset{m}{C}_{l,n}$ of all modes in the m_{th} group becomes [122]:

$$\left|\overset{m}{C}_{l,n}(z)\right| = \sqrt{\frac{\sum_{l,n}\left|\overset{m}{C}_{l,n}(0)\right|^2}{N_m}} \tag{3.18}$$

where N_m is the total mode number in the m_{th} group, and the phase of $\overset{m}{C}_{l,n}(z)$ is assumed to be random with a uniform distribution over 0 and 2π .

In the absence of mode mixing, the modal amplitude C(z) is:

$$C_{l,n}(z) = C_{l,n}(0)\cdot\exp(-j\beta_{l,n}z)\cdot\exp(-\gamma_{l,n}z) \tag{3.19}$$

In practical work, this attenuation effect is very limited and can be approximated to a perturbation in the lossless case [112].

Therefore, the total near field intensity pattern of the LP mode is defined as:

$$E_{l,n}(R,\phi,z) = \Psi_{l,n}(R,\phi)\cdot C_{l,n}(z),$$

$$H_{l,n}(R,\phi,z) = \sqrt{\frac{\varepsilon_0}{\mu_0}}\cdot n_{co}\cdot E_{l,n}(R,\phi,z) \tag{3.20}$$

$$S_m(R,\phi,z) = \frac{1}{2}\mathrm{Re}\left[\sum_{l,n}^{m} E_{l,n}(R,\phi,z)\times H^*_{l,n}(R,\phi,z)\cdot\hat{z} + \sum_{l\neq l',n\neq n'}^{m} E_{l,n}(R,\phi,z)\times H^*_{l',n'}(R,\phi,z)\cdot\hat{z}\right] \tag{3.21}$$

On the right hand of Equation 3.21, the first term is the intensity distribution on each mode, and the second term describes the variation in intensity distribution due to

modal field interference. The total intensity pattern of all the mode groups is given by:

$$S_{total} = \sum_{m=1}^{Q} S_m \tag{3.22}$$

In the case of intra-group mode mixing the optical path $L \times n$ fluctuates over a scale of many wavelengths so that the phase term $\beta \cdot z$ is assumed to be a random variable that is uniformly distributed over 0 and 2π and therefore gives rise to the random nature of the phase. The intensity pattern only changes with this phase term in the modal field equation. Owning to the random phase, the NFP image becomes blurry, while the overall outer shape remains unchanged. The speckle contrast simultaneously becomes weaker. The results are presented in Figure 3.3. To simulate the mode mixing effect, a random phase has been generated in Matlab and added to the modal amplitude.

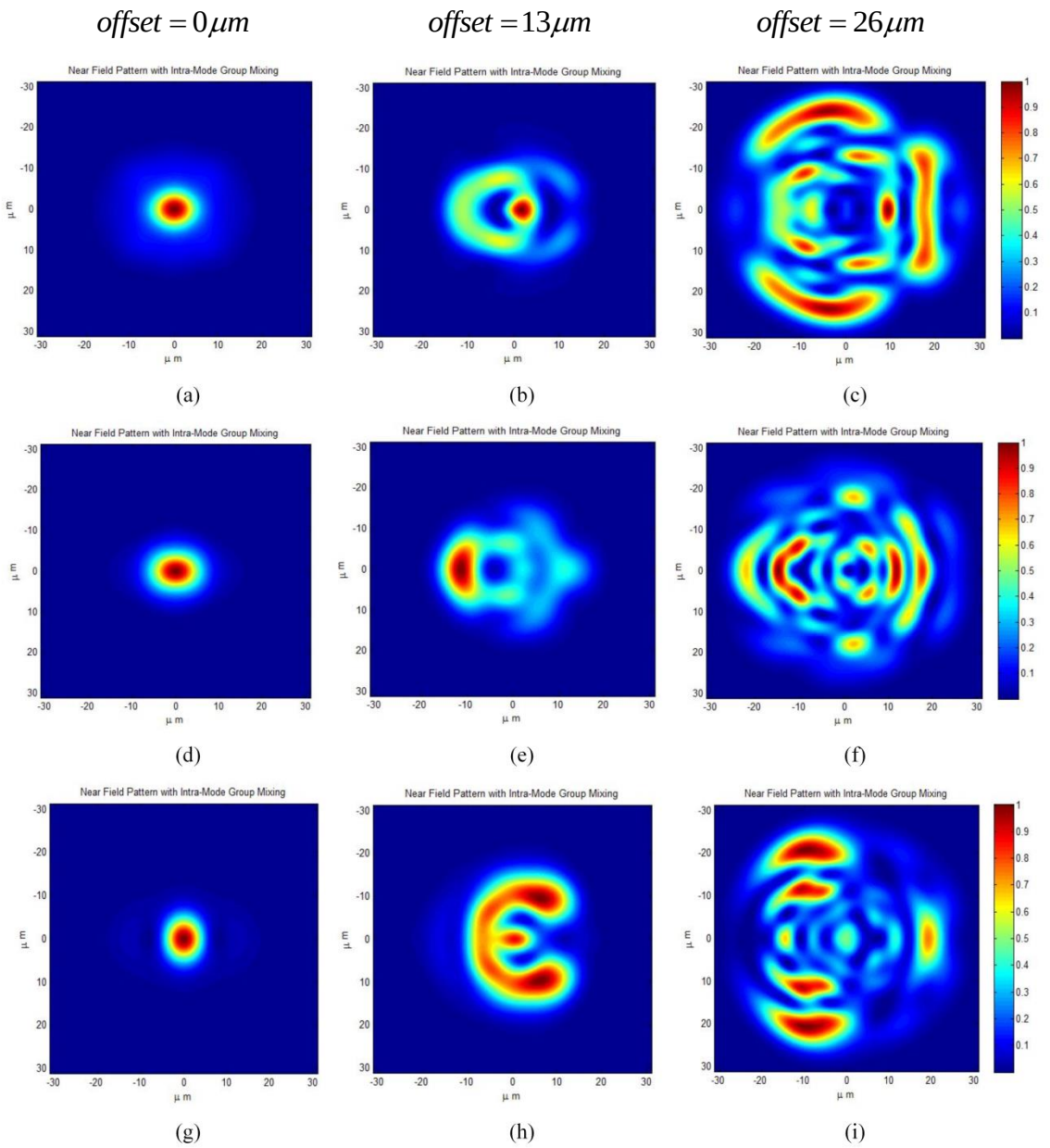

Figure 3.3 Simulation of NFP at the output of a 50m, 500m, 1km long GI-MMF, assuming intra-group mode mixing and differential mode attenuation are both considered, and the index profile is $\alpha = 2, \lambda = 1310nm$. (a-c) NFP of 50m long GI-MMF, (d-f) NFP of 500m long GI-MMF, (g-i) NFP of 1000m long GI-MMF.

A similar NFP simulation with an index profile imperfection is also presented in Figure 3.4. It yields the same result as previously obtained; i.e. that the profile imperfection has little contribution on the overall shape of the NFP, with the exception of the random phase.

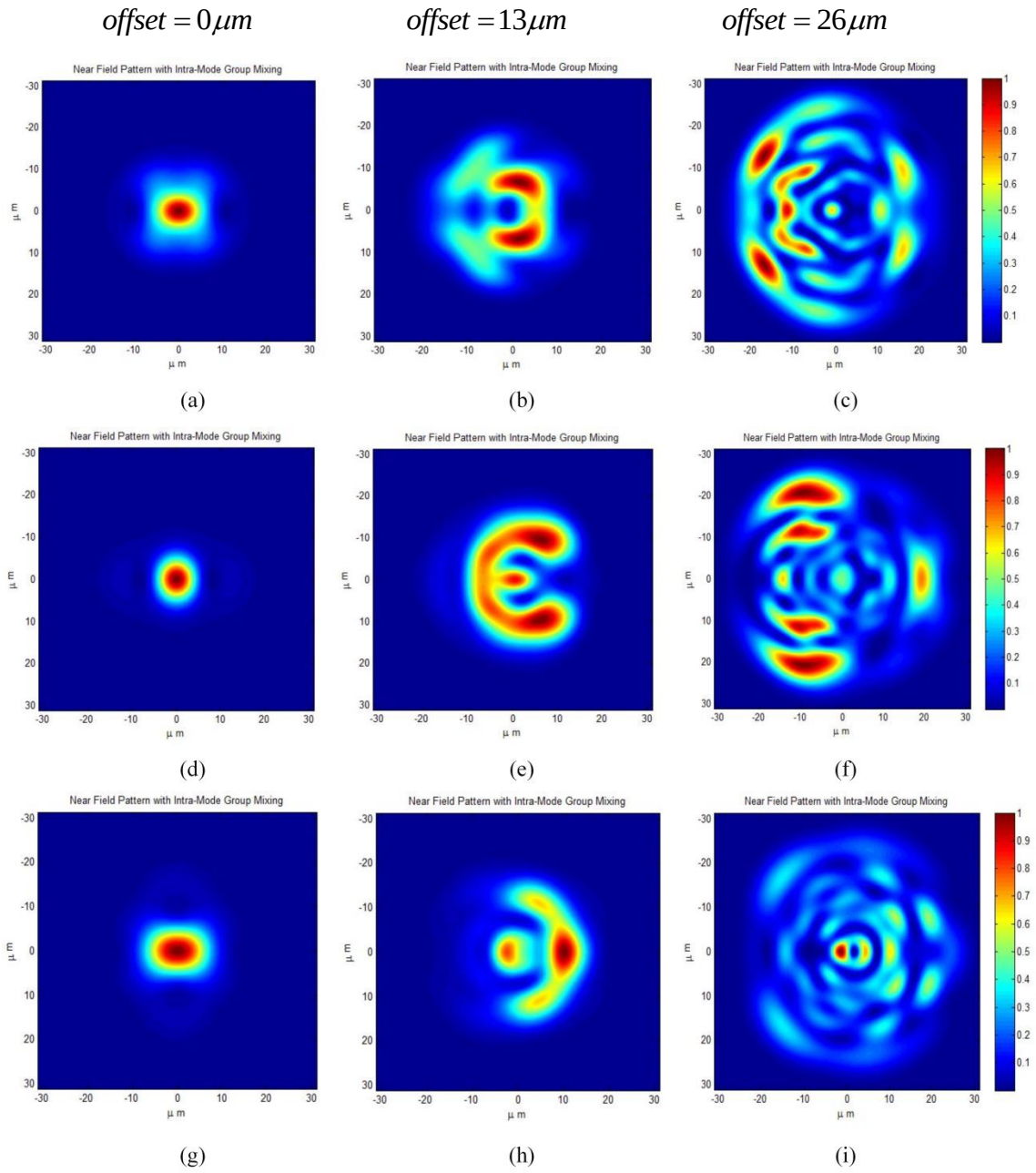

Figure 3.4 Simulation of NFP in a 1km long GI-MMF with different refractive index defects (i.e. $\alpha = 1.9$ or $\alpha = 2.1$) and a perfect index profile of $\alpha = 2$ assuming that the intra-group mode mixing and differential mode attenuation are both considered with $\lambda = 1310nm$. (a-c) NFP of GI-MMF with $\alpha = 1.9$, (d-f) NFP of GI-MMF with $\alpha = 2$, (g-i) NFP of GI-MMF with $\alpha = 2.1$.

Once the near field intensity pattern is obtained, the power can be easily calculated as:

$$Power = \int_A SdA = \frac{1}{2}\mathrm{Re}\int_{r=0}^{\infty}\int_{\phi=0}^{2\pi}\left(E_x \cdot H_y^*\right)\cdot r dr d\phi\,, \tag{3.23}$$

$$P = \iint_A \frac{\rho^2}{2} \mathrm{Re}\left(\sum_{l,n} \sqrt{\eta_{l,n}} \cdot \psi_{l,n} \cdot e^{-j\beta_{l,n} z + \gamma_{l,n} z} \hat{x} \cdot \left(\sqrt{\frac{\varepsilon_0}{\mu_0}} \cdot n_{co} \cdot \sum_{l,n} \sqrt{\eta_{l,n}} \cdot \psi_{l,n} \cdot e^{-j\beta_{l,n} z + \gamma_{l,n} z} \right)^* \hat{y} \right) R dR d\phi \tag{3.24}$$

As the sum of power coupling coefficient is given by: $\sum_{l,n} \eta_{l,n} = 1$

Simplifying,

$$P = \frac{\rho^2}{2} \cdot \sqrt{\frac{\varepsilon_0}{\mu_0}} n_{co} \iint_A \mathrm{Re}\left[\left(\psi_{l,n} \cdot e^{-j\beta_{l,n} z + \gamma_{l,n} z} \right) \hat{x} \cdot \left(\psi_{l,n} \cdot e^{-j\beta_{l,n} z + \gamma_{l,n} z} \right)^* \hat{y} \right] R dR d\phi \tag{3.25}$$

Equation 3.24 denotes the received optical power enclosed in a detector area *A*.

The differential mode attenuation is treated as an extra phase term within the modal amplitude equation. Figures 3.5-3.6 show the effect of differential mode attenuation on NFP; and the results indicate that the overall NFP shape is independent of differential mode attenuation. The NFP remains restricted within a circular shape.

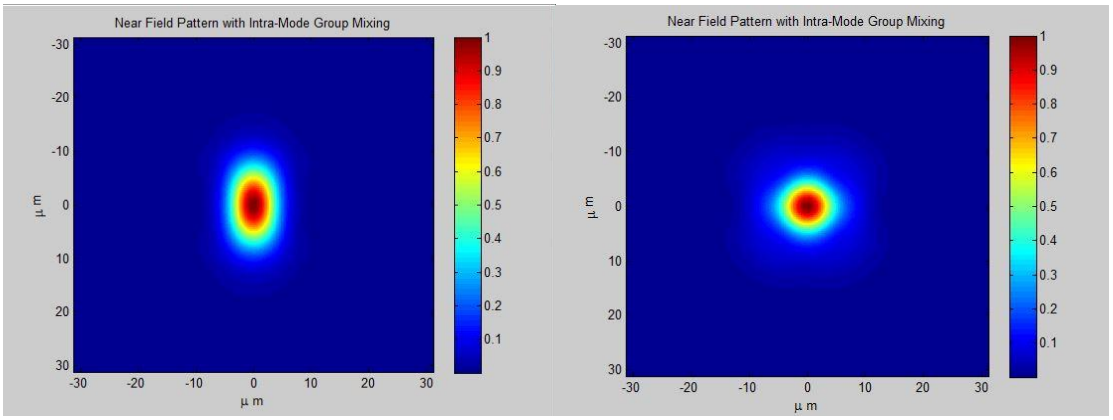

(a) (b)

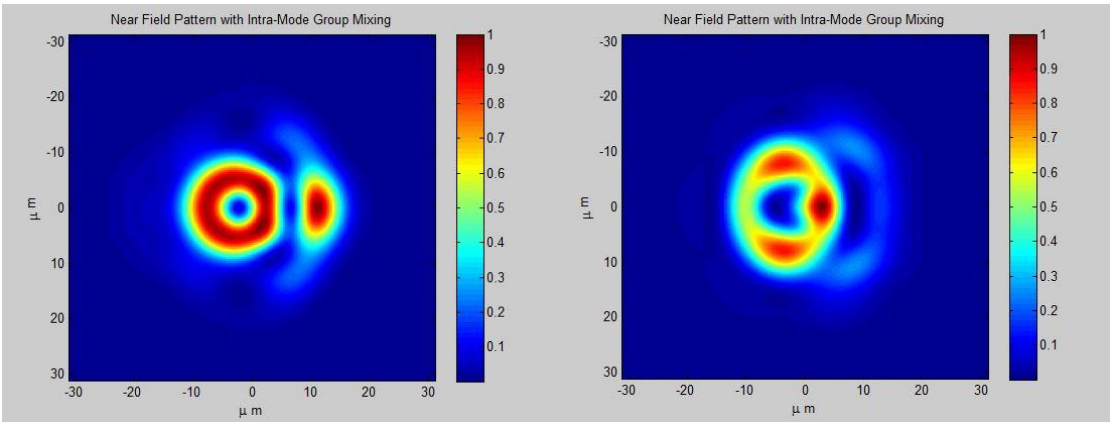

(c) (d)

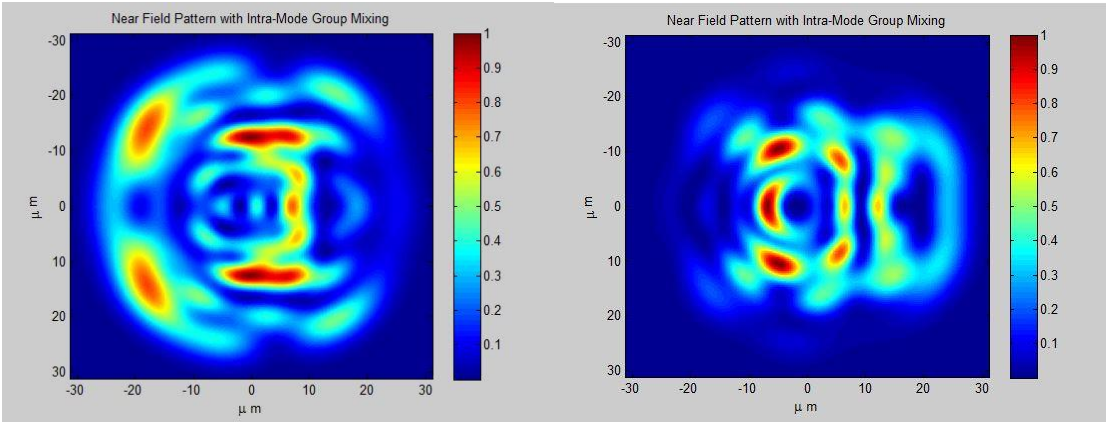

(e) (f)

Figure 3.5 Simulation of NFP with intra-group mode mixing in a 500m long MMF using both centre and offset launching conditions for $\alpha = 2$ and $\lambda = 1310nm$: (a) 0 μm offset launch NFP without mode attenuation, (b) 0 μm offset launch NFP with mode attenuation, (c) 13 μm offset launch NFP without mode attenuation, (d) 13 μm offset launch NFP with mode attenuation, (e) 26 μm offset launch NFP without mode attenuation, (f) 26 μm offset launch NFP with mode attenuation.

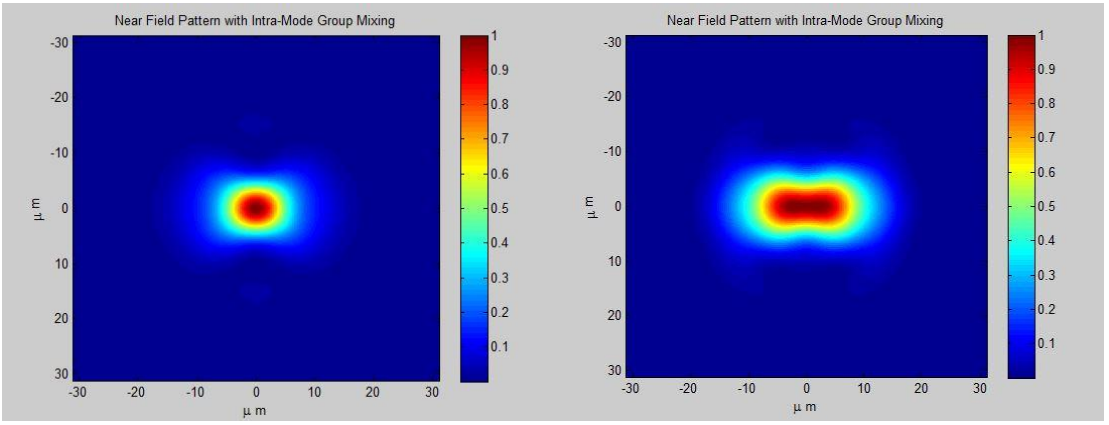

(a) (b)

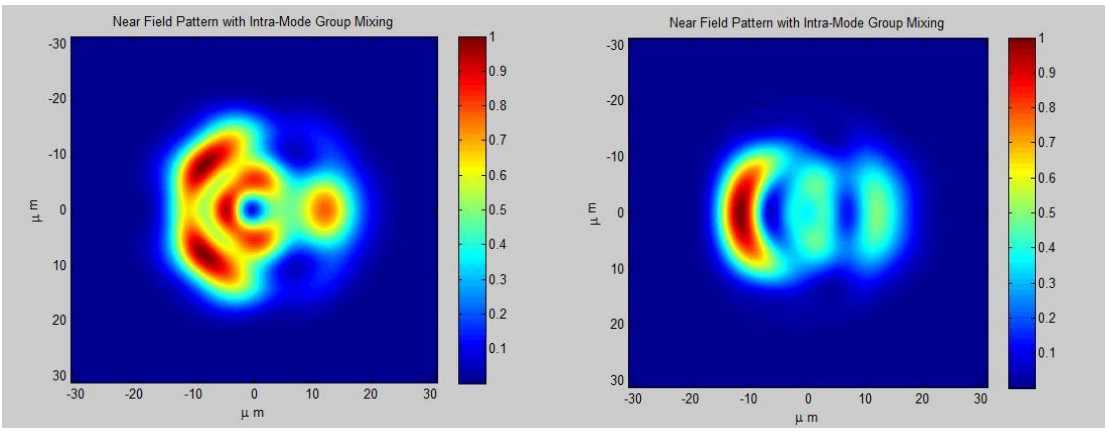

(c) (d)

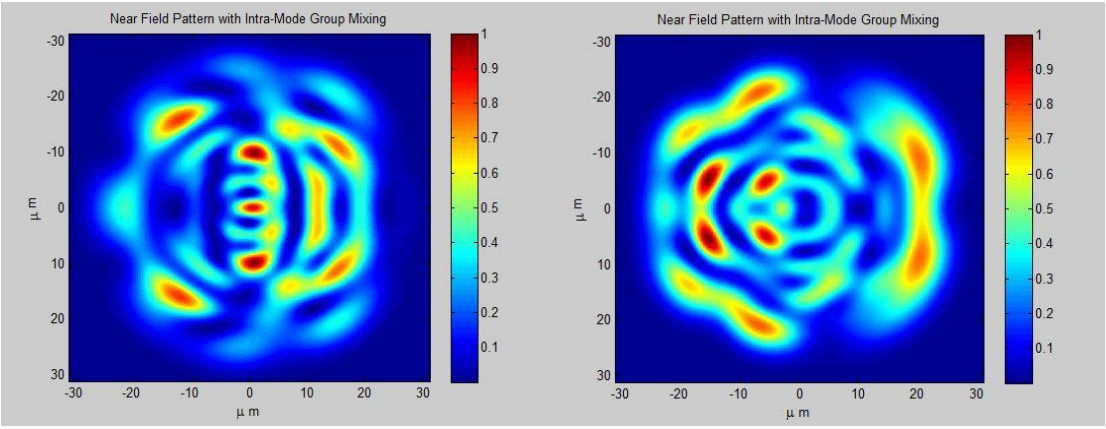

(e) (f)

Figure 3.6 Simulation of NFP with intra-group mode mixing in a 1km long MMF using both centre and offset launching conditions for $\alpha = 2$ and $\lambda = 1310nm$: (a) 0 μm offset launch NFP without mode attenuation, (b) 0 μm offset launch NFP with mode attenuation, (c) 13 μm offset launch NFP without mode attenuation, (d) 13 μm offset launch NFP with mode attenuation, (e) 26 μm offset launch NFP without mode attenuation, (f) 26 μm offset launch NFP with mode attenuation.

Although Equation 3.7 indicates that the higher order modes will be more attenuated than the lower order modes, it is difficult to observe this effect due to the random modal amplitude phase. Indeed, the radius of the disk shaped NFP seems only to change with radial offset launch. If we keep increasing the value of attenuation, the result shown in Figure 3.7 is in good agreement with the analytical result shown in Equation 3.7, which states that the higher order mode group located at the outer region of the core will suffer more attenuation than the lower mode group.

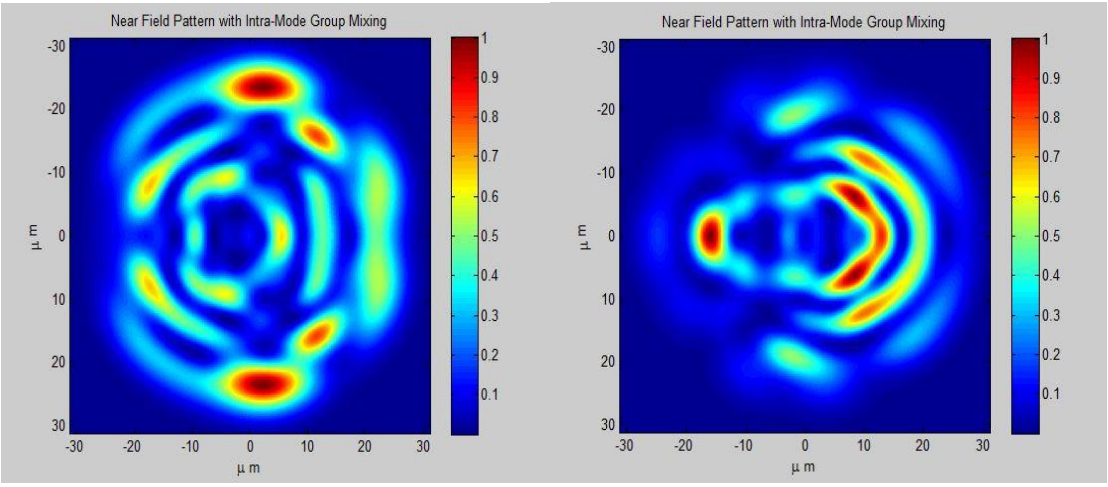

(a) (b)

Figure 3.7 Near field pattern with intra-group mode mixing when offset=26μm, attenuation=3dB/km, L=1km, and $\lambda = 1310nm$: (a) NFP without differential mode attenuation, (b) NFP with differential mode attenuation.

In the above simulations we have not considered modal noise. However, a change in fibre length or other minor parameters such as core diameter and refractive index may result in NFP fluctuations. In order to demonstrate these effects, we assume that the refractive index will change by 10^{-3} when the temperature reaches $100^{\circ}C$, the core diameter extends to $63\mu m$, and the fibre length increases by 1%. The simulated NFPs are shown in Figure 3.8 and Figure 3.9.

$offset = 0\mu m$ $offset = 26\mu m$

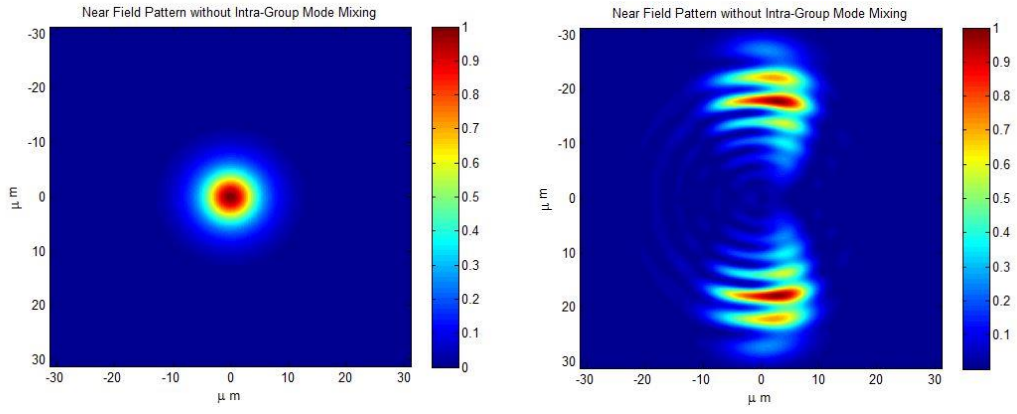

(a) (b)

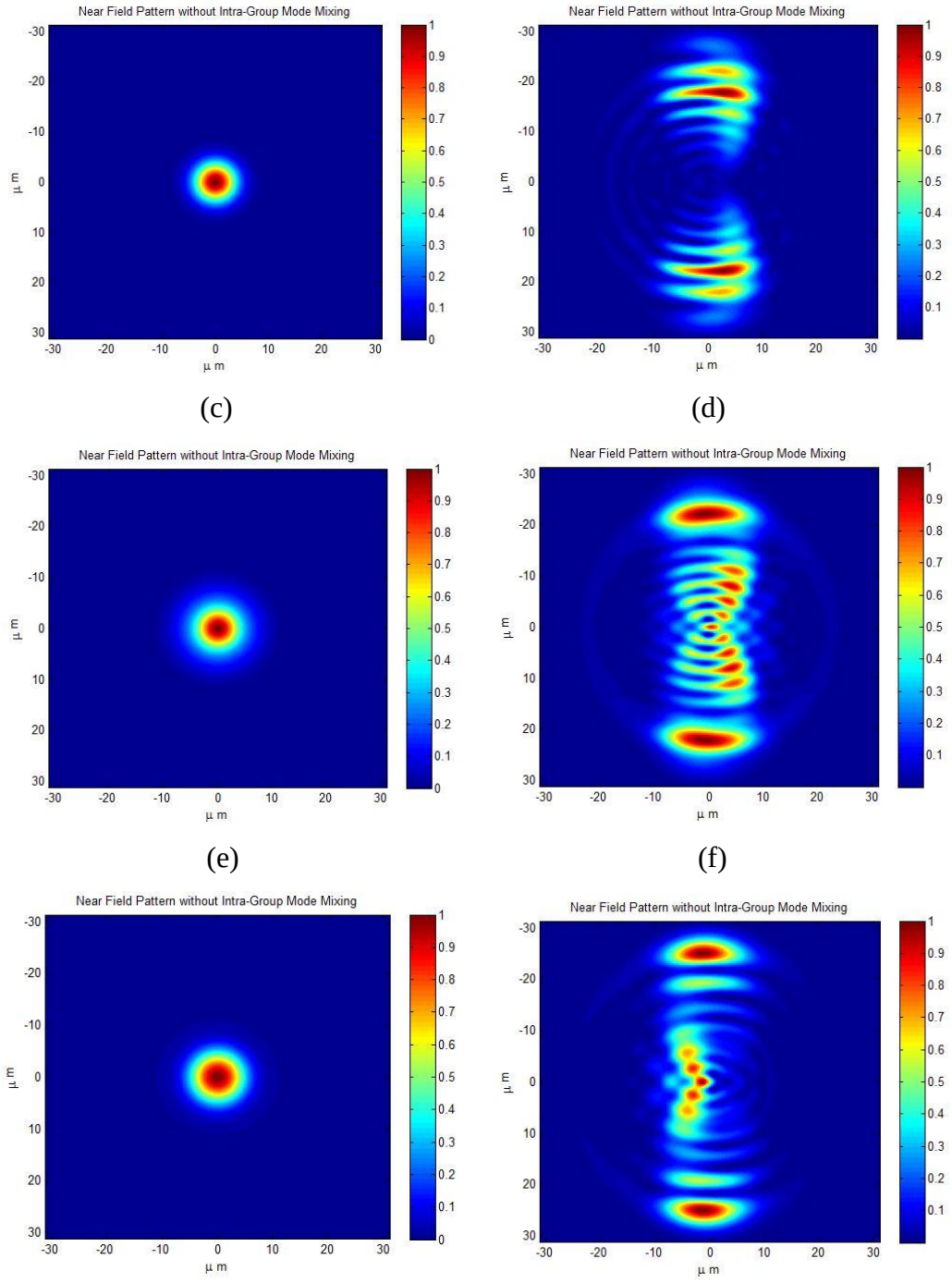

Figure 3.8 NFPs without intra-group mode mixing in a 1km long $62.5/125\mu$m GI-MMF under selective excitation with radial offsets of $0\mu m$ and $26\mu m$, $\alpha = 2$, $\lambda = 850nm$, $n_1 = 1.45$, $n_2 = 1.44$, and spot size= $3.677\mu m$: (a-b) NFP without any changes, (c-d) NFP with a core diameter of $63\mu m$, (e-f) NFP with a 10^{-3} variation in refractive index, (g-h) NFP with a 1% increase in fibre length.

There is no distinct difference among the results in both offset launches, which

indicates that minor changes in parameters do not affect the overall shape of the NFP. In other words, the simulation is reasonably resistant to small fluctuations caused by intentional or unintentional perturbation. This resistance is maintained in the NFP even when we consider full intra-group mode mixing, as can be seen in Figure 3.9.

$offset = 0\mu m$ $offset = 26\mu m$

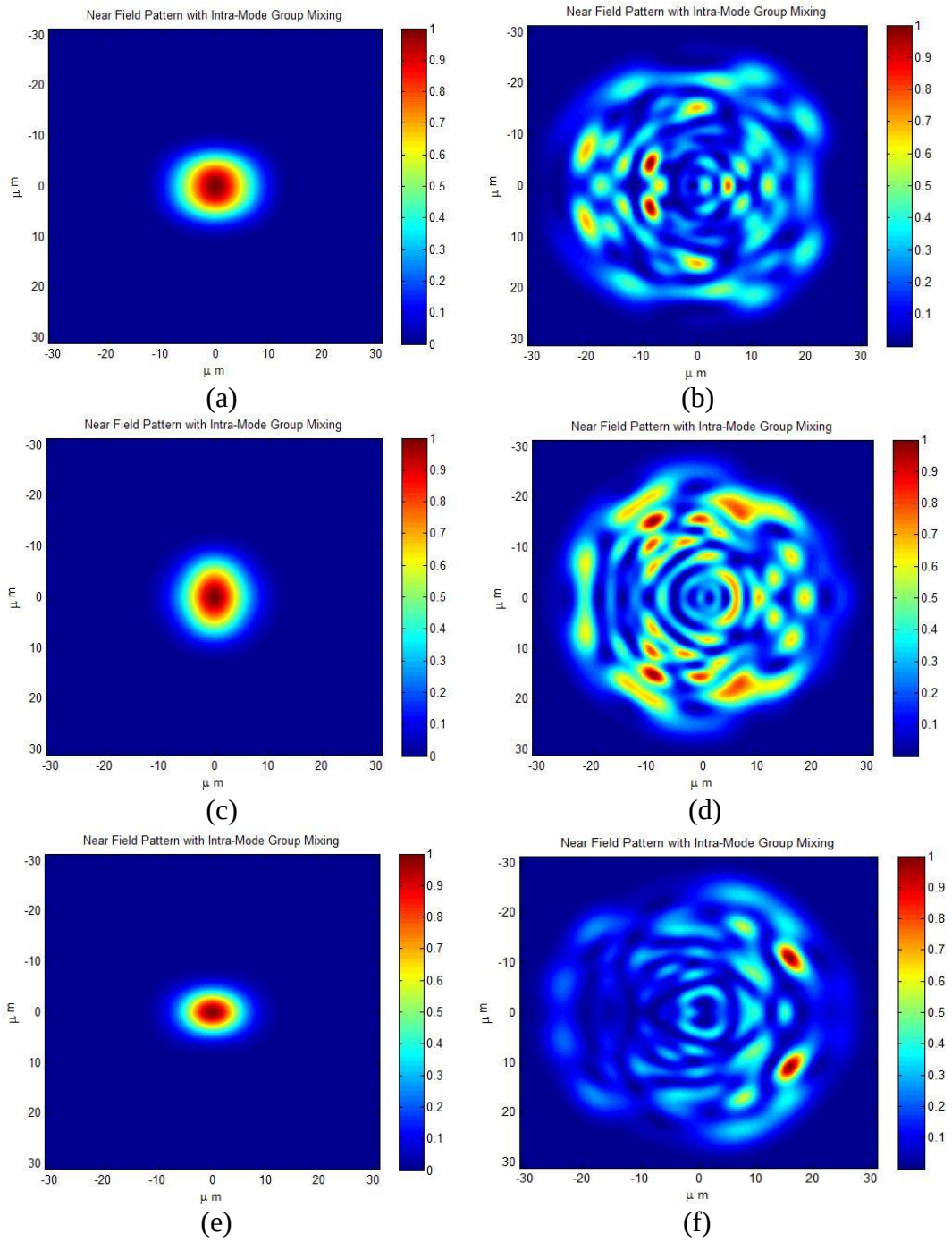

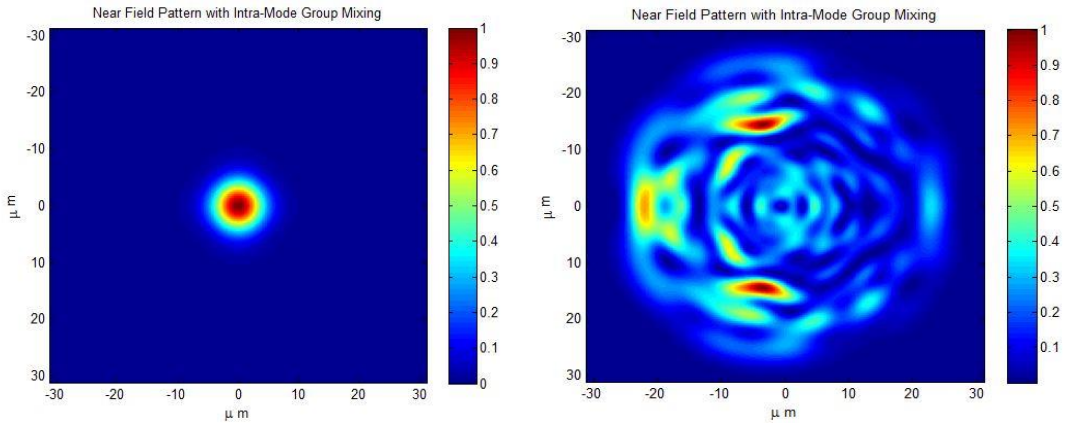

(g) (h)

Figure 3.9 NFPs with intra-group mode mixing in a 1km long $62.5/125\mu$m GI-MMF under selective excitation with radial offsets of $0\mu m$, $26\mu m$, $\alpha = 2$, $\lambda = 850nm$, $n_1 = 1.45, n_2 = 1.44$, and spot size=$3.677\mu m$: (a-b) NFP without any changes, (c-d) NFP with a core diameter of $63\mu m$, (e-f) NFP with a 10^{-3} variation in refractive index, (g-h) NFP with a 1% increase in fibre length.

The results in Figure 3.9 indicate that the overall NFP clearly depends on the input radial offset, but not on small parameter fluctuations. The intensity distribution is directly affected by the random phase.

3.4 Conclusion

This chapter demonstrated the near field intensity patterns with several transmission impairments such as mode mixing, mode attenuation, and refractive index imperfection under different GI-MMF lengths. The results allow us to conclude that small deviations in the refractive index profile, differential mode delay, and differential mode attenuation have limited effects on the overall shape of the near field pattern up to 1km, and its radius is only determined by the radial offset at the input facet of the GI-MMF. However, differential mode attenuation seemed to have a greater impact on higher order mode groups. The results suggest that minor changes in MMF parameters will not severely affect the NFP.

Chapter 4: Optical MIMO Model in a Multimode Fibre System

The development of an optical MIMO MMF system model is presented in this chapter. The mathematical expressions of such a model are derived, which include the channel matrix H and MIMO capacity. Thereafter, the use of the simple zero forcing criterion in offline optical MIMO signal processing is briefly introduced. Lastly, the condition number and crosstalk of channel matrix H are selected to evaluate different MIMO system configurations, for instance, different types of receivers and the number of transceivers.

4.1 General optical MIMO model

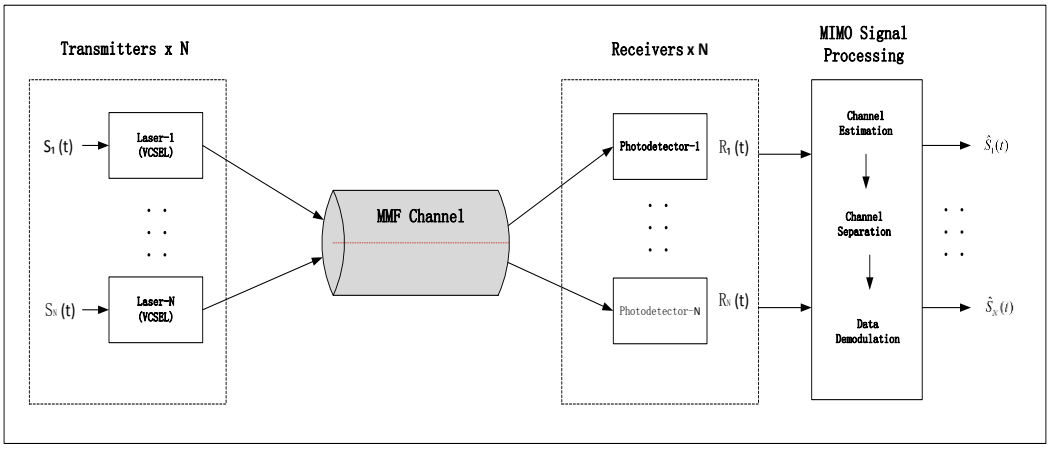

Figure 4.1 General optical MIMO model

Figure 4.1 shows the general optical MIMO model which contains the transmitter, MMF channel, receiver, and off-line MIMO signal processing. MIMO signal processing consists of three steps: channel estimation, channel separation, and data demodulation. Sometimes, the MIMO system can be regarded as a multiple single input and single output (SISO) system; thus, it is a good idea to initially start with the SISO system model. Assuming that both the fibre nonlinear effects and chromatic dispersion are neglected, the FIR model can be used to describe the MMF channel.

The input-output relationship for a SISO over an MMF is given by [84]:

$$y(t) = \sum_{K=1}^{Q} h_k e^{j\omega_c (t-\tau_{pk})} x(t-\tau_{gk}) + v(t) \qquad (4.1)$$

where *x(t)* is the baseband transmitted signal, which is modulated with the optical carrier frequency ω_c, Q is the total number of guided modes in the MMF, h_k is a complex number that represents the gain of the k_{th} guide mode, τ_{gk} and τ_{pk} are the group delay and phase delay of the k_{th} guided mode, respectively, and $v(t)$ is the additive white Gaussian noise.

In the $M \times N$ optical MIMO system, M refers to the total number of transmitters, while N is the total number of receivers, and the MIMO outputs can be written as [84]:

$$y_i(t) = \sum_{j=1}^{M} \sum_{k=1}^{Q} h_{i,j,k} e^{j\omega_c (t-\tau_{pk})} x_j(t-\tau_{gk}) + v_i(t) \qquad (4.2)$$

where $y_i(t)$ represents the received signal by the i_{th} receiver, and $h_{i,j,k}$ is the channel gain from the j_{th} transmitter to the i_{th} receiver through the k_{th} guided mode [84]. If the signals in Equation 4.2 are sampled with a sampling rate of $1/T_s$ and all modes arrive at approximately the same time compared to the symbol period, then Equation 4.2 can be further simplified to [84]:

$$y(n) = Hx(n) + v(n) \qquad (4.3)$$

where n is the total number of samples.

$$H_{i,j} = \sum_{k=1}^{Q} h_k^{i,j} e^{-j\omega\tau_k} \qquad (4.4)$$

As long as the number of modes is sufficiently large, the elements of H will have a complex Gaussian distribution with a Rayleigh distribution for amplitude and a uniform distribution for phase [84]. The parameter τ_k is the delay of the k_{th} mode. In

addition, the optical MIMO model can be represented in matrix form as:

$$\mathrm{Y} = \mathrm{HX} + \mathrm{V} \tag{4.5}$$

$$Y = \begin{bmatrix} y_1(nT_s) \\ .. \\ .. \\ y_N(nT_s) \end{bmatrix} \quad X = \begin{bmatrix} x_1(nT_s) \\ .. \\ .. \\ x_M(nT_s) \end{bmatrix} \quad V = \begin{bmatrix} v_1(nT_s) \\ .. \\ .. \\ v_N(nT_s) \end{bmatrix} \tag{4.6}$$

$$H = \begin{bmatrix} H_{11}\, H_{12}\, ...H_{1M} \\ H_{21}\, H_{22}.....\mathrm{H}_{2M} \\ ..... \\ ..... \\ H_{N1}\, ...H_{NM} \end{bmatrix} \tag{4.7}$$

where *x(n)* is the *M* x1 transmitted vector signals, *y(n)* is the *N* x1 received vector signals, *M* and *N* are the number of transmitters and receivers, respectively, and *H* is an *N x M* channel matrix that corresponds to the channel gain between the j_{th} transmitter and the i_{th} receiver. *V* is the *N*x1 complex Gaussian noise vector in which each element is independent identically distributed. Contrary to a flat fading channel, a frequency selective fading channel imposes frequency dependence on each element in the channel matrix; hence, *H* must be modified as:

$$H = \begin{bmatrix} H_{11}(f)\, H_{12}(f).....H_{1M}(f) \\ H_{21}(f) H_{22}(f).....\mathrm{H}_{2M}(f) \\ .....\\ ..... \\ H_{N1}(f).....H_{NM}(f) \end{bmatrix} \tag{4.8}$$

4.2 Optical MIMO channel matrix H

Each element of the channel matrix in an optical MIMO system not only exhibits the MMF modal time delay, but also the power coupling at the transmitter and power detected at the receiver. Equation 4.9 refers to the power coupling coefficient for the k_{th} mode emitted from the j_{th} transmitter or laser, and the detection coefficient of the i_{th} receiver on the k_{th} mode may be defined as the ratio of the detected power to the power over the entire core region shown in Equation 4.10:

$$\rho s_k^j = \frac{\left| \int_0^{2\pi} \int_0^{\infty} E^j{}_{in}(R) \cdot \psi^k{}_{l,n}{}^*(R,\phi) R dR d\phi \right|^2}{\int_0^{2\pi} \int_0^{\infty} \left| E^j{}_{in}(R) \right|^2 R dR d\phi \int_0^{2\pi} \int_0^{\infty} \left| \psi^k{}_{l,n}(R,\phi) \right|^2 R dR d\phi} \quad (4.9)$$

$$\rho d_k^i = \frac{\iint_{A\_detector} \left| \psi^k{}_{l,n}(R,\phi) \right|^2 R dR d\phi}{\iint_{\infty} \left| \psi^k{}_{l,n}(R,\phi) \right|^2 R dR d\phi} \quad (4.10)$$

In the optical MIMO MMF system, we can assume that signals from different transmitters are incoherent while also exhibiting direct intensity superposition at the receiver end. If we further assume that all modes are orthogonal, the channel impulse response can be written as:

$$h_{i,j}(t,L) = \sum_k \rho s_k^j \cdot \rho d_k^i \delta(t - \tau_k L) \quad (4.11)$$

where τ_k is the modal delay for the k^{th} mode, and L is the transmission distance.

The channel frequency response is given by Equation 4.12:

$$H_{i,j}(\omega, \mathrm{L}) = \sum_k \rho s_k^j \cdot \rho d_k^i \cdot \exp\left(-j\omega\tau_k L\right) \quad (4.12)$$

The transmission matrix element $h_{i,j}$ can be equivalent to a real value if τ_k is the same for all guided modes; thus, the parameter $h_k^{i,j}$ only describes the proportion of power

from the j_{th} transmitter to the i_{th} detector, which is given by the product of the power coupling coefficient and the detection coefficient as:

$$h_k^{i,j} = \rho s_k^j . \rho d_k^i \qquad (4.13)$$

In a linear MGDM system, Equation 4.13 can be utilized to characterise the optical MIMO MMF system performance.

Combining Equations 4.9, 4.10, 4.13 and 4.2, the total received signal at the i_{th} receiver after transmission distance L is:

$$y_i(t,L) = \sum_{j=1}^{M}\sum_{k=1}^{Q} F^{-1}\left\{F\left(h_{ijk} e^{j(w_c \tau_{pk})} x_j(t-\tau_{gk})\right)\cdot e^{-i\beta_{k,}L}\right\} + V_i(t) \qquad (4.14)$$

where F is the Fourier transform, and F^{-1} is the inverse of Fourier transform.

As mentioned above, the power coupling coefficient and incident electrical filed are both normalized. Assuming the linear superposition of power distribution across the entire core area, thus, the near field light flux intensity can be exploited instead of $\sum_k \rho s_k^j \cdot \rho d_k^i$.

$$\sum_k \rho s_k^j \cdot \rho d_k^i = \frac{\iint_{A\_detector} I(r,\phi,L) r \,\mathrm{d}r \,\mathrm{d}\phi}{\int_0^{2\pi}\int_0^{a} I(r,\phi,L) r \,\mathrm{d}r \,\mathrm{d}\phi} \;, a = core\ radius \qquad (4.15)$$

Substituting 4.15 into 4.12, now it becomes:

$$H_{i,j}(\omega,\mathrm{L}) = \frac{\iint_{A\_detector} I(r,\phi,L) r \,\mathrm{d}r \,\mathrm{d}\phi}{\int_0^{2\pi}\int_0^{a} I(r,\phi,L) r \,\mathrm{d}r \,\mathrm{d}\phi} \cdot \sum_k \exp\left(-i\omega\tau_{gk} L\right) \qquad (4.16)$$

$$\text{or } H_{i,j}(\omega,\mathrm{L}) = \frac{\iint_{A\_\text{detector}} I(r,\phi,L) r \,\mathrm{d}r \,\mathrm{d}\phi}{\int_0^{2\pi}\int_0^{a} I(r,\phi,L) r \,\mathrm{d}r \,\mathrm{d}\phi} \cdot \sum_k \exp\left(-i\beta_k L\right) \qquad (4.17)$$

The near field intensity pattern $I(r,\phi,L)$ along the fibre length L is given in Equation 3.22. In Equations 4.12 and 4.16 the temporal properties of channel H due to temperature changes and mechanical vibrations have not been considered. Lastly, another assumption has been made that $H_{i,j}(t)$ varies more slowly than the transmitted signal x(t).

4.3 Optical MIMO capacity

In a MIMO channel the maximum information rate will depend on whether the channel state information is known or unknown at the transmitter. If the channel state information is unknown at the transmitter, an equal power allocation among the transmitters is preferable; otherwise, the optimal water-pouring power allocation scheme is used for the case when a transmitter has knowledge about the CSI [144]. Because the fibre channel varies at a relatively slow speed compared to the signal transmission rate, a feedback carrying CSI from the receiver back to the transmitter is adopted. The system capacity depends on the temporal and spatial static properties of the channel matrix elements *H*. The channel is regarded as constant over a relatively long period [145]. When CSI is known at the receiver, the capacity of the MIMO system is given by [144]:

$$C = B\log_2\left\{\det\left[I_m + \frac{SNR_{average}}{N_T} Q\right]\right\} \qquad (4.18)$$

where $m = \min(N_r, N_t)$, B is the channel bandwidth, N_T is the number of transmitters, I_m is an $N_r \times N_r$ identity matrix, and the matrix Q is expressed as:

$$Q = \begin{cases} H^H H, & N_r < N_t \\ HH^H, & N_r \geq N_t \end{cases} \tag{4.19}$$

Here, H^H is the complex conjugate matrix of *H*, and det (.) denotes the determinant of a matrix. SNR is the average signal to noise ratio. N_t and N_r are the numbers of transmitters and receivers, respectively. Because the signals in an IM-DD system are unipolar, the analyses of the channel capacity of bipolar systems cannot be applied; thus, the classical Shannon capacity formula cannot be directly used in an IM-DD system. In the linear optical channel regime and under the one dimensional Gaussian channel approximation, the IM-DD channel capacity is approximately half of the Shannon limit [146].

As the channel capacity relies on SNR, the channel matrix needs to be normalized in order to maintain the same SNR for different launching conditions and channel scenarios. This is expressed as:

$$\frac{1}{N_t}\sum_{j=1}^{N_t}\left|h_{i,j}\right|^2 = 1, \quad i = 1, 2....., N_r \tag{4.20}$$

Applying the eigenvalue decomposition method to the matrix *Q*, $Q = HH^H = E\Lambda E^H$, where Λ is a diagonal matrix with the eigenvalues on the main diagonal, and *E* is the eigenvector matrix with orthonormal columns [147]. Therefore, the number of sub-channels can be determined by the rank of the matrix *H*, which is defined as:

$$rank(H) = r \leq \min\left\{N_{T,} N_R\right\}$$

As the determinant of a unitary matrix is 1, thus the Equation 4.18 may be rewritten as:

$$C = \sum_{i=1}^{r} \log_2\left(1 + \frac{SNR_{average}}{N_T}\lambda_i\right) \tag{4.21}$$

where *r* is the rank of the channel matrix and λ_i is the positive eigenvalue of the

diagonal matrix Λ [147]. The above expression implies that the MIMO channel capacity can be regarded as the sum of SISO channels assigned by the power gain of λ_i (i=1, 2,…….r) [148].

4.4 Optical MIMO signal processing

When each photodiode captures a mixture of signals in a MIMO system they will be passed through the MIMO signal processing in the digital domain, which takes place in three major stages: channel estimation, channel separation, and signal demodulation. Digital signal processing and efficient algorithms in wireless MIMO can be implemented in optical MIMO to recover the symbols after the optoelectronic conversion.

The channel estimation can be classified into two categories depending on whether the training sequence is used. Using the training sequence is a sophisticated channel estimation method. The principle of this method is to send a receiver known sequence to the transmitter; the estimated channel information can then be obtained through a variety of algorithms by simply comparing the received sequence with the known transmitted sequence. Maximum likelihood (ML), least squares (LS), and minimum mean square error (MMSE) are the three dominant algorithms. If a sequence with a length of L in either the time domain or frequency domain is described as $X = \left[x_1, x_2, x_3 \ldots\ldots\ldots x_L\right]^T$, $Y = \left[y_1, y_2, y_3 \ldots\ldots\ldots y_L\right]^T$ is the received sequence after the channel, and $N = \left[n_1, n_2, n_3 \ldots\ldots\ldots n_L\right]^T$ is the Gaussian noise vector. $(\ )^T$ indicates the transpose of a vector. Therefore, the received signal is given as:

$$Y = HX + N \tag{4.22}$$

The idea of the LS estimation method is to find out: $\hat{H}_{LS} = YX^{*}$ (4.23)

where X^{*} is the pseudoinverse matrix of X. If the vector of X is full rank, $X^{*} = X^{H}\left(XX^{H}\right)^{-1}$, $(\ )^{H}$ is the conjugate transpose, and $\hat{H}_{LS}$ is the LS estimated matrix. As the estimation of the channel matrix is based upon the relationship between the electrical input signal and output signal, its accuracy is very sensitive to the variation in the optical power at the receiver. Despite having a temporally invariable channel, the equalization still must be repeated at fixed time intervals.

However, this estimation method will occupy some bandwidth, so it reduces the channel transmission efficiency. The optimizing training sequence is strongly relevant to the estimation accuracy; for example, the length of the training sequence, correlations between the training sequence and signal sequence, autocorrelations of the sequence itself, and even the sequence power level will all degrade the estimation. An alternative, new estimation method called blind estimation estimates the channel without any information of the transmitted signal. This is manipulated by exploiting the statistical properties of the received sequence [149]. All of the advanced estimation methods in signal processing are beyond the scope of this thesis. For the sake of simplicity and efficiency, the pseudorandom binary sequence combined with the LS estimation method is applied in the remainder of this thesis.

After the channel estimation is completed the symbol recovery can proceed using the zero forcing criterion, which is an algorithm typically employed in MIMO systems. Its simplest receiver architecture is only a matrix inversion, but the zero forcing (ZF) method has an inevitable drawback in that it will amplify the noise. If the channel matrix $\hat{H}$ is accurately estimated, then multiplying the inversion of $\hat{H}$ at both sides of

Equation 4.22 gives $\hat{H}^{-1}Y = XH\hat{H}^{-1} + N\hat{H}^{-1}$. As long as the condition $H = \hat{H}$ is met, the above expression further simplifies to $\hat{X} = X + N\hat{H}^{-1}$, where $\hat{X}$ is the recovered signal, and N is the Gaussian noise. Apparently, the recovered signal has been amplified by a factor of $N\hat{H}^{-1}$. When the received signals have been successfully recovered, the signal demodulation will proceed according to the transmitted signal modulation format.

4.5 Number of receivers and transmitters in optical MIMO

Assuming that the invariant temporal condition is maintained in the IM-DD MIMO system (i.e. the detector only responds to the received optical power), the matrix H is a real valued matrix. We are aware that the MMF channel impairments introduced in chapter two are mainly responsible for the MIMO performance through the channel matrix H. Moreover, the properties of the transmitter and receiver would also have an impact on channel matrix H. The condition number of matrix H and crosstalk at each receiver are two key metrics in judging the MIMO performance. By evaluating these two factors a more efficient MIMO transceiver can be designed.

4.5.1 Condition number of channel matrix H

The ability to invert channel matrix *H* plays an important role in optical MIMO signal processing because the *H*-matrix must be invertible in order to recover signals. When the determinant of the squared *H* matrix is nonzero, the *H* matrix is said to be nonsingular, and the matrix inversion exists so that a condition number is available. From a mathematical view, the condition number is designed to measure the

sensitivity of a matrix with respect to numerical operations performed on the matrix. It is defined as the ratio of the largest singular value to the smallest singular value in the singular value decomposition of a matrix [150]:

$$k = \left\| H^{-1} \right\| \cdot \left\| H \right\| \tag{4.24}$$

where k is the condition number, H^{-1} is the inverse matrix of H, and $\| \ \|$ denotes the matrix norm.

The condition number is a well-known metric of the spatial selectivity of a MIMO wireless channel. It can provide a short term indication of the SNR required for successful signal demodulation [151-153]. Moreover, after it was successfully used to evaluate the performance of a wireless MIMO system, the optical communication research group at Oxford University applied it as a significant evaluative criterion to an optical wireless MIMO system [154]. Similarly, the condition number can in principle be used as an evaluation criterion for optical MIMO MMF systems

When the condition number approaches 1, the matrix is called well- conditioned, in contrast, the matrix H is said to be ill-conditioned with a larger condition number [150]. Strictly speaking, a large condition number is not preferable because even a small variation in the matrix element will cause a significant change in the solution matrix, thereby leading to errors in signal recovery.

The following simulations demonstrate the relationship between the number of transmitters and receivers in an optical MIMO system. An intensity modulation direct detection optical MIMO system has been simulated for simplicity as the transfer function or channel matrix H is only described as the power transfer between the

transmitter and receiver. A standard graded index $62.5/125\mu m$ MMF is used as a transmission medium, and the other parameters used in the simulation are listed in Table 4.1.

Core refractive index	1.45	Laser spot size	$3.677\mu m$
Cladding refractive index	1.44	Wavelength of light source	850 nm
MMF length	$1km$	Index profile	2
Transmitted Power Pt	$1mW$	Total number of groups	19
Fibre attenuation & Chromatic dispersion	Not considered	MMF intra-group mode mixing (mode mixing within the same group)	Considered due to curvature of the MMF fibre

Table 4.1 IM-DD optical MIMO simulation parameters

The first simulation is intended to calculate the condition number for a system that contains five different radial offset launches (i.e. 0, 5, 10, 15, and 20μm) and nine different detectors (i.e. an SMF with a radius of 4μm will be used as a single detector). These detectors are placed 8μm from each other in both the horizontal and vertical axes, and the detectors compose a squared detector array, as shown in Figure 4.2.

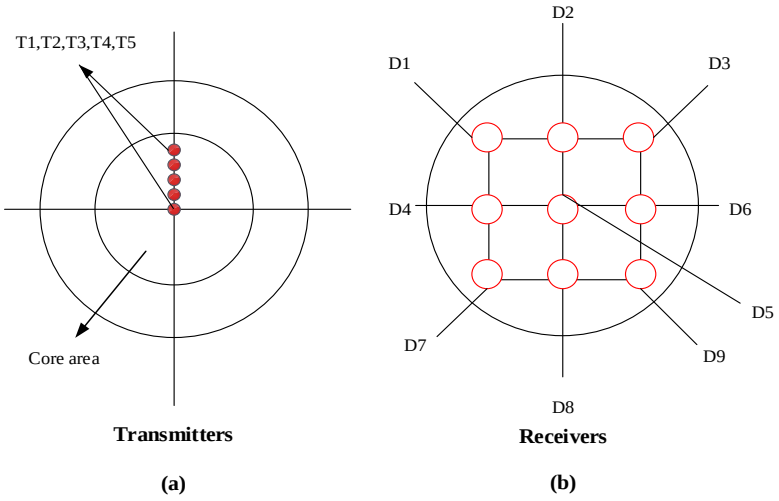

Figure 4.2 The transmitter and detector positions: (a) the five different radial offset launches and (b) the square detector array containing nine circular detectors with radii of 4μm and 8μm distances between each receiver on the horizontal and vertical levels.

The results shown in Figure 4.3 indicate that the condition number decreases as the number of input light sources (radial offset input number) increases. The well-conditioned matrix *H* can be achieved when the number of input sources is less than the number of detectors.

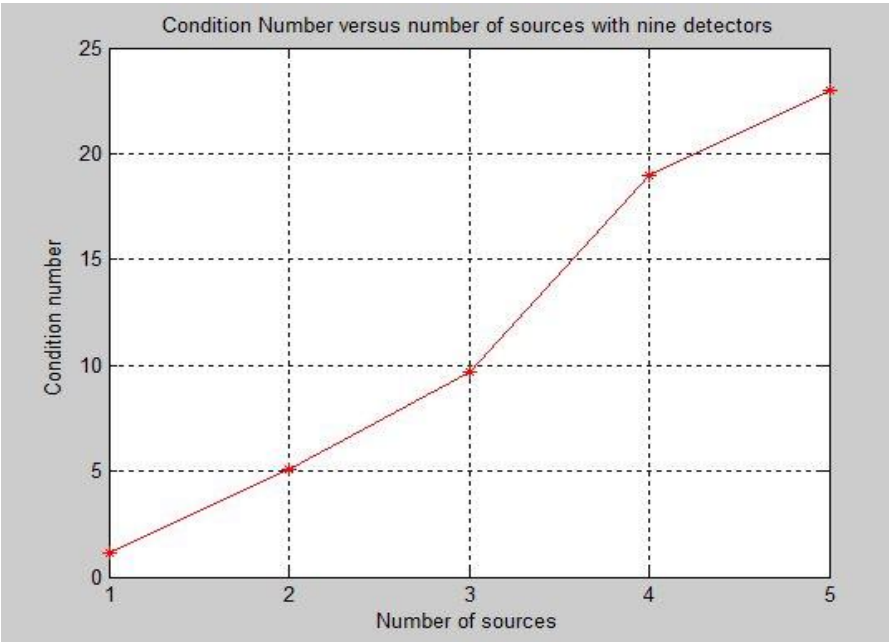

Figure 4.3 Condition number for different numbers of transmitters with nine detectors

The results in Figure 4.3 illustrate the fact that as the number of light sources increases, the spatial degrees of freedom at the transmitter end decrease, resulting in a subsequent increase in crosstalk. Therefore, it is preferable to have a higher number of detectors than light sources. The second simulation simulated the condition number for different detectors by separately applying three input sources with radial offsets of 0, 5, and 10μm. Figure 4.4 shows that the condition number is improved when the number of detectors is greater than the number of transmitters. These indicate that the number of inputs should be less than the number of receivers in order to maintain a well-conditioned channel matrix; in other words, the invertible matrix $H_{m,n}$ exists as long as $m \geq n$, where *m* is the receiver number and *n* is the number of transmitters.

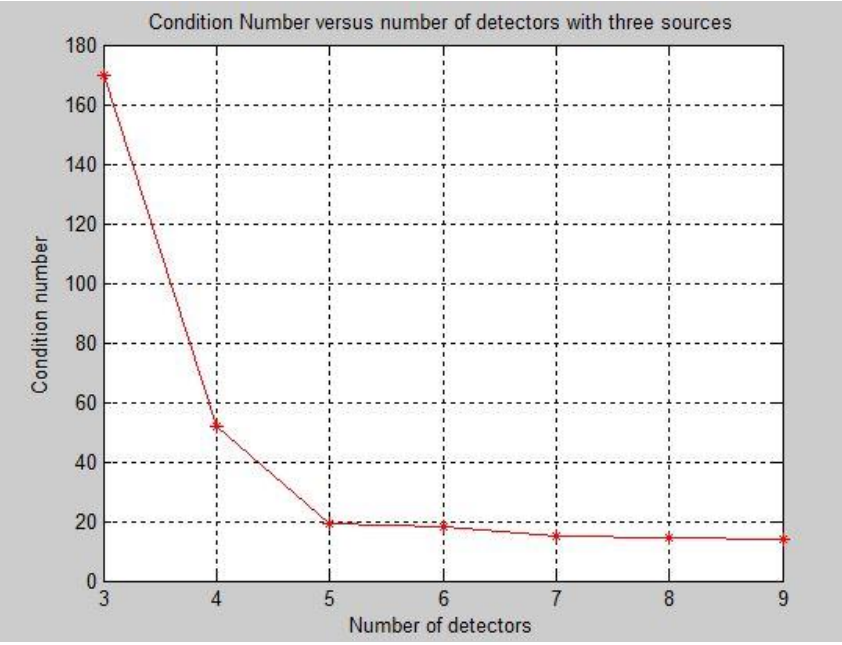

Figure 4.4 Condition number for different numbers of detectors using three radial offset inputs (0, 5, and 10μm)

Although the results in Figures 4.4 and 4.5 provide clear recommendations for the choice of the numbers of sources and detectors in an optical MIMO MMF system, a

demonstration of the effect of condition number on system performance (i.e. the BER or Q factor) is still lacking. In order to characterise this effect a 2x2 IM-DD MIMO system was designed in which the transmitter utilizes two different launches (0 and 15μm offset launching), and the receiver is comprised of two SMFs(with radii of 4μm). For the sake of simplicity, channel estimation is not necessary because we can assume that the channel matrix *H* is known at both the transmitter and receiver and can be obtained from Equation 4.13. Two random binary sequences with the same length of 2^7-1 are used to transmit through such a system with SNR=30dB. The different condition number values can be calculated by modifying each element in the matrix *H*. The results for both receivers are shown in Figure 4.5. The Q factor has been selected as a metric to determine the performance.

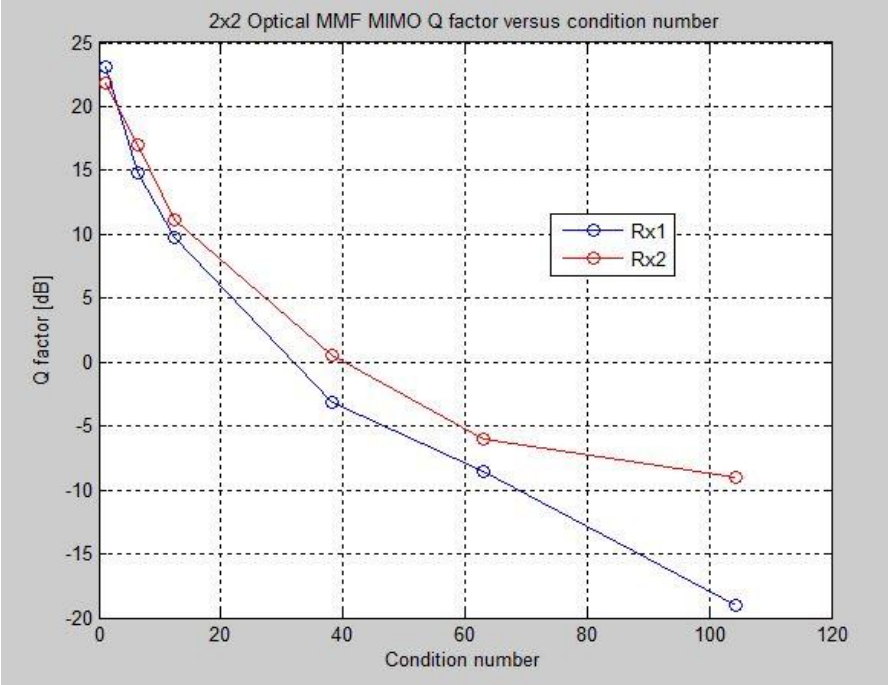

Figure 4.5 Condition number versus Q factor in the 2x2 Optical MIMO MMF system

From the results shown in Figure 4.5, we have learned that the Q factor significantly decreases as the condition number increases for both receivers. Even small changes

(i.e. 5) in the condition number will cause a decrease of approximately 7.5dB in the Q factor; thus, the condition number should be minimized as much as possible when designing a high performance MIMO system.

4.5.2 Transmitter and receiver structure in optical MIMO

From the above subsection, we have learned that in order to keep a low condition number and obtain a good channel matrix H, the number of receivers must be equal to or greater than the number of transmitters.

It is adequate to extend this from a noise point of view because when the system is limited by thermal noise at the receiver, it is favourable for the SNR to have $m=n$. This is because the thermal noise at each output will have a given variance, while an increase in m means that the received optical power at each detector will decrease. If the shot noise is the dominant noise, the signal to noise ratio is proportional to the received optical power; thus, maximizing the received optical power at each detector is a priority. In general, $m=n$ will be chosen in an optical MIMO system; however, the problem identifying the effective placement of receivers in the MIMO system arises. The following simulations shed light on this issue.

In the 2x2 IM-DD optical MIMO MMF system the transmitters launch GI-MMF by two radial offsets (0 and 15μm). The nine-detector array is used, and each individual detector has a radius of 4μm. Thus, any combination of two of the nine detectors can be selected as the two receivers. In total, there are 36 different combinations. The condition number can be utilized to evaluate the best receiver position. Table 4.2 gives the calculated condition numbers for different combinations in the nine-detector array.

Detectors	D1	D2	D3	D4	D5	D6	D7	D8	D9
D1	NA	35.8	56.6	19.3	14.7	18.5	3.6	13.3	17.2
D2	35.8	NA	37	32.4	5.3	29	5.5	5.0	3.4
D3	56.6	37	NA	21.9	21.1	21.2	4.4	22.0	10.8
D4	19.3	32.4	21.9	NA	6.8	2.7	4.41	4.49	83
D5	14.7	5.3	21.1	6.8	NA	6.81	10.1	3.3	**1.8**
D6	18.5	29	21.2	2.7	6.81	NA	4.4	4.41	8.65
D7	3.6	5.5	4.4	4.41	10.1	4.4	NA	15.2	8.67
D8	13.3	5	22	4.49	3.3	4.41	15.2	NA	43.1
D9	17.2	3.4	10.8	83	**1.8**	86.5	8.67	43.1	NA

Table 4.2 The condition numbers for different receiver placements in the 2 x 2 IM-DD MIMO system; the red condition number represents the best receiver position.

In accordance with the value of the condition number, the best configuration of the detector is the combination of detector 5 and detector 9 shown on the right hand side of Figure 4.2. Obviously, it is not trivial to find a standard rule to select the best receiver positions due to the random phase induced by intra-group mode mixing when propagating over a long distance (i.e.1km). The mode mixing breaks the orthogonality of the near field intensity pattern of LP modes, and the intensity pattern starts to rotate in a random nature. Owning to the higher order modes appear at the outside region of the fibre core and the fundamental mode is very stable at the centre of the fibre core. Therefore, annular multi-segment detectors are regarded as promising detectors for optical MIMO MMF systems. The structure of such a detector is shown in Figure 4.6.

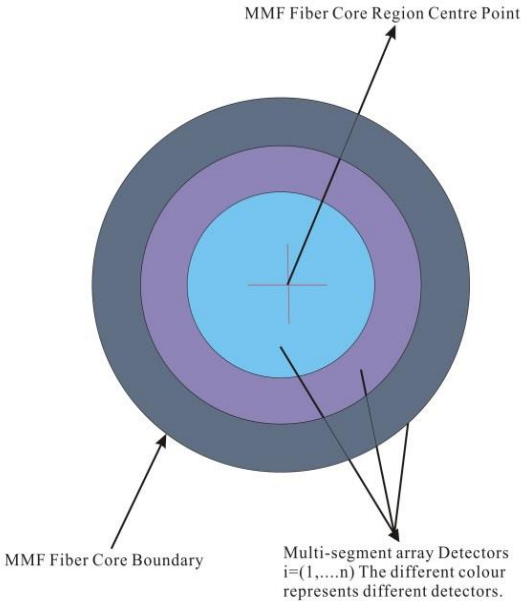

Figure 4.6 The annular multiple-segment detector array

A further simulation based on the previous 2x2 IM-DD optical MIMO MMF model with annular multi-segment detectors was conducted. All system parameters remained the same with the exception of the receiver structure. Two radial offset launches (0 and 15μm) were used. In addition, the newly simulated receiver included two detection areas: one containing a circular detection area with a radius of 10μm located at the centre of the fibre core; and the other having an annular shape with a radius between 10 and 31.25μm. The calculated channel matrix H is shown below:

Radial Offset from centre/μm	0	15
First circular detector: radius of R1=10μm	H=0.8389	H=0.0752
Second annular detector: radius of R2=10-31.25 μm	H=0.2305	H=0.7703

Table 4.3 The IM-DD optical MIMO channel matrix H when using annular multiple-segment detector array

In this particular design, the calculated condition number is 1.4808. Although this value is not very close to 1 (well-conditioned matrix) it is still smaller than most of the detector combinations shown in Table 4.2. Thus, we can conclude that the new type of receiver has the advantage of providing a more efficient channel matrix, which can improve system performance.

4.5.3 Crosstalk in optical MIMO

To ensure that the MIMO system can achieve its maximum capacity, the channel matrix element $h_{i,j}$ must be uncorrelated, and the sufficient spatial diversity condition should be maintained at both the transmitter and receiver. In an annular detector array the optical crosstalk between each detector plays an important role in the MIMO system, for instance, by degrading the system performance, limiting the optical MIMO capacity, and preventing the signal separation from the mixed signal at each detector. The crosstalk can be expressed as:

$$CT = 10\log_{10}\frac{\sum_{i\neq j} h_{i,j}}{h_{i,i}} \qquad \text{(dB)} \qquad (4.25)$$

In order to minimise the crosstalk the annular detector radius must be carefully designed. One effective method for minimising the crosstalk is to find the cross point of the encircled power flux (EF) curves generated by the different radial offset launches. The determination of the optimized annular radius will be introduced in the next chapter.

4.6 Conclusion

This chapter introduced the model of the optical MIMO MMF system and presented the mathematical analysis of channel matrix *H*. Subsequently, the capacity of the optical MIMO system was calculated by utilizing the channel matrix *H*. At the receiver part a simple zero forcing MIMO signal processing was carried out by inverting the channel matrix and multiplexing with the received signal. The initial IM-DD optical MIMO simulations were capable of analysing the relationship between the numbers of transmitters and receivers; the results confirmed that the ideal condition could be obtained when $m \leq n$. The condition number of channel matrix H and receiver crosstalk are two factors that can be used to optimize the MIMO system, especially in the design of receivers. The high sensitivity of the Q factor to the condition number makes it a key metric in evaluating optical MIMO MMF systems. In conclusion, the condition number must be controlled and kept as small as possible in order to achieve high performance. It was also found that annular multiple-segment detector arrays may become simple and efficient receivers for future optical MIMO MMF systems. After developing an optical MIMO MMF model, the next chapter will focus on the simulation of a gigabit IM-DD optical MIMO system in MMF.

Chapter 5: Intensity Modulation and Direct Detection (IM-DD) Optical MIMO System

In the previous chapter the condition number was used as a metric to evaluate different configurations of optical MIMO receivers combined with offset launch. However, the analysis shows the merit of annular receivers. Consequently, in the first half of this chapter, an optimization of such receivers with offset launch is introduced to improve system performance. The clearly defined optimization steps for both the optical MIMO transmitter and receiver are presented, which includes laser spot size and the exact positions of the annular detectors. The first experiment on mode group diversity multiplexing using multiple SMFs as receivers was reported in 2005 [155]. One year later, the same author proposed a new idea related to annular detectors; however, this study did not characterise the overall MIMO system performance, such as BER and power penalty [90]. The content of this chapter extends that work to a 10Gb/s IM-DD optical MIMO MMF system. Meanwhile, many existing high speed MGDM systems [91, 93] assume that the optical MIMO MMF channel is a flat fading channel; in reality, because manufacturing imperfections may cause different time delays for guided modes, this assumption is unrealistic. In the following simulation, the modal time delay is considered when defining a comprehensive channel matrix. Finally, the effects of receiver noise, intra-group mode mixing, modal dispersion, and attenuation are all examined.

5.1 System model

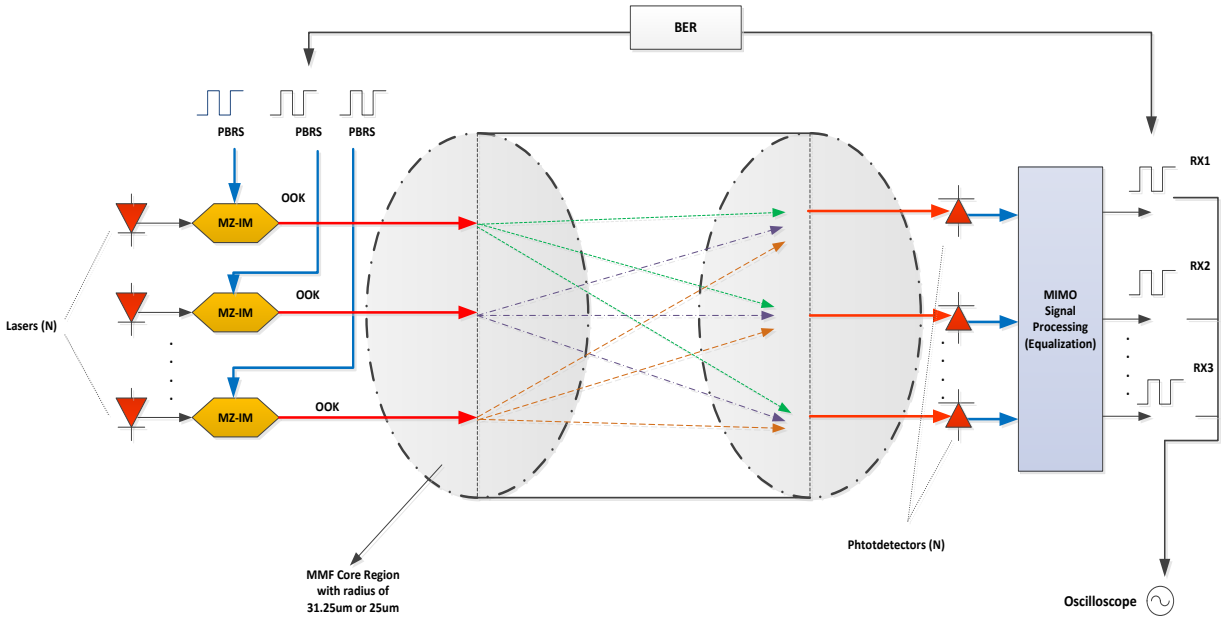

Figure 5.1 Schematic of an IM-DD optical MIMO system in MMF, the red arrowed line indicates the optical signals, while the blue arrowed line indicates the electrical signals.

The intensity modulation direct detection MIMO link model is illustrated in Figure 5.1, and contains three parts: the offset launching, spatial selective detectors, and MIMO signal processing. We assume that transmitter number and receiver number are the same, and each of the N inputs OOK modulated by an independent pseudorandom binary data steam that operates at 10Gb/s is independent to each other. The VCSEL wavelength can be either 850 or 1310nm with the same input optical power of 0dBm at each transmitter. For high speed links, the external modulation is the preferred over direct modulation because it minimises the relative intensity noise (RIN) induced from the fluctuation in laser intensity, and the phase noise is mainly caused by the finite linewidths of the laser sources. However, the most important advantage is the avoidance of the chirp effect, which results in signal spectral broadening and leads to dispersion. The dual drive Mach-Zehnder intensity modulator (MZIM) is commonly

applied [9]. The laser is then biased at a constant current in order to provide the continuous wave (CW) laser, and the generated optical carrier is subsequently led to the external modulator for data modulation. An NRZ format PBRS is chosen as the input electrical signal. Here, for the sake of simplicity, the phase noise, unwanted chirp, and relative intensity noise are all neglected. The receiver noise is regarded as a major impairment in the IM-DD optical MIMO MMF system.

In addition to the assumptions made regarding the transceiver, the coupling effect is also assumed to vary slowly compared with the symbol period. Due to the nature of IM-DD the matrix H is described as the ratio of the j_{th} transmitter input power and the i_{th} receiver output power, as presented in Equation 4.12. Each detector receives a different power distribution from all of the transmitters through the guided modes, and the intensity distribution is linearly superposed. Lastly, the captured mixed signals are passed to the MIMO signal processing, which is a simple matrix inversion to recover the symbols. The received electrical signal is written as:

$$I_i(t) = \mathrm{R}\cdot\left|y_i(t)\right|^2 = \sum_{j=1}^{M}\sum_{k}^{Q} H_{i,j}^{k} x_j\left(t-\tau_k\right) + n_i(t) \qquad (5.1)$$

where $I_i(t)$ is the received electrical signal, R is the responsivity of the detector, $n_i(t)$ is the Gaussian noise, $y_i(t)$ is the received signal at the i_{th} receiver, $x_j\left(t-\tau_k\right)$ is the transmitted electrical signal and the channel matrix is given in Equation 4.12.

The offset launch is applied at the transmitter and can be achieved by a combination of the SMF and MMF connection by using either a computer-controlled micro-positioner [91] or a translational stage [141] to precisely launch on the core of the MMF. Two types of receivers were taken into account: a standard SMF pigtailed

photodiode that can perform spatially selective detection [91]; and the proposed annular multi-segment receivers.

The typical structure of a transmitter with a narrow Gaussian beam of arbitrary offset and annular multi-segment receivers is illustrated in Figure 5.2. The input Gaussian beam is symmetrical about the fibre axis in the MMF fibre input plane.

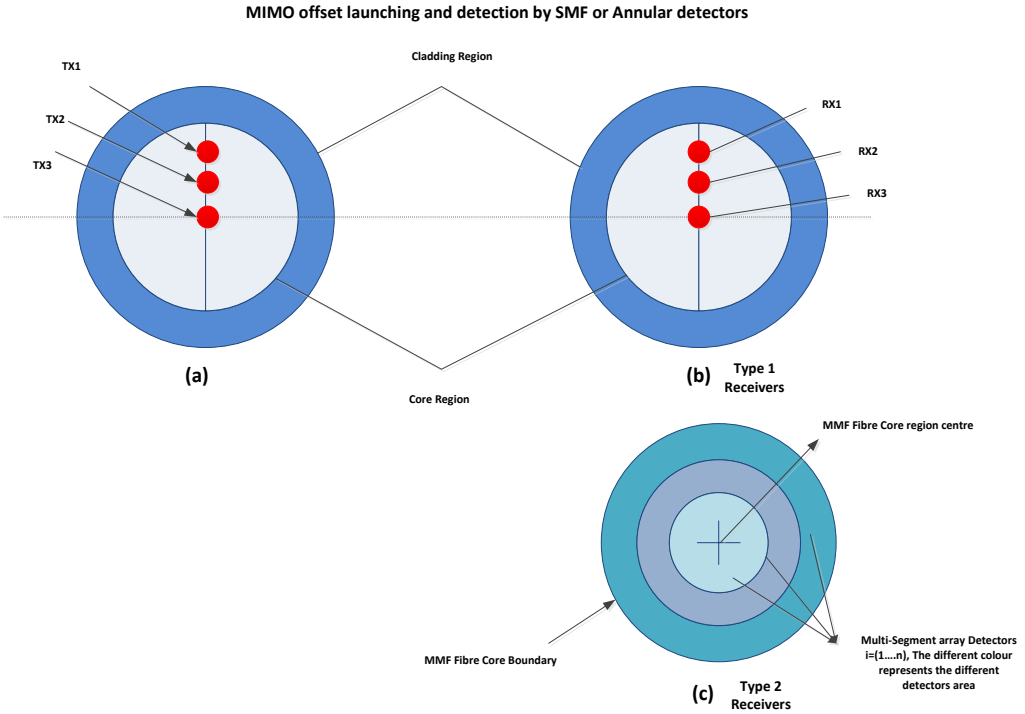

Figure 5.2 The selective launching and detection of the IM-DD optical MIMO MMF system: (a) radial offset launching, (b) selective detection by SMFs, (c) annular Multi-segment photodetectors.

5.2 IM-DD optical MIMO transmitter

The number of excited modes depends on the spatial excitation conditions, for instance, the light source wavelength, spot size, and radial offset value. A single longitudinal mode VCSEL laser source is used in the simulation as it has a relaxed coupling requirement. Moreover, it can also provide a high coupling coefficient in conjugation with a Gaussian beam with a small spot size. The launched Gaussian

beam is aligned to the fibre axis, but the simultaneous launch of different beams at the facet of the MMF becomes a problem. To minimise the correlation of the light sources the input beams are launched through different lengths of SMF, which gives rise to different path delays for each launch. A standard 61.25μm/125μm MMF with NA=0.275, $n_1 = 1.414$, $\Delta = 0.0174$ and index profile=2 was employed in the simulations below. The launched laser spot size was assumed to be 4μm and the optimized value will be investigated in detail in Chapter 5.2.2.

5.2.1 Radial offset launching

The purpose of a radial offset launch is to excite as few modes as possible and to increase the bandwidth. The power distribution of these excited mode groups after manipulating the radial offset value separately from the fibre centre is shown in Figures 5.3-5.4. In order to maximize the MIMO capacity, the transmitters and receivers must have sufficient spacing to maintain sufficient spatial diversity. The radial offset values were set to 0 and 12μm for the 2x2 MIMO system and 0, 12, and 24μm for the 3x3 MIMO system.

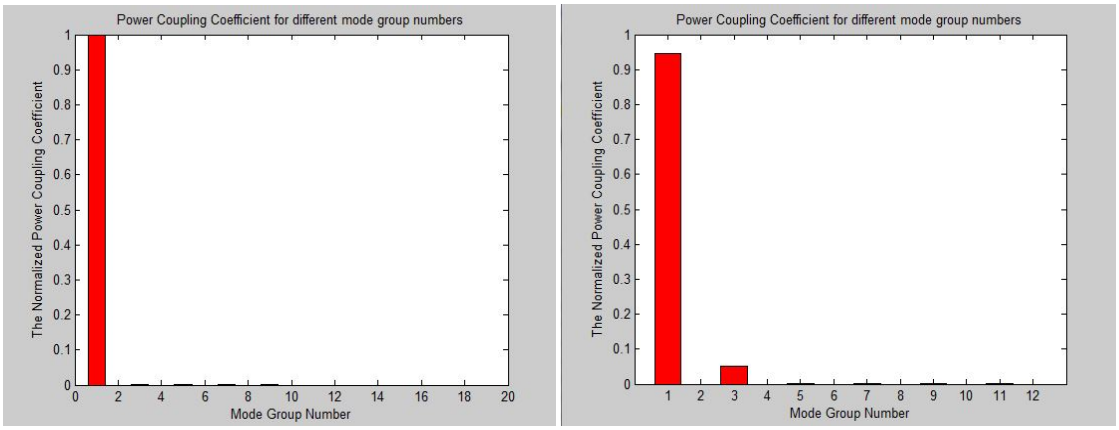

(a) (b)

Figure 5.3 Mode group power distribution when centre launching is applied: (a) $\lambda = 850nm$, (b) $\lambda = 1310nm$.

When using the laser is operated at 850nm, the calculated total mode group number is 20; when operating at 1310nm, the total 12 mode groups belong to MMF. The centre launching couples most power into the fundamental mode, even though a slight amount of power is coupled to the 3rd-order mode group in the 1310nm case.

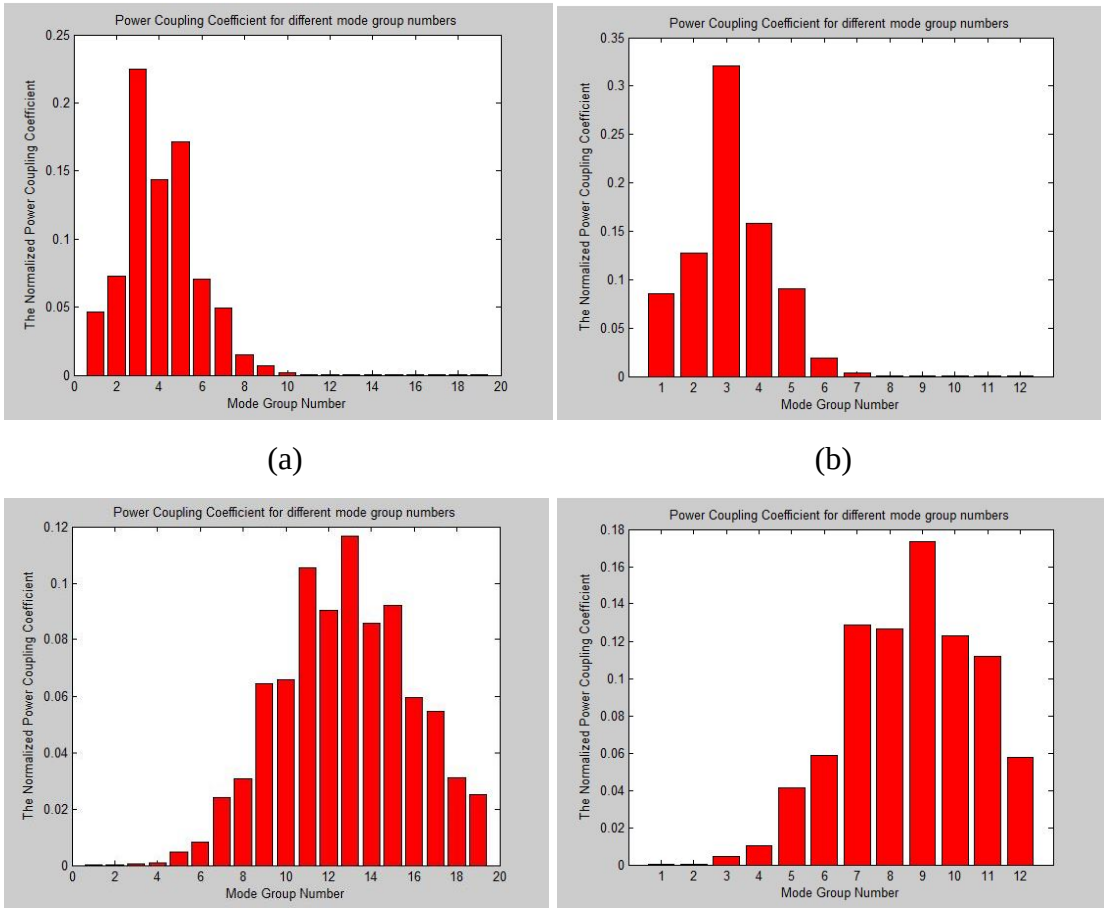

Figure 5.4 Mode group power distribution when offset (12μm, 24μm) launching is applied: (a) at 850nm with a 12μm offset launching, (b) at 1310nm with a 12μm offset launching, (c) at 850nm using a 24μm offset launching, (d) at 1310nm using a 24μm offset launching.

Figure 5.4 shows the tendency of the power coupling coefficient to shift to the higher order mode groups as the radial offset value increases. It is also notable that the modal power is distributed among lower order mode groups at 1310nm, but is gradually

distributed over the higher order mode groups at the 850nm wavelength; this effect is more obvious for a larger radial offset value. The 850nm VCSEL has long been used due to its easy implementation; owing to fewer mode groups being generated by the 1310nm laser source, so that it has become a promising candidate for high speed data transmission systems, such as the optical MIMO MMF system.

5.2.2 Laser spot size

The number of excited modes at each radial offset launching also relies on the Gaussian beam spot size. A Gaussian input beam consists of only the fundamental mode and is initialised and defined as:

$$E_{laser}(\mathrm{r}) = E_{laser}(0)\exp(-\frac{r^2}{w_0}) \qquad (5.2)$$

where $E_{laser}(0)$ is the peak field at the fibre centre, and $2w_0$ is the modal field diameter. Figure 5.5 illustrates the geometrical interpretation of the Gaussian narrow beam distributed across the fibre core.

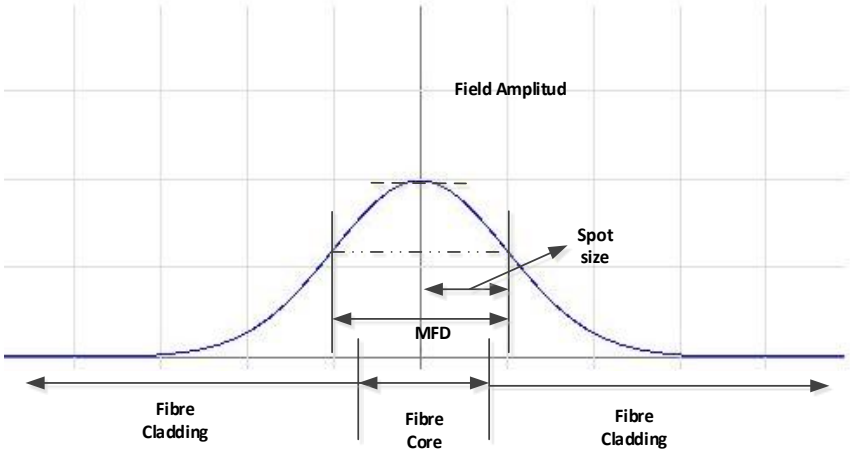

Figure 5.5 Geometry of the input Gaussian beam; MFD stands for modal field diameter, and the spot size is determined as half of the MFD.

The beam waist located at the input facet of MMF is dependent on the MMF

fundamental mode width. This relationship can be expressed in the following equation:

$$w_{fundamental} = \sqrt{\frac{2\rho}{\kappa_0 n_1 \sqrt{2\Delta}}} \qquad (5.3)\ [109]$$

where ρ is the radius of the core, κ_0 is the free space wave number, n_1 is the core peak refractive index value, and Δ is the refractive index profile height parameter. According to the above equation, the fundamental mode width of a typical 61.25/125 μm MMF operated at 1310nm is approximately 7.04 μm. For a zero offset launching, the optimum spot size corresponds to $w_0 = w_{fundamental}$, where all of the power is coupled into the fundamental mode LP_{01}, but this confinement is not suitable for the higher order mode groups excited by arbitrary offset launching. As seen in Figure 5.4, it is clear that with a 24 μm radial offset launch by a 1310 nm narrow Gaussian beam the maximum power is mainly allocated to the mode groups 7 to 11. Now we use these normalized mode group power coupling coefficients to characterise the optimum laser spot size when the radial offset launching is applied.

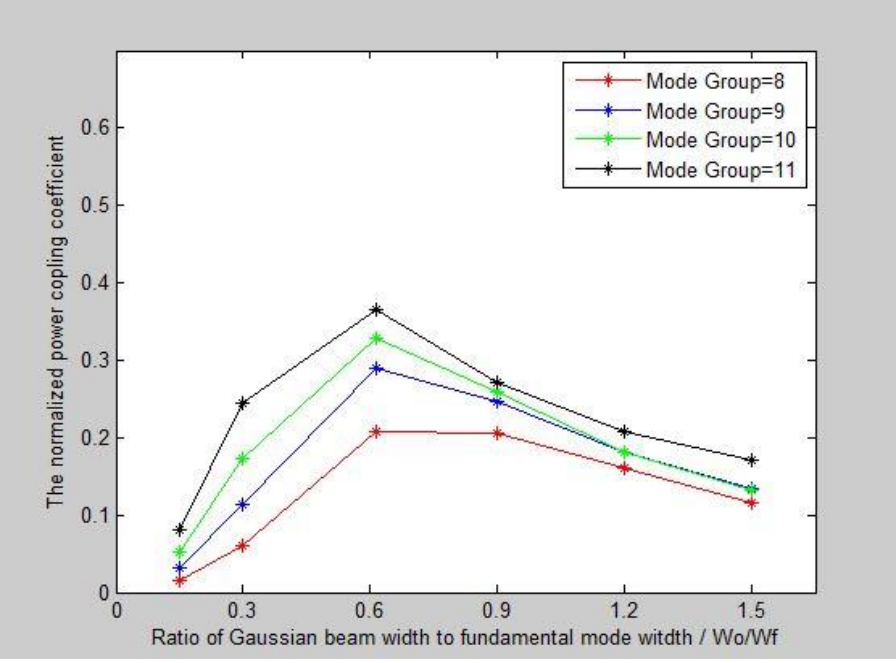

Figure 5.6 The power coupling coefficients on various input Gaussian beam widths for different mode groups (8^{th} -11^{th} group) with offset=24 μm and $\lambda = 1310nm$

Figure 5.6 shows that the power coupling coefficient in these mode groups is sensitive to the variation in the input Gaussian beam width. The power coupling for mode group 11 is reduced by less than 5% from its maximum value when the ratio of the input beam width to the fundamental mode width is changed from 0.4 to 0.6. Figure 5.7 corresponds to the power excitation spectrum at different input beam widths for all mode groups. We can see that the wider the power excitation spectrum, the more mode groups will be excited. Therefore, a narrow power excitation spectrum is preferable for optimizing the laser input beam width in order to reduce the modal dispersion effect. Thus, the results show that $w_0 / \mathrm{w}_f = 0.6$ is the optimal beam width at a radial offset launch of 24 μm.

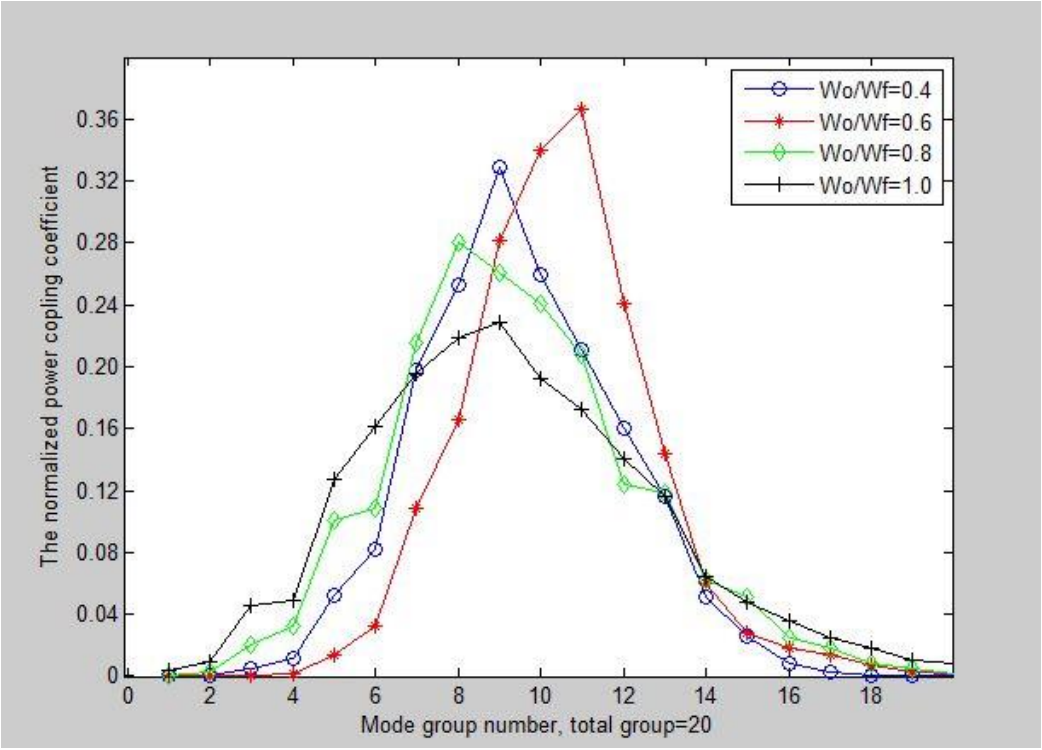

Figure 5.7 The power excitation spectrum of different mode groups excited by a 24 μm radial offset narrow Gaussian beam with a varied input beam width (w_0 / w_f the beam width ratio between the laser source and fundamental mode, $\lambda = 1310nm$, 62.5/125 μm GI-MMF, index profile $\alpha = 2$).

When matching the input beam width with the fundamental mode width, the power excitation spectrum is seen to be broader than the optimal one ($w_0 / w_f = 0.6$). This reveals that optimal condition of the Gaussian input beam used in centre launching is no longer valid in the offset launching condition. In general, a compromise may be made based on $0.4w_{fundamental} \le w_0 \le 0.8w_{fundamental}$. In parabolic index optical fibre the width is found to be optimized at $0.6w_{fundamental}$, which is the optimal excitation of the higher order mode groups and 80% power is retained in fundamental mode using centre launch [145, 156]. The optimized value is sensitive to different system configurations and depends on laser source wavelengths and the fibre refractive index or numerical aperture. To adjust the laser spot size, a focus lens may be effectively utilized. In addition, a procedure for optimizing the narrow input Gaussian beam width as a function of MIMO capacity will be outlined in Section 5.4.

5.3 IM-DD optical MIMO receiver

The spatial selective detector is accomplished by either multiple SMFs or annular multi-segment detectors. A simple PIN photodiode is used in the photodetection process; thus, the system performance is restricted by intrinsic shot noise and thermal noise. However, before the detection process, an ideal lowpass filter is very useful for more accurate channel estimation and detection.

5.3.1 Receiver impairments

At the receiver end the detected optical power is converted to electrical current via the responsivity of the photodetector, which is given by:

$$R = \frac{\eta q}{h\nu} \qquad (AW^{-1}) \qquad (5.4)$$

$$I_p = RP_{in} \tag{5.5}$$

where I_P is the output photocurrent in amperes, P_{in} is the incident optical power, η is the quantum efficiency, which represents the conversion coefficient from the detected photos to electrons, q is the electron charge, and *hv* is the energy of the photon associated with frequency v. The averaged received optical power is can be written as:

$$\bar{P}_{rec} = \left(p_1 + p_0 \right) / 2 \tag{5.6}$$

Noise is an unavoidable limitation in photodetector performance. There are two major noises in photodetectors: thermal noise, induced by the thermal agitation of electrons in a conductor; and shot noise, referring to the generation of a random distribution of electrons [157]. In a specific photodetector, the receiver sensitivity can sometimes be used to characterise the thermal noise. The receiver sensitivity is commonly used to define the minimum average receiver power $\bar{P}_{rec}$ to achieve a BER of 10^{-9}. The relationship between thermal noise and receiver sensitivity may be written as [157]:

$$\bar{P}_{rec} \approx Q\sigma_t / R, \quad \sigma_t = \bar{P}_{rec} R / Q \tag{5.7}$$

The *Q* factor can be calculated from Equation 5.13. The noise generated during the photodetection process is expressed as:

$$I^2{}_{noise} = I_s^2 + I_t^2 = 2eBI_p + \frac{4kTB}{R_L} \tag{5.8}$$

where *T* denotes the absolute temperature, *B* is the effective noise bandwidth of the receiver, *k* is Boltzman's constant, and R_L is the load resistor. For simplicity, the noise is simply added onto the received signal. The signal to noise ratio for each receiver is given as a ratio of average signal power to noise power.

$$\mathrm{SNR}_i = \frac{(R\bar{P}_i)^2}{\sigma_i^2} \tag{5.9}$$

P_i refers to the average received optical power from the i_{th} receiver associated with noise variance σ_i^2.

In IM-DD optical MIMO MMF systems the detection takes place based on the decision threshold level:

$$I_D = \frac{\sigma_0 I_1 + \sigma_1 I_0}{\sigma_0 + \sigma_1} \tag{5.10}$$

where I_D is the decision threshold, which detects bit "1" if above this threshold level and "0" when below it. Once the variance of bit "1" and bit "0" is the same (i.e. $\sigma_0 = \sigma_1$) the decision level can be set in the middle of $I_1 + I_0$. $I_1, I_0, \sigma_1, \sigma_0$ denote the average value and corresponding variance for bits (1, 0), respectively. In addition, BER is always regarded as a major factor for evaluating system performance and is written as:

$$BER = \frac{total\ error\ bits}{total\ bit} = \frac{1}{2}[\mathrm{P}(0/1) + \mathrm{P}(1/0)] \tag{5.11}$$

The analytical expression of BER in the OOK system is derived below [157]:

$$BER = \frac{1}{2} erfc\left(\frac{1}{2}\sqrt{\frac{SNR}{2}}\right) = \frac{1}{2} erfc\left(\frac{Q}{\sqrt{2}}\right),\ where\ Q = \frac{\sqrt{SNR}}{2} \tag{5.12}$$

$$Q = \frac{I_1 - I_0}{\sigma_1 + \sigma_0} \tag{5.13}$$

5.3.2 Optimization of receiver

The two types of receivers used in the optical MIMO MMF system are shown in Figure 5.2. The first one is a spatial selective detector realised by SMF that is placed at the output of MMF assuming that the transmitter and receiver are symmetrically placed across the fibre core. To mitigate the crosstalk caused by different radial offsets the higher order mode groups are detected by placing the SMF at the outer region of the fibre core, and on the other side the SMF at the centre region is used for detecting the lower order mode groups.

The second effective detection scheme is to use annular multi-segment detectors. If it were possible to detect the received power without any power from other transmitters, the receiver would have a high independent spatial diversity and give a high quality transmission channel. This aim can be achieved by finding the cross points from the power flux distribution emitted by transmitters through different launch conditions. The normalized power flux from the j_{th} transmitter is described by the fraction power within a certain fibre area whose radius is between r and $r+dr$. The expression is given as follows:

$$normalized\ \ power\ \ flux_j(r,dr) = \frac{\int_0^{2\pi}\int_r^{r+dr} I_j(r',\varphi)\,r'dr'd\phi}{\int_0^{2\pi}\int_{r'=0}^{\rho} I_j(r',\varphi)\,r'dr'd\phi} \tag{5.14}$$

where $I(r',\varphi)$ is the intensity, the numerator denotes the power enclosed in the area with a radius between r and $r+dr$, and the denominator represents the total power across the fibre core. In the simulation, r was set in the range of (2-30 μm), with an increment of dr=2 μm each time. The next diagram demonstrates the specific steps of such a scheme in detail, where a 3x3 optical MIMO MMF (62.5/125 μm) system with

radial offsets (0, 12, and 24μm) and a narrow Gaussian beam (spot size=4μm) operated at 1310nm wavelength is simulated.

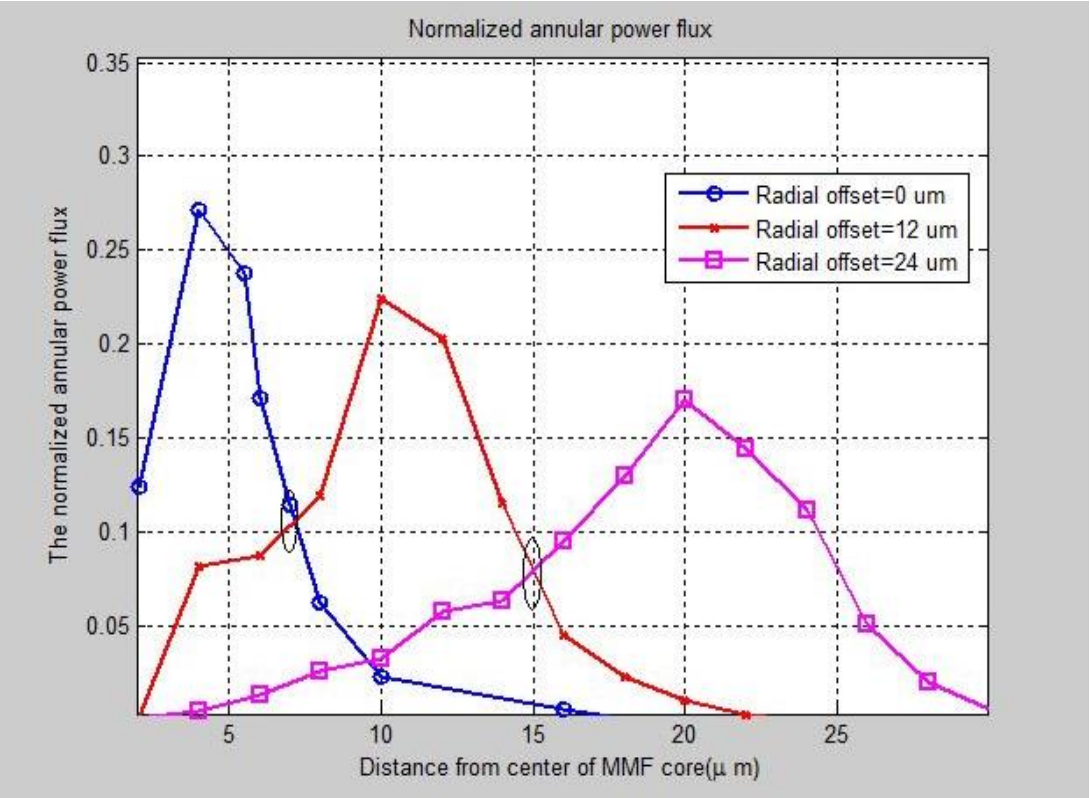

Figure 5.8 Normalized power flux at the output of an infinite parabolic GI-MMF with three different offset launches (0, 12, and 24μm)

Based on the observation in Figure 5.8, the crossing points of three normalized power fluxes are used to determine the annular detector radius. In this 3x3 MIMO system, the first circular detector collects the power within a circular area with a radius of 7μm, the second annular detector contains an area with a radius from 7 to 15μm, and the radius of the third annular detector ranges from 15 to 31.25μm. On this basis, it would seem that this choice yields a diagonally dominant channel matrix H that gives rise to a well-conditioned matrix, which is beneficial for MIMO equalization and reduces the power penalty. Moreover, it is apparent that when using this scheme each receiver is capable of detecting a signal with a minimum averaged crosstalk. Using

the annular detector optimization method the 2x2 and 3x3 IM-DD optical MIMO structure specifications are obtained and summarised in Table 5.1.

***N*x*M* MIMO**	**Input Radial Offset (μm)**	**Output Detector Radii (μm)**
N=*M*=2	0, 12	0-7, 7-31.25
N=*M*=3	0, 12, 24	0-7, 7-15, 15-31.25

Table 5.1 2x2 and 3x3 IM-DD optical MIMO system specifications with annular multi-segment detectors

5.4 IM-DD optical MIMO simulation results

As stated earlier in this chapter, the *N* independent PRBS data streams with a length of $2^{23}-1$ are used for both transmitted signals and training sequences in the simulations, resulting in a more accurate channel estimation. This accuracy also relies on the capability of the lowpass filter that is exploited before detection in order to minimise the noise effect. In the simulation, each laser is used to modulate the binary data at the same wavelength (1310nm) and with the same optical power. Hereafter, the different independent OOK signals are led to the MMF by various launching conditions. The offset launch and design of the annular detectors are optimized in the simulations. The optimized annular receiver specification is summarized in Table 5.1, while the conventional circular detector is designed to use the SMF with an 8μm diameter.

5.4.1 IM-DD optical MIMO capacity

In a deterministic channel, once the channel matrix is calculated the capacity can be obtained by the given SNR. In an IM-DD system, the channel input is proportional to the intensity of the light source and is therefore non-negative; thus, the classical

Shannon channel capacity formula derived for bipolar signals cannot be applied directly [158, 159]. For a linear MMF channel, the IM-DD capacity is approximately half of the Shannon limit based on the one dimensional Gaussian channel approximation [160]. For the $N_r = N_t$ IM-DD optical MIMO MMF system, the capacity is calculated for different numbers of *N*, laser spot sizes, mode mixing, and positions of radial inputs. Annular multi-segment detectors are utilized due to their high effectiveness. Moreover, the further assumption has been made that the receiver noise and modal dispersion are two impairments. The system capacity results obtained using Equation 5.15 are shown in Figures 5.9 to 5.12.

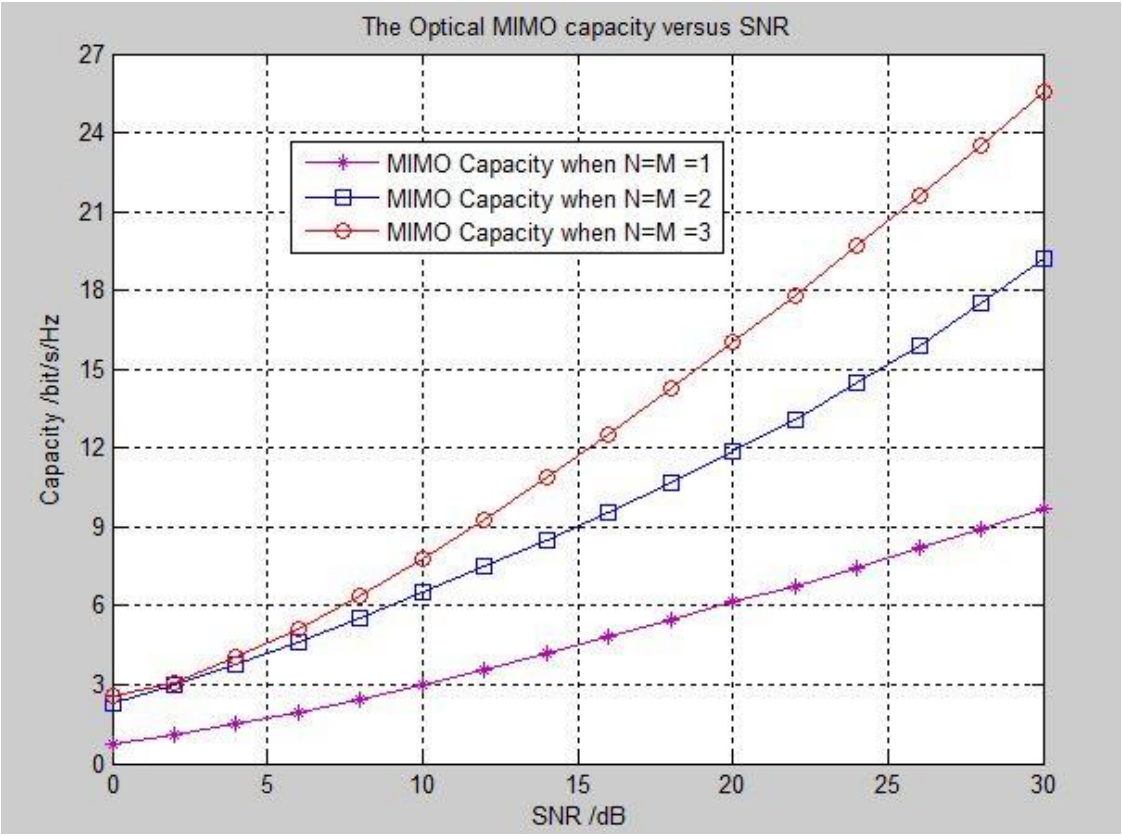

Figure 5.9 The IM-DD optical MIMO capacity versus SNR for N=1,2,3, L=1km, $\omega_0 = 4\mu m$, parabolic index profile 62.5/125 μm GI-MMF, $n_1 = 1.414$, $\Delta = 0.0174$.

The IM-DD optical MIMO capacity is calculated using Equation 5.15 [90-91]:

$$C = B\log_2\left\{\det[I_N + \frac{SNR_{average}}{N_T} HH^H]\right\} \qquad \text{(bit/s/Hz)} \qquad (5.15)$$

where H^H is the complex conjugate matrix, I_N is the $N \times N$ identity matrix, $SNR_{average}$ is the average electrical signal to noise ratio, and B is the bandwidth.

In Figure 5.9, the capacity increases as a function of the number of transmitters and receivers. The capacity in the N=3 optical MIMO system is significantly increased compared to the SISO system. (an increase from 9.6 to 25.5 bits/s/Hz at SNR=30dB). At a fixed SNR and input optical power, the capacity is determined by the launching

and detection at the MMF input and output. Moreover, the independence of each element in the channel matrix H has a great influence on the system capacity. The capacity enhancement moving from N=1 to N=2 (9.5 bits/s/Hz at SNR=30dB) is larger than that moving from N=2 to N=3 (6.2 bits/s/Hz at SNR=30dB) because there are more crosstalk at receivers in the 3x3 optical MIMO system. In the N=3 optical MIMO system, the detected power at receiver 3 may not only contain the desired power emitted from transmitter 3, but also that from transmitter 2; similarly, receiver 2 may collect some detected power from other transmitters. Therefore, it will increase the correlation between different channels and degrade the capacity gain.

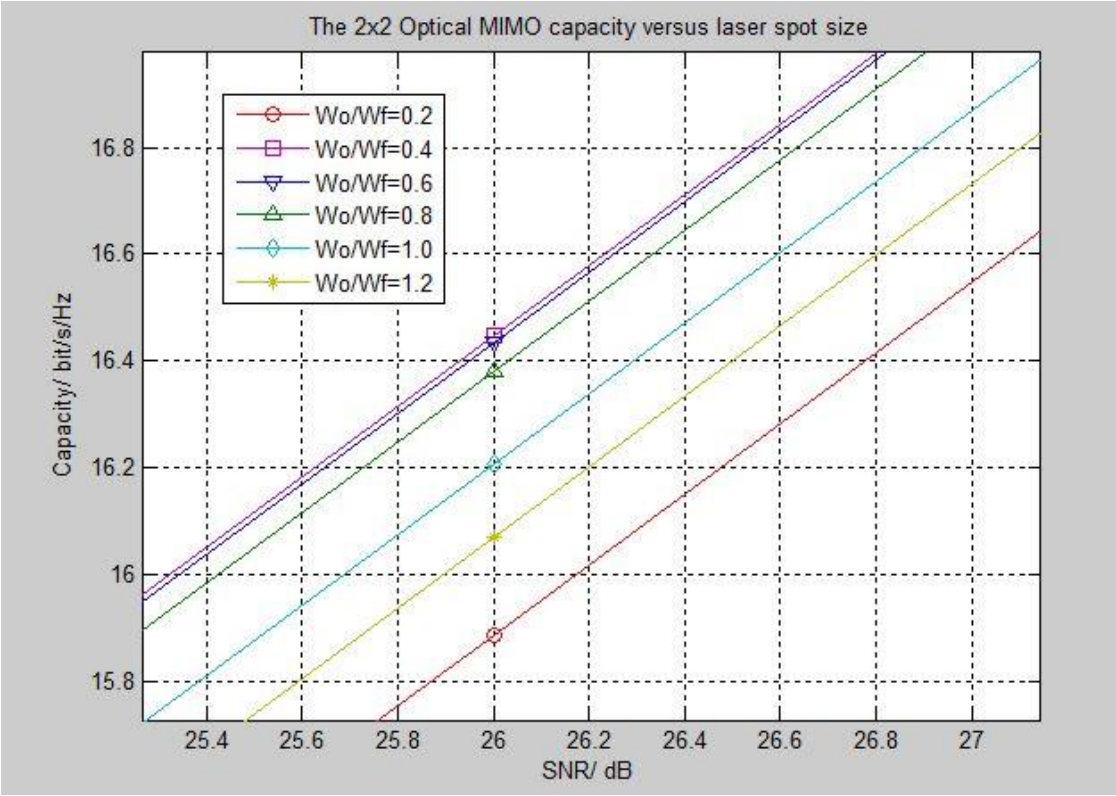

Figure 5.10 The 2x2 IM-DD optical MIMO capacity versus laser spot size (w_0 / w_f)

Figure 5.10 shows the effect of changing the laser spot size on the capacity of a 2x2 optical MIMO system. The capacity is not linearly related to the spot size. The highest

capacity is achieved at $w_o / w_f = 0.4 \, or \, 0.6$, which is in good agreement with the results shown in Figure 5.7. Further increases in spot size cause the capacity to drop slightly from its peak value; this mainly results from a decrease in the launching spatial diversity at the input facet of MMF. For a given SNR of 15dB, the 2x2 optical MIMO capacities with different spot sizes are shown in Figure 5.11. The capacity increases significantly with increasing spot size until $w_o / w_f = 0.6$; upon further increases in spot size, the capacity exhibits a slight descending trend. The theoretical explanation is that more modes are excited by using a larger spot size; thus, the channel has a rich spatial diversity, enabling each spatial channel to be independent. Continuing to increase the spot size could reach a saturation level.

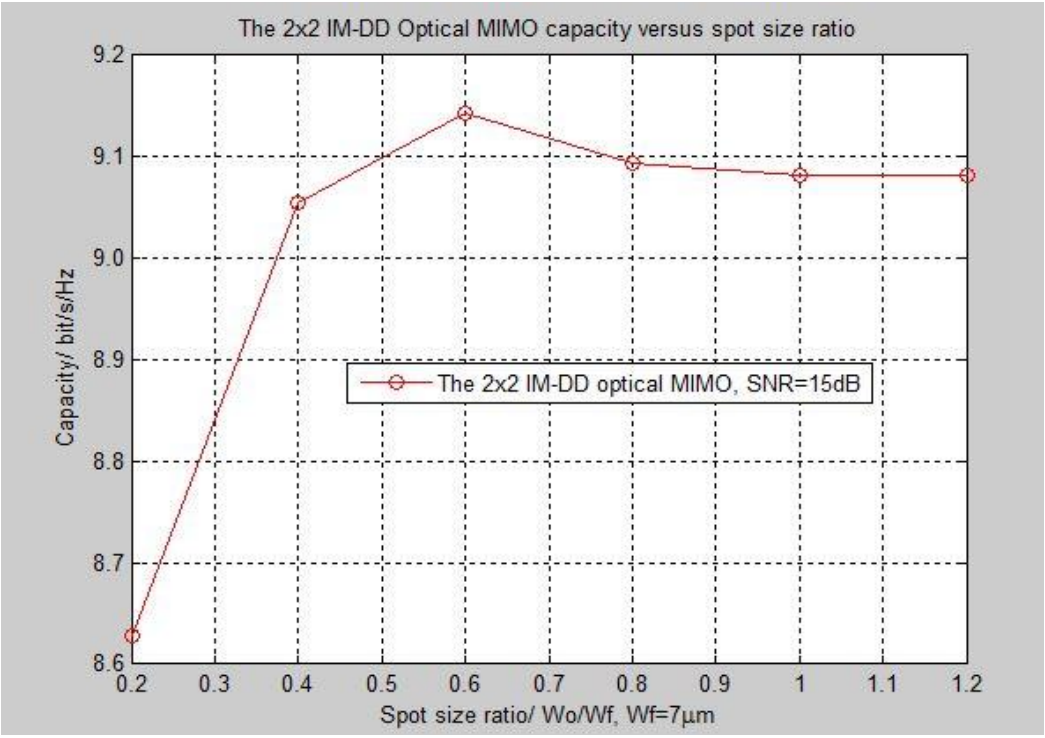

Figure 5.11 Capacity of a 2x2 IM-DD optical MIMO system versus spot size with SNR=15dB, L=1km, 62.5/125μm GI-MMF (index profile=2).

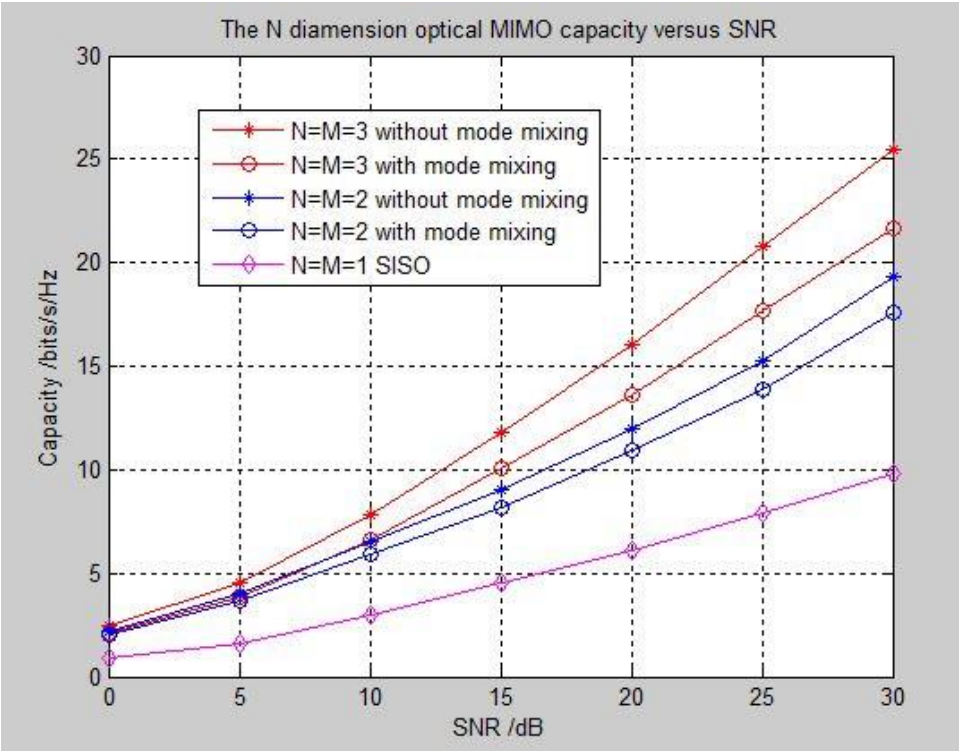

Figure 5.12 The effect of intra-group mode mixing on optical MIMO capacity, L=1km, spot size=4μm, 62.5/125μm GI-MMF (index profile=2).

Under intra-group mode mixing, the total power launched in a principal mode group will redistribute evenly among the modes within that group, and the phase of this principal mode group will become a random phase over $[0, 2\pi]$, which is shown in Equation 3.18. Once the near field intensity pattern with intra-group mode mixing is generated, the channel matrix can be obtained by Equations 4.13 and 4.15. Finally, the capacity is calculated by using Equation 5.15. In Figure 5.12, the 3x3 MIMO system has a more noticeable effect on the intra-group mode mixing than the 2x2 MIMO system. The larger number of detectors requires more spatial degrees of freedom at the receiver end; however, the random phase induced by mode mixing will cause an overlap in the power distribution at each detector, degrading the potential capacity. Contrary to the 3x3 MIMO system, the larger distance between transmitters in the 2x2 MIMO system cause mode mixing to not strongly affect its capacity. The average

receiver crosstalk penalty caused by intra-group mode mixing is only less than 1dB in both the 2x2 and 3x3 MIMO systems, as given in Table 5.2.

Nr=Nt	Average Crosstalk	*Nr=Nt*	Average Crosstalk
2x2 (no mixing)	-10.66dB	3x3 (no mixing)	-4.6dB
2x2 (mixing)	-9.92dB	3x3 (mixing)	-4.3dB

Table 5.2 Average crosstalk for IM-DD optical MIMO system

5.4.2 Results of the 2x2 IM-DD optical MIMO MMF system

In the 2x2 IM-DD optical MIMO model, the two lasers are modulated by the NRZ signals at 10Gb/s. Assuming that the different mode attenuation is the same for all modes, we can consider that the overall average attenuation is 0.38dB/km at the 1310nm transmission window. Because the major impairment in MMF transmission is dominated by modal dispersion, the chromatic dispersion is neglected in the short distance MMF transmission links. In addition, the nonlinear effects are not taken into account. In theory, the complete channel matrix H should be defined as:

$$H(f)_{i,\mathrm{j}} = \sum_{k=1}^{k} P_{i,j}^{k} \exp(-2\pi f \tau_k L) \cdot 10^{-\alpha_K L/10} \cdot \exp\left[i \frac{\pi D \lambda^2 f^2 L}{c} \right] \quad (5.16)$$

The coefficients $P_{i,j}$ should be normalized so that an expression of the average total received optical power from the j_{th} transmitter can be found. The benefit of doing so is to use this figure to describe the spatial diversity of the receivers regardless of the optical received power. The parameters $\tau_{k,}\, \alpha_k$ are the time delay and attenuation of the k_{th} mode, respectively. A schematic of the complete system model is depicted in Figure 5.13.

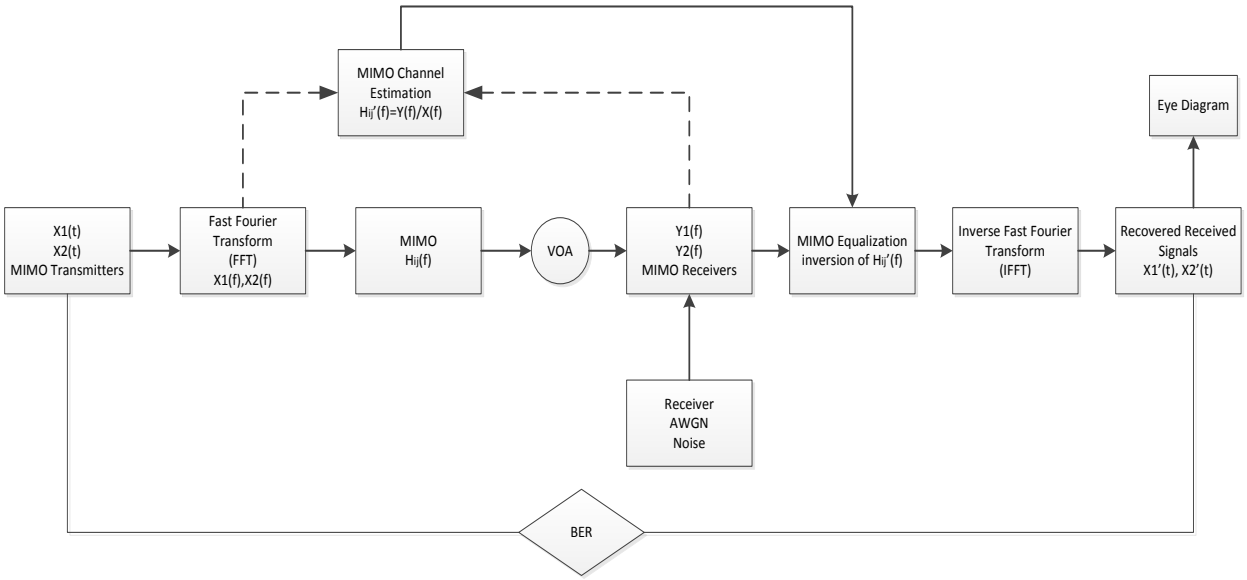

Figure 5.13 Simulation model of the 2x2 IM-DD optical MIMO system

An optical attenuator (VOA) is implemented to modify the total received optical power. The signal data transmission is carried out in the frequency domain, and the frequency domain equalization is then exploited by applying the zero forcing method. The training sequence is sent out from transmitter 1 to estimate H_{11} and H_{12}; in a similar manner, the channel matrices H_{21} and H_{22} are estimated by sending the training sequence from transmitter 2 while switching off the other transmitter. Unlike the previously proposed narrowband MIMO model that assumed all of the optical pulses would arrive at approximately the same time, the model built here is considered as a wideband model that can also evaluate the modal time delay. The parameters used in the simulation model are given in Table 5.3.

Transmitters	Launching position	Receiers	Type of receiver
2x2 MIMO	(0μm,12μm)	2x2 MIMO	SMF at position of 0, 12μm with r= 4μm
3x3 MIMO	(0μm,12μm,24μm)	2x2 MIMO	Annular detector (0-7μm,7-31.25μm)
Laser average optical power	0dBm	3x3 MIMO	Annular detecto (0-7, 7-15, 15-31.25μm)
Wavelength	1310nm	PIN receiver Sensitivity	-19dBm
Laser spot size	4μm	Receiver quantum efficiency	0.8
MMF	31.25/125μm	Receiver responsivity (1310nm)	0.8448 (A/W)
Data rate	10Gb/s		
		Noise at receiver	Shot noise thermal noise
Data format	NRZ-OOK		

Table 5.3 The IM-DD optical MIMO system model simulation parameters

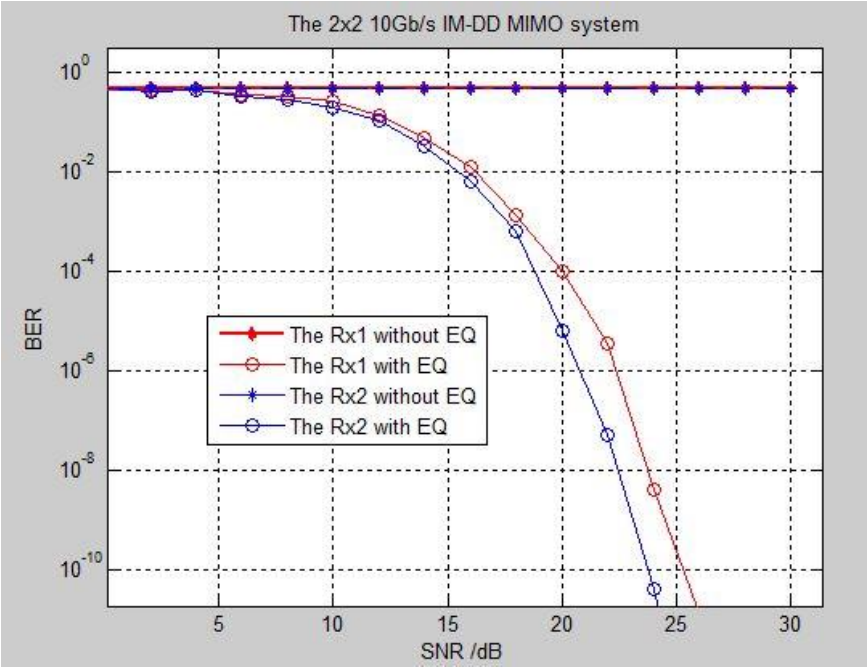

Figure 5.14 The BER of a 10Gb/s 2x2 IM-DD optical MIMO system with L= 1km

The zero forcing method will amplify the receiver noise, so the equalization is not very noticeable in a low SNR region, as shown in Figure 5.14. But it changes quickly

when SNR increases to 12dB because the amplified noise is much less than the signal which demonstrates an apparent equalization effect.

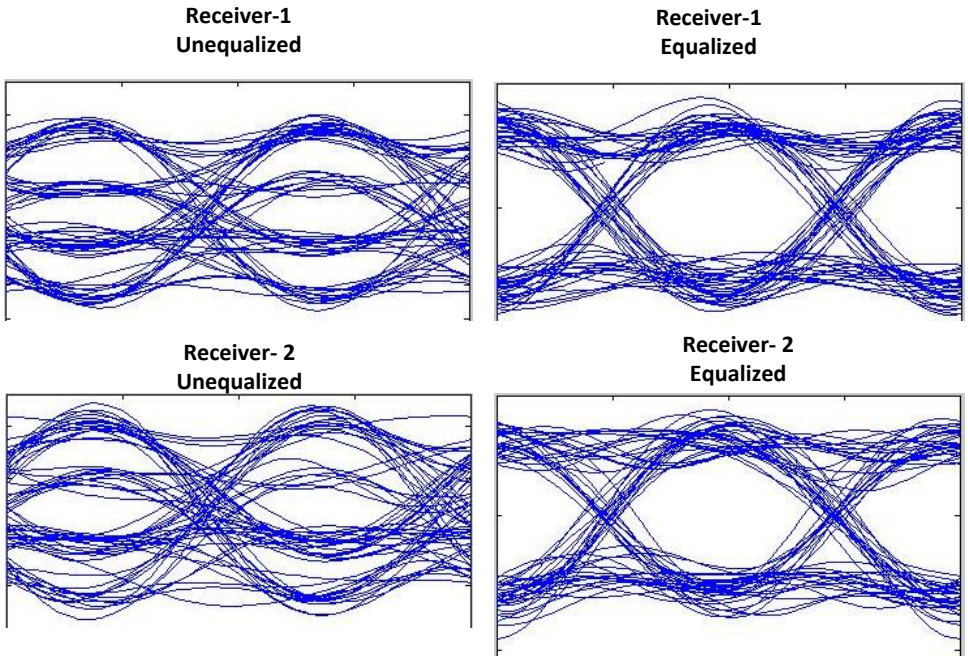

Figure 5.14-a Eye diagrams before and after MIMO equalization at 10Gb/s of L=1km

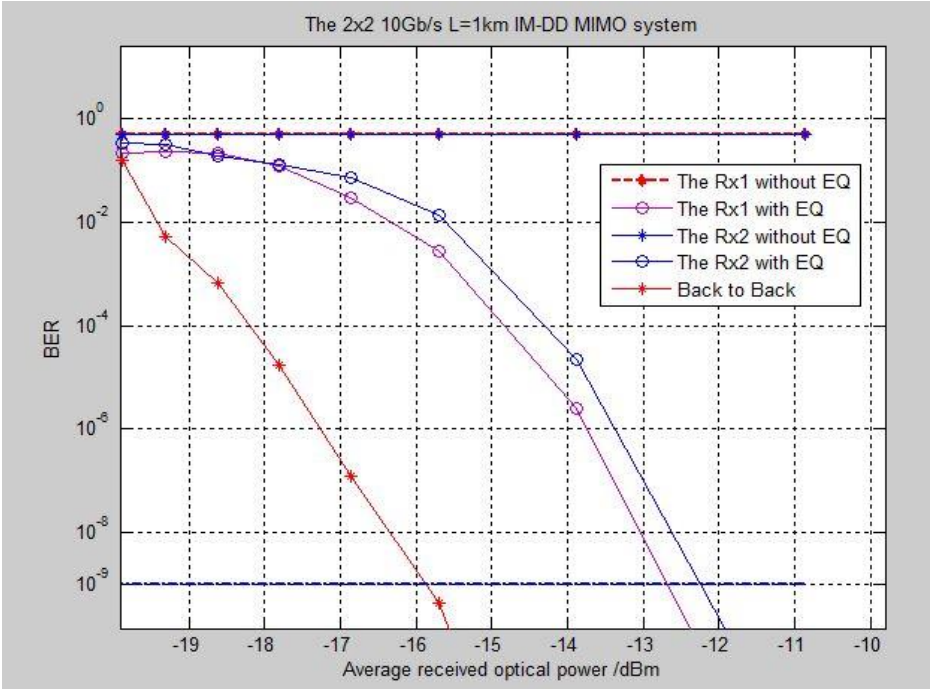

Figure 5.15 The BER versus average received optical power of a 10Gb/s 2x2 IM-DD optical MIMO system with a length of 1km

The MIMO equalization effect is proved by comparing the eye diagrams before and

after equalization at both receivers, the results are shown in Figure 5.14-a. Figure 5.15 shows the variation in BER with the average received optical power. At BER=10^{-9}, compared to a back-to-back link, receivers one and two have power penalties of 3 and 3.5dBm, respectively. The 0.5dBm power penalty difference may be explained by there being less received power at receiver two and a lack of receiver spatial diversity. Moreover, the interference from the higher order groups into the lower order groups seems to be more severe than vice versa. In order to better evaluate the overall optical MIMO performance of different system configurations, the averaged BER will be exploited instead of the BER at each individual receiver. Figure 5.16 shows the averaged BER for different data rates, and it is obviously to obtain that the required optical power for the BER is maintained at a certain level (i.e. 10^{-9}), which is slightly increased (0.5dBm) after 6Gb/s. In contrast, an extra optical power of 1.2dBm is required when the data rate changes from 2 to 4Gb/s.

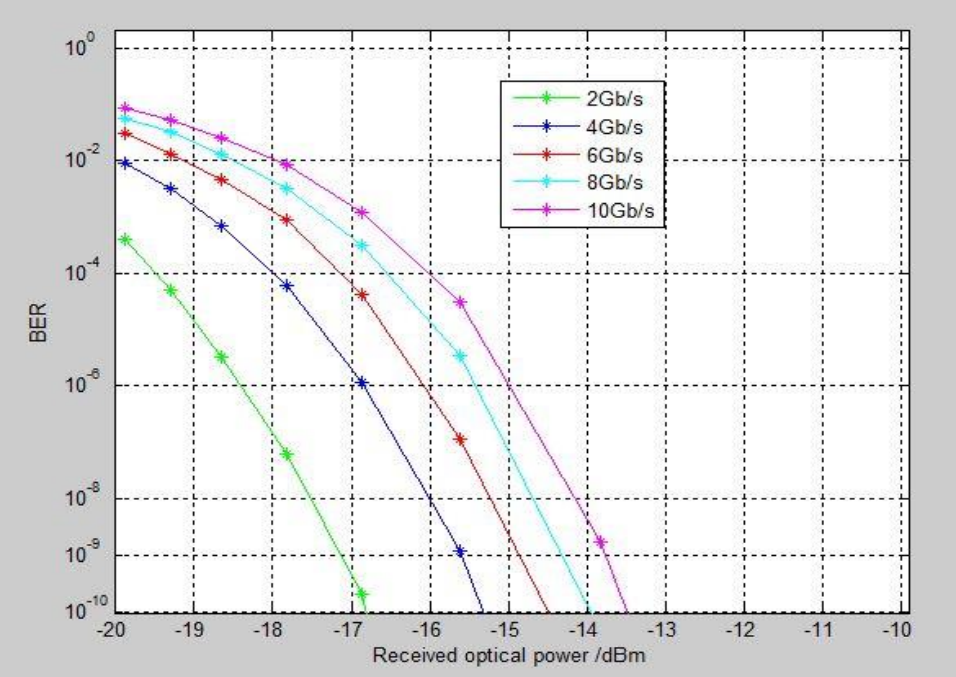

Figure 5.16 The 2x2 IM-DD optical MIMO simulated averaged BER versus data rate of 2, 4, 6, 8, and 10Gb/s at a fibre length of L=1km.

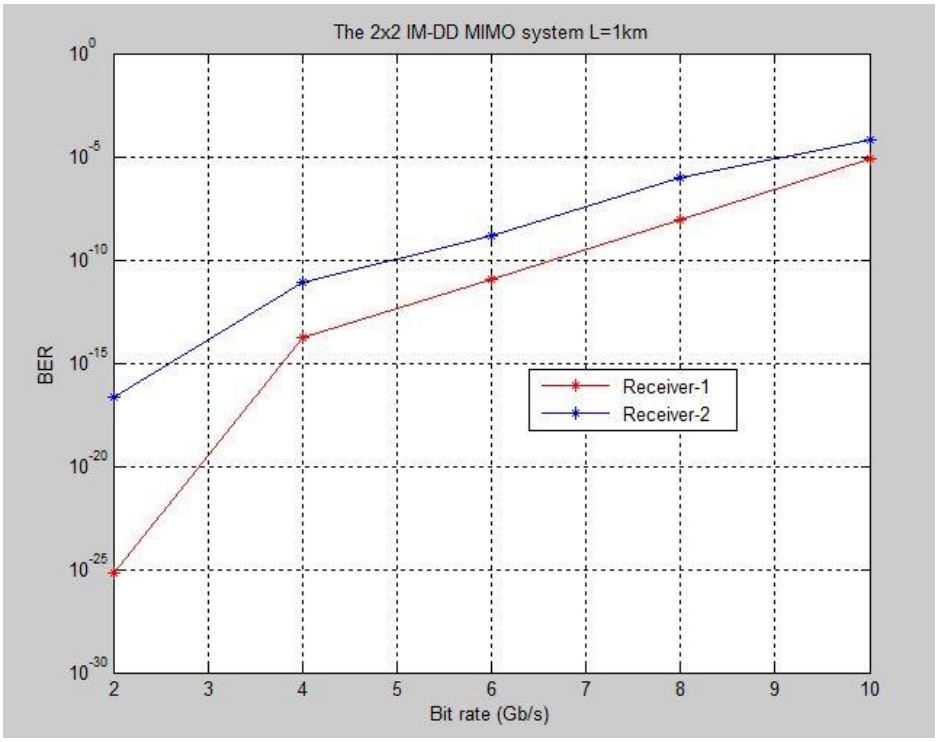

Figure 5.17 The 2x2 optical IM-DD MIMO BER for each receiver at different bit rates, L=1km, and an averaged received optical power of -15.4dBm.

Figure 5.17 emphasizes the changes in BER at different bit rates for the two sub-channels at a fixed average optical received power of -15.4dBm. At 2Gb/s the BER changes from 10^{-16} to 10^{-5}, at which point the data rate reaches 10Gb/s for receiver two, while similarly, the better performing receiver one has the same tendency as receiver two. From the results in Figure 5.16 and 5.17 we have learnt that the optical MIMO system performance is significantly reduced with increasing of the data rate. This indicates that the noise effect is still a major restriction in the IM-DD optical MIMO system since the added receiver noise (AWGN noise) is proportional to the signal bandwidth. This drawback limits the usage of the proposed IM-DD optical MIMO system in data networks with even higher data rates (i.e. 40Gb/s). Therefore, a more advanced MIMO signal processing method may be needed to minimise the noise effect. (i.e. MMSE)

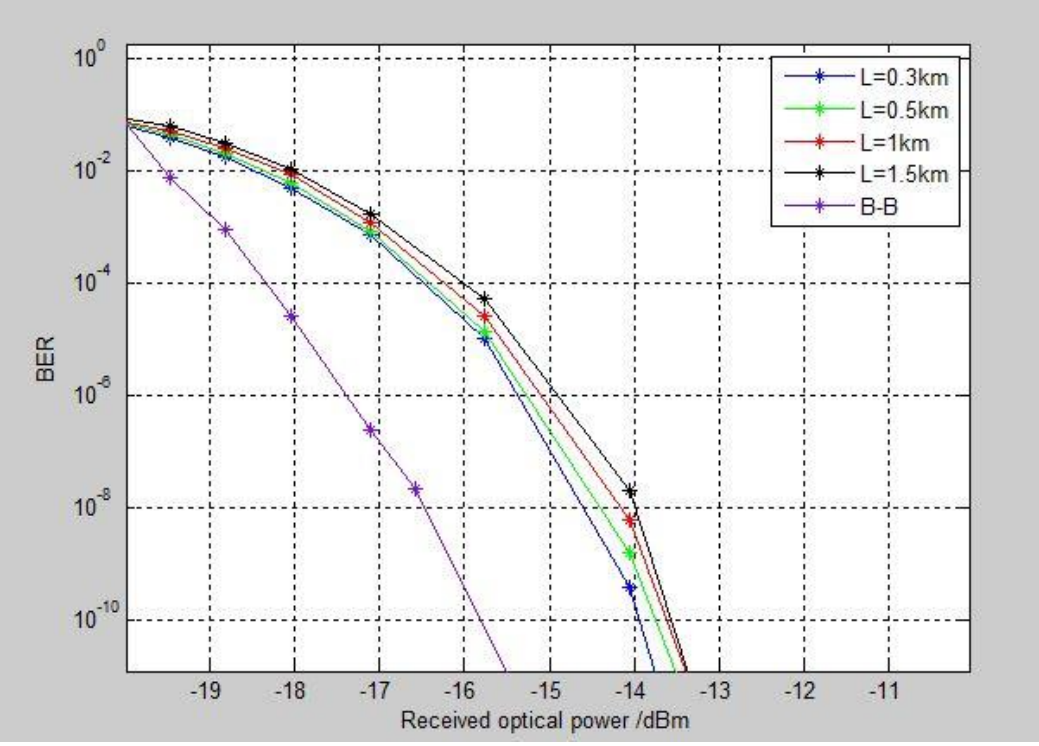

Figure 5.18 The 2x2 IM-DD optical MIMO simulated average BER versus fibre length of 0.3km, 0.5km, 1km, 1.5km, and a back-to-back at a data rate of 10Gb/s.

By using the frequency domain equalization, the mixed signals at each receiver can be successfully separated, however, a small power penalty difference of approximately 0.15dBm still exists at different transmission lengths, and the results are depicted in Figure 5.18. In this IM-DD optical MIMO system, the crosstalk at receivers and intra-group mode mixing will become two major determining factors. Figure 5.19 indicates how the intra-group mode mixing affects the overall 2x2 IM-DD optical MIMO system performance, and the BERs for both receivers are estimated.

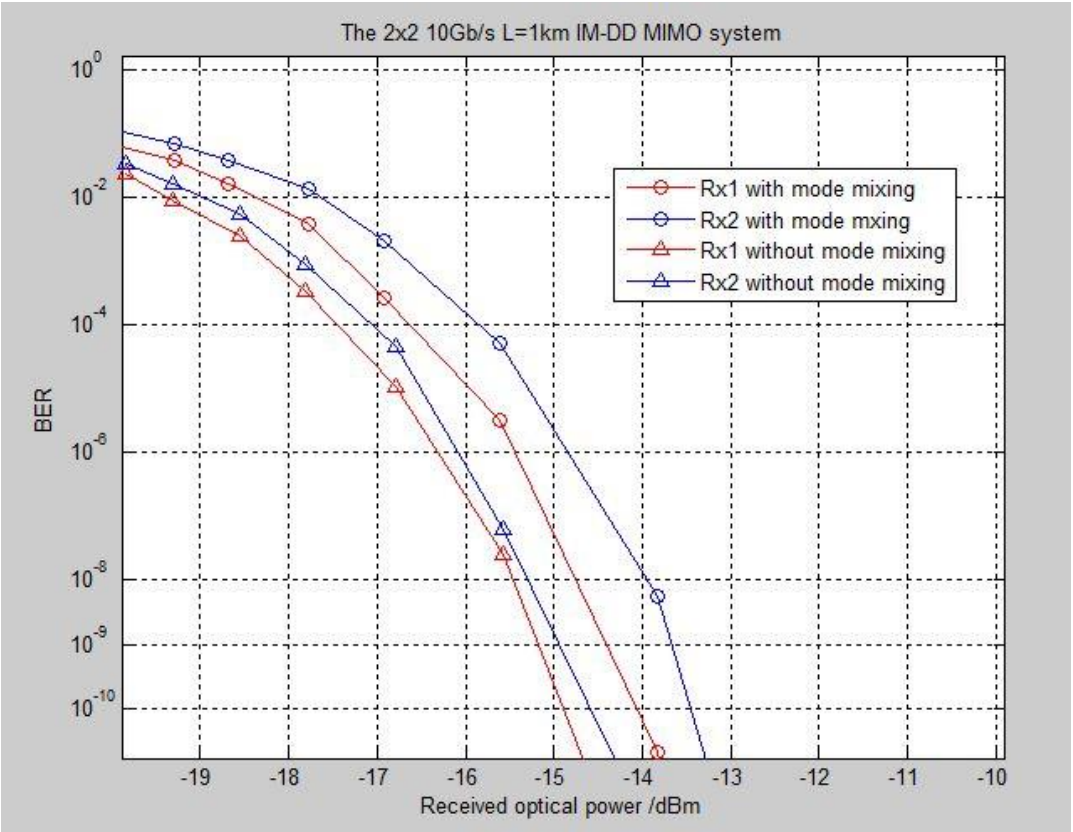

Figure 5.19 The 2x2 optical MIMO BER versus received optical power under mode mixing and without mode mixing for different detectors, L=1km, and data rate=10 Gb/s.

It was found that there is an approximate power penalty of 1dBm at each receiver when considering intra-group mode mixing in comparison to the case with no intra-group mode mixing. This mixing has a small impact on system performance due to the nature of the intensity modulation and direct detection, which means that the detected signal is only dependent on the received optical power. So far the MIMO detectors have only been implemented by annular multi-segment detectors and have not yet been compared with conventional multiple-SMF detectors. The next simulation evaluates and compares these two types of receivers based on the averaged BER values and received optical powers (Figure 5.20). The influence of intra-group mode mixing is also considered.

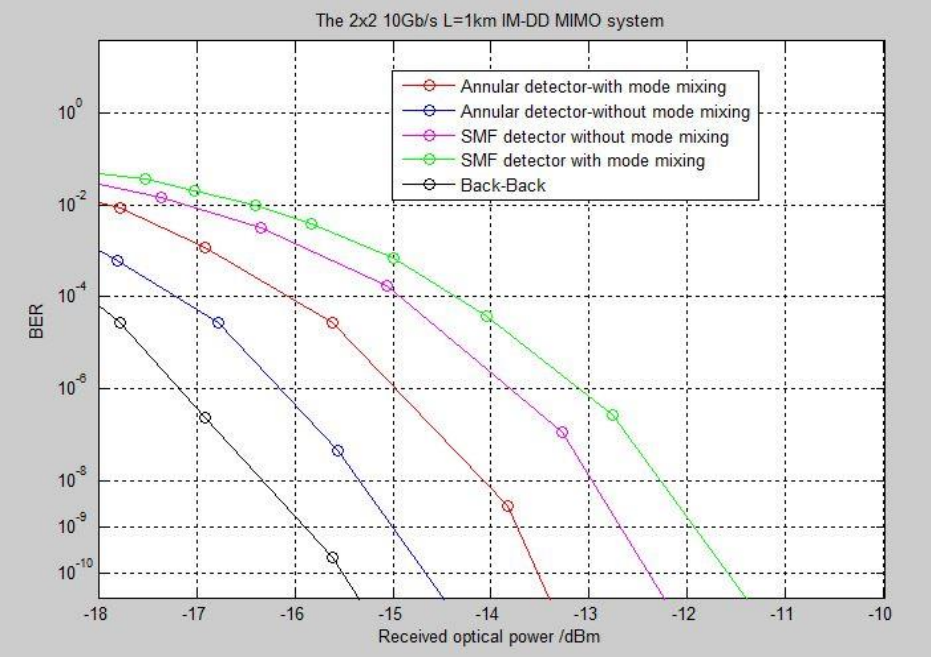

Figure 5.20 The averaged 2x2 IM-DD optical MIMO BER versus received optical power for different types of detectors (annular multi-segment detectors and SMF detectors)

In Figure 5.20, the annular multi-segment detectors exhibit a superior performance compared to the conventional SMF detectors under intra-group mode mixing; a power penalty of 1.9dBm is observed compared to the back-to-back link. On the other hand, the SMF detector encounters a power penalty of about 4dBm, which is at least twice that of the annular detectors. Therefore, the desirable result achieved by the annular multi-segment detectors is preferable for the optical MIMO system; at the same time, the annular detectors provide a relatively low receiver crosstalk (demonstrated in Chapter 4.5.3).

The last simulation is to determine the power penalty with an increasing number of transceivers (e.g. to compare the 3x3 system with the 2x2 system). The changes in power penalty with the number of channels created in the MMF for different fibre lengths are given in Figures 5.21 to 5.23.

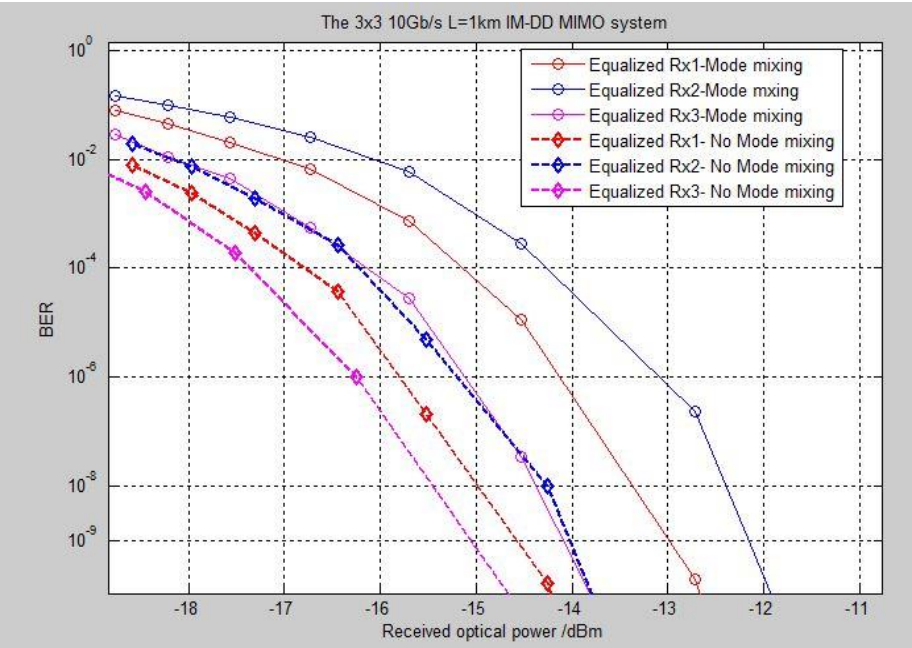

Figure 5.21 The 3x3 IM-DD optical MIMO BER changes with various received optical power for three receivers when intra-group mode mixing is involved

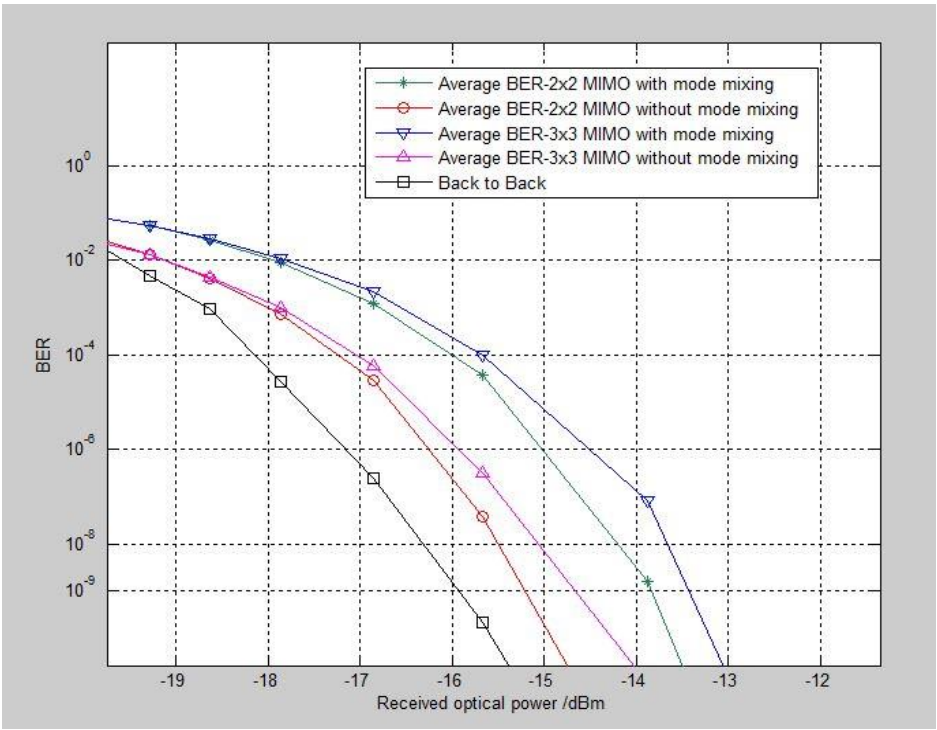

Figure 5.22 Average BER versus the received optical power for the 2x2 and 3x3 MIMO systems

In Figure 5.21, it shows the different characteristics of three detectors in the 3x3 optical MIMO MMF system, and the crosstalk between each detector is mainly

responsible for the observed differences. Figure 5.8 shows that the power flux distribution at receiver one is mainly interfered with the receiver two, and although the power emitted from transmitter one contributes more at receiver one there is still one third of the total detected power is emitted by transmitter two. In the same manner as previously shown, detector two will experience serious interference from both detectors one and three, and the power flux distribution from transmitters one and three make up nearly half of the total power received by annular detector two. Because of that, it significantly degrades the performance of detector two and makes it the worst sub-channel in the 3x3 MIMO system. Finally, detector three shows the best performance among all three detectors due to the aid of a lower portion of the total received power induced by emission from transmitter two. In summary, if the detector power comes mostly from the desired transmitter, a high performance MIMO system can be achieved.

Figure 5.22 shows that the received power penalty increases with the number of transmitters and receivers (N), and as in the IM-DD case, both the thermal noise and shot noise become the dominant noises during the detection process. Therefore, at lower power levels (below -18dBm) there is no significant difference between the 2x2 and 3x3 MIMO systems. However, the power penalty caused by the 3x3 MIMO system starts to increase gradually after receiving an optical power of -18dBm. This may be explained by the extra detector inducing more receiver noise, especially when the received optical power becomes larger. The extra power penalty caused by the 3x3 MIMO system is approximately 0.5 and 0.4 dBm in cases with and without mode mixing, respectively, when compared to the 2x2 MIMO system at BER=10^{-9}.

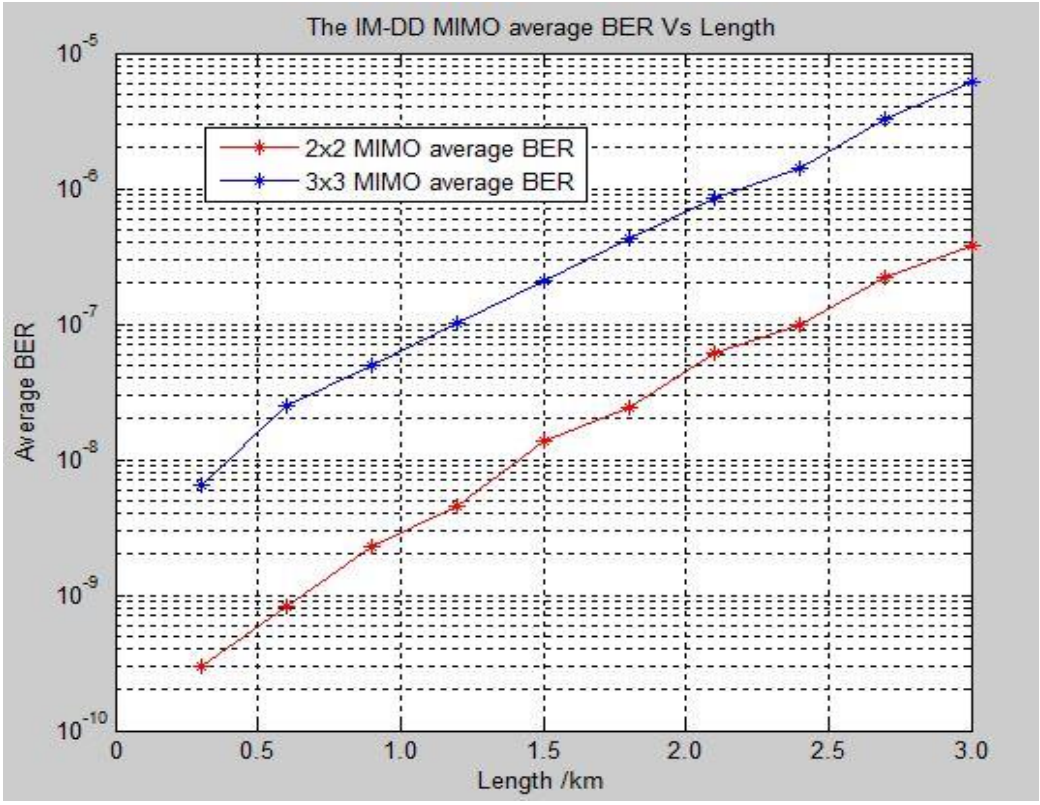

Figure 5.23 The average BER values of 2x2 and 3x3 IM-DD optical MIMO at various fibre lengths for SNR=22dB

Figure 5.23 shows that in the 10Gb/s MIMO system with SNR=22dB, the average BER decreases with MMF length because the differential model delay is proportional to the transmission distance; thus, the longer the distance, the larger the differential model delay, which limits the exploitation of the IM-DD MIMO system in long distance transmission links. In the 3x3 MIMO system, a BER of 10^{-8} is observed at a length of 0.3km, but this value reaches 10^{-5} once the MMF length exceeds 2.5km. Moreover, the 2x2 MIMO system average BER is superior to that of the 3x3 MIMO system by approximately 10^{-1}, even though the 3x3 MIMO system can provide more capacity than the 2x2 MIMO system.

5.5 Conclusion

In this chapter, an intensity modulation and direct detection MIMO system model was built and simulated. Firstly, the optimization of the Gaussian beam spot size and radial offset value were studied and their results indicated that the optimized spot size value was around 0.4-0.6 times the fundamental mode width. Moreover, the radial offset value must be carefully chosen in order to maintain sufficient spatial degrees of freedom for the transmitter. The annular detector radius can be determined by choosing the appropriate cross points generated from the power flux distribution emitted by transmitters.

Secondly, the deterministic IM-DD optical MIMO capacity was obtained by employing the channel matrix H. The results show that the capacity increases linearly with the number of transceivers and is also affected by the laser spot size. The maximum capacity can be achieved when the laser spot size is about 0.6 times the fundamental mode width. Continuing to increase the laser spot size, the capacity of the 2x2 MIMO system tends to be saturated. However, the capacity is also limited by the intra-group mode mixing, which becomes worse in the 3x3 MIMO system.

The two types of receivers were studied, and the annular multi-segment detectors proved to be the best choice for the optical MIMO MMF system as the conventional multiple-SMF detectors suffer a 2dBm power penalty compared to the annular multi-segment detectors. The average BER is not only dependent on different bit rates but also on the mode mixing effect. The intra-group mode mixing imposed an extra 0.5dBm power penalty on the optical MIMO MMF system at BER=10^{-9}; thus, it might not restrain the optical MIMO MMF system performance.

In addition, the 3x3 optical IM-DD MIMO system is more sensitive to transmission length than the 2x2 MIMO system. Although the 3x3 MIMO system can provide more capacity, it comes at the expense of greater power penalty and greater sensitivity to mode mixing. By using the zero forcing method, the mixed signal at each receiver can be separated, but due to the fact that the modal time delay is larger at a longer distance the IM-DD MIMO will lose its attraction in long distance networks (i.e. long haul networks). The simulations show the potential of this proposed system, indicating that the simple design can provide a stable IM-DD optical MIMO system.

Chapter 6: Coherent Optical MIMO System

Recently, some experimental works have studied coherent MIMO systems over two or three mode FMFs [105, 107, 108, 161]; but in these experiments beam optic or fibre optic devices served as mode splitters are needed in both transmitters and receivers, this increases the complexity in practical systems. Apart from demonstrations of high speed coherent MIMO systems in MMFs or FMFs, the spatial multiplexing and de-multiplexing schemes have also attracted many researchers. In general, there are two types of mode multiplexers: phase plate based mode multiplexers [162] and spot based mode multiplexers [163]. Ring launching has become a hotspot in realizing spatial transceivers [101, 164]; however, mode converters are still required as extra components. Although transmission using two coherent 2x4Gb/s OFDM transmitters with centre and offset launching in a 5km long MMF was experimentally demonstrated [165], no study has combined radial offset launching and annular detectors, which can considerably reduce the complexity at the both transmitter and receiver.

The proposed system also relaxes the requirement for coherent MIMO signal processing because the degree of complication of coherent MIMO signal processing is proportional to the number of guided modes. In addition, no complete simulation model for a coherent MIMO system with DPSK modulation format in FMF has been reported. In this chapter, based on the prototype of a commercial two mode GI-FMF, frequency domain equalization, offset launching and annular detectors, the coherent MIMO system is investigated and optimized. The optical DPSK in both heterodyne detection and intradyne with phase diversity detection are simulated and compared.

6.1 Optical coherent detection

Although the IM-DD system is easy to implement, it has poor receiver sensitivity. The better receiver sensitivity, the less required optical power is needed to achieve a given BER. However, another disadvantage of IM-DD MIMO system is that it cannot fully recover all the electric field signal information, which can be exploited to compensate the linear impairments using advanced signal processing [166]. The name coherent usually refers to a system in which the optical signal is mixed at the receiver with another optical signal generated by a local oscillator, and the combined signal is then directed towards a photodetector. The current generated after photodetection is centred at an intermediate frequency (IF) that is equal to the difference between the LO and the carrier frequency. According to the intermediate frequency value, the coherent system is generally defined as either intradyne or heterodyne detection, and there is an intradyne detection between them. Coherent detection is also an advanced technique that provides high spectral efficiency while maximizing power efficiency and allowing information to be encoded in all degrees of freedom [166]. For next generation 40 and 100Gb/s systems, coherent detection is the most promising solution.

6.1.1 Coherent detection impairments

Coherent systems provide a huge benefit over traditional IM-DD systems; nevertheless, they create several problems for implementation in practical systems.

Amplified spontaneous emission (ASE) noise

An optical amplifier (EDFA) is usually employed in long distance systems. Consequently, the ASE noise is an important issue in coherent systems. The ASE noise can be modelled as an AWGN with a one-sided power spectral density in each

polarization, as given by [157]:

$$\mathrm{N} = n_{sp} \cdot (G-1)hf \qquad (6.1)$$

where G is amplifier gain, hf is photo energy, h is the Planck constant, and f is the optical frequency. If $G \geq 1$, $n_{sp} = \frac{1}{2} NF$ is related to the noise figure (NF). For an ideal EDFA the spontaneous emission parameter n_{sp}=1. NF is defined as the ratio of the SNR at the input of the amplifier to that at the output of the amplifier. ASE induced noise consists of two noise sources: spontaneous to spontaneous beating noise (ASE-ASE), which is caused by the interference of the spontaneous photos; and the ASE-signal beating noise, which is generated by the beating process between signal photos and the random spontaneous emission. In a practical system, the ASE-ASE noise is normally negligible because of its small effect on receiver performance compared to the ASE-signal noise. The variance of this noise induced photocurrent may be written as [157] :

$$\sigma^2 = 2q(R_d G P_{in})\Delta f + 4(R_d G P_{in})\mathrm{R}_d \, N\Delta f \qquad (6.2)$$

where R_d is receiver responsivity and Δf is receiver bandwidth.

Polarization state matching

Due to coherent detection systems requiring the incoming optical signal to be mixed with the LO optical signal, it requires the polarization state of LO and the incoming optical signal is identically matched. Here, the random fluctuations in polarization state induced by temperature and structural changes are all neglected.

Laser intensity noise

The random fluctuations of spontaneous emission will give rise to an unstable laser intensity output, and this amplitude noise is called laser intensity noise. However, this noise can be compensated by the aid of a balanced receiver. All receivers in the following simulated coherent systems use a balanced receiver.

Laser phase noise

Spontaneous emission not only leads to intensity noise but also imposes phase noise in optical laser sources (both LO and transmitter lasers). This phenomenon is due to the finite laser linewidth at the laser output that has a frequency spread, resulting in the degradation of the receiver sensitivity. This particular noise is more severe in phase modulation systems. A Brownian motion model is employed to describe this phase noise effect, and the power spectrum of the laser output has a Lorentzian shape that is located at the laser centre frequency with a 3dB bandwidth of β. In general, β is a combined linewidth of the transmitter laser and LO [167, 168].

6.1.2 Optical DPSK coherent detection

This subsection describes the system model of binary optical DPSK in a coherent system. Two types of coherent DPSK systems are studied: the heterodyne system and the intradyne system with phase diversity receiver. The standard delay and multiple receiver structure in conjunction with the balanced receiver is utilized in both systems. In comparison to the OOK modulation format, DPSK has a lower OSNR requirement, which increases the transmission distance and relaxes the requirements on optical power. It is also more tolerant of PMD and chromatic dispersion (CD). Furthermore,

the nonlinear effect has a limited impact on the DPSK signal due to a lower peak optical power (3dB) compared to the OOK signals [166, 169]. The DPSK conveys information in the phase difference between two neighbouring bits rather than the instantaneous phase value, and this makes it more robust against phase noise than PSK modulation. DPSK also has the advantage of 3dB more receiver sensitivity than OOK. As the PIN photodetector only responds to the detected signal intensity and is not capable of detecting the phase information, the phase information in DPSK must be converted to intensity information for further decision processes [157]. The above advantages make DPSK a potential modulation format for future high speed and long distance systems.

6.1.2.1 Optical heterodyne DPSK coherent detection system model

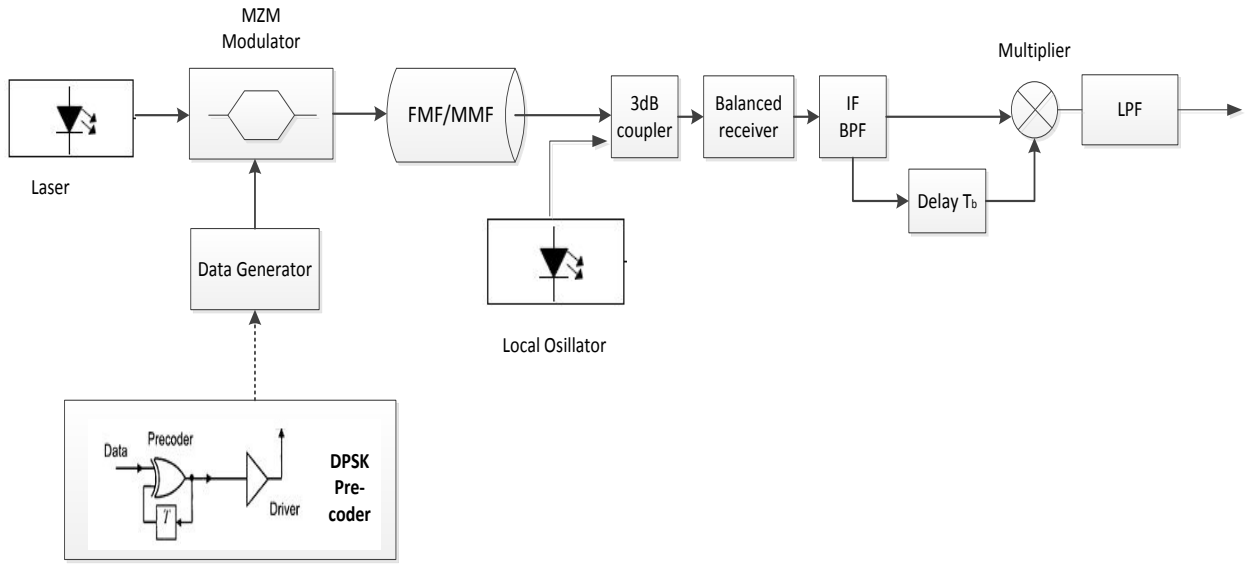

Figure 6.1 Schematic of the optical heterodyne DPSK with the delay and multiply receiver, BPF and LPF represent the bandpass filter and lowpass filter, respectively.

The input binary signal data needs to be electrically pre-coded by using logical gate XOR and then passed through the MZM phase modulator. The operation of XOR (exclusive OR) is described by: $P_k = NOT(b_k)\, XOR\, P_{k-1}$ (6.3)

The k_{th} bit of the pre-code data P_k is generated by XOR the k_{th} bit of the original data sequence b_k and the previous pre-code bit P_{k-1}. The previous pre-coded bit is produced by delay one bit period of the output of XOR gate, which is shown below,

(Assuming that the initial pre-coded data will be set to 0)

i.e. Input pseudorandom binary sequence : 1110101000100111000

The electrical pre-coded data becomes: 0 0001100101101111010

In this simulation a lithium niobate crystal modulator (chirp free single electrode MZM modulator) that generates a phase shift of (0, π) is employed. The MZM phase modulator has a transfer function which is given by:

$$\mathrm{H}_{MZM} = \cos\left(\frac{\text{pre}-\text{coded data}\times\pi}{V_\pi}\right) \qquad (6.4)$$

where V_π is the voltage needed to cause a phase shift of π, which is set to 1 for simplicity. When the value of the pre-coded data is "1", the output of MZM is "-1" (as cos(π)= -1), which indicates a phase shift of π. In contrast, when the value of the pre-coded data is "0", the output of MZM becomes "1" (as cos(0) =1), which corresponds to a zero phase shift.

The baseband signal at the input of FMF can be expressed as:

$$x(t) = \sum_n I_n\, p(t - nMT_b) \qquad (6.5)$$

The symbol sequence is represented by $I_n = \left\{e^{j0}, e^{j\pi}\right\} = \{1, -1\}$ in the DPSK system, where T_b is the bit duration, MT_b is the symbol period, and M is the number of bits

per symbol. In the NRZ format signal, the optical pulse occupies the entire symbol duration, and *P(t)* is written as:

$$p(t)_{NRZ} = \sqrt{\frac{E_b}{T_b}} \qquad (6.6)$$

where E_b refers to the energy per bit.

The two mode FMF contains LP01 and LP11 guided modes, and the modal impulse response is described as the superposition of the impulse response on each excited mode. In a long distance transmission system, the chromatic dispersion, intermodal dispersion, and attenuation effect need to be taken into account, but the nonlinear effect and polarization mode dispersion are all neglected. Therefore, the transfer function or frequency response of this FMF channel can be defined by modifying the Equation 5.16, giving:

$$H_{FMF}(f) = \sum_{l,n}^{LP01,LP11} \eta_{l,n} \exp(-2\pi f \tau_{l,n} L) \cdot 10^{-\alpha_{l,n} L/10} \cdot \exp\left[i \frac{\pi D_{l,n} \lambda^2 f^2 L}{c} \right] \qquad (6.7)$$

where $\eta_{l,n}$ is the power coupling coefficient, $\alpha_{l,n}$ is the attenuation for different modes, $\tau_{l,n}$ is the group delay per unit length (/1km), D is the chromatic dispersion coefficient, and L is the FMF length. It should be noted that the signal at the input of FMF is transformed to the frequency domain by Fourier transform in order to multiply the transfer function. In other words, the transmitted signal passing through the FMF channel is implemented in the frequency domain.

The typical optical heterodyne DPSK receiver contains a local oscillator (LO) and a 3dB coupler is connected to a balanced receiver. The output photocurrent is then sent to a delay loop and is typically delayed by one symbol period. Finally, the upper and lower branches are multiplied together at the multiplier. The multiplied current is used

to extract the phase difference between the two neighbouring bits, and the detected phase information is then converted to detector signals. In practice, a bandpass filter and a lowpass filter will be employed in the system, and the bandpass filter only allows the intermediate frequency (IF) components to be passed and attenuates all other parts of the received signal. The wideband bandpass filter is exploited and followed by "integrate and dump" detection in our system model. The detection of DPSK data is carried out by comparing the phase of the multiplied output signal $[I(t)\cdot I(t-1)]$ with the phase of $[0,\pi]$; a binary 1 is detected if the phase is π, and a binary 0 is generated when the phase changes to 0.

The mathematical derivation of optical heterodyne DPSK with the integrate and dump detection is shown below.

The received field is defined as: $E_r(t) = A_s(t)\exp[j(\phi_s(t)+\omega_c t)]$ (6.8)

where ω_c is the carrier frequency of the optical signal, A is the amplitude, and $A_s(t)\exp[j\phi_s(t)]$ is the low-pass representation of the signal, $A_s(t)\exp[j\phi_s(t)] = \pm A_s$ for DPSK signal.

It is assumed that the polarization of the received field is perfectly matched with the local oscillator signal, and similarly, the LO signal field is given by:

$$E_{LO}(t) = A_{LO}(t)\exp[j(\phi_{LO}(t)+\omega_{LO}t)] \quad (6.9)$$

Both the LO signal and incoming signal will pass through a 3dB coupler, which has the following relationship between input and output :

$$S = \frac{1}{\sqrt{2}}\begin{bmatrix} 1 & 1 \\ 1 & -1 \end{bmatrix} \quad (6.10)$$

Figure 6.2 shows the 3dB coupler.

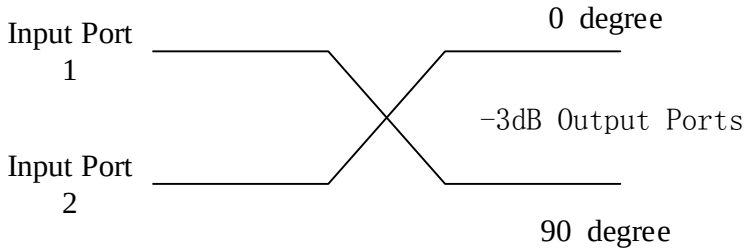

Figure 6.2 Schematic of the 3dB coupler

As $I \infty R|E|^2$, the detected currents at the upper arm of the balanced receiver and lower arm of the balanced receiver are defined as:

$$i_+(t) = \frac{R}{2}\left|E_r(t) + E_{LO}(t)\right|^2 + i_{n1} \tag{6.11}$$

$$i_-(t) = \frac{R}{2}\left|E_r(t) - E_{LO}(t)\right|^2 + i_{n2} \tag{6.12}$$

Therefore, the output of the balanced receiver is given as:

$$I(t) = i_+(t) - i_-(t) = 2R \cdot real[E_r(t) \cdot E^*_{LO}(t)] + i_n$$

(where * is the complex conjugate operator) (6.13)

The amplitudes of LO and the incoming signal can be represented in terms of the average power, as $A_s \cong \sqrt{P_s}$ and $A_{LO} \cong \sqrt{P_{LO}}$, respectively, where P_{LO} and P_s are the average LO power and average incoming optical signal power, respectively. Substituting Equations 6.8 and 6.9 into 6.13 gives:

$$I(t) = 2RA_{LO}A_s \cos[\omega_{IF}t + \phi_s - \phi_{LO}] + i_n \tag{6.14}$$

where $\omega_{IF} = \omega_c - \omega_{LO}$ is the intermediate frequency and noise i_n can be regarded as a narrow bandwidth receiver noise; the quadrature noise form is written as:

$$n_x(t)\cos\omega_{IF}t + n_y(t)\sin\omega_{IF}t \tag{6.15}$$

where n_x n_y are the Gaussian noise with zero mean and standard derivation of σ_n. The additive noise at the receiver can be modelled as a two-sided power spectrum

density $\frac{N_o}{2}$ Gaussian noise. If random phase noise ϕ_N is caused by LO and transmitter lasers, Equation 6.14 may be rewritten as:

$$I(t) = 2RA_{LO}A_s \cos[\omega_{IF}t + \phi_s - \phi_{LO} + \phi_N] + i_n \qquad (6.16)$$

For simplicity, the various noise terms are removed when deriving the mathematical expression of detected signal. After detection by the balanced receiver the detected current *I(t)* will pass to a delay and multiplier circuit:

$$I(t) = 2RA_{LO}A_s \cos[\omega_{IF}t + \phi_s - \phi_{LO}] \qquad (6.17)$$

The phase in the LO remains at a constant value; thus, the useful information is the phase difference between ϕ_s and ϕ_{s-1}, and the phase term ϕ_{LO} can be neglected.

After the first two bits have been successfully received, for a proper demodulation, the IF carrier frequency must be an integer multiple of the symbol frequency (i.e. $\omega_{IF} = \frac{2\pi k}{T}$, where *k* is a positive integer); in other words, the phase term will be varied by an integer multiple of 2π. If the first input signal and delayed or reference signal have the same phase "0", then:

$$\begin{aligned} &I_1(t) = 2RA_{LO}A_S \cos\left[\omega_{IF}t + \phi_s\right] = 2RA_{LO}A_S \cos\omega_{IF}t \\ &I_{delay}(t) = 2RA_{LO}A_S \cos\left[\omega_{IF}t + \phi_{delay}\right] = 2RA_{LO}A_S \cos\omega_{IF}t \\ &when\ \ both\ \ \phi_s = \phi_{delay} = 0 \end{aligned} \qquad (6.18)$$

After the multiplier and integrator , the output becomes:

$$S_1 = \int_0^T 4R^2A^2{}_{lo}A^2{}_s \cos^2(\omega_{IF}t)\, dt = 2R^2A^2{}_{lo}A^2{}_s \qquad (6.19)$$

Hence, the decision bit "0" is recovered. For the next bit interval "*T*", the new input signal now changes to:

$$I_2(t) = 2RA_{LO}A_S \cos\left[\omega_{IF}t + \phi_2\right] = -2RA_{LO}A_S \cos\omega_{IF}t, \ \ when\ \ \phi_2 = \pi \qquad (6.20)$$

The previous signal $I_1(t)$ becomes a delayed signal, and the output is thus:

$$S_2 = \int_0^T I_2(t) \cdot I_1(t) = -\int_0^T 4R^2 A^2{}_{lo} A^2{}_s \cos^2(\omega_{IF} t)\, dt = -2R^2 A^2{}_{lo} A^2{}_s \qquad (6.21)$$

A decision "1" is recovered (phase difference $\Delta\phi = \pi$) as a negative output has been detected. Continuing this process, all the detected sequences can be obtained. For a balanced detection optical DPSK system, the BER is defined as [157]:

$$BER = \frac{1}{2}\exp\left(-\frac{E_b}{2\sigma^2}\right) \qquad (6.22)$$

where E_b is the energy per bit, and σ is the zero mean Gaussian distributed noise variance. Due to its ability to greatly reduce the computation time when counting the bit error rate, the Q factor BER estimation method is utilized. However, in a DPSK system, the direct use of the conventional Q factor used in OOK is no longer reliable because of the non-Gaussian nature of the noise distribution in the output signal of the balanced receiver. However, it is helpful to evaluate Q in the signal phase domain when phase noise is included. Much research has acknowledged this problem and proposed an alternative differential phase Q factor [170-173]. The differential phase denotes the phase difference between two sampling points separated by the bit period in the range of $[-\frac{\pi}{2}\ \frac{3\pi}{2}]$. The Gaussian noise at the centre of each bit with a differential phase Q factor is defined as [173]:

$$Q_{\Delta\phi} = \frac{0.87\pi}{\sigma_{\Delta\phi,0} + \sigma_{\Delta\phi,\pi}} \qquad (6.23)$$

$$BER = erfc(\frac{Q_{\Delta\phi}}{\sqrt{2}}) \qquad (6.24)$$

6.1.2.2 Optical intradyne DPSK coherent detection system model

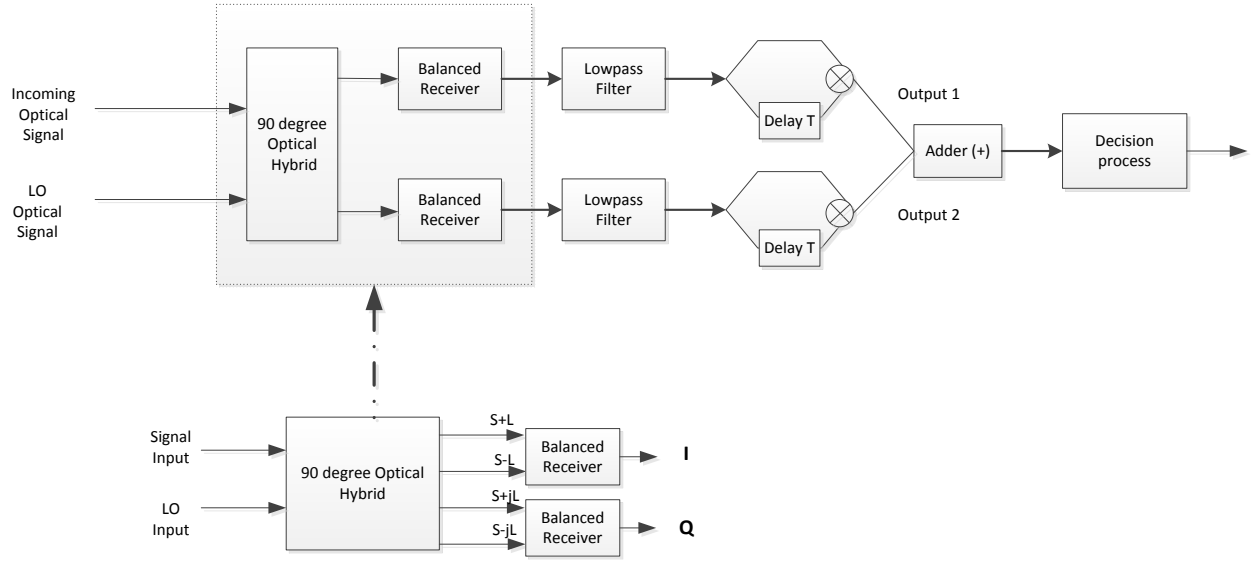

Figure 6.3 Schematic of the optical intradyne DPSK phase diversity receiver

In this system, a 90 degree hybrid is used, resulting in two ports after photodetection. These two received electrical signals are filtered by lowpass filters before being passed through a delay and multiply circuit. The two arms signals are then demodulated to the baseband and finally combined together, as shown in Figure 6.3. The 90 degree optical hybrid is shown in Figure 6.4 and its transfer function is given as:

$$S = \frac{1}{2}\begin{bmatrix} 1 & 1 \\ 1 & j \\ 1 & -1 \\ 1 & -j \end{bmatrix} \qquad (6.25)$$

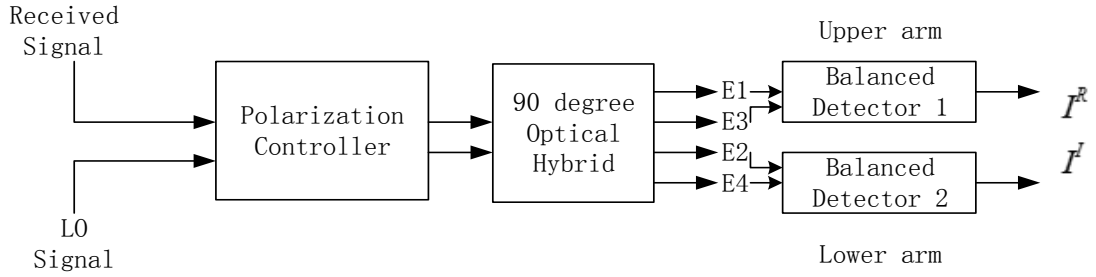

Figure 6.4 Schematic of the 90^0 optical hybrid

E_s , E_{LO} are the electrical field of received signal and LO signal, respectively. By using the balanced receiver at both the real and imaginary parts, the signals at the four output ports are written as:

$$\begin{bmatrix} E1 \\ E2 \\ E3 \\ E4 \end{bmatrix} = \begin{bmatrix} E_s \\ E_{LO} \end{bmatrix} \cdot S = \frac{1}{2} \begin{bmatrix} E_s + E_{LO} \\ E_s + jE_{LO} \\ E_s - E_{LO} \\ E_s - jE_{LO} \end{bmatrix} \qquad (6.26)$$

where E1 and E3 denote the signals detected by the upper arm of balanced receiver, and E2 and E4 are the signals detected by the lower arm of the balanced receiver. As the current is proportional to power, $I \propto R \cdot |E|^2$, thus, for the upper arm case, the output current is given by:

$$I^R = I^R{}_+ - I^R{}_- = R \cdot \left[|E1|^2 - |E3|^2 \right] = R \cdot \left| E_s \cdot E^*{}_{LO} \right| \qquad (6.27)$$

and

$$\begin{aligned} E_s &= A_s \cdot \exp[\, j \cdot (\phi_s + \omega_s t + \Phi_d + \phi_{sNoise})] \\ E_{Lo} &= A_{LO} \cdot \exp[\, j \cdot (\phi_{LO} + \omega_{lo} t + \phi_{loNoise})] \end{aligned} \qquad (6.28)$$

where ϕ_{sNoise} and $\phi_{loNoise}$ are the phase noise in the LO and transmitter laser, respectively, ϕ_s and ϕ_{LO} are the initial phase of the optical incoming signal and LO signal, respectively, and Φ_d is the modulation phase π *or* 0 in DPSK.

$$\begin{aligned} &I^R = R \cdot \left| A_{LO} \cdot A_s \cdot \exp[\, j \cdot (\omega_s t - \omega_{lo} t + \phi_s - \phi_{LO} + \phi_{sNoise} - \phi_{loNoise} + \Phi_d)] \right| \\ &\textit{as } \omega_s - \omega_{lo} = 0, \ \textit{thus} \\ &I^R = R \cdot \left| A_{LO} \cdot A_s \cdot \exp[\, j \cdot (\phi_s - \phi_{LO} + \phi_{sNoise} - \phi_{loNoise} + \Phi_d)] \right| \end{aligned} \qquad (6.29)$$

If $\Delta = \phi_s - \phi_{LO} + \phi_{sNoise} - \phi_{loNoise}$, ,

$$I^R = R \cdot A_{LO} \cdot A_s \cdot \cos(\Delta + \Phi_d) \qquad (6.30)$$

Similarly, the current in the lower arm case is given as:

$$I^I = R \cdot A_{LO} \cdot A_s \cdot \sin(\Delta + \Phi_d) \qquad (6.31)$$

Both the currents will pass through a delay and multiply circuit, thus:

$$I^R = I^R(t)\cdot I^R(t-1) = R^2\cdot A^2{}_{LO}\cdot A^2{}_s\cdot\cos(\Delta+\Phi_d)\cdot\cos(\Delta_{t-1}+\Phi_{d_{t-1}})$$
$$I^I = I^I(t)\cdot I^I(t-1) = R^2\cdot A^2{}_{LO}\cdot A^2{}_s\cdot\sin(\Delta+\Phi_d)\cdot\sin(\Delta_{t-1}+\Phi_{d_{t-1}}) \quad (6.32)$$

It is assumed that the frequency drift and phase noise change slowly compared to the signal bit rate; thus, $\Delta \cong \Delta_{t-1}$ and:

$$I^R = I^R(t)\cdot I^R(t-1) = R^2\cdot A^2{}_{LO}\cdot A^2{}_s\cdot\cos(\Delta+\Phi_d)\cdot\cos(\Delta+\Phi_{d_{t-1}})$$
$$I^I = I^I(t)\cdot I^I(t-1) = R^2\cdot A^2{}_{LO}\cdot A^2{}_s\cdot\sin(\Delta+\Phi_d)\cdot\sin(\Delta+\Phi_{d_{t-1}}) \quad (6.33)$$

In a DPSK system the relationship of the modulation phase between two neighboring bits is either 0 or π, and it is given below:

$$\Phi_{d_{t-1}} = \begin{bmatrix} \Phi_d+\pi \\ or \\ \Phi_d+0 \end{bmatrix} \quad (6.34)$$

Substituting Equation 6.34 into Equation 6.33, the current at the upper arm simplifies to:

$$I^R = R^2\cdot A^2{}_{LO}\cdot A^2{}_s\cdot\cos(\theta)\cdot\cos(\theta+0) = R^2\cdot A^2{}_{LO}\cdot A^2{}_s\cdot\cos^2(\theta) \quad for\ "0"\ phase\ change$$
$$I^R = R^2\cdot A^2{}_{LO}\cdot A^2{}_s\cdot\cos(\theta)\cdot\cos(\theta+\pi) = -R^2\cdot A^2{}_{LO}\cdot A^2{}_s\cdot\cos^2(\theta) \quad for\ "\pi"\ phase\ change$$
where $\theta = \Delta+\Phi_d$. (6.35)

At the lower arm, the current is given by:

$$I^I = R^2\cdot A^2{}_{LO}\cdot A^2{}_s\cdot\sin(\theta)\cdot\sin(\theta+0) = R^2\cdot A^2{}_{LO}\cdot A^2{}_s\cdot\sin^2(\theta) \quad for\ "0"\ phase\ change$$
$$I^I = R^2\cdot A^2{}_{LO}\cdot A^2{}_s\cdot\sin(\theta)\cdot\sin(\theta+\pi) = -R^2\cdot A^2{}_{LO}\cdot A^2{}_s\cdot\sin^2(\theta) \quad for\ "\pi"\ phase\ change$$
(6.36)

Subsequently, combining the signals in both arms yields the final expression:

$$I = I^R + I^I = \begin{bmatrix} R^2\cdot A^2{}_{LO}\cdot A^2{}_s + Noise & for\ phase\ change\ "0" \\ -R^2\cdot A^2{}_{LO}\cdot A^2{}_s + Noise & for\ phase\ change\ "\pi" \end{bmatrix} \quad (6.37)$$

The decision variables in the phase diversity DPSK receiver are $\pm R^2\cdot A^2{}_{LO}\cdot A^2{}_s$ when $\Phi_d - \Phi_{d_{t-1}} = 0,\ \pi$. Therefore, the DPSK phase diversity receiver has the same performance as the DPSK heterodyne receiver.

6.2 Simulation of coherent optical DPSK MIMO in few mode fibre

A complete analytical model of a coherent 2x2 optical MIMO system over FMF with radial offset launching and an annular detector was built. With this model, we transmitted 2x10Gb/s NRZ-DPSK signals over two mode graded index FMF. The two mode GI-FMF (LP01, LP11a and LP11b are two degenerated forms of the LP11 mode) is adopted in the following simulation with the specifications shown in Table 6.1 [174, 175].

Core diameter (μm)	12
GI-FMF index profile	2
Numerical aperture (NA)	0.17
Cladding diameter	125 ± 0.7
Refractive index difference (Δ)	0.37 %
Attenuation all modes (dB/km)	0.2
Chromatic dispersion (ps/km/nm)	LP01=19.9; LP11=20
DMD (ps/km)	0.2

Table 6.1 Parameters of the graded index two mode FMF used in the simulation at a wavelength of 1550nm, DMD is defined as $1/V_{g_{11}} - 1/V_{g_{01}}$, where $V_{g_{11}}$ and $V_{g_{01}}$ are the group velocities of the LP_{11} and LP_{01} modes, respectively, and the two mode GI- FMF normalized frequency is in the region of $2.5 \le V < 4.5$ [174].

In this 2x2 coherent optical MIMO system, modal dispersion, chromatic dispersion, mode dependent loss and intra-group mode mixing are all considered. We assume that all modes have the same attenuation and the nonlinear effects are neglected. In addition, we further assume that the laser linewidth is not considered. The channel matrix of such a system is given in Equation 6.7, while the relationship between the two input signals and two output signals is illustrated in Figure 6.5.

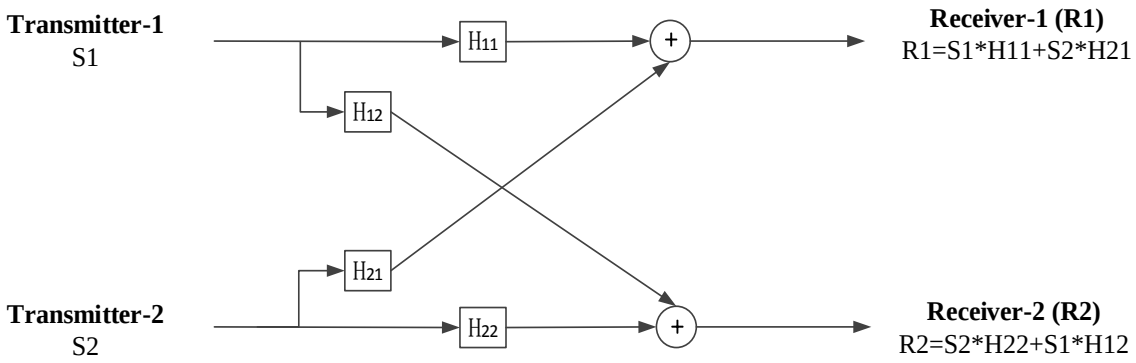

Figure 6.5 The 2x2 optical MIMO signal transmission in a two mode GI-FMF, S1 and S2 are the two input signals, R1 and R2 are the two received signals.

In Figure 6.5, each receiver will receive all the signals from both transmitters. The different annular receivers can be determined by an inner radius and outer radius. Figure 6.6 shows a schematic of the simulation procedures used to simulate the coherent optical MIMO model. In the simulation, the MIMO channel matrix H is estimated by initially sending two individual training sequences and evaluated the in frequency domain. After obtaining the estimated channel matrix $\tilde{H}$, a simple zero forcing technique in the frequency domain is used in MIMO signal processing. This step is necessary to compensate all linear impairments that result from the mutual effects of the propagation modes.

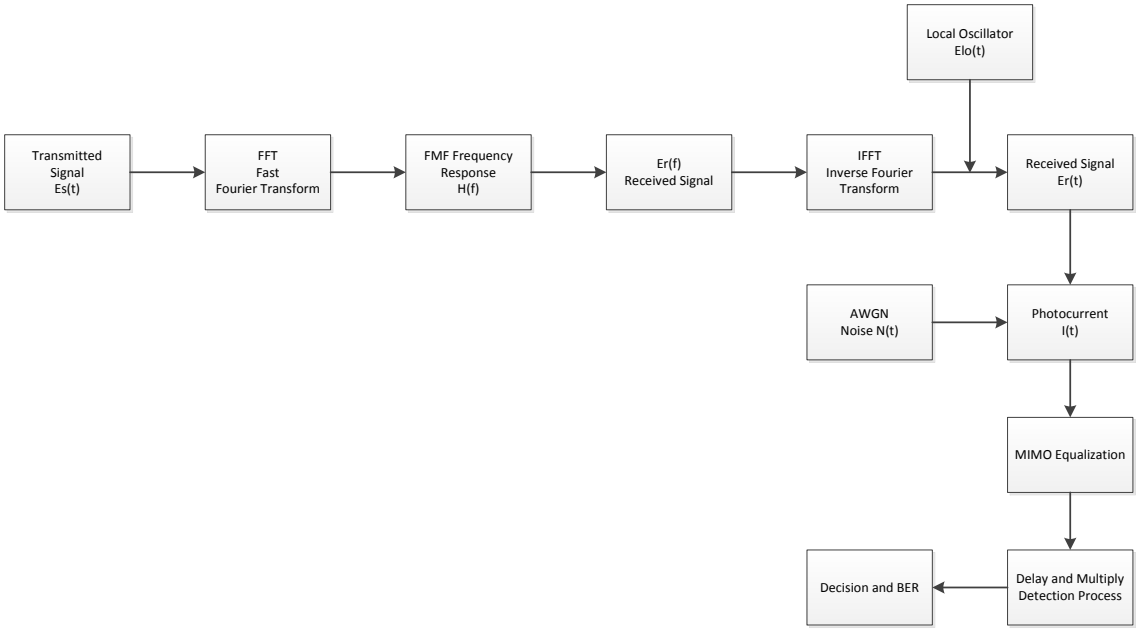

Figure 6.6 The simulation procedures of a coherent optical MIMO in a two mode GI-FMF system

For a coherent MIMO system, full signal information can be detected, including the amplitude and phase. Therefore, the optimization of transceiver design should consider the DMD effect caused by modal dispersion and the power coupling coefficient. In order to keep sufficient diversity of the two transmitted signals, we select a radial offset value of 4μm; hence, the launching conditions are 0 and 4μm. In the two mode FMF the radial offset launching will excite all modes, which results in a modal dispersion and causes ISI. To minimise this effect, we can make the difference in power coupling coefficient between these two modes as large as possible. The principle behind this strategy is that the multimode fibre channel frequency response relies on the LP mode power coupling coefficient, as shown in Equation 2.64; meanwhile, the channel diversity gain may also be affected by the DMD and power coupling coefficient. Thus, both the amplitude part and the phase part of the channel frequency response will affect the optimization. The following Tables 6.2-6.3 show the variation in the calculated power coupling coefficients with different laser spot

sizes under the two launching conditions.

Laser spot size (μm)	Normalized power coupling coefficient LP01 mode	Normalized power coupling coefficient LP11 mode
1	0.3951	0
2	0.8892	0
3	0.9964	0
4	0.8812	0

Table 6.2 Power coupling coefficients for LP01 and LP11 modes with various laser spot sizes when offset value =0 μm

Laser spot size (μm)	Normalized power coupling coefficient LP01 mode	Normalized power coupling coefficient LP11 mode
1	0.0664	0.2110
2	0.2340	0.4160
3	0.3883	0.3439
4	0.4557	0.2024

Table 6.3 Power coupling coefficients for LP01 and LP11 modes with various laser spot sizes when offset value =4 μm

It is very noticeable that the laser spot size of 1μm will produce the largest power coupling coefficient difference under the radial offset launching condition. In practice, optic lenses can be employed to launch this small laser spot onto the FMF. The annular multi-segment detectors can be characterised by a radius R_{de}; hence, the two annular detectors can be designed by carefully optimizing R_{de} (receiver one= $0-R_{de}$, receiver two = $R_{de}-6\mu m$). The subsequent optical heterodyne DPSK MIMO simulations evaluate the R_{de} and the optimized value can be analysed by comparing the estimated BER with different values of R_{de}.

6.2.1 Optical heterodyne DPSK MIMO system

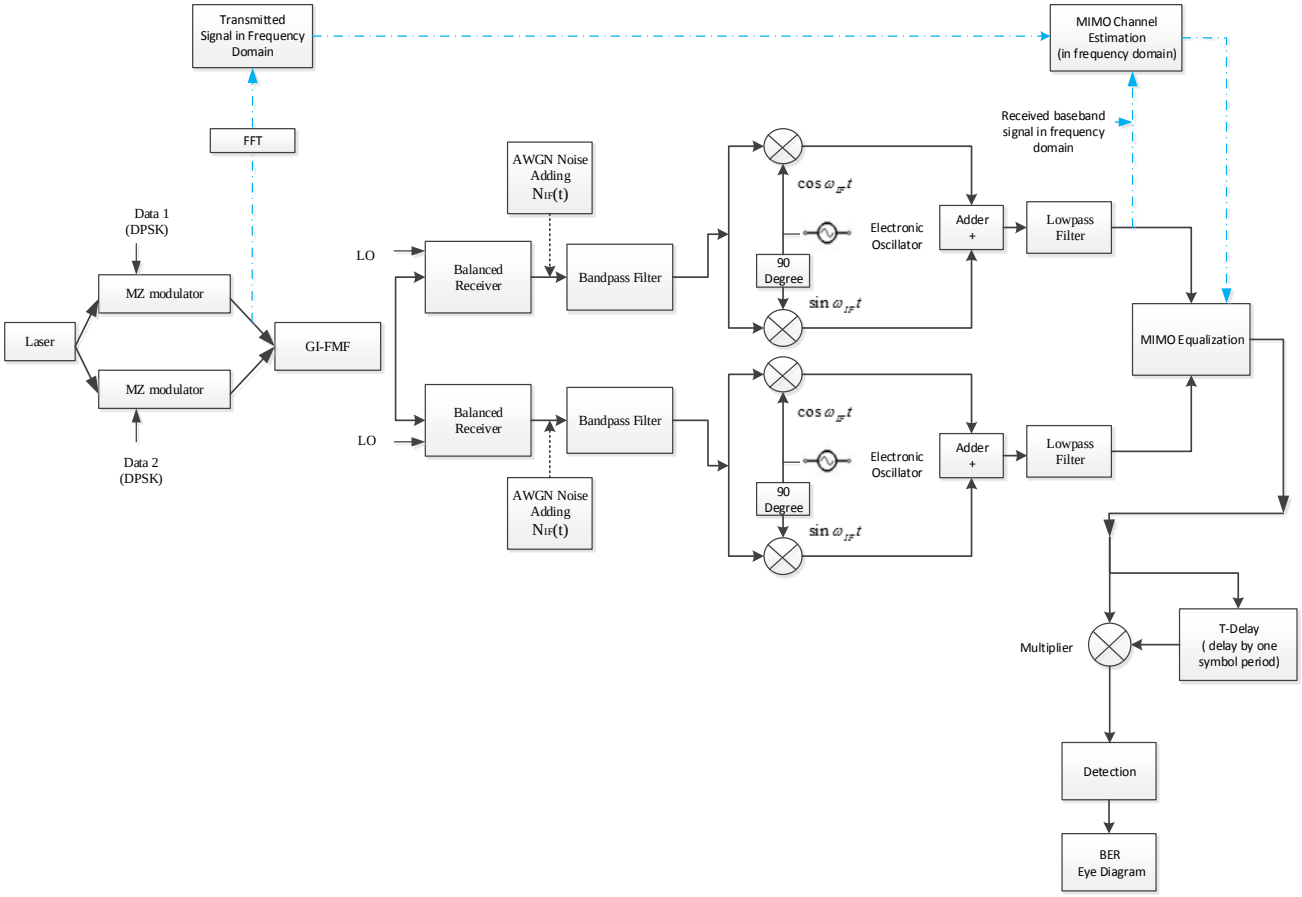

Figure 6.7 Optical DPSK heterodyne MIMO with delay and multiply detection in a two mode GI-FMF, the blue dotted line represents the MIMO equalization process.

Figure 6.7 illustrates the simulation of the 10Gb/s 2x2 coherent optical DPSK heterodyne MIMO system in a two mode GI-FMF. The single mode CW laser (1550nm) is split into two arms and modulated by two Mach-Zehnder modulators. The modulators are driven with two pseudorandom bit sequences with lengths of $2^{23}-1$and 32 samples per bit. The data rate is set to 10Gb/s, producing a total data rate of 20Gb/s, and the input signal power at the two arms remains equal. We assume that there is no correlation between these two data streams. Two small Gaussian laser spots (1μm) are launched into GI-FMF with $0\mu m$ and $4\mu m$ radial offset from the

fibre axis and selected to assign the two signals to different LP modes. Therefore, two channels are created, one containing the LP01 mode, and the other consisting of the LP11 and LP01 modes. Noise in this system is modelled as a Gaussian noise and added to balanced receivers, as given in Equation 6.15. Since the IF signal is detected in heterodyne systems, it is necessary to convert the IF band signal to a baseband signal to proceed with the MIMO channel estimation by comparing the baseband signal in frequency domain at both the transmitter and receiver. For this reason, another electrical oscillator followed by a lowpass filter is utilized to down-convert the IF signal to a baseband signal. As noise effects significantly impact channel estimation, we neglect them during the channel estimation process. Subsequently, all signals will be recovered by MIMO equalization (zero forcing method), at which point they are ready for the decision process. Table 6.4 shows the system parameters used in the simulation.

Bit rate	10 Gb/s
Averaged input optical power	1e-3 W
Modulation format	DPSK
CW laser wavelength	1550nm
PBRS sequence length	$2^{23}-1$
FMF fibre length	5 km
Sampling rate	320 GHz
IF value	3*bit rate
Filter type (LPF, and BPF)	Ideal filters
Channel estimation	Ideal channel estimation without noise

Table 6.4 The optical heterodyne DPSK MIMO system simulation parameters

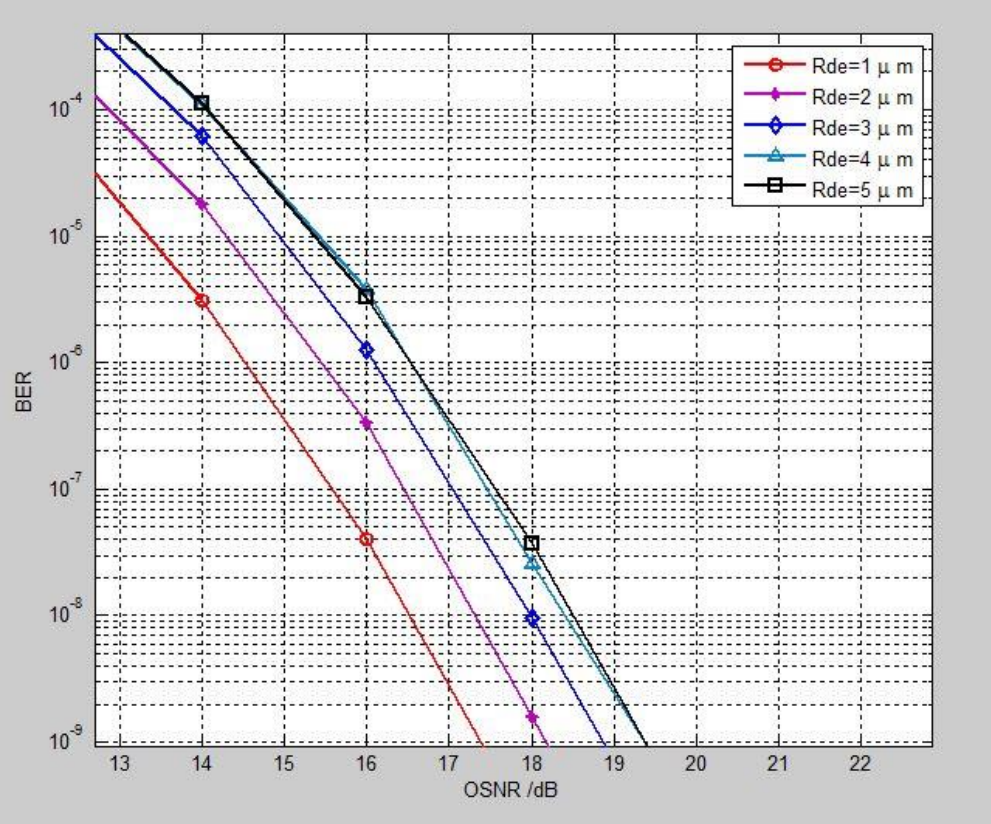

Figure 6.8 BER of receiver one of the 2x2 optical heterodyne DPSK MIMO system with an FMF length of 5km, launching conditions of 0 and 4μm, data rate of 10Gb/s, and spot size of 1μm.

Figure 6.8 shows the estimated BER as a function of OSNR when the different R_{de} is chosen. The OSNR of receiver one (Rx1) at BER=10^{-9} increases with detector radius R_{de}; an OSNR penalty of approximately 1dB is incurred when R_{de} increases by 1μm. In contrast, for receiver two (Rx2), OSNR decreases with increasing R_{de} at BER= 10^{-9}, and the difference in OSNR (5dB) between R_{de}=1 and 5μm is more than twice as large as that of receiver one. This indicates that receiver two is more sensitive to the annular receiver radius. The results for receiver two are shown in Figure 6.9.

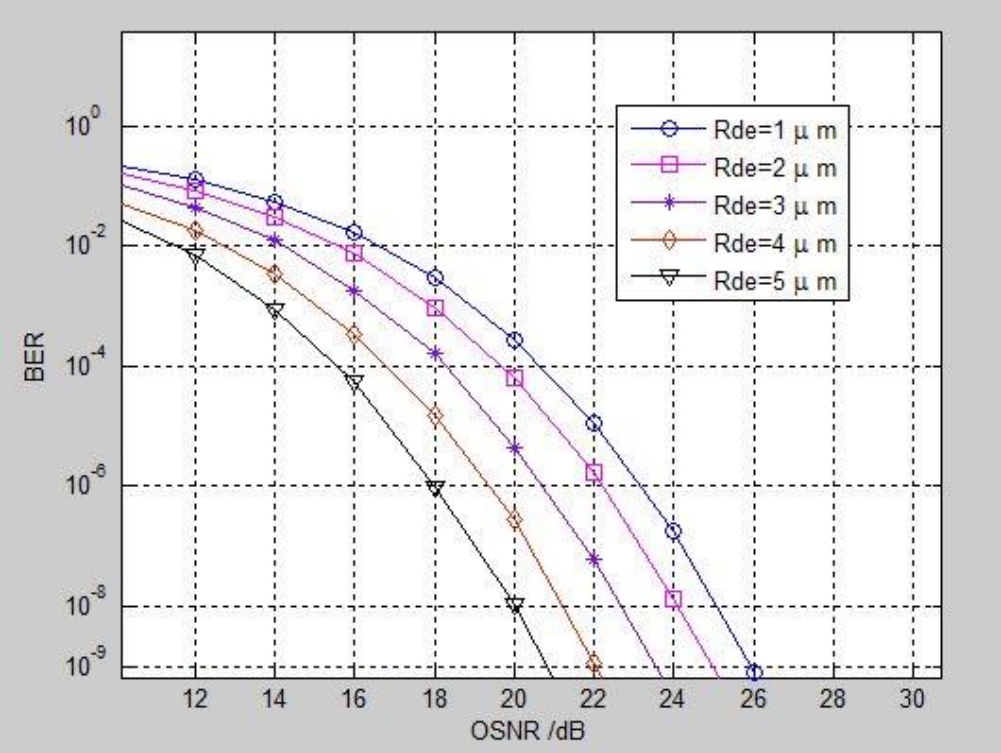

Figure 6.9 BER of receiver two of the 2x2 optical heterodyne DPSK MIMO system with an FMF length of 5km, launching conditions of 0 and 4μm, data rate of 10Gb/s, and spot size of 1μm.

The desired optical MIMO system has a system configuration that can achieve the same performance at all receivers. Moreover, from previous studies on mode division multiplexing we know that mode mixing and DMD are the two key factors that increase the complexity of optical MIMO signal processing. Hence, a compromise must be made when selecting the R_{de} of both receivers. The optimization of receiver two is considered as a priority; therefore, R_{de} =5μm is chosen as the optimized choice when using radial offset launchings of 0 and 4μm. In order to verify this system, a comparison between the estimated channel matrix and actual channel matrix is needed. If the estimated channel matrix and actual channel matrix have a high degree of similarity, therefore it will provide reliable results of the simulated model. Such a comparison can be made by sending only one training sequence to the SISO GI-FMF

system (with a 4μm radial offset launching and a 1μm laser spot size). The results are shown in Figure 6.10.

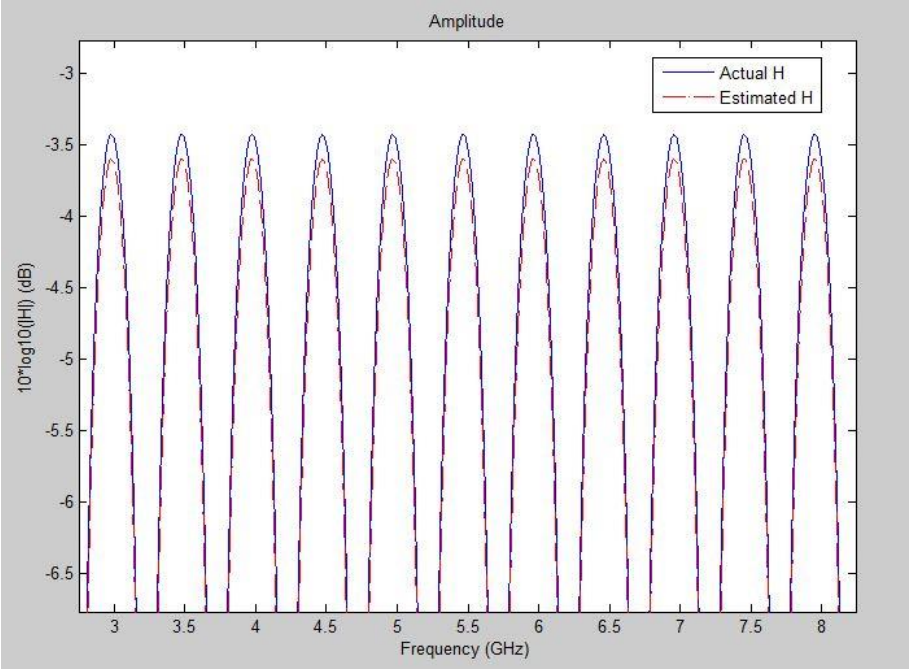

(a)

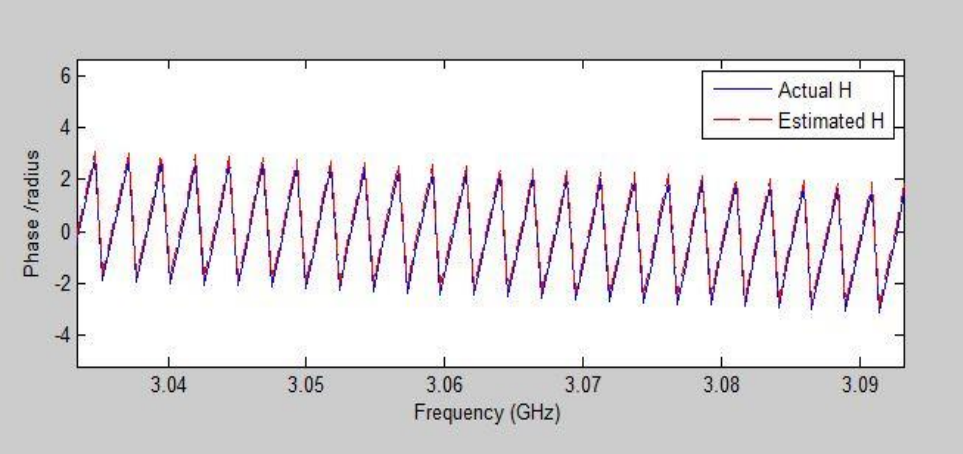

(b)

Figure 6.10 Comparison of the estimated SISO GI-FMF channel matrix and the actual SISO GI-FMF channel matrix when noise is not included: (a) the amplitude of *H* and (b) the phase of *H*.

The results show a good agreement between the estimated channel matrix and the

actual channel matrix. This proves the accuracy of our channel estimation along with the system model itself. Furthermore, comparing the transmitted and received data is another way to verify the system model. Thus, a 10Gb/s 2x2 MIMO system with an optimized transceiver design (radial offset=0 and 4μm, R_{de}=5μm) is simulated, and the results are given in Figure 6.11.

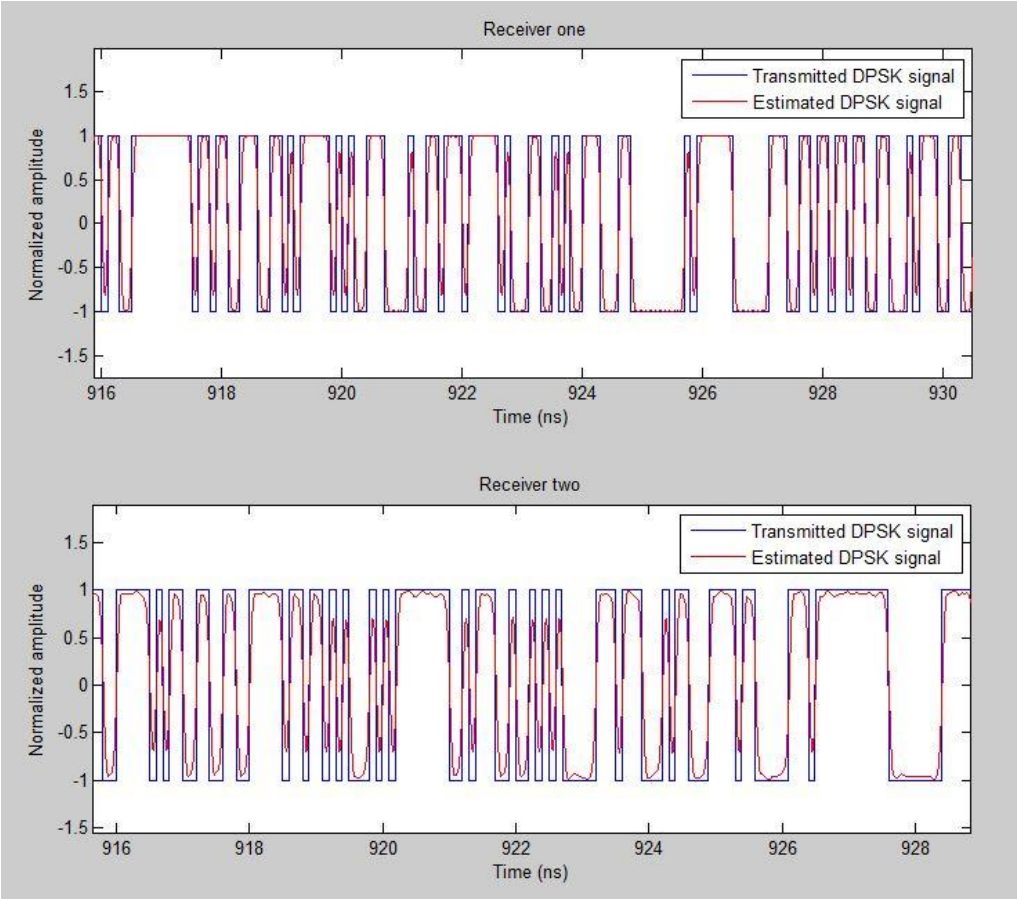

Figure 6.11 Transmitted and recovered waveforms for the 10Gb/s 2x2 coherent optical MIMO system without noise

Figure 6.11 shows the transmitted and recovered waveforms. The recovered waveform coincides with the transmitted waveform, further confirming the stability and accuracy of our simulated system model. Following the successful verification of this system model, we can now evaluate the overall system performance with various

system parameters. Figure 6.12 refers to the estimated BER by using the optimized system configurations.

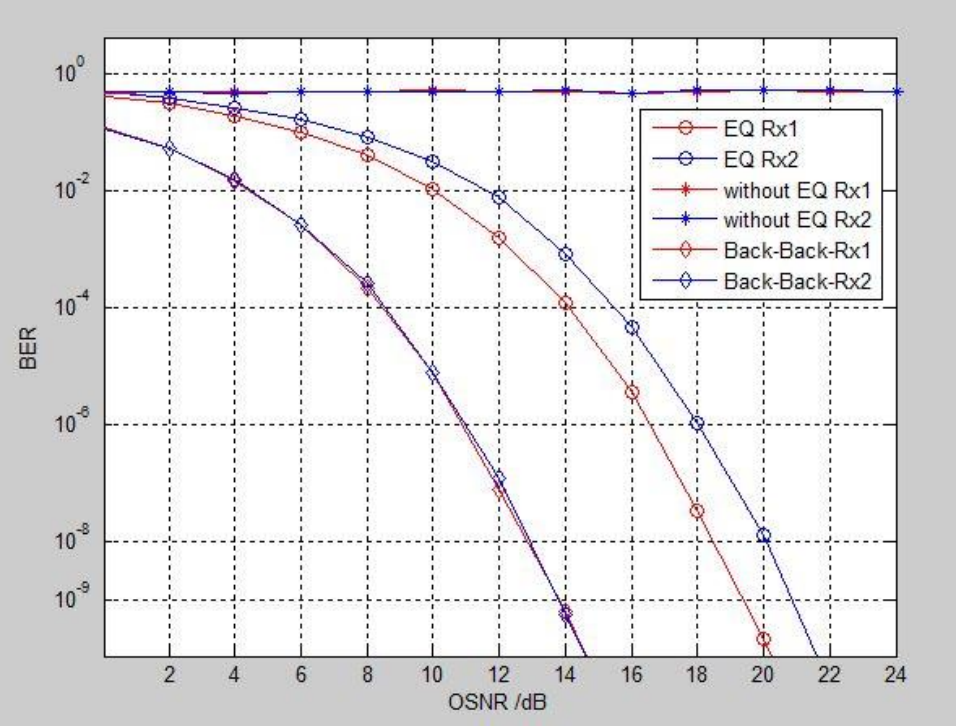

Figure 6.12 The 2x2 optical heterodyne DPSK MIMO system BER with an FMF length of 5km. The launching conditions are 0 and 4μm. At the receiver multi-segment annular detectors are used with R_{de}=5μm. Symbol EQ stands for the MIMO equalization, and the data rate is 10Gb/s.

In centre launching the fundamental mode LP01 is excited so that there is no modal dispersion in the channel. Hence, receiver one gives a good result, as shown in Figure 6.12. It can be seen that the difference in OSNR between the two receivers at BER= 10^{-9} is distinct and corresponds to an OSNR penalty of nearly 1.5dB. This is explained by the occurrence of modal dispersion in channel 2, which gives rise to a degradation of the receiver performance. Moreover, the difference may also be attributed to the higher chromatic dispersion caused by the higher order mode (LP11) compared to the fundamental mode (LP01) in channel 1. Comparing with the back-to-back result, the OSNR penalties are 5.2 and 6.7dB for receivers one and two,

respectively. An example of the BER sensitivity to OSNR is shown in Figure 6.13, which presents an eye diagram of the real value of the recovered DPSK signal after MIMO equalization at both receivers. The eye diagram is generated over two symbol time intervals (with 32 samples per symbol) and repeated 100 times. The results indicate that eye-closure degradation is observed at smaller OSNR.

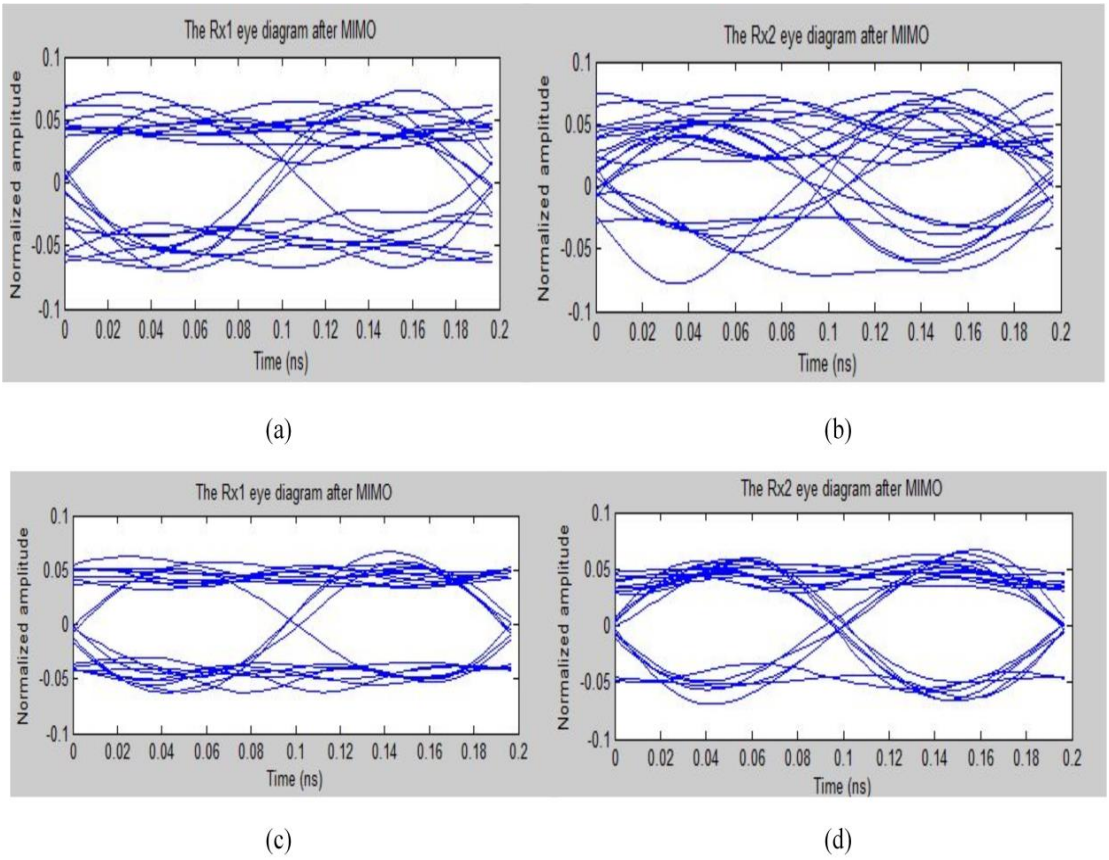

Figure 6.13 Eye diagrams at different receivers with OSNR=14dB and 20dB, FMF length=5km, and data rate=10Gb/s: (a) receiver one with OSNR=14dB, (b) receiver two with OSNR=14dB, (c) receiver one with OSNR=20dB, (d) receiver two with OSNR=20dB.

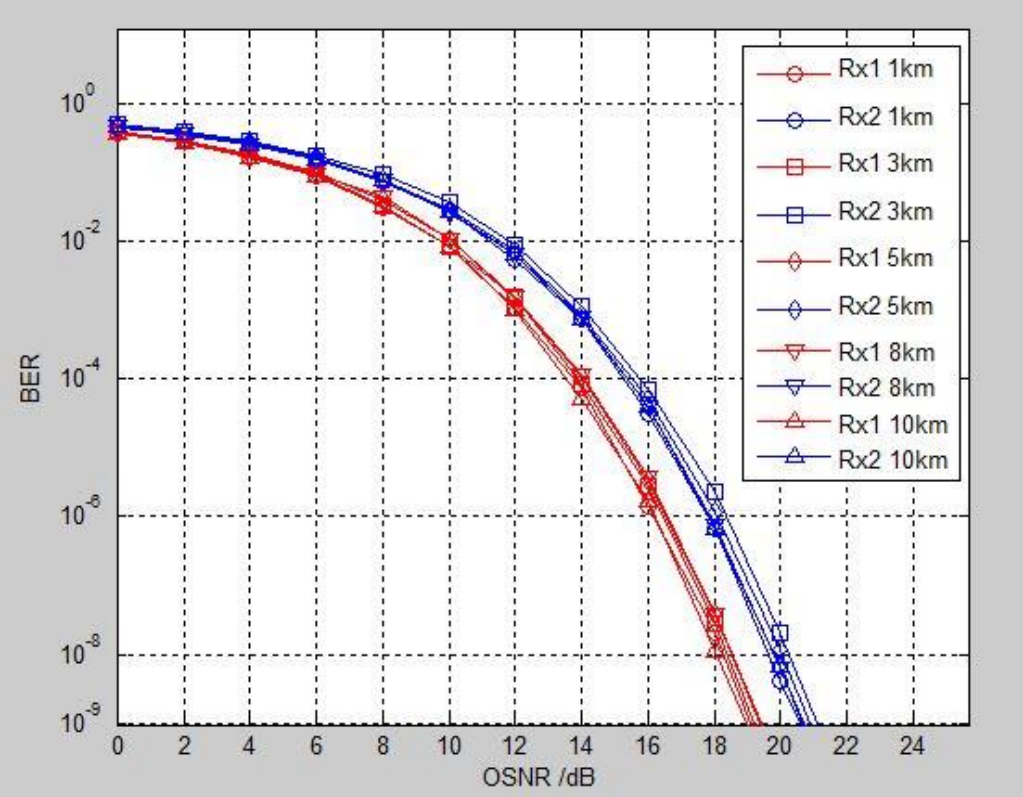

Figure 6.14 BER versus OSNR at different transmission distances /L (1km, 3km, 5km, 8km, 10km) for both receivers at a data rate of 10Gb/s.

MIMO equalization in the frequency domain can largely reduce modal dispersion effect caused by a long distance transmission, and the results are shown in Figure 6.14. In addition, there is no evident change in the receiver BER with increasing transmission distance, so we can conclude that the advanced coherent MIMO signal processing can fully compensate all linear impairments. From the preceding equation of FMF frequency response (Equation 6.7), we know that frequency response not only depends on the modal dispersion, chromatic dispersion and attenuation, but also on the power coupling coefficient from the light source to the individual mode. A comparison of the power coupling coefficients of the two modes with full BER analysis is given in Figure 6.15, in which $\Delta = \eta_{11} - \eta_{10}$ characterises the percentage difference in the power coupling coefficient.

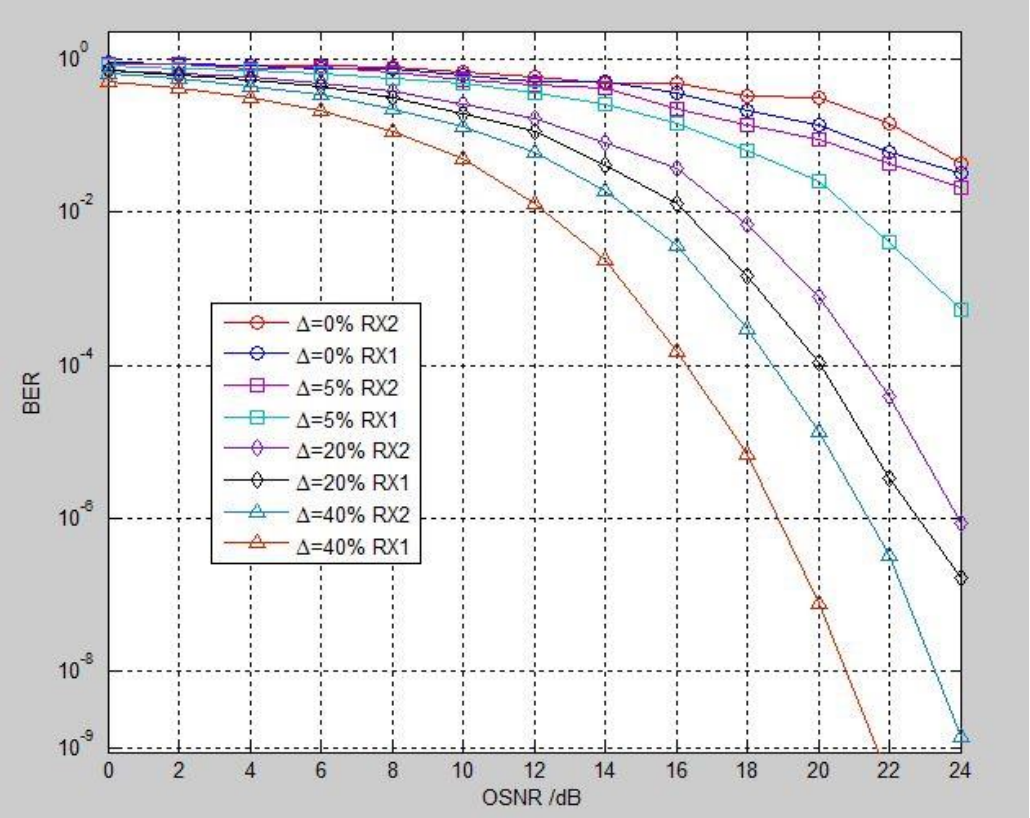

Figure 6.15 BER versus the difference in power coupling coefficient (Δ) of receivers one and two for L=5km and data rate=10Gb/s

In Figure 6.15, receivers one and two require an additional OSNR to keep the BER at 10^{-3} level when the power coupling difference is reduced. This effect is most pronounced around Δ =5%, where at a BER above 10^{-3} the system is unable to operate correctly even when utilizing the Forward Error Correction (FEC). Analysis of the impact of power coupling difference reveals that the larger the power coupling difference, the smaller BER can be achieved. The results also verify the correct choice of spot size of 1μm, as it produces a large power coupling difference (more than 65%). Therefore, we have learned that increasing the power coupling difference is essential to enable the system to work appropriately. In addition, this larger power coupling difference can be realised with either the aid of a small laser spot or by changing the radial offset condition. Due to the relatively small diameter of FMF, the smaller laser

spot size seems to be the most promising solution. The difference between the power coupling coefficients of the LP01 and LP11 modes during transmission may also be affected by inter-group mode mixing, resulting in significant system degradation in a long haul optical MIMO system. In other words, avoiding mode mixing between these two modes is the primary task in the FMF design. In order to determine the dominant limiting factors in this 2x2 coherent MIMO system, we need to recall the channel matrix equation *H*, which is defined as:

$$H_{i,j-FMF}(f) = \sum_{l,n}^{LP01,LP11} \gamma_{l,n}\eta_{l,n} \exp(-2\pi f \tau_{l,n} L) \cdot 10^{-\alpha_{l,n} L/10} \cdot \exp\left[i \frac{\pi D_{l,n} \lambda^2 f^2 L}{c} \right] \quad (6.38)$$

where $\gamma_{l,n}$ is the receiver detection coefficient of the i_{th} receiver, and $\eta_{l,n}$ is the power coupling coefficient for different LP modes.

From the above equation, we know that four factors could lead to channel degradation: chromatic dispersion, modal dispersion, power coupling coefficient, and detection coefficient. Now, a diagonal power detection matrix $\gamma_{i,j}$ is selected to ensure sufficient receiver diversity; with the aim of evaluating other limited factors, $\gamma_{i,j}$ is given by:

$$\gamma_{i,j} = \begin{bmatrix} 0.7 & 0.3 \\ 0.4 & 0.6 \end{bmatrix} \quad (6.39)$$

The results are illustrated in Figure 6.16. When both modal dispersion and chromatic dispersion are involved, and then only modal dispersion occurs, finally the chromatic dispersion is assumed to be the only impairment in FMF. From the results the OSNR penalty compared to the back-to-back transmission can be obtained numerically and is summarised in Table 6.5.

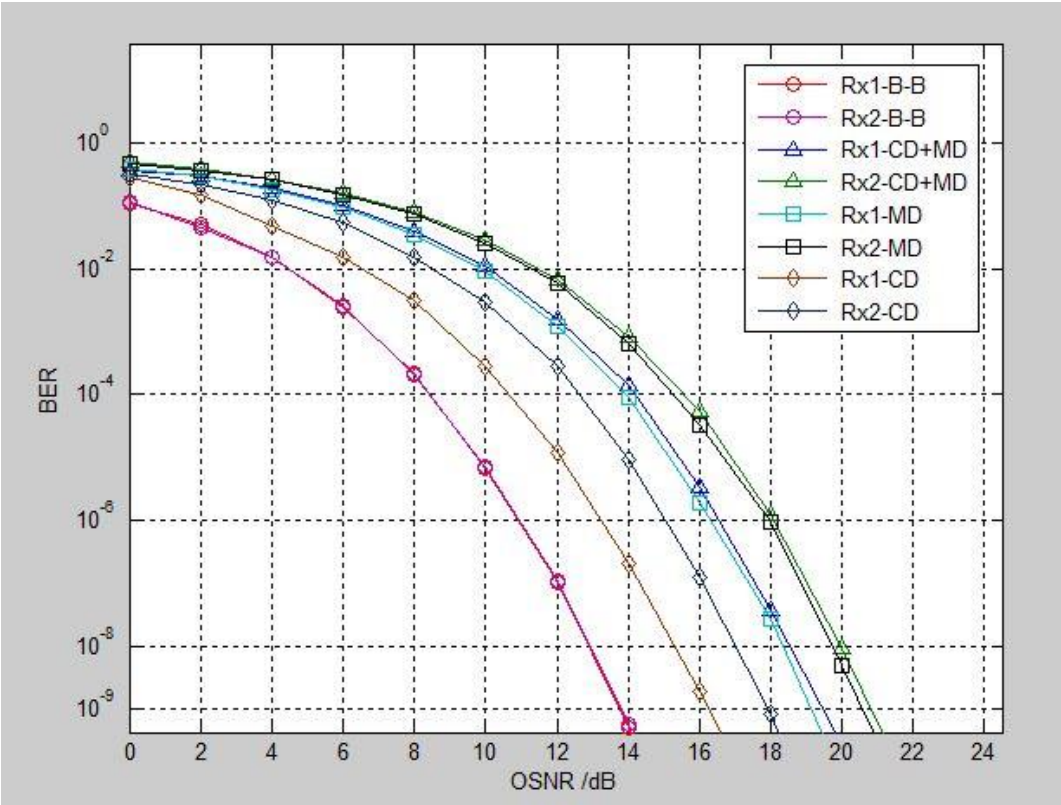

Figure 6.16 BER versus OSNR for different channel impairments. B-B is the back-to-back transmission, CD denotes chromatic dispersion existed only case, MD represents modal dispersion existed only case. The simulation data rate is 10Gb/s, and the FMF length is 5km.

OSNR Penalty/ dB	**Neglect chromatic dispersion effect**	**Neglect modal dispersion effect**	**Chromatic dispersion and modal dispersion effect**
Receiver Rx1	5.4 dB	2.4 dB	5.7 dB
Receiver Rx2	6.9 dB	4 dB	7.2 dB

Table 6.5 OSNR penalties caused by chromatic dispersion and modal dispersion in the 2x2 optical heterodyne DPSK FMF MIMO system for both receivers (Rx1, Rx2) compared to the back-to-back transmission at BER=10^{-9}

Both receivers have large power penalties when both chromatic dispersion and modal dispersion are active in the FMF channel. Chromatic dispersion seems to have a small effect on BER; its OSNR penalty is only 0.3dB less than in the case when both dispersions are considered. The biggest improvement in OSNR penalty is achieved by

neglecting the modal dispersion effect, which improves the OSNR penalty by approximately 3.3dB. Thus, we can conclude that modal dispersion is the major limiting factor in proposed coherent optical DPSK MIMO system. Respective power penalties of 2.4 and 4dB are still incurred at receivers one and two when modal dispersion is neglected; thus, receiver diversity seems to be another factor limiting system performance.

6.2.2 Optical intradyne DPSK MIMO system

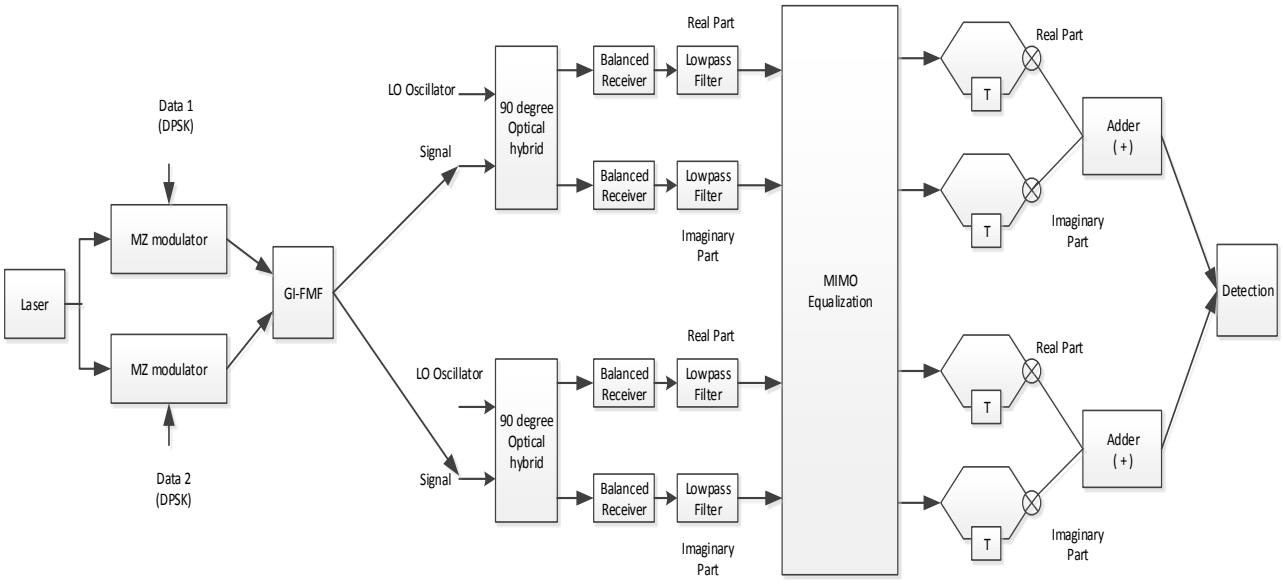

Figure 6.17 Optical DPSK intradyne MIMO system with phase diversity receiver in a two mode GI-FMF

Figure 6.17 shows the simulation model of the optical intradyne DPSK MIMO system. Both the real and imaginary parts of the signal are detected separately. The performances of the two receivers have been analysed under the assumptions and parameters used in the previous simulation, with the exception of the absence of a bandpass filter because the received signal is already in baseband. The system has

been simulated under the assumption that intensity noise is neglected. The numerical results indicate BER as a function of OSNR at both receivers (Figure 6.18). In Figure 6.18, the two receivers exhibit a similar response to BER with varying OSNR, and there is no significant difference between this intradyne phase diversity MIMO system and the previous heterodyne MIMO system.

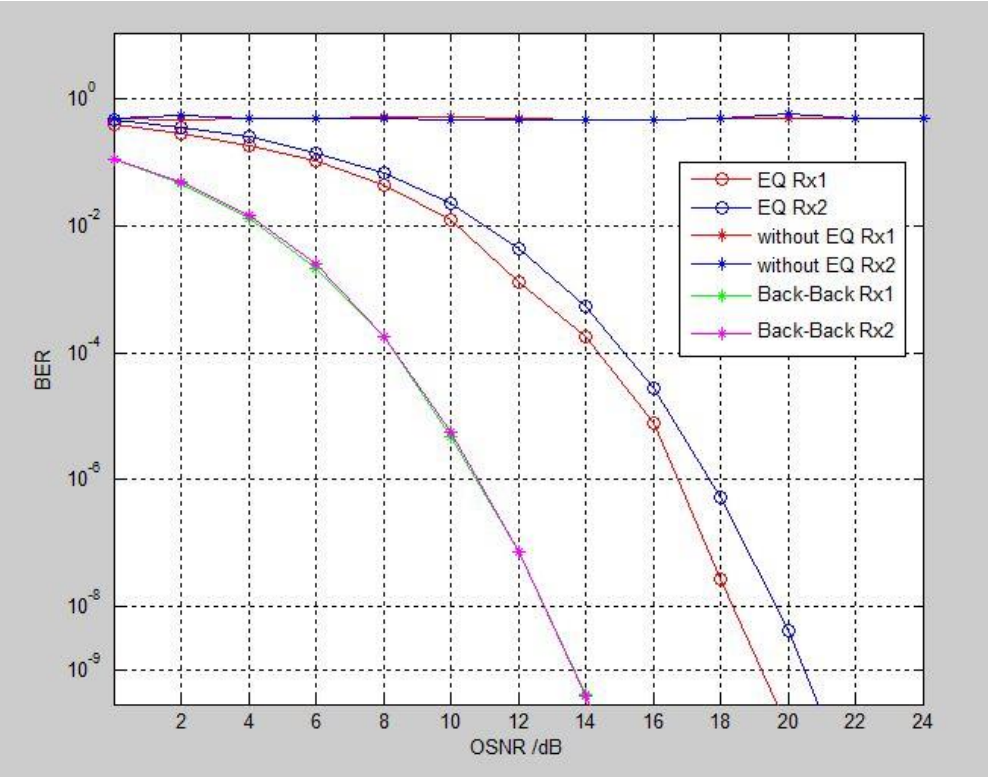

Figure 6.18 The 2x2 optical intradyne DPSK MIMO system with an FMF length of 5km under launching conditions of 0 and 4μm. Multi-segment annular detectors with R_{de}=5μm are used at the receiver. Symbol EQ stands for MIMO equalization, and the data rate is 10Gb/s.

The last Figure 6.19 shows the 10Gb/s 2x2 GI-FMF MIMO system using different detection methods, which includes optical heterodyne and optical intradyne detections. The IM-DD scheme is also implemented for comparison using identical system parameters. The results demonstrate the advantage of the coherent optical MIMO

system over the IM-DD MIMO system, and the optical DPSK system also extends its merit (less 3dB OSNR requirement) to the optical MIMO system. The optical heterodyne DPSK MIMO and optical intradyne DPSK MIMO systems can achieve the same system performance.

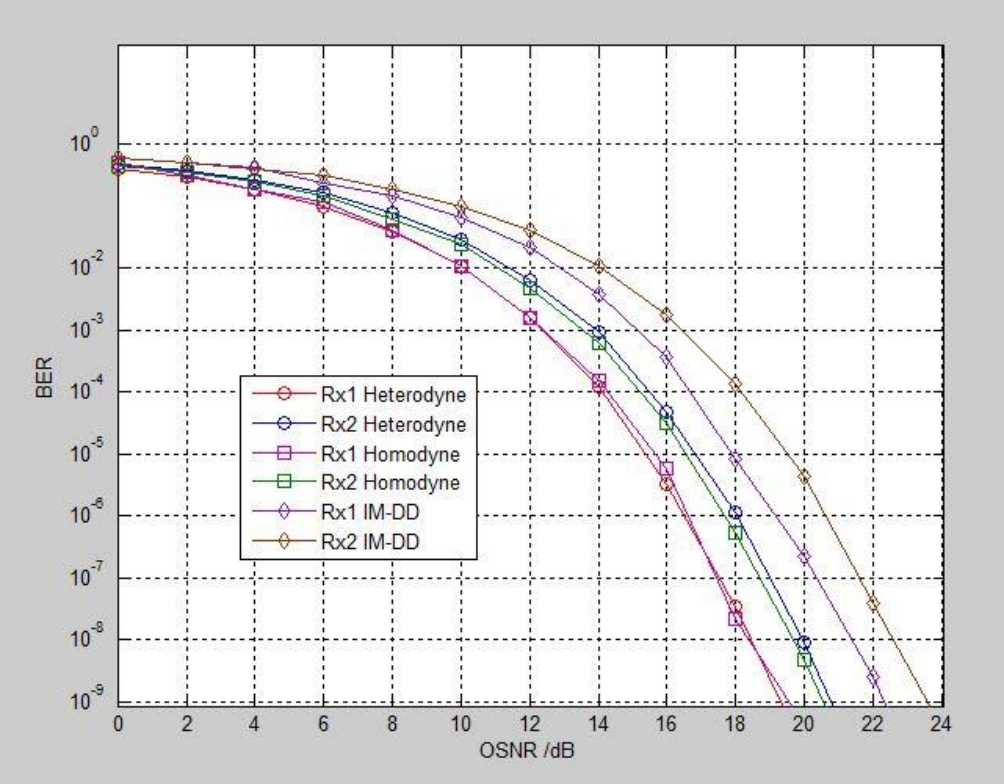

Figure 6.19 Comparison of the IM-DD MIMO system, optical heterodyne DPSK MIMO system and optical intradyne DPSK MIMO system in the two mode GI-FMF with L=5km and data rate=10Gb/s.

6.3 Conclusion

In this chapter, the basic concepts of coherent optical communication systems were discussed. We introduced the principle of the optical DPSK by using either a heterodyne or intradyne phase diversity detection scheme, and the mathematical models of the two detections and the coherent optical MIMO channel matrix were discussed. Simulations were performed under various impairments, including modal

dispersion, chromatic dispersion, attenuation, and intra-group mode mixing, and the BERs were evaluated as a performance metric.

A simple 2x2 optical DPSK coherent MIMO model in FMF using conventional radial offset selective launching in conjunction with annular multi-segment detectors was designed. MIMO equalization in the frequency domain compensated all linear impairments in the FMF. As FMF is a new type of multimode fibre with a design that relies on the normalized frequency (V), a two mode (LP01 and LP11) graded index few mode fibre can be designed and utilized as the transmission medium in our coherent optical MIMO system by precisely controlling the parameter V.

In addition, an optimization method to enhance the system and restrict the crosstalk between the two receivers was demonstrated. In contrast to the IM-DD optical MIMO system, the coherent optical MIMO optimization must consider the trade-off between sufficient spatial diversity at the transceivers and the DMD caused by modal dispersion. To minimise the interference between two channels, the optimization of laser spot size appears to be very useful; this makes the power coupling coefficient difference between the LP01 and LP11 modes very large, resulting in a more relaxed requirement for the modal dispersion effect. The simulation results showed that the proposed coherent optical DPSK MIMO performance at receiver one was more stable than at receiver two since only the fundamental mode was excited at zero offset launching; meanwhile, receiver one had more immunity to chromatic dispersion and modal dispersion, although it was still limited by the receiver spatial diversity. On the other hand, receiver two was very sensitive to modal dispersion. The OSNR penalty difference between the two receivers was approximately 1.5dB compared to the back-

to-back result at BER= 10^{-9} . The simulations also demonstrated that the optical heterodyne DPSK MIMO and optical intradyne DPSK MIMO systems have the same MIMO system performances.

Lastly, the optical heterodyne and intradyne DPSK MIMO systems are superior to the conventional IM-DD MIMO system due to the lower OSNR (approximately 3dB) requirement at BER = 10^{-9} .

Chapter 7: Conclusions and Future Work

7.1 Conclusions

Due to the rapid development of high speed Internet and LANs in recent years, it is imperative that the next generation of networks have greater transmission bandwidth, longer transmission distance, higher transmission speeds and the full ability to maximize the spectrum efficiency. On account of their sufficient spatial resources multimode fibres have once again become a research hotspot in high speed optical networks. However, the modal dispersion seriously limits their usage and makes multimode fibres impractical in high speed transmission networks. To overcome this bandwidth bottleneck, optical MIMO appears to be a most promising technique for future networks. This thesis proposed a simple optical MIMO MMF system using conventional intensity modulation direct detection or more advanced coherent detection schemes. The results indicate the feasibility and high efficiency of optical MIMO, which can be implemented in both short distance MMF systems and long distance FMF systems. Our proposed method can largely reduce the system complexity, energy consumption and cost, and make it more suitable for integration, while maintaining a performance similar to those achieved by mode division multiplexing systems without the use of active devices. In brief, this method has been realised by conventional radial offset launching in conjunction with annular multi-segment receivers. This design exhibits good performance in a 10Gb/s system and can now be employed in long distance coherent MIMO systems.

In order to illustrate the principle of an optical MIMO system, we first briefly introduced the basis of MMF, and the transmission impairments were analysed

theoretically by performing a mathematical model of MMF frequency response. We then simulated the guided mode propagation along with the MMF. The NFP at the output facet of MMF was simulated and analysed in Matlab both with and without intra-group mode mixing. The differential mode attenuation, power coupling coefficient, and modal dispersion were all identified and discussed. According to the spatial position of the NFP under various radial offset launchings, a more efficient annular detector was designed. Before the formal presentation of the optical MIMO system it was vital to study the general MIMO structure, which consisted of MIMO channel estimation, MIMO channel matrix H, MIMO equalization, and MIMO capacity. In the proposed method, channel estimation in the frequency domain was carried out by sending training sequences followed by applying the zero forcing equalization method. The condition number and receiver crosstalk indicated the superior performance of annular multi-segment receivers compared to conventional single mode fibre detectors, and from these results, the optimal number of transceivers was determined.

After providing the necessary foundation of the optical MIMO system, an intensity modulation and direct detection MIMO system in MMF was modelled. The IM-DD MIMO system optimization was implemented by adjusting the laser spot size and carefully choosing the appropriate radii of annular detectors based upon the cross points generated from the power flux distribution emitted by all transmitters. Meanwhile, the best performance was achieved when the laser spot size was 0.6 times the fundamental mode width, and the deterministic MIMO capacity results confirmed this optimal value. Annular multi-segment detectors exhibit a 2dBm less power penalty compared to SMF detectors. In addition, the results revealed that the average

BER not only relied on the data rate, but also on the intra-group mode mixing, even though the power penalty at BER=10^{-9} was only 0.5dBm; therefore, we concluded that the intra-group mode mixing had a limited effect on system performance. Although the 3x3 MIMO system provided more capacity, it came at the expense of greater power penalties, more susceptibility to intra-group mode mixing, and more sensitivity to transmission length. Lastly, the IM-DD optical MIMO system was not suitable for long distance networks as it lacked the ability to compensate linear impairments such as modal dispersion and chromatic dispersion.

In chapter 6, the combination of few mode fibre (FMF) and coherent DPSK in a 2x2 10Gb/s optical MIMO system was simulated, and both heterodyne DPSK and intradyne DPSK systems were simultaneously studied using mathematical models. The DPSK seems to be a promising candidate for future long distance and high speed systems due to its high tolerance to nonlinear effects, insensitivity to random phase noise compared to the phase shift keying modulation format, and less stringent 3dB OSNR requirement compared to on-off keying (OOK) systems. The few mode fibre is the physical basis in coherent optical MIMO systems, thus, a two mode graded index few mode fibre was designed and used as the transmission medium. Thereafter, the channel matrix H was redefined by accounting for chromatic dispersion, modal dispersion, mode attenuation, the mode power coupling coefficient, and the power detection coefficient at the i_{th} receiver. The system performance metric BER was estimated, and the results indicated that the frequency domain equalization almost compensated all linear impairments in the FMF and made the coherent MIMO system independent of transmission distance up to 10km in the absence of inter-group mode mixing. Using the proposed design, the 2x2 heterodyne DPSK MIMO system and the

2x2 intradyne DPSK MIMO system with phase diversity reception achieved a similar performance, but the receiver two suffered an extra 1.5dB OSNR penalty compared to receiver one because the LP01 and LP11 modes were both excited in channel 2.

Next, the coherent DPSK MIMO system was optimized by considering the trade-off between sufficient spatial diversity at the transceiver and the DMD caused by modal dispersion. The solution could be found by maximising the difference in the power coupling coefficient between these two modes by narrowing the laser spot size when the radial offset launching was applied.

The numerical results also demonstrated that modal dispersion seemed to be a dominant source in coherent optical MIMO systems. This affected our proposed coherent DPSK MIMO system performance because receiver one was more stable than receiver two due to the fact that only the fundamental mode was excited in FMF. In summary, the proposed low complexity design can achieve a reasonably good system performance in both short distance IM-DD MMF MIMO systems and long distance coherent DPSK FMF MIMO systems, which proves the feasibility of the implementation of this system in high speed optical fibre systems.

7.2 Future work

The theoretical and simulation studies have provided us with a comprehensive tool to aid further research into the optical MIMO in the MMF system. On this basis, the next phase of our work or the potential research directions will be discussed in the following section.

From the results on coherent optical MIMO systems, we have learned the major limiting factor in such systems is modal dispersion. Hence, the design and fabrication of a FMF with low DMD, low mode mixing, and larger effective area is a primary concern. In addition, the multiplexing of optical orbital angular momentum modes in ring fibres using the proposed system configuration may be another valuable research direction.

There is another selective launching scheme that may be seen as promising, in which a single mode fibre connected with hollow fibre is used to generate annular shape modes, called a ring launching scheme[176]. In contrast to the previous radial offset launching scheme, this new scheme maintains the receiver transmitter symmetrical. Meanwhile, only $LP_{0,N}$ modes in multimode fibres can be excited using hollow fibre launching. This will relax the requirement on modal dispersion and enhance the bandwidth distance product. Furthermore, this scheme may also be implemented in the four modes FMF MIMO system, but the disadvantage of this scheme is the extra time delay caused by propagation through the hollow fibre. Consequently, this selective launching scheme should be carefully exploited in our proposed system in order to explore its huge potential.

For a longer distance (>100km) system the nonlinear effects cannot be easily neglected. The intensity induced nonlinear effects will give rise to self-phase modulation, cross-phase modulation, and four wave mixing. Obviously, the nonlinear self-phase modulation seems to affect the optical DPSK system. A detailed study of nonlinear relations among guided modes is necessary.

In this thesis, intra-group mode mixing was assumed to be the only mode mixing factor that had to be accounted for; however, this assumption is unrealistic for long-haul transmission systems. Thus, a full analysis of inter-mode mixing starting with the field coupling model is necessary. Once the complex mode coupling coefficient can be numerically solved, a diagonal mode coupling matrix is used to characterise the coupling process. The complete system channel matrix H can then be rewritten as a product of this coupling matrix and Equation 6.38. An in-depth analysis of mode mixing in coherent optical MIMO systems is needed.

Finally, to realise practical systems, experimental work is needed to verify the theoretical results. In addition, industrial applications require on chip solutions; hence, a practical coherent MIMO system component in FMF is very important.

References

1. Molin, D., et al. *Multimode fibers for cost-effective high-speed, short-range networks*. in *Optical Communications (ECOC), 2012 38th European Conference and Exhibition on*. 2012.

2. Gasulla, I. and J. Capmany. *RF transfer function of analogue multimode fiber links using an electric field propagation model: Application to Broadband Radio over fiber systems*. in *Microwave Photonics, 2006. MWP '06. International Topical Meeting on*. 2006.

3. Bottacchi, S., *Multi-Gigabit transmission over Multimode Optical fibre.* 2006.

4. Babla, C., *Addressing challenges in serial 10 Gb/s multimode fiber enterprise networks.* Communications Magazine, IEEE, 2005. **43**(2): p. S22-S28.

5. *Hewlett Packard development company , 10 Gigabit Ethernet Cabling, in Procurve Networking Technical Brief* 2006: p. 1-11.

6. Tyler, E.J., et al., *Toward terabit-per-second capacities over multimode fiber links using SCM/WDM techniques.* Lightwave Technology, Journal of, 2003. **21**(12): p. 3237-3243.

7. Healy, S.B., et al., *Active Region Design for High-Speed 850 VCSELs.* Quantum Electronics, IEEE Journal of, 2010. **46**(4): p. 506-512.

8. Iwai, N., N. Yokouchi, and A. Kasukawa. *850nm VCSELs for 10Gb/s operation*. in *All-Optical Networking: Existing and Emerging Architecture and Applications/Dynamic Enablers of Next-Generation Optical Communications Systems/Fast Optical Processing in Optical Transmission/VCSEL and*. 2002.

9. Senior, J., *Optical fiber communications.* Prentice Hall International 1992.

10. Devaney, J., *Versatile VCSELs ready to shine at long wavelengths in Fibre systems Europe.* 2002: p. 28.

11. Schlager, J.B., et al., *Measurements for enhanced bandwidth performance over 62.5-μm multimode fiber in short-wavelength local area networks.* Lightwave Technology, Journal of, 2003. **21**(5): p. 1276-1285.

12. Pepeljugoski, P., et al., *Development of system specification for laser-optimized 50-μm multimode fiber for multigigabit short-wavelength LANs.* Lightwave Technology, Journal of, 2003. **21**(5): p. 1256-1275.

13. *ISO/IEC 11801 ed 2.2- Information technology- Generic cabling for customer premises (2011).*

14. *IEC 60793-2-10 Ed. 4.0: Optical fibres- Part 2-10: Product specifications- Sectional specification for category A1 multimode fibres (2011).*

15. *IEEE 10GBASE-S (802.3ae), "Media Access Control (MAC) Para*

meters,Physical Layer, and Management Parameters for 10Gb/s Operation"(2002).

16. Hardy, S., *Long wave VCSEL products reach production.* in Lightwave 2005.

17. A. Blokhin et al., *"850 nm VCSELs operating at bit rates up to 40 Gbit/s," Electron. Lett., 45, p.501 (2009).*

18. *IEEE 802.3bh (IEEE 802.3 Maintenance Task Force; Revision to IEEE Std 802.3-2008); scheduled publication 2012.*

19. Haglund, E., et al., *25 Gbit/s transmission over 500 m multimode fibre using 850 nm VCSEL with integrated mode filter.* Electronics Letters, 2012. **48**(9): p. 517-519.

20. Westbergh, P., et al., *Impact of Photon Lifetime on High-Speed VCSEL Performance.* Selected Topics in Quantum Electronics, IEEE Journal of, 2011. **17**(6): p. 1603-1613.

21. Westbergh, P., et al. *High-speed oxide confined 850-nm VCSELs operating error-free at 47 Gbit/s at room temperature and 40 Gbit/s at 85 degree*. in *Lasers and Electro-Optics Europe (CLEO EUROPE/IQEC), 2013 Conference on and International Quantum Electronics Conference*. 2013.

22. Xin, C., et al. *Chromatic dispersion compensated 25Gb/s multimode VCSEL transmission around 850nm with a MMF jumper*. in *Optical Fiber Communication Conference and Exposition and the National Fiber Optic Engineers Conference (OFC/NFOEC), 2013*. 2013.

23. Molin, D., M. Bigot-Astruc, and P. Sillard. *Reach extensions with chromatic dispersion compensated multimode fibers*. in *Optical Communication (ECOC 2013), 39th European Conference and Exhibition on*. 2013.

24. Siuzdak, J., M. Kowalczyk, and L. Maksymiuk. *4-Channel incoherent MIMO transmission over MM fiber with different offset light launch*. in *Wireless and Optical Communications Conference (WOCC), 2011 20th Annual*. 2011.

25. Franz, B. and H. Bulow. *Mode group multiplexing over graded-index multimode fiber*. in *Transparent Optical Networks (ICTON), 2012 14th International Conference on*. 2012.

26. Schollmann, S., S. Soneff, and W. Rosenkranz. *10.7 Gb/s Over 300 m GI-MMF Using a 2 by 2 MIMO System Based on Mode Group Diversity Multiplexing*. in *Optical Fiber Communication and the National Fiber Optic Engineers Conference, 2007. OFC/NFOEC 2007. Conference on*. 2007.

27. Siuzdak, J. and M. Kowalczyk. *3 by 3 incoherent MIMO transmission over MM fiber*. in *Photonics (ICP), 2011 IEEE 2nd International Conference on*. 2011.

28. Salsi, M., et al., *Mode-Division Multiplexing of 2x100 Gb/s Channels Using an LCOS-Based Spatial Modulator.* Lightwave Technology, Journal of, 2012. **30**(4): p. 618-623.

29. Ryf, R., et al. *Mode-multiplexed transmission over a 184-km DGD-compensated few-mode fiber span*. in *Photonics Society Summer Topical Meeting Series, 2012 IEEE*. 2012.

30. Ip, E., et al. *6x6 MIMO transmission over 50+20+10 km heterogeneous spans of few-mode fiber with inline erbium-doped fiber amplifier*. in *Optical Fiber Communication Conference and Exposition (OFC/NFOEC), 2012 and the National Fiber Optic Engineers Conference*. 2012.

31. Chralyvy, A. *Plenary paper: The coming capacity crunch*. in *Optical Communication, 2009. ECOC '09. 35th European Conference on*. 2009.

32. Antonelli, C., A. Mecozzi, and M. Shtaif. *Mode-division multiplexing for next-generation optical transport*. in *Electrical & Electronics Engineers in Israel (IEEEI), 2012 IEEE 27th Convention of*. 2012.

33. D.Marcuse, *Calculation of bandwidth from index profiles of optical fibres, Appl.Opt, Vol.18, page:2073-2080, 1979.*

34. Raddatz, L., et al., *Influence of restricted mode excitation on bandwidth of multimode fiber links.* Photonics Technology Letters, IEEE, 1998. **10**(4): p. 534-536.

35. Raddatz, L., et al., *Increasing the bandwidth-distance product of multimode fibre using offset launch.* Electronics Letters, 1997. **33**(3): p. 232-233.

36. Raddatz, L., et al., *An experimental and theoretical study of the offset launch technique for the enhancement of the bandwidth of multimode fiber links.* Lightwave Technology, Journal of, 1998. **16**(3): p. 324-331.

37. Oh, C.W., S. Moon, and D.Y. Kim. *A new selective mode excitation method for a multimode fiber with larger alignment tolerance*. in *Lasers and Electro-Optics, 2004. (CLEO). Conference on*. 2004.

38. Dubois, F., P. Emplit, and O. Hugon, *Selective mode excitation in graded-index multimode fiber by a computer-generated optical mask.* Opt. Lett., 1994. **19**(7): p. 433-435.

39. Kwok, C.H., et al. *Novel passive launch scheme for ultimate bandwidth improvement of graded-index multimode fibers*. in *Optical Fiber Communication (OFC), collocated National Fiber Optic Engineers Conference, 2010 Conference on (OFC/NFOEC)*. 2010.

40. Neo, P.L., J.P. Freeman, and T.D. Wilkinson. *Modal control of a 50um core diameter multimode fiber using a spatial light modulator*. in *Optical Fiber Communication and the National Fiber Optic Engineers Conference, 2007.*

OFC/NFOEC 2007. Conference on. 2007.

41. Stepniak, G., L. Maksymiuk, and J. Siuzdak, *Binary-Phase Spatial Light Filters for Mode-Selective Excitation of Multimode Fibers.* Lightwave Technology, Journal of, 2011. **29**(13): p. 1980-1987.

42. Stepniak, G., L. Maksymiuk, and J. Siuzdak. *Increasing multimode fiber transmission capacity by mode selective spatial light phase modulation*. in *Optical Communication (ECOC), 2010 36th European Conference and Exhibition on*. 2010.

43. Khosla, R., et al. *Equalization of 10 GbE multimode fiber links*. in *Lasers and Electro-Optics Society, 2003. LEOS 2003. The 16th Annual Meeting of the IEEE*. 2003.

44. Ingham, J.D., R.V. Penty, and I.H. White. *10 Gb/s transmitter-based equalization for extended-reach multimode-fiber datacommunication links*. in *Optical Fiber Communication and the National Fiber Optic Engineers Conference, 2007. OFC/NFOEC 2007. Conference on*. 2007.

45. Pepeljugoski, P., et al. *Improved performance of 10 Gb/s multimode fiber optic links using equalization*. in *Optical Fiber Communications Conference, 2003. OFC 2003*. 2003.

46. Xia, C., M. Ajgaonkar, and W. Rosenkranz, *On the performance of the electrical equalization technique in MMF links for 10-gigabit ethernet.* Lightwave Technology, Journal of, 2005. **23**(6): p. 2001-2011.

47. Weem, J.P., P. Kirkpatrick, and J. Verdiell. *Electronic dispersion compensation for 10 Gigabit communication links over FDDI legacy multimode fiber*. in *Optical Fiber Communication Conference, 2005. Technical Digest. OFC/NFOEC*. 2005.

48. Balemarthy, K., A. Polley, and S.E. Ralph, *Electronic Equalization of Multikilometer 10-Gb/s Multimode Fiber Links: Mode-Coupling Effects.* Lightwave Technology, Journal of, 2006. **24**(12): p. 4885-4894.

49. Balemarthy, K., et al. *Electronic dispersion compensation of non-ideal multimode fiber links*. in *Optical Fiber Communication Conference, 2005. Technical Digest. OFC/NFOEC*. 2005.

50. Zhao, X. and F.S. Choa, *Demonstration of 10-Gb/s transmissions over a 1.5-km-long multimode fiber using equalization techniques.* Photonics Technology Letters, IEEE, 2002. **14**(8): p. 1187-1189.

51. Ng, G. and A.C. Carusone. *Electronic Dispersion Compensation of 40-Gb/s Multimode Fiber Links Using IIR Equalization*. in *Optical Fiber Communication and the National Fiber Optic Engineers Conference, 2007. OFC/NFOEC 2007. Conference on*. 2007.

52. Mammei, E., et al. *8.3 A power-scalable 7-tap FIR equalizer with tunable active delay line for 10-to-25Gb/s multi-mode fiber EDC in 28nm LP-CMOS*. in *Solid-State Circuits Conference Digest of Technical Papers (ISSCC), 2014 IEEE International*. 2014.

53. Ralph, S.E. *Signal processing and impairments in Next-Generation MMF links*. in *Avionics, Fiber- Optics and Photonics Technology Conference (AVFOP), 2012 IEEE*. 2012.

54. *Ali Ghiasi et al "Measured Results of 25.78G VCSEL over OM3 Fiber with and without Equalization", IEEE 100GNGOPTX Study Group meeting, January 2012.*

55. Keiser, G., *Optical fiber communications, third edition, McGraw-Hill Companies, 2000.*

56. Ishigure, T., et al., *Accurate refractive index profiling in a graded-index plastic optical fiber exceeding gigabit transmission rates.* Lightwave Technology, Journal of, 2002. **20**(8): p. 1449-1456.

57. Kondo, A., T. Ishigure, and Y. Koike, *Fabrication process and optical properties of perdeuterated graded-index polymer optical fiber.* Lightwave Technology, Journal of, 2005. **23**(8): p. 2443-2448.

58. Pepeljugoski, P., et al., *15.6-Gb/s transmission over 1 km of next generation multimode fiber.* Photonics Technology Letters, IEEE, 2002. **14**(5): p. 717-719.

59. Aronson, L.B., et al., *Low-cost multimode WDM for local area networks up to 10 Gb/s.* Photonics Technology Letters, IEEE, 1998. **10**(10): p. 1489-1491.

60. Lemoff, B.E., L.B. Aronson, and L.A. Buckman, *Zigzag waveguide demultiplexer for multimode WDM LAN.* Electronics Letters, 1998. **34**(10): p. 1014-1016.

61. Buckman, L.A., et al., *Demonstration of a small-form-factor WWDM transceiver module for 10-Gb/s local area networks.* Photonics Technology Letters, IEEE, 2002. **14**(5): p. 702-704.

62. Kourtessis, P., et al., *0.6 Tbit/s/km multimode fibre feasibility experiment using 40 channel DWDM over quadrature-subcarrier transmission.* Electronics Letters, 2002. **38**(15): p. 813-815.

63. Panicker, R.A., et al., *10*10 Gb/s DWDM Transmission Through 2.2-km Multimode Fiber Using Adaptive Optics.* Photonics Technology Letters, IEEE, 2007. **19**(15): p. 1154-1156.

64. Senior, J.M., *Optical fiber communications principles and practices, 2rd edition, Prentice Hall.* 1992.

65. Gu, X.J., W. Mohammed, and P.W. Smith, *Demonstration of all-fiber WDM*

for multimode fiber local area networks. Photonics Technology Letters, IEEE, 2006. **18**(1): p. 244-246.

66. Gasulla, I. and J. Capmany. *1 Tb/s.km WDM transmission over multimode fibre link*. in *Optical Communication, 2008. ECOC 2008. 34th European Conference on*. 2008.

67. Lin, M., et al. *Ultra-wideband WDM transmission in multi-mode fiber using PCF devices*. in *OptoeElectronics and Communications Conference (OECC), 2011 16th*. 2011.

68. Chen, H.S., P.A. van den Boom, and A.J. Koonen, *WDM 2 x 2 mode group division multiplexing system and investigation of polarisation division multiplexing.* Electronics Letters, 2011. **47**(23): p. 1289-1290.

69. Raddatz, L., et al. *High data rate transmission of subcarrier multiplexed signals using vertical cavity surface emitting lasers and multimode fibre*. in *Integrated Optics and Optical Fibre Communications, 11th International Conference on, and 23rd European Conference on Optical Communications (Conf. Publ. No.: 448)*. 1997.

70. Raddatz, L., et al. *High bandwidth multimode fiber links using subcarrier muitiplexing in vertical-cavity surface-emitting lasers*. in *Optical Fiber Communication Conference and Exhibit, 1998. OFC '98., Technical Digest*. 1998.

71. Raddatz, L., et al., *High bandwidth data transmission in multimode fibre links using subcarrier multiplexing with VCSELs.* Electronics Letters, 1998. **34**(7): p. 686-688.

72. Hui, R., et al., *Subcarrier multiplexing for high-speed optical transmission.* Lightwave Technology, Journal of, 2002. **20**(3): p. 417-427.

73. Kanprachar, S. and F. Jacobs. *Bit-rate and distance limitations of subcarrier multiplexing on multimode fiber*. in *Lasers and Electro-Optics, 2003. CLEO '03. Conference on*. 2003.

74. Tyler, E.J., et al. *Transmission of a single 2.5 Gb/s subcarrier modulated channel over 300 m of 62.5 um multimode fibre*. in *Lasers and Electro-Optics Society 2000 Annual Meeting. LEOS 2000. 13th Annual Meeting. IEEE*. 2000.

75. Zeng, J., et al. *Transmission of 1.25 Gb/s per Channel over 4.4 km Silica Multimode Fibre Using QAM Subcarrier Multiplexing*. in *Optical Communication (ECOC), 2007 33rd European Conference and Ehxibition of*. 2007.

76. Zhang, Y. and K. Iwashita. *MIMO transmission using SCM with modal diversity in multimode fiber systems*. in *Optical Communications and Networks (ICOCN 2011), 10th International Conference on*. 2011.

77. Kanprachar, S. and F. Jacobs, *Diversity coding for subcarrier multiplexing on multimode fibers.* Communications, IEEE Transactions on, 2003. **51**(9): p. 1546-1553.

78. Kanprachar, S. *Effects of bandpass bandwidth in bit-rate and distance of subcarrier multiplexing on multimode fiber*. in *Optical Communications and Networks (ICOCN), 2012 11th International Conference on*. 2012.

79. Ma, Y., Y. Tang, and W. Shieh, *107 Gbit/s transmission over multimode fibre with coherent optical OFDM using centre launching technique.* Electronics Letters, 2009. **45**(16): p. 848-849.

80. Tong, Z., et al., *21.4 Gbit/s transmission over 200 km multimode fibre using coherent optical OFDM.* Electronics Letters, 2008. **44**(23): p. 1373-1374.

81. Yang, Z. and K. Iwashita. *MIMO transmission using SCM with modal diversity in multimode fiber systems*. in *Optical Communications and Networks (ICOCN 2011), 10th International Conference on*. 2011.

82. Stuart, H.R. *Dispersive multiplexing in multimode fiber*. in *Optical Fiber Communication Conference, 2000*. 2000.

83. Paulraj, A.J., et al., *An overview of MIMO communications - a key to gigabit wireless.* Proceedings of the IEEE, 2004. **92**(2): p. 198-218.

84. Tarighat, A., et al., *Fundamentals and challenges of optical multiple-input multiple-output multimode fiber links [Topics in Optical Communications]*. Communications Magazine, IEEE, 2007. **45**(5): p. 57-63.

85. Hsu, R.C.J., A. Shah, and B. Jalali. *Coherent optical multiple-input multiple-output communication over multimode fiber*. in *Microwave Photonics, 2004. MWP'04. 2004 IEEE International Topical Meeting on*. 2004.

86. Lenz, D., et al. *MIMO channel for modal multiplexing in highly overmoded optical waveguides*. in *Communications, 2004 International Zurich Seminar on*. 2004.

87. Saffman, M. and D.Z. Anderson, *Mode multiplexing and holographic demultiplexing communication channels on a multimode fiber.* Opt. Lett., 1991. **16**(5): p. 300-302.

88. Neo, P.L. and T.D. Wilkinson. *Holographic implementation of optical multiple-inputs, multiple-outputs (MIMO) on a multimode fiber*. in *Lasers and Electro-Optics, 2006 and 2006 Quantum Electronics and Laser Science Conference. CLEO/QELS 2006. Conference on*. 2006.

89. Chen, H.S., H.P.A. Van den Boom, and A.M.J. Koonen. *Experimental demonstration of 2 by 2 MIMO based on mode group division multiplexing over 250m GI-MMF*. in *Communications and Photonics Conference and Exhibition (ACP), 2010 Asia*. 2010.

90. Tsekrekos, C.P., et al., *Design Considerations for a Transparent Mode Group Diversity Multiplexing Link.* Photonics Technology Letters, IEEE, 2006. **18**(22): p. 2359-2361.

91. Chen, H.S., H.P.A. Van den Boom, and A.M.J. Koonen, *30-Gb/s 3x3 Optical Mode Group-Division-Multiplexing System With Optimized Joint Detection.* Photonics Technology Letters, IEEE, 2011. **23**(18): p. 1283-1285.

92. Schollmann, S., N. Schrammar, and W. Rosenkranz. *Experimental Realisation of 3 by 3 MIMO System with Mode Group Diversity Multiplexing Limited by Modal Noise*. in *Optical Fiber communication/National Fiber Optic Engineers Conference, 2008. OFC/NFOEC 2008. Conference on*. 2008.

93. Schollmann, S., S. Soneff, and W. Rosenkranz. *10.7 Gb/s Over 300 m GI-MMF Using a 2x2 MIMO System Based on Mode Group Diversity Multiplexing*. in *Optical Fiber Communication and the National Fiber Optic Engineers Conference, 2007. OFC/NFOEC 2007. Conference on*. 2007.

94. Stepniak, G., L. Maksymiuk, and J. Siuzdak. *A mode group diversity multiplexing system for step and graded index multimode fibers*. in *Transparent Optical Networks, 2008. ICTON 2008. 10th Anniversary International Conference on*. 2008.

95. Zhou, H., et al. *An optical MMF communication system based on mode group diversity multiplexing and Space Time coding*. in *Communications and Photonics Conference and Exhibition (ACP), 2010 Asia*. 2010.

96. Keiser, G., *Optical fiber communication. New York,McGraw Hill.* 2000.

97. Shah, A.R., et al., *Coherent optical MIMO (COMIMO).* Lightwave Technology, Journal of, 2005. **23**(8): p. 2410-2419.

98. Mori, T., et al. *Wideband WDM coherent optical MIMO transmission over GI-MMF by using selective mode excitation*. in *Optical Fiber Communication Conference and Exposition (OFC/NFOEC), 2012 and the National Fiber Optic Engineers Conference*. 2012.

99. Bulow, H., H. Al-Hashimi, and B. Schmauss. *Coherent multimode-fiber MIMO transmission with spatial constellation modulation*. in *Optical Communication (ECOC), 2011 37th European Conference and Exhibition on*. 2011.

100. Al-Hashimi, H., H. Bulow, and B. Schmauss. *Effect of bend radius on equalizer complexity for multimode coherent MIMO transmission*. in *Photonics Conference (IPC), 2012 IEEE*. 2012.

101. Ziran, Z., et al. *Frequency pre-distortion for coherent optical MIMO system over MMF*. in *OptoElectronics and Communications Conference held jointly with 2013 International Conference on Photonics in Switching (OECC/PS), 2013 18th*. 2013.

102. Yaman, F., et al., *Long distance transmission in few-mode fibers.* Opt. Express, 2010. **18**(12): p. 13250-13257.

103. Ryf, R., et al. *Space-division multiplexing over 10 km of three-mode fiber using coherent 6 x 6 MIMO processing*. in *Optical Fiber Communication Conference and Exposition (OFC/NFOEC), 2011 and the National Fiber Optic Engineers Conference*. 2011.

104. Chen, H.S., et al. *20Gbit/s Two LP11 modes transmission over 10km two-moded fiber without crosstalk compensation*. in *Opto-Electronics and Communications Conference (OECC), 2012 17th*. 2012.

105. Salsi, M., et al. *Transmission at 2x100Gb/s, over two modes of 40km-long prototype few-mode fiber, using LCOS-based mode multiplexer and demultiplexer*. in *Optical Fiber Communication Conference and Exposition (OFC/NFOEC), 2011 and the National Fiber Optic Engineers Conference*. 2011.

106. Okamoto, A., et al. *Multi-excitation of spatial modes using single spatial light modulator for mode division multiplexing*. in *Optical Fiber Communication Conference and Exposition (OFC/NFOEC), 2012 and the National Fiber Optic Engineers Conference*. 2012.

107. Li, A., et al. *Reception of mode and polarization multiplexed 107-Gb/s CO-OFDM signal over a two-mode fiber*. in *Optical Fiber Communication Conference and Exposition (OFC/NFOEC), 2011 and the National Fiber Optic Engineers Conference*. 2011.

108. Ryf, R., et al., *Mode-Division Multiplexing Over 96 km of Few-Mode Fiber Using Coherent 6x6 MIMO Processing.* Lightwave Technology, Journal of, 2012. **30**(4): p. 521-531.

109. Snyder, A.W.a.L., J.D, *Optical waveguide theory, London,Chapman and Hall. Viii, 734.* 1983.

110. Ajoy, G., K.Thyagarajan, *Introduction to Fiber Optics, Cambridge University Press.* 2000.

111. Irujo, T., *OM4 The next generation of multomode fiber, Optical fiber in enterprise applications, OFS,Furukawa company.*

112. Love, A.W.S.a.J.D., *Optical Waveguide Theory,2000,, Kluwer Academic Publishers, original published by Chapman and Hall Ltd in 1983.*

113. Spain, B.a.M.G.S., *Functions of Mathematical physics, 1970,London, Van Nostrand Reinhold, Xi, p208.*

114. Yabre, G., *Comprehensive theory of dispersion in graded-index optical fibers.* Lightwave Technology, Journal of, 2000. **18**(2): p. 166-177.

115. Amphawan, A., et al., *Derivation of an Analytical Expression for the Power Coupling Coefficient for Offset Launch Into Multimode Fiber.* Lightwave Technology, Journal of, 2010. **28**(6): p. 861-869.

116. Gary Shaulov, B.W., *Multimode fibre communication system simulation. 2004, Rsoft Design Group, Inc:Ossining, NY 10562,USA.*

117. Amphawan, A., *Holographic selective mode excitation in multimode fibre, 2009, page:155.*

118. Keck, R.O.a.D.B., *Pulse broadening in graded-index optical fibers, Applied Optics, Vol. 15, Issue 2, pp. 483-491 (1976).*

119. Morishita, K., *Numerical Analysis of Pulse Broadening in Graded Index Optical Fibers.* Microwave Theory and Techniques, IEEE Transactions on, 1981. **29**(4): p. 348-352.

120. Louvros, S. and A.C. Iossifides, *Impulse response analysis of graded index polymer optical fiber.* Optical Fiber Technology, 2006. **12**(3): p. 262-264.

121. Greenberg, M., M. Nazarathy, and M. Orenstein, *Data Parallelization by Optical MIMO Transmission Over Multimode Fiber With Intermodal Coupling.* Lightwave Technology, Journal of, 2007. **25**(6): p. 1503-1514.

122. C. P. Tsekrekos, R.W.S., B. P. de Hon, A. G. Tijhuis, and A. M. J. Koonen *Near-field intensity pattern at the output of silica-based graded-index multimode fibers under selective excitation with a single-mode fiber, Optics Express, Vol. 15, Issue 7, pp. 3656-3664 (2007).*

123. Kahn, J.M., H. Keang-Po, and M.B. Shemirani. *Mode coupling effects in multi-mode fibers*. in *Optical Fiber Communication Conference and Exposition (OFC/NFOEC), 2012 and the National Fiber Optic Engineers Conference*. 2012.

124. Cancellieri, G., *Mode coupling in graded-index optical fibres due to perturbation of the index profile.* Applied physics, 1980. **23**(1): p. 99-105.

125. Olshansky, R., *Mode Coupling Effects in Graded-index Optical Fibers, Applied Optics, Vol. 14, Issue 4, pp. 935-945, 1975.*

126. Molin, D., M. Bigot-Astruc, and P. Sillard. *Chromatic dispersion compensated multimode fibers for data communications*. in *Optical Communication (ECOC), 2011 37th European Conference and Exhibition on*. 2011.

127. Molin, D., M. Bigot-Astruc, and P. Sillard. *Chromatic dispersion compensation in regular and bend-insensitive multimode fibers*. in *Optical Fiber Communication Conference and Exposition (OFC/NFOEC), 2012 and the National Fiber Optic Engineers Conference*. 2012.

128. Arnaud, J.A., *Effect of polarisation on pulse broadening in multimode graded-*

index optical fibres. Electronics Letters, 1975. **11**(23): p. 554-556.

129. Wagner, R.E., R.H. Stolen, and W. Pleibel, *Polarisation preservation in multimode fibres.* Electronics Letters, 1981. **17**(5): p. 177-178.

130. *Definition of polarization mode dispersion and first results of the COST 241 round-robin measurements N Gisin et al 1995 Pure Appl. Opt. 4 511.*

131. Kutz, J.N., J.A. Cox, and D. Smith, *Mode mixing and power diffusion in multimode optical fibers.* Lightwave Technology, Journal of, 1998. **16**(7): p. 1195-1202.

132. Kawakami, S. and H. Tanji, *Evolution of power distribution in graded-index fibres.* Electronics Letters, 1983. **19**(3): p. 100-102.

133. Pepeljugoski, P., et al., *Modeling and simulation of next-generation multimode fiber links.* Lightwave Technology, Journal of, 2003. **21**(5): p. 1242-1255.

134. Willner, I.P.K.T.L.A.E., *Optical Fiber Telecommunications VIB Systems and Networks.* 2013.

135. Kitayama, K., S. Seikai, and N. Uchida, *Impulse response prediction based on experimental mode coupling coefficient in a 10-km long graded-index fiber.* Quantum Electronics, IEEE Journal of, 1980. **16**(3): p. 356-362.

136. Olshansky, R. and S.M. Oaks, *Differential mode attenuation measurements in graded-index fibers.* Appl. Opt., 1978. **17**(11): p. 1830-1835.

137. Olshansky, R. and D.A. Nolan, *Mode-dependent attenuation of optical fibers: excess loss.* Appl. Opt., 1976. **15**(4): p. 1045-1047.

138. Rousseau, M. and L. Jeunhomme, *Optimum index profile in multimode optical fiber with respect to mode coupling.* Optics Communications, 1977. **23**(2): p. 275-278.

139. Leminger, O.G. and G.K. Grau, *Near-field intensity and modal power distribution in multimode graded-index fibres.* Electronics Letters, 1980. **16**(17): p. 678-679.

140. R.W.Smink, C.P.T., B.P.de Hon, A.M.J.Koonen and A.G.Tijhuis, *Near fild pattern simulations of graded index multimode fibres, Proceedings Symposium IEEE/LEOS Benelux Chapter, 2006, Eindhoven.*

141. C.P.Tsekrekos, R.W.S., B.P.de Hon, A.G.Tijhuis and A.M.J.Koonen,, *Near field intensity pattern at the output of silica based graded index multimode fibers under selective excitation with a single mode fibers.* OSA Opt. Express, vol.15, pp.3656-3664, Apr.2007.

142. Dandliker, R., A. Bertholds, and F. Maystre, *How modal noise in multimode fibers depends on source spectrum and fiber dispersion.* Lightwave

Technology, Journal of, 1985. **3**(1): p. 7-12.

143. Wegmuller, M., et al., *Evolution of the beam diameter in a multimode fiber link through offset connectors.* Photonics Technology Letters, IEEE, 2001. **13**(6): p. 574-576.

144. David Tse, P.V., *Fundamentals of wireless communication, cambridge univeristy press 2005, .*

145. Awad, M., et al., *The inter-modes mixing effects in Mode Group Diversity Multiplexing.* Optics Communications, 2009. **282**(19): p. 3908-3917.

146. Mecozzi, A. and M. Shtaif, *On the capacity of intensity modulated systems using optical amplifiers.* Photonics Technology Letters, IEEE, 2001. **13**(9): p. 1029-1031.

147. Goldsmith, A., et al., *Capacity limits of MIMO channels.* Selected Areas in Communications, IEEE Journal on, 2003. **21**(5): p. 684-702.

148. Tim Brown, E.D.C., Persefoni Kyritsi, *Practical Guide to the MIMO Radio Channel, John Wiley & Sons Ltd, 2012.*

149. Mannerkoski, J. and D.P. Taylor, *Blind equalization using least-squares lattice prediction.* Signal Processing, IEEE Transactions on, 1999. **47**(3): p. 630-640.

150. J.Booth, K.A.S.w.A.b.D., *Advanced Engineering Mathematics, Fourth Edition, Published by PALGRAVE MACMILLAN, 2003.*

151. Ping-Heng, K., P.J. Smith, and L.M. Garth. *A Markov Model for MIMO Channel Condition Number with Application to Dual-Mode Antenna Selection*. in *Vehicular Technology Conference, 2007. VTC2007-Spring. IEEE 65th*. 2007.

152. Maurer, J., G. Matz, and D. Seethaler. *Low-Complexity and Full-Diversity MIMO Detection Based on Condition Number Thresholding*. in *Acoustics, Speech and Signal Processing, 2007. ICASSP 2007. IEEE International Conference on*. 2007.

153. Gesbert, D., et al., *Outdoor MIMO wireless channels: models and performance prediction.* Communications, IEEE Transactions on, 2002. **50**(12): p. 1926-1934.

154. Dambul, K.D., *Multiple Input Multiple Output (MIMO) in Optical Wireless Communications.* 2010.

155. de Boer, M., et al. *A first demonstrator for a mode group diversity multiplexing communication system*. in *Optical Fibre Communications and Electronic Signal Processing, 2005. The IEE Seminar on (Ref. No. 2005-11310)*. 2005.

156. Grau, G.K., O.G. Leminger, and E.G. Sauter, *Selective excitation of parabolic-*

index optical fibers by Gaussian beams: comment. Appl. Opt., 1981. **20**(3): p. 381-381.

157. Agrawal, G.P., *Fiber optic communication systems, Fourth Edition, John Wiley & Sons Publishes, 2010, page:165.*

158. Farid, A.A. and S. Hranilovic. *Upper and Lower Bounds on the Capacity of Wireless Optical Intensity Channels*. in *Information Theory, 2007. ISIT 2007. IEEE International Symposium on*. 2007.

159. Lapidoth, A., S.M. Moser, and M.A. Wigger. *On the capacity of free-space optical intensity channels*. in *Information Theory, 2008. ISIT 2008. IEEE International Symposium on*. 2008.

160. Keang-Po, H., *Exact evaluation of the capacity for intensity-modulated direct-detection channels with optical amplifier noises.* Photonics Technology Letters, IEEE, 2005. **17**(4): p. 858-860.

161. N. Hanzawa et al., *Demonstration of mode-division multiplexing transmission over 10 km two-mode fiber with mode coupler, in: Proc. OFC, OWA4, 2011*.

162. W. Q. Thornburg, B.J.C., and X. D. Zhu, *Selective launching of higher-order modes into an optical fiber with an optical phase shifter, Optics Letters, Vol. 19, Issue 7, pp. 454-456 (1994).*

163. Ryf, R., N.K. Fontaine, and R. Essiambre. *Spot-based mode coupler for mode-multiplexed transmission in few-mode fiber*. in *Photonics Society Summer Topical Meeting Series, 2012 IEEE*. 2012.

164. Yuanquan Wang, Y.S., Nan Chi, *Multiple-Inputs Multiple-Outputs Combining Center Launch and Ring Launch for High-Speed Transmission in Multimode Fiber Links, Future Wireless Networks and Information Systems, 2012.*

165. al., B.F.e., High speed OFDM data transmission over 5 km GI-multimode fiber using spatial multiplexing with 2 × 4 MIMO processing, Proc. ECOC, Tu.3.C.4, 2010.

166. Ip, E., et al., *Coherent detection in optical fiber systems*. Optics Express, 2008. **16**(2): p. 753-791.

167. Azizoglu, M. and P.A. Humblet. *Optical DPSK with generalized phase noise model and narrowband reception*. in *Communications, 1993. ICC '93 Geneva. Technical Program, Conference Record, IEEE International Conference on*. 1993.

168. Kaiser, C.P., M. Shafi, and P.J. Smith, *Analysis methods for optical heterodyne DPSK receivers corrupted by laser phase noise.* Lightwave Technology, Journal of, 1993. **11**(11): p. 1820-1830.

169. Barry, J.R. and E.A. Lee, *Performance of coherent optical receivers.*

Proceedings of the IEEE, 1990. **78**(8): p. 1369-1394.

170. Xing, W., L. Xiang, and C. Xu, *Numerical simulation of the SPM penalty in a 10-Gb/s RZ-DPSK system.* Photonics Technology Letters, IEEE, 2003. **15**(11): p. 1636-1638.

171. Bosco, G. and P. Poggiolini, *On the Q factor inaccuracy in the performance analysis of optical direct-detection DPSK systems.* Photonics Technology Letters, IEEE, 2004. **16**(2): p. 665-667.

172. Slater, B., et al., *Comparative Analysis of BER Estimation Methods in Numerical Simulation of 40-Gb/s RZ-DPSK Transmission With In-Line SOAs.* Photonics Technology Letters, IEEE, 2007. **19**(8): p. 607-609.

173. Slater, B., et al. *Comparison of BER estimation methods in numerical simulation of 40 Gbit/s RZ-DPSK transmission*. in *Lasers and Electro-Optics, 2007 and the International Quantum Electronics Conference. CLEOE-IQEC 2007. European Conference on*. 2007.

174. Sato, K., et al., *Optimized graded index two-mode optical fiber with low DMD, large Aeff and low bending loss.* Optics Express, 2013. **21**(14): p. 16231-16238.

175. *http://ofscatalog.specialtyphotonics.com/viewitems/non-standard-optical-fibers/non-standard-optical-fibers-few-mode-fibers-series?forward=1*.

176. Choi, S., et al., *Novel mode converter based on hollow optical fiber for Gigabit LAN communication.* Photonics Technology Letters, IEEE, 2002. **14**(2): p. 248-250.

Appendix

(a) Derivation of normalized incident Gaussian beam field equation

Assuming input Gaussian field is described as:

$$E_{inc} = C\exp\left(-\frac{R^2}{2\Omega^2}\right), \qquad \text{(a.1)}$$

where $\Omega = \frac{\rho_s}{\rho}$, $\rho_s = spot\ size, \rho = core\ radius, \Omega = normalized\ spot\ size$.

To normalize the input filed, it needs $\iint_{Acore}\left|C\exp\left(-\frac{R^2}{2\Omega^2}\right)\right|^2 RdRd\phi = 1$ (a.2)

thus, $C^2\iint_{Acore}\left|\exp\left(-\frac{R^2}{2\Omega^2}\right)\right|^2 RdRd\phi = 1$ (a.3)

$$\frac{1}{C^2} = \iint_{Acore}\left|\exp\left(-\frac{R^2}{\Omega^2}\right)\right| RdRd\phi \quad \text{or} \quad \frac{1}{C^2} = \int_0^{2\pi}\int_0^{\infty}\left|\exp\left(-\frac{R^2}{\Omega^2}\right)\right| RdRd\phi \qquad \text{(a.4)}$$

By using the given analytical solution of integration of exponent shown below:

$$\int_0^{\infty} R\cdot e^{-kR^2}\,dR = \frac{1}{2k} \qquad \text{(a.5)}$$

Substituting $k = \frac{1}{\Omega^2}$ into Equation a.5, then the right hand of Equation a.4 becomes:

$$\int_0^{2\pi}\int_0^{\infty}\left|\exp\left(-\frac{R^2}{\Omega^2}\right)\right| RdRd\phi = \int_0^{2\pi}\frac{\Omega^2}{2}d\phi$$

$$= \frac{\Omega^2}{2}\int_0^{2\pi} 1\,d\phi = \Omega^2\pi \qquad \text{(a.6)}$$

which gives: $\frac{1}{C^2} = \Omega^2\pi$ (a.7)

$$C = \frac{1}{\sqrt{\pi}\Omega} \qquad \text{(a.8)}$$

Finally, the normalized incident electrical field of Gaussian beam is given by:

$$E_{in} = \frac{1}{\sqrt{\pi}\Omega}\exp\left(-\frac{R^2}{2\Omega^2}\right) \qquad \text{(a.9)}$$

(b) Derivation of Modal time delay in infinite parabolic index profile ($\alpha = 2$) GI-MMF

Under the weakly guiding approximation, the modes within same principal mode group "q" will propagate through the MMF at the same group velocity, which is derived from the scalar propagation constant associated with this mode group.

$$\beta_q = \frac{\omega n_{co}}{c}\left[1-\frac{2NAn_{co}^2 cq}{\omega\rho}\right]^{\frac{1}{2}} \qquad \text{(a.10)}$$

$$v_g = \frac{d\omega}{d\beta_q} = 1/\frac{d\beta_q}{d\omega} \qquad \text{(a.11)}$$

Using the product rule to find the derivatives of product of two functions, it may be stated thus:

$$\frac{d}{d\omega}(u\cdot v) = u\cdot\frac{dv}{d\omega} + v\cdot\frac{du}{d\omega} \qquad \text{(a.12)}$$

so

$$u = \frac{\omega n_{co}}{c}, \quad \frac{du}{d\omega} = \frac{n_{co}}{c}, \qquad \text{(a.13)}$$

$$v = \left[1-\frac{2NAn_{co}^2 cq}{\omega\rho}\right]^{\frac{1}{2}} \qquad \text{(a.14)}$$

For computing $\frac{dv}{d\omega}$, the derivative of the composition of two or more functions can be solved by chain rule,

$$\frac{df}{d\omega} = \frac{df}{dg}\cdot\frac{dg}{d\omega} \qquad \text{(a.15)}$$

Let

$$g = \left[1-\frac{2NAn_{co}^2 cq}{\omega\rho}\right], \quad f = g^{\frac{1}{2}} = v,$$

therefore,
$$\frac{df}{dg} = \frac{1}{2} g^{-\frac{1}{2}} = \frac{1}{2}\left[1 - \frac{2NAn_{co}^2 cq}{\omega\rho}\right]^{-\frac{1}{2}} \qquad \text{(a.16)}$$

$$\frac{dg}{d\omega} = \left(\frac{2NAn_{co}^2 cq}{\omega\rho}\right)\frac{1}{\omega}, \qquad \text{(a.17)}$$

$$\frac{df}{d\omega} = \frac{df}{dg}\cdot\frac{dg}{d\omega} = \frac{1}{2}\left[1 - \frac{2NAn_{co}^2 cq}{\omega\rho}\right]^{-\frac{1}{2}} \cdot \left(\frac{2NAn_{co}^2 cq}{\omega\rho}\right)\frac{1}{\omega} \qquad \text{(a.18)}$$

Simplifying of the Equation a.18:

$$\frac{df}{d\omega} = \frac{dv}{d\omega} = \frac{\sqrt{\omega\rho}}{\omega}\cdot\frac{1}{\sqrt{\omega\rho - 2NAn_{co}^2 cq}}\cdot\left(\frac{NAn_{co}^2 cq}{\omega\rho}\right) \qquad \text{(a.19)}$$

Multiply Equation a.19 and left hand part of Equation a.13 together,

$$u\cdot\frac{dv}{d\omega} = n_{co}\cdot\sqrt{\omega\rho}\cdot\frac{1}{\sqrt{\omega\rho - 2NAn_{co}^2 cq}}\cdot\left(\frac{NAn_{co}^2 q}{\omega\rho}\right)$$

$$= n_{co}\cdot\sqrt{\omega\rho}\cdot\frac{1}{\sqrt{\omega\rho - 2NAn_{co}^2 cq}}\cdot\left(\frac{NAn_{co}^2 q}{\sqrt{\omega\rho}\cdot\sqrt{\omega\rho}}\right)$$

$$= n_{co}\cdot\frac{1}{\sqrt{\omega\rho - 2NAn_{co}^2 cq}}\cdot\left(\frac{NAn_{co}^2 q}{\sqrt{\omega\rho}}\right) \qquad \text{(a.20)}$$

Similarly,

$$v\cdot\frac{du}{d\omega} = \frac{n_{co}}{c}\cdot\left(1 - \frac{2NAn_{co}^2 cq}{\omega\rho}\right)^{\frac{1}{2}}$$

$$= \frac{n_{co}}{c}\cdot\left(\omega\rho - 2NAn_{co}^2 cq\right)^{\frac{1}{2}}\cdot\left(\omega\rho\right)^{-\frac{1}{2}}$$

$$= \sqrt{\omega\rho - 2NAn_{co}^2 cq}\cdot\frac{n_{co}}{c\sqrt{\omega\rho}} \qquad \text{(a.21)}$$

Substituting a.20 and a.21 into a.12,

$$\frac{d\beta_q}{d\omega} = u\cdot\frac{dv}{d\omega} + v\cdot\frac{du}{d\omega}$$

$$= n_{co} \cdot \frac{1}{\sqrt{\omega\rho - 2NAn_{co}^2 cq}} \cdot \left(\frac{NAn_{co}^2 q}{\sqrt{\omega\rho}} \right) + \sqrt{\omega\rho - 2NAn_{co}^2 cq} \cdot \frac{n_{co}}{c\sqrt{\omega\rho}}$$

$$= \frac{n_{co}}{\sqrt{\omega\rho}} \cdot \frac{NAn_{co}^2 q}{\sqrt{\omega\rho - 2NAn_{co}^2 cq}} + \frac{n_{co}}{c\sqrt{\omega\rho}} \cdot \sqrt{\omega\rho - 2NAn_{co}^2 cq}$$

$$= \frac{n_{co}}{c\sqrt{\omega\rho}} \cdot \left(\frac{NAn_{co}^2 qc}{\sqrt{\omega\rho - 2NAn_{co}^2 cq}} + \sqrt{\omega\rho - 2NAn_{co}^2 cq} \right)$$

$$= \frac{n_{co}}{c\sqrt{\omega\rho}} \cdot \left(\frac{NAn_{co}^2 qc + \omega\rho - 2NAn_{co}^2 cq}{\sqrt{\omega\rho - 2NAn_{co}^2 cq}} \right)$$

$$= \frac{n_{co}}{c\sqrt{\omega\rho}} \cdot \left(\frac{\omega\rho - NAn_{co}^2 cq}{\sqrt{\omega\rho - 2NAn_{co}^2 cq}} \right) \qquad \text{(a.22)}$$

(c) Derivation of Modal time delay in any index profile α GI-MMF

$$\beta_q = \left(\frac{\omega n_{co}}{c} \right) \left[1 - \left(\frac{NA}{n_{co}} \right)^2 \left(\frac{\alpha + 2}{\alpha} \right)^{\frac{\alpha}{\alpha+2}} \left(\frac{\sqrt{2}qc}{\rho\omega NA} \right)^{\frac{2\alpha}{\alpha+2}} \right]^{\frac{1}{2}} \qquad \text{(a.23)} \quad [3,9]$$

$$V_g = \frac{d\omega}{d\beta_q} = 1 / \frac{d\beta_q}{d\omega} \qquad \text{(a.24)}$$

$$u = \frac{\omega n_{co}}{c}, \quad \frac{du}{d\omega} = \frac{n_{co}}{c} \qquad \text{(a.25)}$$

$$v = \left[1 - \left(\frac{NA}{n_{co}} \right)^2 \left(\frac{\alpha + 2}{\alpha} \right)^{\frac{\alpha}{\alpha+2}} \left(\frac{\sqrt{2}qc}{\rho\omega NA} \right)^{\frac{2\alpha}{\alpha+2}} \right]^{\frac{1}{2}} \qquad \text{(a.26)}$$

$$\frac{d\beta_q}{d\omega} = u \cdot \frac{dv}{d\omega} + v \cdot \frac{du}{d\omega} \qquad \text{(a.27)}$$

Setting $g = \left[1 - \left(\frac{NA}{n_{co}}\right)^2 \left(\frac{\alpha+2}{\alpha}\right)^{\frac{\alpha}{\alpha+2}} \left(\frac{\sqrt{2}qc}{\rho\omega NA}\right)^{\frac{2\alpha}{\alpha+2}}\right]$ $\qquad f = g^{\frac{1}{2}} = v$ (a.28)

$$\frac{dv}{d\omega} = \frac{df}{d\omega} = \frac{df}{dg} \cdot \frac{dg}{d\omega} \tag{a.29}$$

$$\frac{df}{dg} = \frac{1}{2} g^{-\frac{1}{2}} = \frac{1}{2}\left[1 - \left(\frac{NA}{n_{co}}\right)^2 \left(\frac{\alpha+2}{\alpha}\right)^{\frac{\alpha}{\alpha+2}} \left(\frac{\sqrt{2}qc}{\rho\omega NA}\right)^{\frac{2\alpha}{\alpha+2}}\right]^{-\frac{1}{2}} \tag{a.30}$$

$$\frac{dg}{d\omega} = -\left(\frac{NA}{n_{co}}\right)^2 \left(\frac{\alpha+2}{\alpha}\right)^{\frac{\alpha}{\alpha+2}} \left(\frac{\sqrt{2}qc}{\rho NA} \cdot \omega^{-1}\right)^{\frac{2\alpha}{\alpha+2}} \left(\omega^{-1}\right)\left(-\frac{2\alpha}{\alpha+2}\right) \tag{a.31}$$

$$= \left(\frac{NA}{n_{co}}\right)^2 \left(\frac{\alpha+2}{\alpha}\right)^{\frac{\alpha}{\alpha+2}} \left(\frac{2\alpha}{\alpha+2}\right)\left(\frac{\sqrt{2}qc}{\rho NA\omega}\right)^{\frac{2\alpha}{\alpha+2}} \left(\frac{1}{\omega}\right)$$

$$= \left(\frac{NA}{n_{co}}\right)^2 \left(\frac{\alpha}{\alpha+2}\right)^{-\frac{\alpha}{\alpha+2}} \left(2 \cdot \frac{\alpha}{\alpha+2}\right)\left(\frac{\sqrt{2}qc}{\rho NA\omega}\right)^{\frac{2\alpha}{\alpha+2}} \left(\frac{1}{\omega}\right)$$

$$= \frac{2}{\omega}\left(\frac{NA}{n_{co}}\right)^2 \left(\frac{\sqrt{2}qc}{\rho NA\omega}\right)^{\frac{2\alpha}{\alpha+2}} \left(\frac{\alpha}{\alpha+2}\right)^{\left(-\frac{\alpha}{\alpha+2}+1\right)}$$

$$= \frac{2}{\omega}\left(\frac{NA}{n_{co}}\right)^2 \left(\frac{\sqrt{2}qc}{\rho NA\omega}\right)^{\frac{2\alpha}{\alpha+2}} \left(\frac{\alpha}{\alpha+2}\right)^{\left(\frac{2}{\alpha+2}\right)}$$

$$\frac{dv}{d\omega} = \frac{df}{dg} \cdot \frac{dg}{d\omega}$$

$$= \frac{1}{\omega}\left(\frac{NA}{n_{co}}\right)^2 \left(\frac{\sqrt{2}qc}{\rho NA\omega}\right)^{\frac{2\alpha}{\alpha+2}} \left(\frac{\alpha}{\alpha+2}\right)^{\left(\frac{2}{\alpha+2}\right)} \cdot \left[1 - \left(\frac{NA}{n_{co}}\right)^2 \left(\frac{\alpha+2}{\alpha}\right)^{\frac{\alpha}{\alpha+2}} \left(\frac{\sqrt{2}qc}{\rho\omega NA}\right)^{\frac{2\alpha}{\alpha+2}}\right]^{-\frac{1}{2}} \tag{a.32}$$

$$u \cdot \frac{dv}{d\omega} = \frac{n_{co}}{c}\left(\frac{NA}{n_{co}}\right)^2\left(\frac{\sqrt{2}qc}{\rho NA\omega}\right)^{\frac{2\alpha}{\alpha+2}}\left(\frac{\alpha}{\alpha+2}\right)^{\left(\frac{2}{\alpha+2}\right)}\cdot\left[1-\left(\frac{NA}{n_{co}}\right)^2\left(\frac{\alpha+2}{\alpha}\right)^{\frac{\alpha}{\alpha+2}}\left(\frac{\sqrt{2}qc}{\rho\omega NA}\right)^{\frac{2\alpha}{\alpha+2}}\right]^{-\frac{1}{2}} \tag{a.33}$$

$$v \cdot \frac{du}{d\omega} = \frac{n_{co}}{c}\left[1-\left(\frac{NA}{n_{co}}\right)^2\left(\frac{\alpha+2}{\alpha}\right)^{\frac{\alpha}{\alpha+2}}\left(\frac{\sqrt{2}qc}{\rho\omega NA}\right)^{\frac{2\alpha}{\alpha+2}}\right]^{\frac{1}{2}} \tag{a.34}$$

$$\frac{d\beta_q}{d\omega} = u \cdot \frac{dv}{d\omega} + v \cdot \frac{du}{d\omega} \tag{a.35}$$

$$= \frac{n_{co}}{c}\left\{1-\left(\frac{NA}{n_{co}}\right)^2\left(\frac{\alpha+2}{\alpha}\right)^{\frac{\alpha}{\alpha+2}}\left(\frac{\sqrt{2}qc}{\rho\omega NA}\right)^{\frac{2\alpha}{\alpha+2}}\right\}^{-\frac{1}{2}} \cdot \left\{\left(\frac{NA}{n_{co}}\right)^2\left(\frac{\sqrt{2}qc}{\rho\omega NA}\right)^{\frac{2\alpha}{\alpha+2}}\left(\frac{\alpha}{\alpha+2}\right)^{\frac{2}{\alpha+2}} + \left[1-\left(\frac{NA}{n_{co}}\right)^2\left(\frac{\alpha+2}{\alpha}\right)^{\frac{\alpha}{\alpha+2}}\left(\frac{\sqrt{2}qc}{\rho\omega NA}\right)^{\frac{2\alpha}{\alpha+2}}\right]\right\}$$

Further simplify the second part of Equation a.35,

$$\left\{\left(\frac{NA}{n_{co}}\right)^2\left(\frac{\sqrt{2}qc}{\rho\omega NA}\right)^{\frac{2\alpha}{\alpha+2}}\left(\frac{\alpha}{\alpha+2}\right)^{\frac{2}{\alpha+2}} + \left[1-\left(\frac{NA}{n_{co}}\right)^2\left(\frac{\alpha+2}{\alpha}\right)^{\frac{\alpha}{\alpha+2}}\left(\frac{\sqrt{2}qc}{\rho\omega NA}\right)^{\frac{2\alpha}{\alpha+2}}\right]\right\}$$

$$= 1 + \left\{\left(\frac{NA}{n_{co}}\right)^2\left(\frac{\sqrt{2}qc}{\rho\omega NA}\right)^{\frac{2\alpha}{\alpha+2}}\left(\frac{\alpha}{\alpha+2}\right)^{\frac{2}{\alpha+2}} - \left(\frac{NA}{n_{co}}\right)^2\left(\frac{\alpha+2}{\alpha}\right)^{\frac{\alpha}{\alpha+2}}\left(\frac{\sqrt{2}qc}{\rho\omega NA}\right)^{\frac{2\alpha}{\alpha+2}}\right\}$$

$$= 1 + \left\{\left(\frac{NA}{n_{co}}\right)^2\left(\frac{\sqrt{2}qc}{\rho\omega NA}\right)^{\frac{2\alpha}{\alpha+2}} \cdot \left[\left(\frac{\alpha}{\alpha+2}\right)^{\frac{2}{\alpha+2}} - \left(\frac{\alpha+2}{\alpha}\right)^{\frac{\alpha}{\alpha+2}}\right]\right\}$$

$$= 1 - \left\{\left(\frac{NA}{n_{co}}\right)^2\left(\frac{\sqrt{2}qc}{\rho\omega NA}\right)^{\frac{2\alpha}{\alpha+2}} \cdot \left[\left(\frac{\alpha+2}{\alpha}\right)^{\frac{\alpha}{\alpha+2}} - \left(\frac{\alpha}{\alpha+2}\right)^{\frac{2}{\alpha+2}}\right]\right\}$$

$$=1-\left\{\left(\frac{NA}{n_{co}}\right)^2\left(\frac{\sqrt{2}qc}{\rho\omega NA}\right)^{\frac{2\alpha}{\alpha+2}}\cdot\left\{\left(\frac{\alpha}{\alpha+2}\right)^{\frac{2}{\alpha+2}}\cdot\left[\left(\frac{\alpha}{\alpha+2}\right)^{\frac{2+\alpha}{\alpha+2}}-1\right]\right\}\right\}$$

$$=1-\left\{\left(\frac{NA}{n_{co}}\right)^2\left(\frac{\sqrt{2}qc}{\rho\omega NA}\right)^{\frac{2\alpha}{\alpha+2}}\cdot\left[\left(\frac{\alpha}{\alpha+2}\right)^{\frac{2}{2+\alpha}}\left(\frac{2}{\alpha}\right)\right]\right\} \qquad \text{(a.36)}$$

Rearrange the $\frac{d\beta_q}{d\omega}=\frac{n_{co}}{c}\left\{1-\left(\frac{NA}{n_{co}}\right)^2\left(\frac{\alpha+2}{\alpha}\right)^{\frac{\alpha}{\alpha+2}}\left(\frac{\sqrt{2}qc}{\rho\omega NA}\right)^{\frac{2\alpha}{\alpha+2}}\right\}^{-\frac{1}{2}}\cdot$

$$\left\{1-\left(\frac{NA}{n_{co}}\right)^2\left(\frac{\sqrt{2}qc}{\rho\omega NA}\right)^{\frac{2\alpha}{\alpha+2}}\left(\frac{\alpha}{\alpha+2}\right)^{\frac{2}{\alpha+2}}\left(\frac{2}{\alpha}\right)\right\} \qquad \text{(a.37)}$$

$$V_g=\frac{c}{n_{co}}\left\{1-\left(\frac{NA}{n_{co}}\right)^2\left(\frac{\alpha+2}{\alpha}\right)^{\frac{\alpha}{\alpha+2}}\left(\frac{\sqrt{2}qc}{\rho\omega NA}\right)^{\frac{2\alpha}{\alpha+2}}\right\}^{\frac{1}{2}}\cdot\left\{1-\left(\frac{NA}{n_{co}}\right)^2\left(\frac{\sqrt{2}qc}{\rho\omega NA}\right)^{\frac{2\alpha}{\alpha+2}}\left(\frac{\alpha}{\alpha+2}\right)^{\frac{2}{\alpha+2}}\left(\frac{2}{\alpha}\right)\right\}^{-1}$$

(a.38)

$$\tau_q=\frac{L}{V_g}=$$

$$\frac{n_{co}L}{c}\left\{1-\left(\frac{NA}{n_{co}}\right)^2\left(\frac{\alpha+2}{\alpha}\right)^{\frac{\alpha}{\alpha+2}}\left(\frac{\sqrt{2}qc}{\rho\omega NA}\right)^{\frac{2\alpha}{\alpha+2}}\right\}^{-\frac{1}{2}}\cdot\left\{1-\left(\frac{NA}{n_{co}}\right)^2\left(\frac{\sqrt{2}qc}{\rho\omega NA}\right)^{\frac{2\alpha}{\alpha+2}}\left(\frac{\alpha}{\alpha+2}\right)^{\frac{2}{\alpha+2}}\left(\frac{2}{\alpha}\right)\right\}$$

(a.39)